SCUOLA DI DOTTORATO
UNIVERSITÀ DEGLI STUDI DI MILANO-BICOCCA

Dipartimento di / Department of

Fisica “G. Occhialini”

Dottorato di Ricerca in / PhD program Fisica e Astronomia Ciclo / Cycle XXXVIII

Curriculum in Fisica dei Plasmi e Biofisica

DEVELOPMENT OF X-RAY DIAGNOSTICS AND STUDIES ON VACUUM DISCHARGES AT THE HIGH VOLTAGE PADOVA TEST FACILITY

Cognome / Surname CARUGGI Nome / Name FEDERICO

Matricola / Registration number 896465

Tutore / Tutor: dott. Marco Tardocchi

Supervisor: prof. Gabriele Croci

Coordinatore / Coordinator: prof. Stefano Ragazzi

ANNO ACCADEMICO / ACADEMIC YEAR 2024/2025

Abstract

Most of the current world research efforts for the development of power production through the process of nuclear fusion are currently invested in the realization of ITER, a magnetic confinement machine (tokamak) that aims at demonstrating the feasibility of power production with a gain factor of 10. This operation relies critically on plasma external heating systems, among which the Neutral Beam Injector (NBI) is one of the most important. The acceleration of negative ion beams up to the required energies is hindered by the issues related to high voltage holding in vacuum, as the occurrence of electrical micro-discharges and breakdown phenomena. In support of the operation of the main prototype for the development of the NBI (MITICA), the High Voltage Padova Test Facility (HVPTF) has been operating with a focus on the analysis and characterisation of the discharge phenomena in conditioning experiments in vacuum. In this context, analysis of X-ray emission has proven to be a good tool for the investigation of the processes involved. This work presents the development of different micro-pattern gaseous detectors, based on the Gaseous Electron Multiplier (GEM) technology, for the measurement of X-rays fluxes resolved in time, space and energy. The detectors were installed at HVPTF and integrated in its set of diagnostics. Data collected during multiple experimental campaigns are studied and new insights based on the analyses are proposed, to offer some justifications of the observed phenomenology. Additionally, the design and implementation of a synchronization system are presented, to enable consistent timing across instruments and supporting more robust studies in the future. The experimental activities are complemented by the development of a modular simulation framework, in which distinct processes are modelled with different software and combined to interpret the observations made on micro-discharges. The approach focuses on the interchange of particles between electrodes and on secondary processes at surfaces, aiming at an explanation of the experimental data. Preliminary results of the model are presented, together with a discussion on potential future improvements of the framework, which stands as a good first basis for interpreting past measurements and planning future targeted tests. The results of this work contribute to the study of the discharge phenomena in the experiments of HVPTF, support the operations of MITICA and, ultimately, the development of the NBI system for ITER.

Estratto

La gran parte degli sforzi odierni per lo sviluppo della produzione di energia tramite fusione nucleare è concentrata sullo sviluppo del tokamak ITER, una macchina a confinamento magnetico in stato di costruzione. ITER mira a dimostrare la fattibilità della produzione di energia con un fattore di guadagno pari a 10 e il suo funzionamento dipende in modo cruciale dai sistemi esterni di riscaldamento del plasma, tra cui l'Iniettore di Fasci Neutri (NBI). L'accelerazione di fasci di ioni negativi fino alle energie necessarie è limitata, tra le altre cose, dai problemi di tenuta di alta tensione in vuoto, dove microscariche e breakdown possono compromettere prestazioni e funzionamento. A supporto dello sviluppo del prototipo del NBI (MITICA), la High Voltage Padova Test Facility (HVPTF) opera con l'obiettivo di studiare e caratterizzare i fenomeni di scarica durante il condizionamento in vuoto. In questo contesto, lo studio dell'emissione di raggi X si è rivelato un buono strumento per la comprensione dei processi in atto. Questo lavoro descrive lo sviluppo di diversi rivelatori gassosi basati sulla tecnologia Gaseous Electron Multiplier (GEM), per la misura di flussi di raggi X con risoluzione temporale, spaziale ed energetica. I rivelatori sono stati installati presso HVPTF e integrati nel sistema diagnostico dell'esperimento. I dati acquisiti durante varie campagne sperimentali sono stati analizzati per estrarre informazioni sulla fenomenologia osservata e proporre interpretazioni coerenti con le misure. La tesi presenta inoltre lo sviluppo di un sistema di sincronizzazione dei segnali che garantisce allineamento temporale tra misure di diverse diagnostiche, permettendo correlazioni più robuste nelle analisi future. Le attività sperimentali sono complementate dallo sviluppo di un framework di simulazione modulare, in cui processi distinti sono modellati con strumenti dedicati e poi combinati per interpretare le osservazioni sperimentali delle micro-scariche. L'approccio è basato sullo scambio di particelle tra gli elettrodi e sui processi secondari alle superfici, con l'obiettivo di riprodurre le osservazioni dei dati sperimentali. Risultati preliminari e possibili miglioramenti da implementare vengono entrambi discussi, definendo il framework come una base consistente per l'interpretazione delle misure pregresse e per la pianificazione di nuovi esperimenti. I risultati di questo lavoro contribuiscono allo studio dei fenomeni di scarica presso HVPTF, supportano le operazioni di MITICA e, in ultimo, lo sviluppo dei sistemi NBI per ITER.

Contents

Introduction **1**

1 Electric discharges in vacuum **5**
1.1 DC electric discharges in gases 5
1.1.1 Townsend's theory of breakdown 7
1.2 Discharges in vacuum 9
1.2.1 Theories for breakdowns in vacuum 10
1.2.2 Electron emission models 12
1.2.3 Other influencing factors 14

2 The High Voltage Padova Test Facility **17**
2.1 The 300 kV configuration 17
2.2 The 800 kV configuration 20
2.3 Diagnostics and control systems 21
2.3.1 X-Ray diagnostics 22
2.4 Conditioning experiments 24

3 Gas Electron Multiplier Detectors **27**
3.1 Principles of operation 27
3.1.1 Soft X-rays interaction with matter 28
3.1.2 Interactions in gases 30
3.1.3 Gas Electron Multiplier foils 31
3.2 Detector design 33
3.2.1 Triple GEMs and HVGEM 33
3.2.2 Anodes and readout 34
3.2.3 Applications 36
3.3 The data analysis software 37
3.3.1 Event clusterization 37
3.3.2 Data visualization 39

4 Experimental Activities **45**
4.1 Detector characterization 46
4.1.1 Characterization of Al-coated GEM foils 50
4.2 The XR-GEM-1 detector 53

4.2.1 Installation 53
4.2.2 Preliminary tests on insulators 54
4.2.3 Needle-plane configuration 55
4.3 The XR-GEM-2 detector 75
4.3.1 Counting rate characterization 75
4.3.2 Imaging characterization 77
4.3.3 Installation and use at HVPTF 80
4.4 The XR-GEM-3 detector 82
4.5 The synchronization system 84
4.5.1 The hardware and firmware setup 84
4.5.2 The synchronization software 88

5 Modelling and Simulation **91**
5.1 Theoretical basis 91
5.2 Single phenomena simulations 94
5.2.1 Geant4 simulations 94
5.2.2 TRIM simulations 97
5.2.3 Molflow simulations 98
5.3 Integrated simulations 106
5.4 Considerations and outlook 115

Conclusions and perspectives **117**

Bibliography **119**

List of Publications **129**

Publications attached to this thesis **133**

Introduction

One of the major open problems that the scientific community is trying to tackle nowadays is the search for sustainable and clean energy sources, in order to be able to satisfy the always growing global demands, without having to rely on extensive use of fossil fuels. One of the most promising technologies standing out in this framework is nuclear fusion, a process analogous to the one that powers the sun and the stars. Fusion reactions are physical interactions where two light nuclei, under the right conditions of density and temperature, combine to form heavier products, releasing energy in the process, a process in some ways opposite to the one of fission, where a heavy nucleus is split into lighter products.

Nuclear fusion presents some clear advantages with respect to fission, as for example the abundance of fuel and the absence of long-lived radioactive waste, as well as the intrinsic absence of a chain reaction that can escape control. On the other hand, however, the technological maturity of power production through fusion is still very far from the levels of fission, with many challenges, both technological and physical, still present in the development of fusion reactors, such as the confinement of the plasma, the control of instabilities and the extraction of the produced energy.

In order for the fusion process to happen, the nuclei must be brought to very high temperatures, in order to overcome the Coulomb barrier that prevents them to get close enough to each other to interact. One of the most common methods to achieve this is to create a plasma and to confine it in a toroidal metallic structure (tokamak) by means of magnetic fields (magnetic confinement fusion), making it avoid contact with the walls. The prevalent reaction that is considered for power production is the one between deuterium and tritium, which produces a neutron and a helium nucleus, with a total energy release of 17.6 MeV. To achieve this reaction consistently, the plasma must be heated up to temperatures of the order of 100 MK.

The efforts of the European community in the research for nuclear fusion power production are currently focused on the development of magnetic confinement devices, such as tokamaks. The main efforts are currently invested, in collaboration with other parties around the world, in the construction of the ITER reactor prototype, in the south of France, an experimental toka-

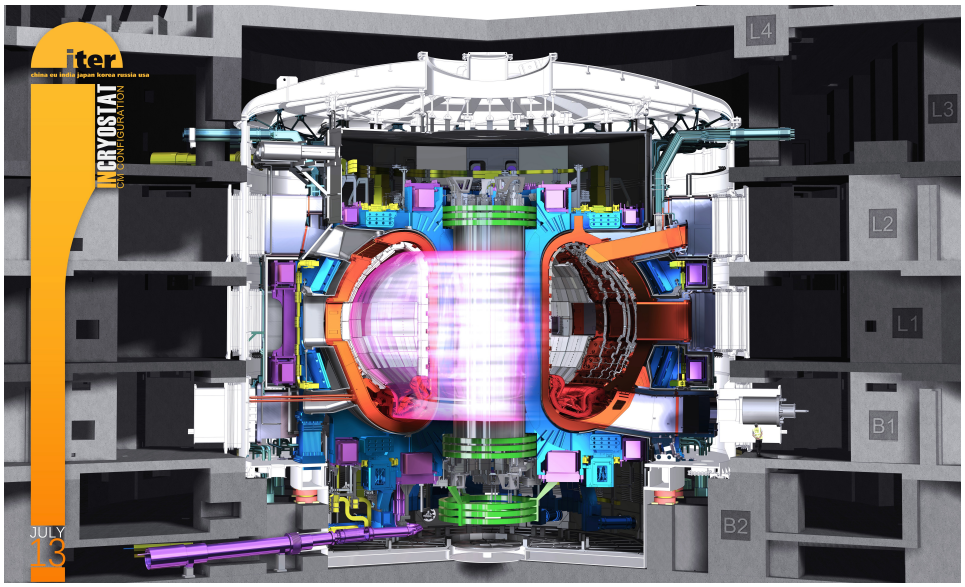

Figure 1: Render image of the ITER tokamak [ITER, 2025].

mak that aims at demonstrating the feasibility of power production through fusion with a gain factor of at least 10. At full regime, the facility will output 500 MW of thermal nuclear power with a cumulative external heating of 50 MW. According to the latest schedule, the first plasma is expected to be produced in 2034, with the first deuterium-tritium plasma in 2039 [ITER, 2025]. A rendering of the tokamak structure is shown in Figure 1.

External heating for ITER will be mostly provided by Neutral Beam Injection (NBI) technique, which relies on beams of high-speed, high-energy particles that penetrate into the plasma core, transferring their energy through collisions. ITER will be equipped with two NBI systems, each delivering up to 16.5 MW of power and operating for up to 3600 s. The NBI is based on the extraction of a 40 A negative deuterium ion beam, its acceleration up to energies of 1 MeV and its injection in the plasma after neutralization [Hemsworth et al., 2017]. A rendered image of the NBI is shown in Figure 2.

The research and development plan of ITER NBI system is mainly carried on with the activities of the Neutral Beam Test Facility (NBTF), located at Consorzio RFX, in Padova, Italy. The facility hosts two test stands: the Source for Production of Ion of Deuterium Extracted from RF plasma (SPIDER), which is a prototype of the negative ion source, and the Megavolt ITER Injector and Concept Advancement (MITICA), which is a full-scale NBI prototype, capable of full acceleration voltage and power [Toigo et al., 2017]. The SPIDER facility has been in operation since 2018, while MITICA is currently in an advanced stage of construction. One of the most critical components of MITICA, the acceleration stage, is based on a set of

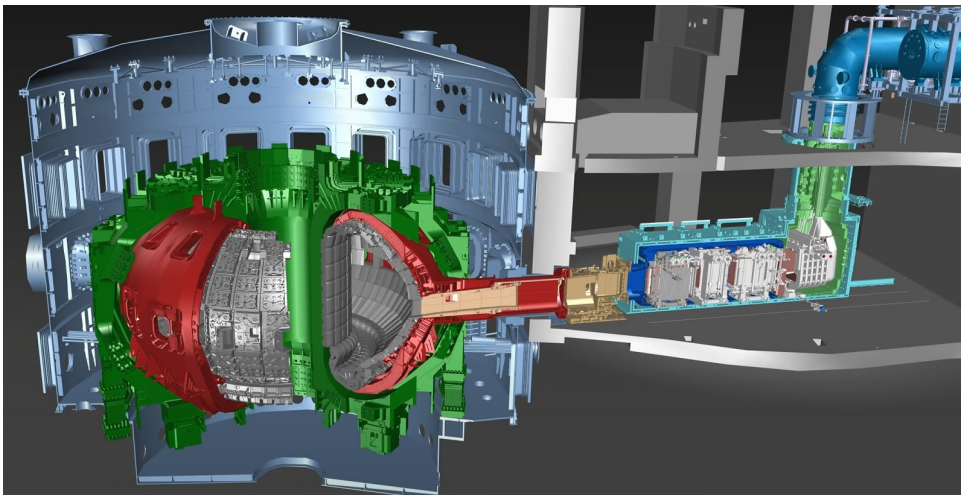

Figure 2: Render image of the NBI system for the ITER tokamak [MITICA, 2025].

5 multi-aperture grids, with progressive steps of 200 kV each, for the total acceleration voltage of 1 MV. The accelerating grids are kept in vacuum in order to avoid the formation of plasma from the ion beam, but the intense electric fields that develop in the environment can lead to the occurrence of discharges, with a risk of damage for the components of the system.

For this reason, in order to study the phenomenology of the discharges and to develop control systems for their management, the High Voltage Padova Test Facility (HVPTF) has been set up in Padova as well, in support of the operations of MITICA [De Lorenzi et al., 2011]. Studies at HVPTF mainly focus on the analysis of the signals that can be detected during the discharges, as for example X-rays, trying to correlate them with the physical processes that are happening in the system. The final aim is to characterize the discharges and to develop a control system able to foresee their occurrence, mitigating their negative effects, or preventing them from happening altogether.

This thesis presents the results of experimental campaigns of HVPTF of the past years, and the advancements in the development of the monitoring systems for the discharges. The data presented mainly refer to the Gas Electron Multiplier diagnostic, and they are then compared with results of software simulations set up in order to try to understand the phenomenology of the discharges. The rest of the thesis is organized as follows. The first chapter introduces the theoretical background of the discharges in vacuum, with a brief review of the main articles in the literature. The second chapter presents the experimental setup of the HVPTF facility and its data acquisition and control systems. The third chapter details the principles and the developments of the GEM detectors. The fourth chapter presents the exper-

imental results of the campaigns, and the advancements and developments of the monitoring systems for the discharges. The fifth chapter is focused on the development of a simulation framework to interpret the experimental data. The last chapter presents the conclusions and the future perspectives of the research.

Chapter 1

Electric discharges in vacuum

The phenomenology of electric discharges in vacuum has been subject of intensive theoretical and experimental analysis over the years. This chapter presents a brief overview of the key points of study of the field, mainly in the context of the environments which can be similar to the case of study of HVPTF.

An electric discharge is the release and transmission of electricity in an applied electric field. This flow of electric current is well known for its properties when it occurs through a medium, in which case the collisions between electrons and atoms or molecules play a critical role. Different is the case when the discharge occurs in vacuum (i.e. at very low pressures), where the mean free path of electrons in the gas is generally much greater than the distance between the electrodes. In this instance, the dynamics related to electron-gas collisions cannot fully explain the phenomena, and different theories and models were developed in the years to account for this.

1.1 DC electric discharges in gases

The first physical phenomenon to be addressed is the breakdown of the insulating properties of a gas, which is commonly initiated by the ionization of the background gas by a few free electrons. These seeding electrons can be produced by various causes, and they are accelerated by the applied electric field up to the ionization threshold of the gas, giving rise to a charge avalanche process. In order to enable this mechanism, a minimum electric field strength is required, which can also be translated to an equivalent breakdown voltage when considering a pair of electrodes at a fixed distance.

During an electric discharge, a state can be reached where the current continues to flow in the circuit even when the external ionizing source (the seeding electrons) is removed. This is referred to as a self-sustaining discharge, or Townsend discharge, and it has been demonstrated that it occurs when the applied voltage exceeds the breakdown value. On the contrary, if

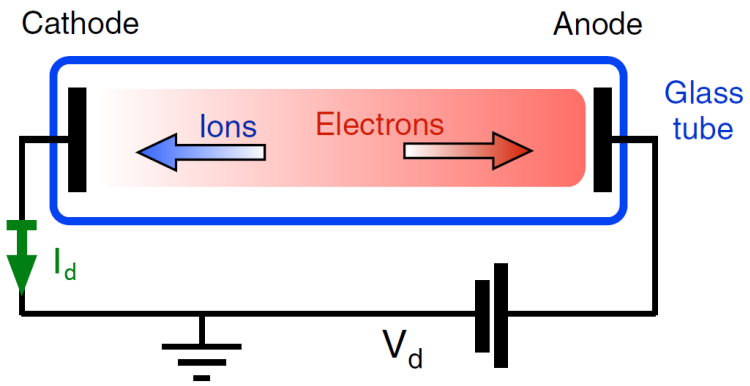

Figure 1.1: Schematic diagram of the DC discharge circuit between two parallel electrodes [Conde, 2020].

the action of the external ionizing agent is still needed for the discharge process to continue in time, the discharge is referred to as non-self-sustaining. The breakdown voltage value for DC gas discharges is influenced by characteristics of both the electrodes and the background gas. In this instance, the main factors to consider are the secondary electron emission by ion impact of the surface and the gas ionization dynamics.

A schematic representation of a DC discharge circuit between two parallel electrodes in a low pressure environment of a glass tube is shown in Figure 1.1. Referring to that diagram, the values of the discharge voltage V_d and the current I_d can define the regime of the discharge, when compared to the idealized current-voltage characteristic curve of Figure 1.2 [Conde, 2020].

With voltages below the breakdown value (on the left of point B of the plot), the currents are very low, with electron losses of the system much higher than the number of free charges produced. When the strength of the electric field is high enough to have electrons ionize the neutral gas, at the breakdown voltage, a self-sustained discharge is triggered (point B). At this point, the process of electric charge multiplication makes the current increase by orders of magnitude with only a small increase of the applied voltage (up to point C). This condition is exactly that of the Townsend discharge mentioned above, also corresponding to the so-called regime of dark discharge, due to the low intensity of the light emitted by the gas. Further increase of the discharge current leads to an intensification of the space charge effects at the electrodes and to shape the plasma potential with a non-uniform axial profile. This in turn leads to the formation of a region of ion accumulation in front of the cathode, with high electric field strength and increased local impact ionization rate. In this regime, named subnormal glow, higher currents require lower breakdown voltages to sustain the discharges (between points C and D of the plot). In the glow discharge regime (between points D and E), the discharge volume expands, electric

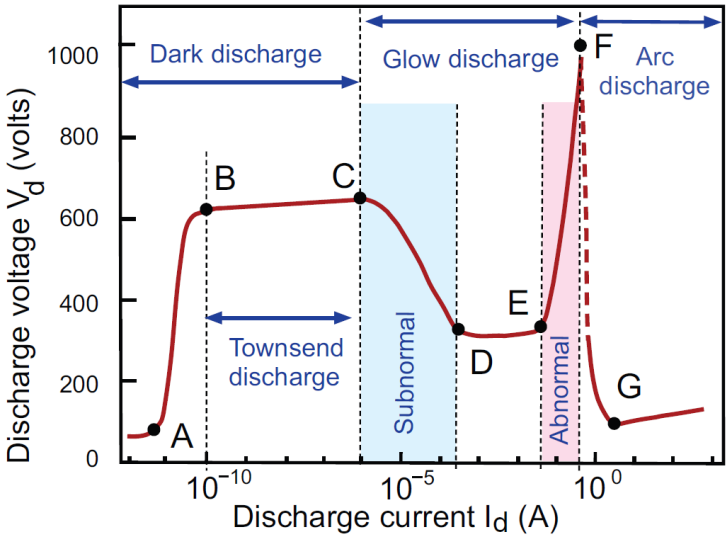

Figure 1.2: Idealized characteristic I-V curve with indications about the different discharge regimes [Conde, 2020].

charges are collected over larger surfaces of the electrodes, and for small increments in the discharge voltage the current grows, with a plateau on the I-V curve. When the glow discharge expands enough to cover all the surface of the electrodes, the abnormal regime is reached (from point E to F), and higher currents require higher voltages. As the values of the two parameters become high enough, the arc discharge regimen takes place (to the right of point F). Here, various phenomena concur in making the voltage drop as the discharge current increases, as the ionized gas becomes essentially a local thermodynamic equilibrium plasma.

1.1.1 Townsend's theory of breakdown

Following the early studies of Townsend [Townsend, 1910], the steady state experimental conditions of a gas discharge can be studied considering the motion of ions and electrons in the constant electric field between two parallel electrodes at a fixed voltage difference, following the scheme shown in Figure 1.3.

The cathode is placed at coordinate $z = 0$, the anode at coordinate $z = d$, and between the two plates, a voltage V_d is applied. Each electron moving in the inter-electrode space produces on average a number of ionization events that can be defined empirically using the first Townsend coefficient [Huxley and Crompton, 1974]:

$$\alpha = \frac{< \nu_i >}{u_d} \tag{1.1}$$

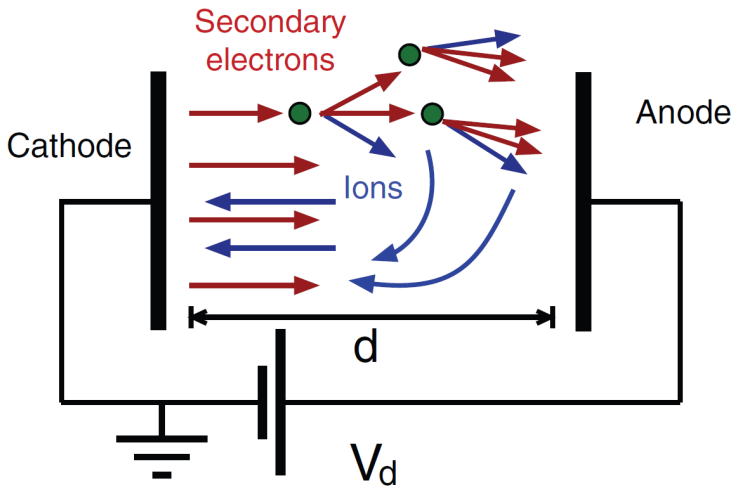

Figure 1.3: Schematic diagram of the electron multiplication in a DC discharge between two parallel electrodes [Conde, 2020].

This corresponds to the ratio between the ionization collision frequency ν_i (the average number of ionization events of an electron moving in the gas per unit time) and the component of the drift velocity of electrons along the gap, u_d. Assuming a large uniform ionization cross-section, the coefficients can be understood as the number of secondary electrons generated by an electron as it travels a unit distance in the direction of the field. Electron multiplication, or charge avalanche, is considered to be initiated by a few electrons emitted at the cathode, $N_e(0)$. The evolution along the gap (in direction z) of the number of electrons can then be modelled with:

$$dN_e(z) = N_e(0)\,\exp\left(\int_0^z \alpha(z')\,dz'\right) \approx N_e(0)\,e^{\alpha z} \tag{1.2}$$

And the number of electrons at the anode is equal to:

$$N_e(d) = N_e(0)\,e^{\alpha d} \tag{1.3}$$

Thus, from cathode to anode, the number of electrons increases as:

$$\Delta N_e = N_e(d) - N_e(0) = N_e(0)\cdot(e^{\alpha d} - 1) \tag{1.4}$$

At steady state, since ions and electrons are created in pairs, the number of ions impacting the cathode is the same as the number of electrons impacting the anode. If the electrons at the cathode are considered only to be produced by secondary emission of ion impact, modelled with the coefficient γ_{se}, we obtain:

$$N_e(0) = \Delta N_i \cdot \gamma_{se} = \Delta N_e \cdot \gamma_{se} = \gamma_{se} N_e(0)(e^{\alpha d} - 1) \tag{1.5}$$

A breakdown condition for a DC self-sustained discharge can be thus derived as:

$$\alpha\, d = \ln\left(1 + \frac{1}{\gamma_{se}}\right) \Leftrightarrow \exp\left(\int_0^z \alpha(z')\, dz'\right) = 1 + \frac{1}{\gamma_{se}} \tag{1.6}$$

An empirical formula can be introduced for the coefficient α, based on gas-specific constants (A and B) and the pressure of the inter-electrode space (p_a) [Von Engel, 1955]:

$$\alpha = A\, p_a\, \exp\left(-\frac{B}{(E_d/p_a)}\right) \tag{1.7}$$

With this, a final expression for the breakdown voltage can be derived:

$$V_b = \frac{B(p_a d)}{\ln[A(p_a d)] - \ln[\ln(1 + 1/\gamma_{se})]} \tag{1.8}$$

This equation is known as Paschen law, and it relates the DC breakdown voltage value between parallel electrodes to the product $(p_a d)$ and the secondary electron emission coefficient of the cathode γ_{se}. The curves defined by this formula for different gases are plotted in Figure 1.4.

It can be seen that the curves exhibit a minimum, named the Paschen minimum, which can be obtained by differentiating the formula and equating the derivative to zero:

$$V_{b,min} = e\frac{B}{A} \ln\left(1 + \frac{1}{\gamma_{se}}\right) \tag{1.9}$$

The corresponding minimum in $p_a d$ value is:

$$(p_a d)_{min} = \frac{e}{A} \ln\left(1 + \frac{1}{\gamma_{se}}\right) \tag{1.10}$$

This result means that at voltage values lower than $V_{b,min}$ the breakdown of a uniform field gap is not obtainable, no matter the gap distance or the pressure of the gas. Experimental values observed for breakdown voltages are generally in agreement with the predictions of Paschen law. Deviations from this simple model can be found at high pressures due to additional effects arising in importance [Kunhardt, 1990].

1.2 Discharges in vacuum

As described above, DC discharges in gas are largely determined by the properties of the gas itself, and the mechanisms are based on the extensive presence of molecules to be ionized. In vacuum, the situation is different.

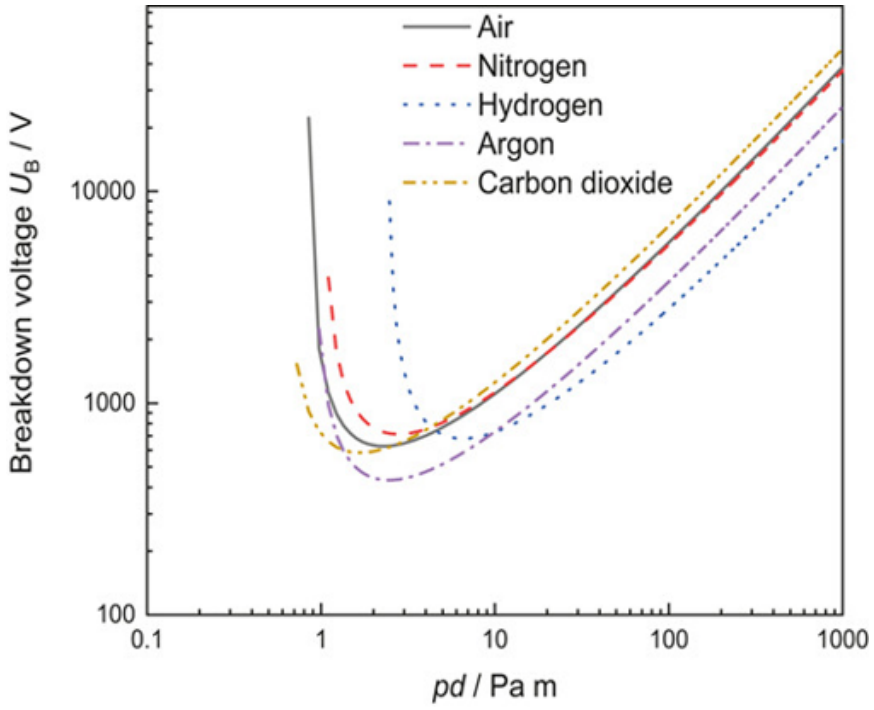

Figure 1.4: Plot of the Paschen law curve for different gases [Ollegott et al., 2020].

The experimental conditions can place the system on the left of the Paschen curve (Figure 1.4), and the early stages of breakdown cannot be explained directly by ionizing collisions in the gap volume between the electrodes. The case of electric discharges in vacuum thus needs to be studied considering the production and introduction of ionizable or ionized material in the system.

1.2.1 Theories for breakdowns in vacuum

The field of study of electric discharges in vacuum can be generally split in two main categories, although with many instances of overlapping subjects. Firstly, there is the study of electrical breakdown in vacuum, which is focused on the phenomena happening before and up to the moment of the vacuum breakdown (i.e. the occurrence of the discharge). The second branch is that of arcing in vacuum, which instead focuses on the development of the discharge after breakdown, in the cases where a quasi steady state is approached [Miller, 1990].

Theories and explanations for electrical breakdown in vacuum found in literature are generally classified in four different categories, depending on which elements of the system directly take part in the phenomenon. A suitable combination of parameters such as gap geometry, electrode material, and voltage profile, can make either one of the options the main cause of the

breakdown.

The first category is that of "clump" theories, where the detachment of a particle, or a clump, occurs from an electrode, leading to it crossing the gap and striking the other electrode with enough energy to directly trigger the breakdown.

Interaction theories instead postulate the occurrence of chain reactions among electrons, positive ions, negative ions and photons, because of which the increase in the pre-breakdown current is fast enough that the breakdown is triggered. These theories are commonly regarded as relevant only for devices such as accelerators, because they would not apply to the cases of clean vacuums and surfaces.

Cathodic theories are those based on the presence of vapour or plasma in the gap with quantities sufficient to cause breakdown in a manner similar to what has been described in section 1.1. The presence of this gaseous material is caused by the heating and vaporization of cathode material, either by Joule heating or by explosion of the projections that are interested in the field emission phenomenon, described in the following.

The last category is that of anodic theories, which usually involve both the cathode and the anode. They assume that a beam of electrons is continuously emitted from the cathode and, upon impinging on the anode, it causes different effects that in their combination trigger the breakdown. The beam can produce vapour, either by heating the anode surface and evaporating its material, or by desorption of contaminants from the surface, or both. The produced vapour is then ionized, as it is for cathodic theories, and the breakdown occurs. Alternatively, the vapour produced by the electron beam can be the cause of a regenerative process which enhances the electron current, leading to a thermal runaway in the strike region of the beam and generating enough anode vapour to trigger the breakdown. Other anodic theories state that the beam releases one particle from the anode surface, which then travels to the cathode following the electric field, and that the breakdown is then caused either by interaction of the original beam with this particle, or by strong field emission discharges between the particle and the cathode.

Instances of current exchange between electrodes in vacuum are not limited to breakdowns only, but there are also less violent phenomena that occur more frequently and do not necessarily evolve into breakdowns. These are generally classified in two families. There can be steady or quasi-steady currents emitted from cathode to anode, deriving from field emission, either by the effect of electromagnetism alone or thermally assisted. These currents are commonly caused by the presence of metal protrusions on the surface, or interfaces between insulating inclusions and the electrode metal, or other similar characteristics that act as emission sites. The other category of pre-breakdown phenomena is that of the micro-discharges, which can be defined as self-limiting bursts of current. These can be produced directly by the

detachment of small clumps of material from one electrode that follow the electric field to impinge on the other, or as a consequence of electron-induced vaporization of material on the anode surface. Micro-discharges are observed more likely when contaminants are present on the surfaces of the electrodes.

Pre-breakdown phenomena, as mentioned above, can lead directly to breakdowns, but not necessarily. Subjecting electrodes to micro-discharges in a controlled manner is known to help reduce the risk of breakdowns during operations, by removing surface imperfections and reducing outgassing occurrences. This is one example of a family of processes defined "electrode conditioning", which in general are procedures aiming at improving the original dielectric state of a vacuum gap. Other kinds of conditioning can consist of subjecting the electrodes to full breakdown events consecutively, or performing glow discharge sessions in an atmosphere of noble gas (generally argon) for positive ion bombardment, that can also help in bettering the surfaces.

1.2.2 Electron emission models

As mentioned above, one of the main occurring pre-breakdown phenomena is the development of steady or quasi-steady currents from cathode to anode. When a high voltage difference is applied between two electrodes in vacuum, a small electron emission current can be measured, and small changes in the voltage value can bring large changes in the current value, especially when close to the breakdown voltage of the gap. In order to understand why this current is generated, there is the need to mention the physical basis of the emission processes that allow free electrons at the metal boundary to escape to the gap [Farrall, 1990].

Figure 1.5 models the potential energy of an electron as a function of position, when it is near a metal surface (located at coordinate $x = 0$). On the left of the border between metal and space, the energy distribution of the free electrons inside the metal is limited under the Fermi level, with the most energetic electrons needing an energy equal to the work function of the material (ϕ) to become available outside the surface.

The potential energy of an electron in the space near a metal surface is a function of its distance from it, and it can be described with the hypothesis that there is an image of equal charge and opposite sign at the same distance inside the metal material. The resulting profile is shown in Figure 1.5b. If an electric field is applied uniformly on the metal surface, as is the case of two electrodes set at a voltage difference, the resulting potential takes the shape of Figure 1.5c, under the assumption that the metal surface under consideration is the one negatively charged (the cathode).

From the picture, it can be seen that the electrons inside the cathode metal, when near the gap, have to overcome a potential barrier to be extracted from the surface. Classical electron emission can thus happen only if

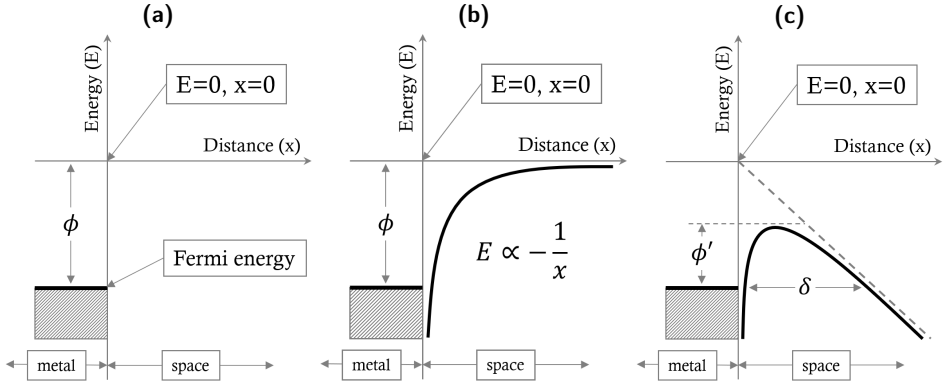

Figure 1.5: Sketch of the potential energy as a function of distance for an electron close to a metal surface. (a) In absence of fields. (b) With image charge field. (c) With both image charge and external field.

an energy higher than the work function is given to the electrons themselves with an external source. This can be done by heating the cathode, in which case a phenomenon named thermionic emission occurs, and some electrons will be extracted outside the surface generating the thermionic emission current. It can be observed that in cases where the cathode is heated, and the electric field applied is above $10^7\,\mathrm{V\,m^{-1}}$, the height of the potential barrier is effectively reduced, producing an increase in the electron emission. This condition is referred to as Schottky enhanced thermionic emission.

Introducing the principles of quantum mechanics in the formulation, the chance for the electrons to tunnel through the potential barrier without going over it becomes relevant. The probability for this phenomenon to occur strongly depends on the applied electric field, since the width of the barrier (corresponding to δ at the Fermi level) is reduced for increasing field. This occurrence of cold electron emission takes the name of field emission, and it can be explained by the formulation of the Fowler-Nordheim theory [Fowler and Nordheim, 1928, Nordheim, 1928].

Within this model, the current density J can be expressed as a function of the electric field E and the work function of the cathode material ϕ as:

$$J = 1.541 \cdot 10^{-2} \frac{E^2}{\phi\, t^2\,(y)}\ \exp\left(-6.831 \cdot 10^9 \frac{\phi^{3/2} v(y)}{E}\right) \tag{1.11}$$

Where:

$$y = \frac{3.795 \cdot 10^{-3} E^{1/2}}{\phi} \tag{1.12}$$

Functions v and t, which are tabulated, depend themselves on electric field and work function, but since they are slowly varying over the relevant

ranges of parameters, they are often replaced by constants. It is important to mention that, historically, experimental results at first seemed to be in contrast with the prediction of this model for the large surface electrodes. In particular, the emission current was observed for voltage differences lower than what expected. It is now a widely held view that this is caused by the fact that the emission phenomenon itself occurs on microscopic protrusions present on the metal surface. These sharp, needle-like defects can exhibit on their tips electric fields with magnitudes that are orders of magnitude higher than the average field across the gap. Since current density and electric field are seldom used in experiments, Equation 1.11 is commonly rewritten in terms of voltage difference and current between the electrodes, following:

$$J = \frac{I}{A} \qquad E = \beta \frac{V}{d} \tag{1.13}$$

These transformations introduce an effective emission area for the protrusion on the surface A, and an enhancement factor for the electric field at the protrusion tip β. The re-written Fowler-Nordheim equation thus becomes:

$$I = 1.541 \cdot 10^{-2} \frac{\beta^2 V^2}{\phi\, t^2(y)\, d^2} A \, \exp\left(-6.831 \cdot 10^{-9} \frac{\phi^{3/2}\, v(y)\, d}{\beta V}\right) \tag{1.14}$$

The field enhancement factor β, in particular, is of much importance for the determination of the breakdown characteristics of a vacuum gapù. In particular, various experimental findings have demonstrated that the breakdown field is essentially a constant depending on the cathode metal, named critical field (E_c). With a precise control on the conditions of the experiment, provided that the value of β is known, the breakdown voltage can theoretically be computed as:

$$V_b = \frac{E_c\, d}{\beta} \tag{1.15}$$

1.2.3 Other influencing factors

The studies on field emission and vacuum electric breakdown have spanned a vast landscape of different approaches and hypotheses, with different aspects of the phenomena being investigated in multiple works. In the following, a brief summary of the additional findings that can be relevant in the case of study of this work is presented [Farrall, 1990].

In the case of study of vacuum breakdowns over long gaps, it has been found that the critical field at the cathode needed diminishes relevantly. Additionally, various investigations have highlighted evidence that the anode, while not being the main subject of interest in the beginning of the phenomenon, can strongly influence the breakdown voltage value in these

conditions, suggesting a distinction between cathode- and anode-dominated breakdowns. These works led to consider and try to model anode related processes that can help trigger the breakdown, as for example the heating of the anode surface due to the electron bombardment. Results showed also that, together with gap length, another factor that could influence the transition from cathode to anode breakdown is the length of the voltage pulses applied to the system. Pulses of short duration can favour cathode initiated breakdown, while longer pulses are more likely to translate in anode instabilities. As mentioned above, in the case of anode contribution to the breakdown trigger, it is postulated that the discharge starts from production of vapours from the anode surface, due to bombardment heating and correlated removal of impurities.

Another aspect that can influence the vacuum breakdown phenomena in the case of electrodes with large area surfaces is the combination of multiple gas and impurity related effects that can impact on the conditions of the surfaces themselves. For example, the exposure of vacuum gaps to gas with higher pressures (but still lower than the Paschen curve limit) for short periods of time has proven beneficial to the gap performance when brought back to better vacuum, for a number of combinations of electrode metal and fill gas. This effect has been found to be consistent in time, but with the limiting factor being the approach from the left side to the Paschen curve, over which volume collisional effects become relevant and classical gas discharges can occur. There are also conditions where the phenomenon of gas desorption from the surfaces of the electrodes can influence critically the breakdown initiation in vacuum, constituting another source of vapour emission from the surfaces to be ionized. As mentioned before, microscopic metal protrusions on the metal surfaces play an important role in the vacuum breakdown initiation. This can be true also in the cases of presence of contaminants on the surfaces themselves, especially for organic residuals like oil or alcohol that can be present as a by-product of cleaning processes.

Chapter 2

The High Voltage Padova Test Facility

The High Voltage Padova Test Facility (HVPTF) is a test laboratory located in Padova, Italy, that has been set up in order to study the phenomenology of discharges in high voltage systems in vacuum. The facility is mainly employed in support of the operations of the Megavolt ITER Injector and Concept Advancement (MITICA), the Neutral Beam Injector (NBI) prototype for ITER, currently under construction at Consorzio RFX. The experimental activities of HVPTF focus on the characterization of the discharges, with the aim of developing control systems to prevent or mitigate their occurrence.

The facility has been in operation since 2010, firstly with a configuration suitable for experiments up to 300 kV DC, which was later upgraded to the current configuration, allowing for voltage differences up to 800 kV DC. The laboratory is equipped with a set of diagnostics, used to monitor the discharges in terms of physical parameters of the system and emissions coming from the chamber. This chapter presents an overview of the facility and the instruments that are hosted in it.

2.1 The 300 kV configuration

The first experimental setup was rated to carry out experiments up to 300 kV DC, and it was devoted to the studies needed for the validation of a first breakdown model developed at Consorzio RFX [Pilan et al., 2010]. The design featured a symmetric electrode structure, with two independent power supplies, and alumina feedthrough, each designed for 150 kV [De Lorenzi et al., 2011]. A plot of the electrostatic field distribution is shown in Figure 2.1, together with a picture of the setup.

The vacuum tank, made of AISI 304L stainless steel, was a 5 mm thick cylinder, with a diameter of 960 mm and a height of 759 mm, equipped with three viewports for the diagnostics and one port dedicated to the vacuum

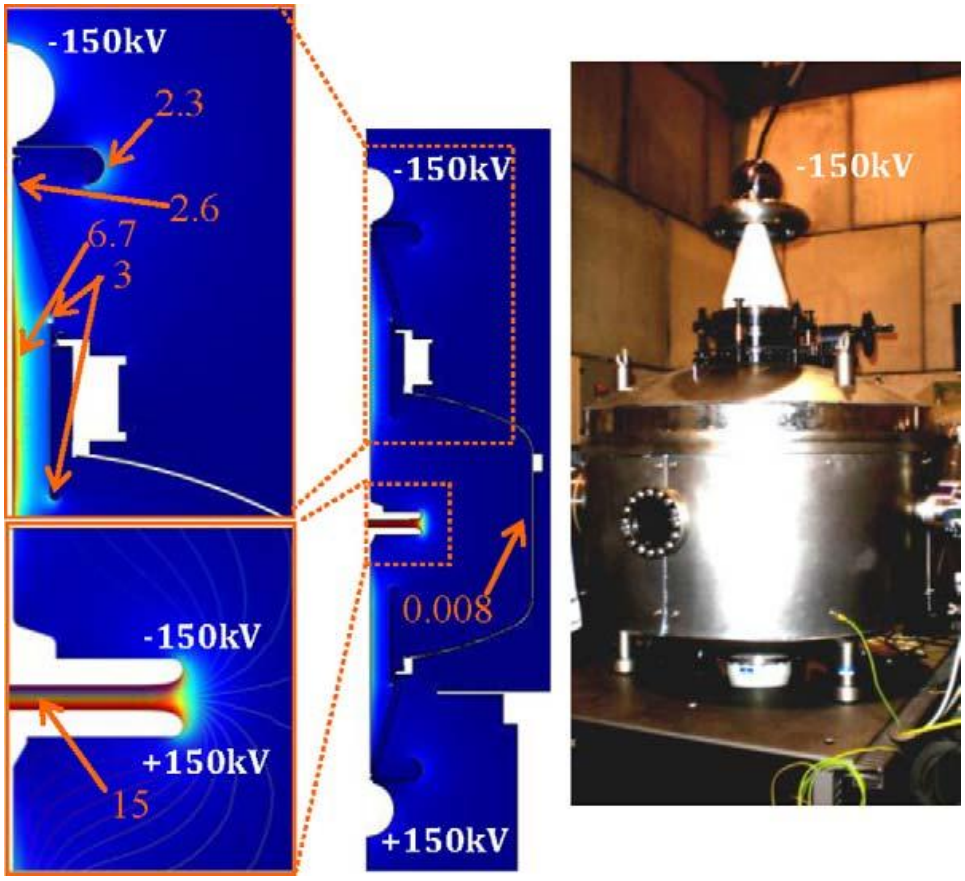

Figure 2.1: On the left: electrostatic distribution of the Electric Field (in units of $\mathrm{MV\,m^{-1}}$) in the 300 kV setup. On the right: a picture of the setup [De Lorenzi et al., 2011].

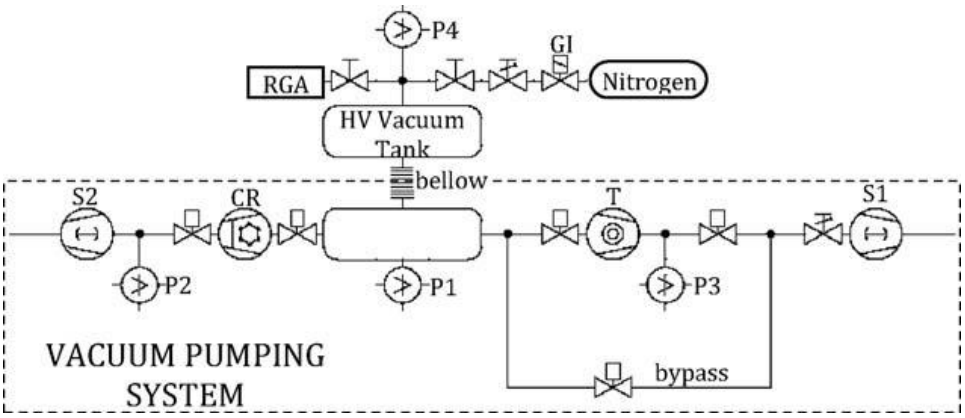

Figure 2.2: Schematic of the vacuum system of the 300 kV setup [De Lorenzi et al., 2011].

system. The inner tank surface was satin-finished, cleaned by means of ethanol, and underwent baking in vacuum up to 130 °C for 3 h. A heating cables system, temperature controlled by means of a PID circuit, was installed to reduce vacuum recovery after air venting of the tank. The vacuum system, with a dedicated vacuum chamber and based on a combination of a turbo-molecular pump, a cryopump and rotative and scroll pumps, was able to reach a pressure of 8×10^{-8} mbar only using the turbo-molecular pump, and better than 1×10^{-9} mbar with the cryopump. An ionization head pressure gauge, a Residual Gas Analyser and the electro-valve for gas injection completed the setup. The latter allowed making experiments at different pressures of different gases. A schematic of the vacuum system is shown in Figure 2.2.

Potential to the electrodes was brought by a rod brazed to the tip of the alumina cone, with the feedthrough custom designed to fit with a linear translator, manually operated, giving the ability to modify the gap length between electrodes without breaking vacuum, up to 50 mm. The independent polarization of the two electrodes was achieved with the HV circuit, as mentioned before, by means of two HV power supplies, one for the positive voltage and one for the negative. A sketch of the layout of the circuit is presented in Figure 2.3. The power supplies were equipped with a remote control interface, to act for voltage and current regulation during the experiments, and a measurement system, in order to collect current and voltage data.

The experimental campaign of this version of the facility was focused on the study of the behaviour of four sets of electrodes, mainly parallel planar ones, but also with the addition of a spherical one. The main task was the validation of a voltage holding prediction model that had been developed previously at Consorzio RFX for application on MITICA [Pilan et al., 2011].

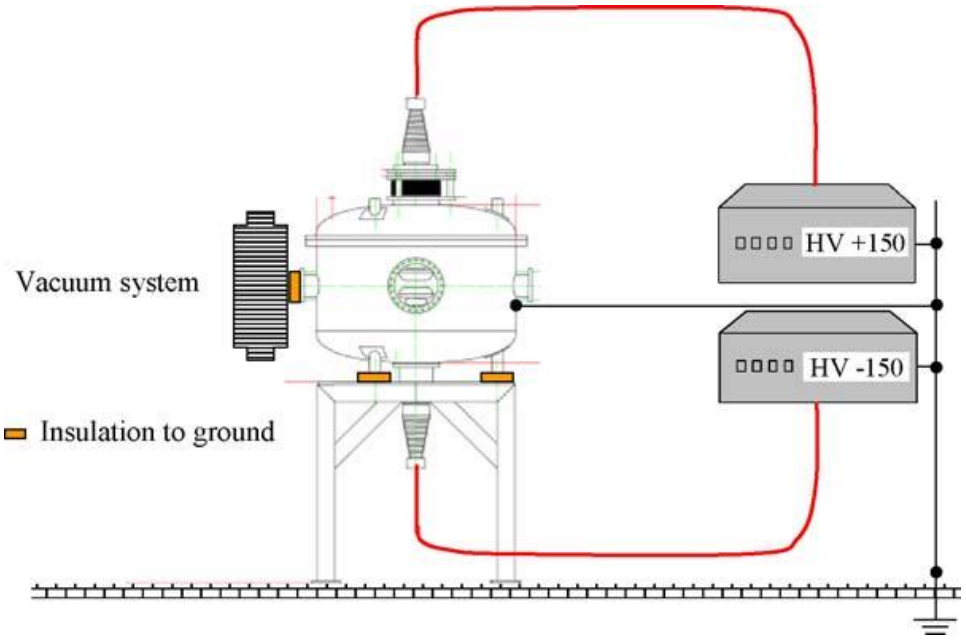

Figure 2.3: Schematic of the HV circuit of the 300 kV setup [De Lorenzi et al., 2011].

The experimental results were fairly positive, but further testing at higher voltage was deemed necessary, leading to the development of the next configuration for the facility, as a replacement for the first one [De Lorenzi et al., 2013].

2.2 The 800 kV configuration

The current experimental setup, which is the reference for this work, is composed by a horizontal axis AISI 304L vacuum tank, with a diameter of 1.2 m and a length of 2.4 m. Two independent Heinzinger power supplies, rated for ±400 kV and 1 mA each, are connected to the electrodes through two SF_6 insulated feedthroughs, with a coaxial connection which lessened the EMI problems of the previous installation. The vacuum and the control systems are directly inherited from the previous setup, with minor changes for the commands and measurements. A picture of the setup is shown in Figure 2.4.

The main upgrades that occurred from one configuration to the next one have been regarding the acquisition and control systems, with the introduction of an analog system to monitor voltage and current measurements, the addition of new pressure sensors, and the installation of a better vacuum monitoring system.

During the years, multiple experimental campaigns have been carried on in the current setup. Relevant work has been presented both in the context of

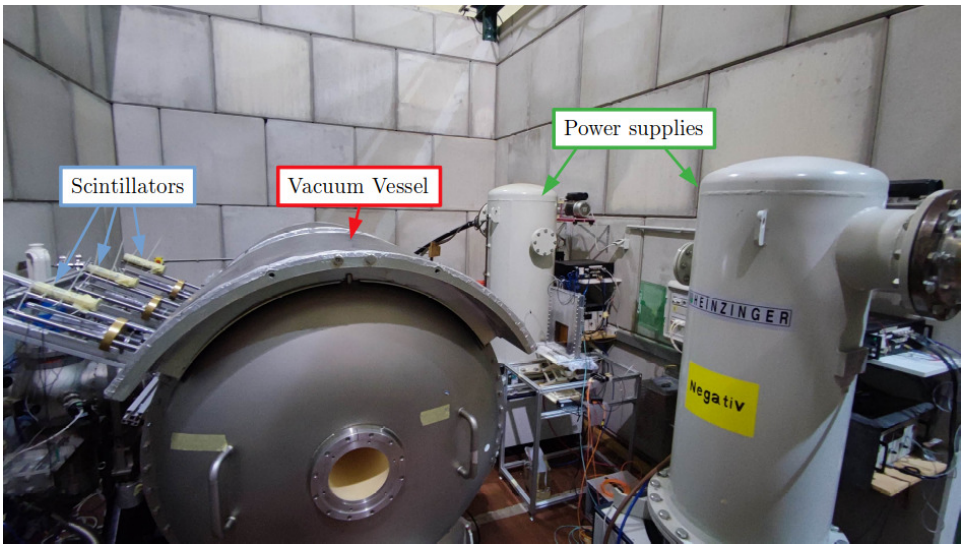

Figure 2.4: A picture of the 800 kV setup.

the study and characterization of the in-vacuum discharge phenomenology (see for example [Pilan et al., 2020, Pilan et al., 2022, Pilan et al., 2024]), and in the testing of electrical components for MITICA (especially for what concerns the electrical insulators), aiding in the design of the beam source and accelerator [Pilan et al., 2015, Marcuzzi et al., 2015].

2.3 Diagnostics and control systems

The control system designed for the first experimental setup was flexible enough to be directly implemented in the second one. The system comprises a subsystem dedicated to the Vacuum Plant, a Safety and Interlock (S&I) System and a Supervisor System, with a strategy based on the block diagram shown in Figure 2.5.

The Vacuum Control is based on a National Instruments CompactRIO 9400 (NI-CRIO 9400) controller, which is a dedicated PLC that provides the operational sequences needed to reliably reach Ultra High Vacuum (UHV). The Safety and Interlock System is implemented with hardwired fail-safe logic, and comprises mainly a sequence for the access control inside the HV area before starting the HV operation, and an inhibition rule for the Power Supplies based on the monitoring of an X-ray dose rate threshold.

The Supervisor system interacts directly with the PLC through dedicated LAN connection, in order to send start and stop sequence commands. It is interfaced with the S&I system as well, to receive the status of the interlocks and the safety signals. It is employed to send voltage and current reference waveforms to the power supplies, acquiring at the same times the analog

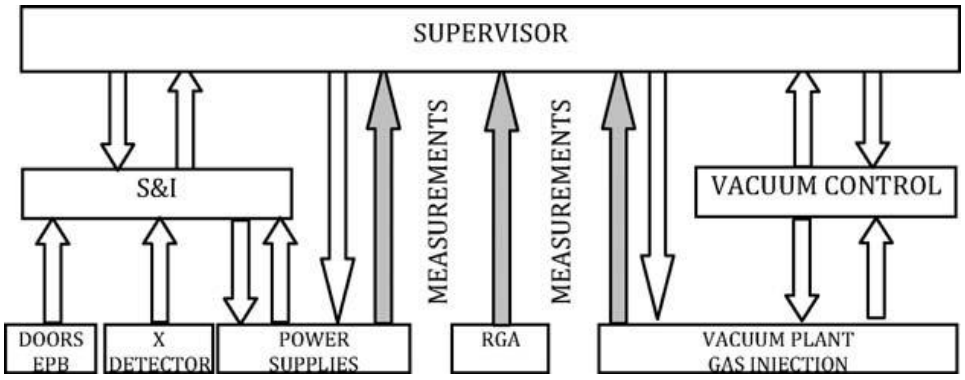

Figure 2.5: Block diagram of the control system of the HVPTF [De Lorenzi et al., 2011].

measurements (voltage and current), and to command the piezoelectric valve for gas injection, monitoring the pressure from an ionization probe and the signal from the RGA. The Supervisor System is interfaced using a platform based on the LabVIEW software, which allows to implement any kind of voltage and current waveform generation, as well as monitoring and recording data from the diagnostics, and implementing the control algorithms for the experiments.

As mentioned above, the facility hosts a variety of diagnostics systems, which can be installed on different lines of sight pointing to the interior of the vessel. The system is very flexible, with the single components being exchanged both between campaigns and during single experiments, depending on the needs of the actual measurements to be performed. The main data that is observed and collected, in addition to the analog electrical and vessel measurements (current and voltage of the power supplies and pressure in the chamber), is the emission profile coming from the electrodes during the discharges in the conditioning processes. Visible light can be observed with a fast camera (Phantom v2012 high speed camera), or other instruments sensitive to UV (EHD imaging SCM2020-UV-TR) and IR (FLIR A655sc) can be used in place. Experimental data collected with these cameras have helped in the studies and the activities of the facility [Pilan et al., 2020, Pilan et al., 2022, Pilan et al., 2024].

2.3.1 X-Ray diagnostics

During electric discharges, emitted electrons are free to travel around the vessel, and they impinge on the metal surfaces. This can lead to the emission of X-rays via the Bremsstrahlung effect, and the study of this phenomenon can be insightful in the context of the characterization of the discharge processes. In addition to electrical and optical diagnostics, thus, X-ray detectors are installed at the facility, mounted on supports across the side of the vessel. The

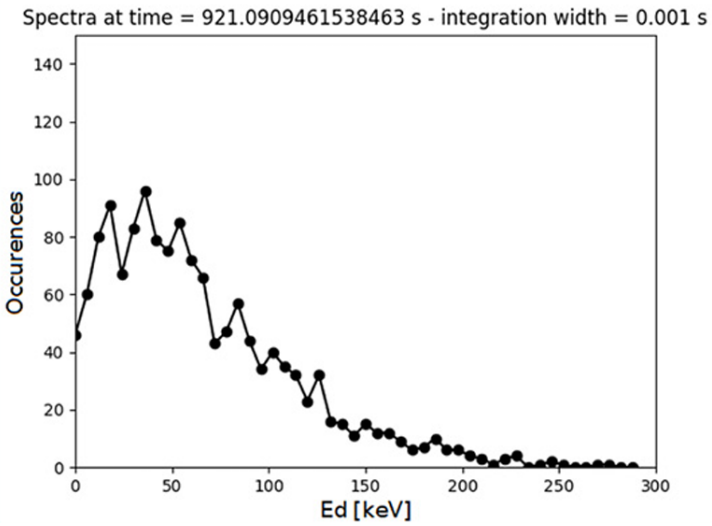

Figure 2.6: Energy spectrum of the X-ray radiation coming from the HVPTF vessel, collected with a LYSO scintillator [Kushoro et al., 2022].

mounting places can be simple mechanical structures, or they can be integrated with collimators, in order to better define and limit the line of view of the instruments. In particular, state-of-the-art detectors based on inorganic scintillation crystals, as LYSO and $LaBr_3(Ce)$, have been used in the years to characterize the X-ray emissions. Particular focus was put on the micro-discharge occurrence, leading to the verification of a correlation between the X-ray and the current signals [Spagnolo et al., 2021, Kushoro et al., 2022], and giving the basis for the experimental measurements performed in this work.

The scintillator detectors were advantageous for their good time resolution and their ability to provide spectroscopic measurements of the radiation coming from the vessel, up to energies corresponding to the voltage difference between the electrodes. This observation was instrumental in confirming that the main X-ray emission detected in the experiments at HVPTF is that of Bremsstrahlung of the electrons involved in both dark current phenomena and discharge occurrences, as shown in Figure 2.6.

Furthermore, employing multiple detectors on different lines of sight over the side of the chamber allowed for considerations related to the spatial distribution of the emission, by taking into account the ratio of count rates among the instruments. The use of the scintillators, however, presented some limitations. In particular, their high detection efficiency implies a high probability that, when the signal coming from the chamber is too intense (i.e. during discharges), the diagnostics can be affected by pile-up and even be paralysed, as detailed in [Kushoro et al., 2022].

Within this context, in recent years new X-ray detectors have been pro-

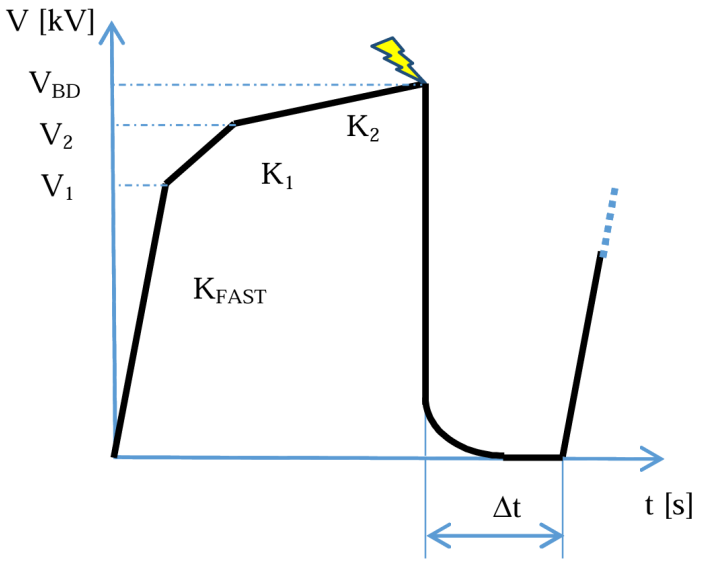

Figure 2.7: Time evolution of voltage applied during the automatic conditioning procedure [Pilan et al., 2020].

posed and installed at HVPTF, mainly based on the Gas Electron Multiplier technology. Gaseous detectors have in general a lower efficiency than scintillators and are more focused on the soft X-ray detection rather than on the full spectrum found in the previous experiments, but these characteristics can be of aid in the study of the fast transients of the micro-discharges, where scintillators can lose information due to the aforementioned pile-up occurrences. The capabilities of GEM detectors to provide a measurement of X-ray fluxes resolved in time, space and energy altogether, allow for complementary measurements to those obtained with the scintillators, leading to new studies and the results presented in the following.

2.4 Conditioning experiments

Most of the experimental measurements discussed in this work come from the analysis of electric discharges in conditioning experiments. As mentioned in the previous chapter, these procedures are generally attempts at bettering the voltage holding capabilities of electrodes in vacuum. In the case of HVPTF, the conditioning procedures are standardized and automatic, in order to guarantee a high level of reproducibility, at least for what concerns the external experimental conditions [Pilan et al., 2020]. The general structure of an automatic conditioning ramp is shown in Figure 2.7, and it is characterized by four phases.

It starts with a rapid ramp up, having a rate of voltage rise K_{FAST} of $50\,\mathrm{kV\,min^{-1}}$, that lasts up to 90% of the breakdown voltage reached in the

previous ramp (an arbitrary upper value of voltage is set for the first ramp of the experimental session). Following the fast ramp up, the rise slope is changed to K_1, equal to $1\,\mathrm{kV\,min^{-1}}$, until reaching the last breakdown voltage value. From this point, the voltage is increased even more slowly, with a rate K_2 of $0.5\,\mathrm{kV\,min^{-1}}$, until a new breakdown event occurs. Finally, the power supplies are switched off and a period Δt of 120 s is spent before turning them back on again.

During the rise in voltage, the analysis of the experimental data can help identify three threshold values: V_d, $V_{\mu d}$ and V_{BD}. The first one corresponds to the onset of the spontaneous electron emission described in section 1.2.2, with low current values and X-ray intensity, and with no significant pressure increase. $V_{\mu d}$ is the point at which the occurrence of micro-discharges starts, with current (and X-rays) bursts and gas desorption. Finally, as already described, V_{BD} is the breakdown voltage, the point at which the system is not able to recover from the fall in voltage and the power supplies switch off.

The experimental data of a conditioning ramp are shown for example in Figure 2.8. In this case, the dark current threshold V_d is about 120 kV, crossed around the time 1760 s, the micro-discharge onset $V_{\mu d}$ is reached shortly after, around 1850 s and 140 kV, and the breakdown occurs at about 2350 s, with a value for V_{BD} around 155 kV.

Additional considerations related to this example conditioning ramp, and on the X-ray data collected from the experiment, will be presented in chapter 4. Further details on other results obtained in similar conditions can be found in [Pilan et al., 2020, Pilan et al., 2022].

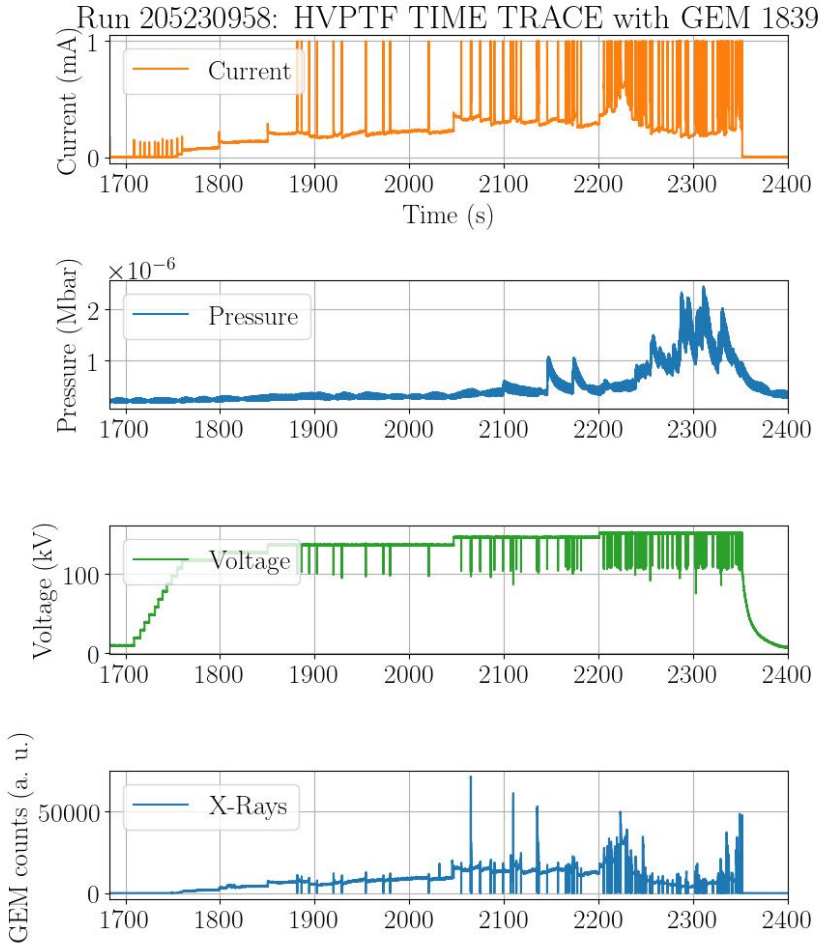

Figure 2.8: Time evolution of different signals during a conditioning ramp. From top to bottom: current, pressure, voltage and X-ray intensity are plotted.

Chapter 3

Gas Electron Multiplier Detectors

The Gas Electron Multiplier (GEM) detectors are gaseous detectors used for ionizing radiation. They are a kind of Micro-Pattern Gas Detector (MPGD), invented by F. Sauli and developed at CERN since 1997 [Sauli, 2016]. They are based on the ionization of gas by the impinging radiation and on the multiplication of the charge carriers by means of electric fields. GEM detectors generally offer advantages in terms of high signal gain, good radiation hardness, good spatial resolution, and moderate energy resolution, all combined with a high temporal resolution.

GEM detectors were initially developed as particle trackers for high-energy physics experiments, but they have been adapted for X-ray detection as single photon counting devices, or as neutron detectors when equipped with suitable converters. Due to their versatility, they are widely used in physical studies, medical imaging, and other applications. This chapter details the principles of operation of GEM detectors, their design, and the readout systems employed for them.

3.1 Principles of operation

GEM detectors, as already mentioned, are gaseous detectors. This means that the generation of the signal is based on the interaction between the radiation and the gas contained in the detector volume, followed by its amplification and transfer to a charge collection anode. In particular, as described in the following, the focus of this kind of instruments is on the detection of soft X-rays, meaning photons with energies of units or tens of keV.

3.1.1 Soft X-rays interaction with matter

Unlike charged particles, that release energy continuously on their tracks, photons interact with matter in single discrete interactions. In the case of atomic gases, the main process of photon absorption occurs with the emission of other radiation, for energies above the first ionization potential of the atom (few eV, depending on the gas mass and temperature). In the case of molecules, the existence of mechanical excitation states facilitates radiationless absorption below the ionization threshold. [Sauli, 2023] In general, the absorption probability for a mono-energetic photon beam in a uniform layer of material is described by:

$$I = I_0 e^{-\mu\rho x} = I_0 e^{-\alpha x} \tag{3.1}$$

Where I_0 is the initial photon flux, I is the transmitted one, ρ is the density of the material, and μ is called the mass absorption coefficient, which takes the units of $\mathrm{cm}^2\,\mathrm{g}^{-1}$. The product $\alpha = \mu\rho$ is the linear absorption coefficient, i.e. the probability of photon interaction per unit length of the material. This coefficient is related to the absorption cross-section of the medium through:

$$\alpha = N\sigma = N_A \frac{\rho}{A}\sigma \tag{3.2}$$

Where N is the number of atoms or molecules per unit volume, given by the ratio of density ρ over surface area A multiplied by the Avogadro number N_A. Various processes are available for the interactions of photons with matter, but the three main options are: photoelectric absorption, Compton scattering and pair production. The probability of occurrence of either one of these depends on the energy of the photon and the characteristics of the medium in terms of density and atomic number. The dependence of the cross-section components on the photon energy is displayed as an example for Tungsten in Figure 3.1.

From the onset of ionization and up to energies of few tens of keV, the dominant process is that of photoelectric absorption, in which the photon completely disappears upon interaction with an atom, transferring its energy for the extraction of a photoelectron from a bound shell, with energy equal to the difference between that of the incoming photon and the binding energy of the electron, E_b:

$$E_{e^-} = h\nu - E_b \tag{3.3}$$

The atom that participated in the photoelectric absorption process is left with an electron vacancy, which is generally quickly filled by capture of a free electron or a rearrangement of other bound electrons, which can cause the emission of one or more characteristic X-rays.

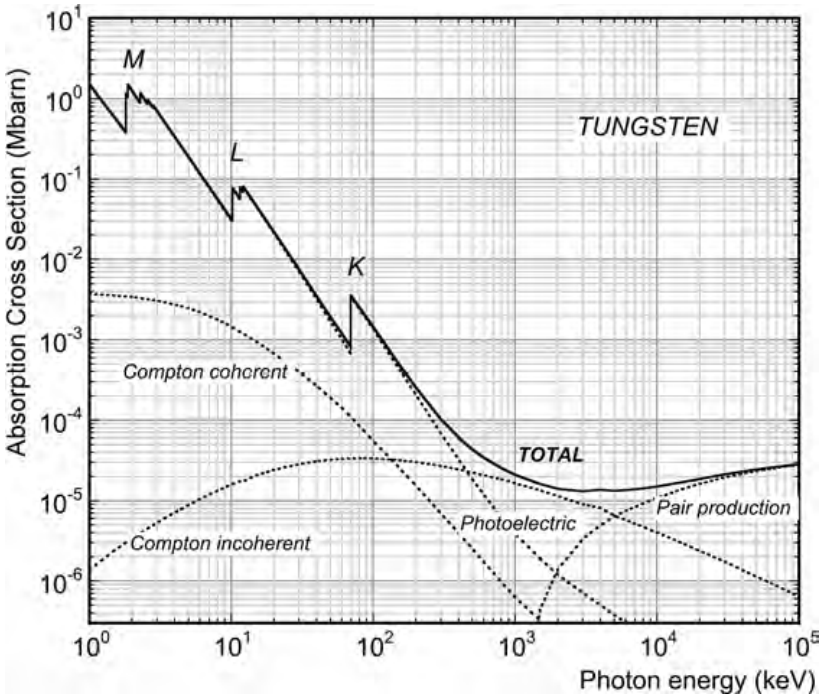

Figure 3.1: Photon absorption cross-section for tungsten, with trends of single components. [Sauli, 2023]

For higher photon energies, Compton scattering becomes more relevant. This process consists in the scattering of the photon upon hitting an electron, involving a partial energy transfer. The scattered photon energy is given by:

$$h\nu' = \frac{h\nu}{1 + \frac{h\nu}{m_e c^2}(1 - \cos\theta)} \tag{3.4}$$

Where θ is the scattering angle, m_e the electron mass and c the speed of light. The energy transferred to the electron can vary from zero, in case of forward scattering, to a maximum, corresponding to back scattering (θ = 180 deg).

For photon energies higher than double the rest mass of an electron (i.e. above 1.022 MeV), the process of pair production becomes available and gradually dominant. This interaction implies the interaction of the photon with the nucleus of an atom, with its disappearance and the production of an electron-positron pair in place, with kinetic energy equal to the excess of the initial photon energy with respect to the 1.022 MeV threshold. The positron of the pair then slows down and undergoes annihilation with an electron, generating secondary photons.

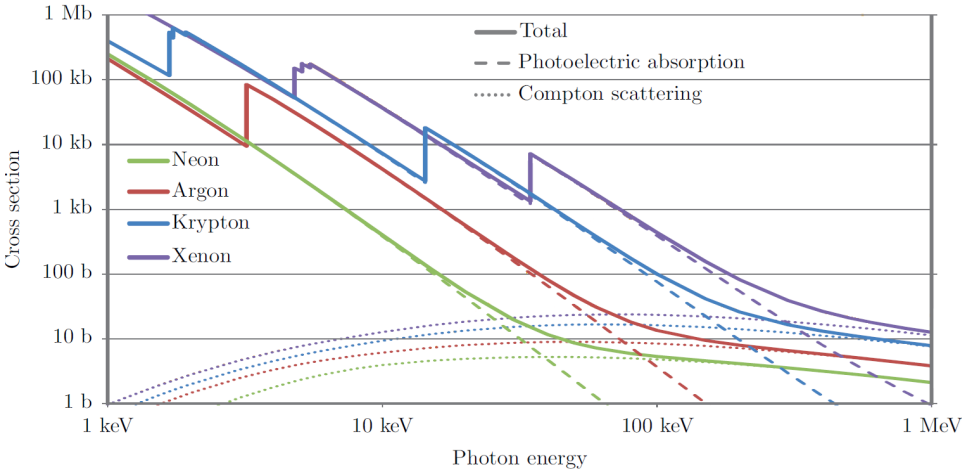

Figure 3.2: Photon absorption cross-section for the noble gases, with indication of photoelectric effect and Compton scattering components. Adapted from [Pinto, 2013]

3.1.2 Interactions in gases

In the context of gaseous radiation detectors, the dominant photon interaction process is photo-ionization, mainly through photoelectric effect, with Compton scattering becoming relevant only at the highest energies of the soft X-ray range, but other competing processes not resulting in ionization may occur. The trends of total photon absorption cross-section and its components for the noble gases which are commonly used are shown in Figure 3.2.

The number of electron-ion pairs produced by the interaction of the primary photon, and the consequent effects, can be estimated by:

$$N = \frac{E_x}{W_i} \tag{3.5}$$

Where E_x is the energy loss of the photon (equal to the total energy of the photon in case of photoelectric absorption), and W_i is the empirical average energy for the production of a pair, which is related to the ionization potential of the gas but generally higher than its value due to energy losses in non-ionizing processes.

In a gaseous detector, the charged particles produced by the radiation interaction are transported to the electrodes under influence of an external electric field. During their movement, the particles can take part in additional processes of collision and interaction with the background neutral molecules. The main occurrences relevant for gas detectors are those of charge transfer, electron attachment, recombination and secondary ionization. [Knoll, 2010]

Charge transfer collisions can occur between a positive ion and a neu-

tral gas molecule, with the transfer of one electron between them and the effective reversal of their states. Electron attachment is the production of a negative ion from the combination of a free moving electron and a neutral atom. Recombination is the neutralization of a positive ion by absorption of a free electron, or the exchange of an electron from a negative to a positive ion, resulting in the production of two neutral molecules. Finally, secondary ionization occurs when a free moving electron of sufficient energy ionizes additional neutral molecules, producing new electron-ion pairs. These process can all influence the production of signal in a gaseous detector, increasing or decreasing the number of charges travelling in the medium.

The electrons generated in the initial cluster by the interaction of the incoming radiation can also take part in the processes of excitation of the gas molecules, with the transition to a higher state and the return to ground often characterized by the emission of additional photons. In this context, the choice of gaseous mixture for a detector must be balanced in order to guarantee a reliable signal formation process, while keeping proportionality between the initial energy of the incident photon and the charge collected at the anode. The primary component of the mixture is usually a noble gas, such as argon, which has a low ionization energy, improving sensitivity to low energy photons. The primary gas is typically mixed with a secondary quenching gas, often a molecular one, such as carbon dioxide, serving several functions.

The primary role of the quenching gas is to absorb the photons emitted during atomic or molecular de-excitation process, preventing secondary ionization. The molecular gas dissipates the excess energy through vibrational and rotational modes, inhibiting further ionization and preventing the development of an uncontrolled avalanche. This leads to the possibility to use a higher external field (and thus operating with a higher signal gain) without the risk of discharges. Additionally, the use of the quenching gas reduces the mobility of the charged species in the gas mixture, which translates in a better confinement of the electron-ion pairs in the region where the radiation has interacted. While it may also increase the probability of recombination, this effect can improve the spatial resolution of the detector by limiting the spread of charge collection.

3.1.3 Gas Electron Multiplier foils

Gas Electron Multiplier foils are sheets of kapton, a polymer, 50 µm thick, metal-coated on both sides by a thin layer (5 µm) of copper (other metals like aluminium can be used as well, as in [Caruggi et al., 2023]). The foils are pierced by a high-density hexagonal pattern of holes, with a typical diameter of 70 µm and a pitch of 140 µm (see Figure 3.3). The holes are produced by a chemical etching process, and they are usually bi-conical. When a potential difference, commonly of the order of 300 V is applied between the two faces

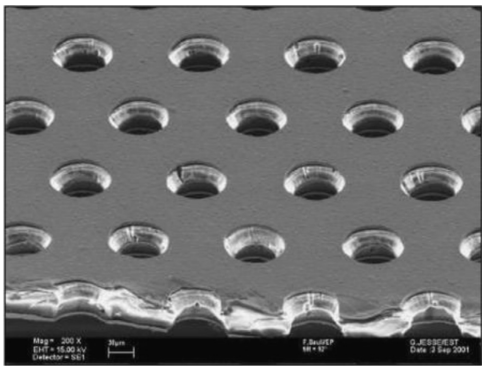

Figure 3.3: Electron microscope picture of a section of typical GEM foil. [GEM, 2025]

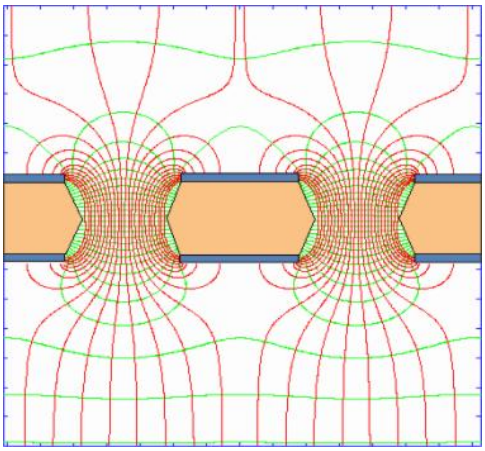

Figure 3.4: Electric field lines and equipotential in the region of holes of a GEM foil. [GEM, 2025]

of the foil, strong (of the order of $10\,\mathrm{kV\,cm^{-1}}$) and concentrated electric field dipoles are produced in the holes, with field lines and equipotential as shown in Figure 3.4.

The electric field in the holes, when combined with external electric fields in the regions surrounding the foil, allows for multiplication of the primary electrons (generated by the impinging radiation in the drift region) in the passage through the holes. The process is based on the Townsend avalanche, where the electrons, accelerated by the electric fields of the regions surrounding the foil, collide with the gas atoms in the region of the holes, ionizing them and creating more electrons. The multiplication factor is typically of the order of 10^2 to 10^3 per foil, so that the signal is greatly amplified. The use of a single GEM foil is usually not enough to reach the desired signal gain levels without risks of discharges. GEM detectors are thus composed commonly of multiple foils in a cascade configuration, to attain very high

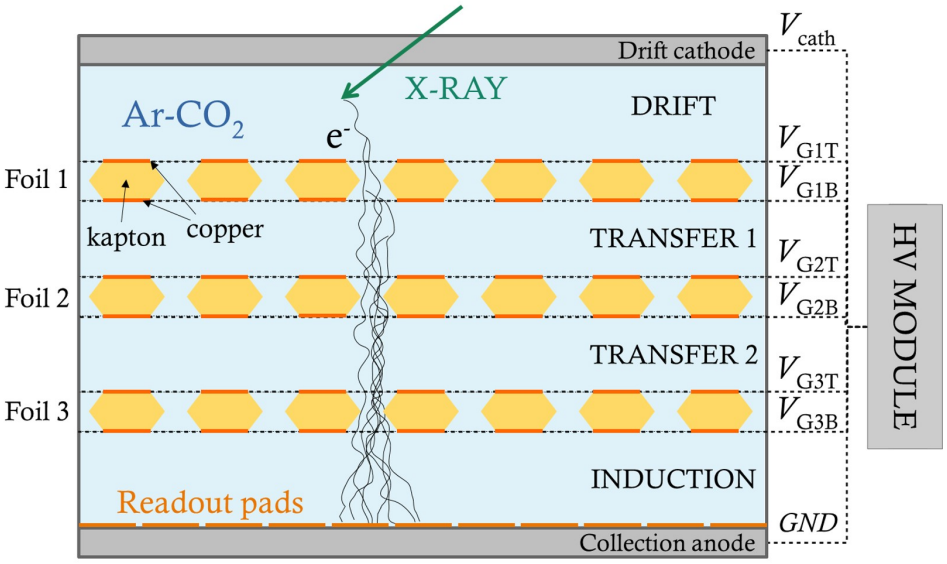

Figure 3.5: Schematic representation of a Triple-GEM detector.

proportional gains with lower voltage difference values on the single foils.

3.2 Detector design

3.2.1 Triple GEMs and HVGEM

As mentioned in the previous section, GEM detectors are usually composed of multiple foils stacked in a cascade configuration between the cathode (generally made of aluminized mylar) and the anode (for signal collection). The most common design is the Triple-GEM detector, where three foils are used in sequence, as shown schematically in Figure 3.5. The gaps between foils, set by the thickness of the frames employed to mount the foils, are generally of 2 mm, while the drift region is thicker to ensure efficient detection of the impinging radiation. The assembled detector is usually operated in an open gas flow (with dedicated inlet and outlet channels) at controlled pressure, with the foils enclosed in a gas-tight box. The standard mixture employed in GEM detectors is Ar-CO_2, with a 70-30% ratio.

For the voltage configuration, as mentioned previously, the sides of the single foil are commonly put at a potential difference of the order of 300 V. The drift cathode is put at the highest (negative) voltage, and the anode is kept at ground, while the other voltages are chosen to obtain fields in the different regions in the order of 1 kV cm^{-1} to 4 kV cm^{-1}. Voltages are set individually, using an active HV divider, called HVGEM, similar to a set of seven batteries stacked in a row [Corradi et al., 2007]. The use of a module

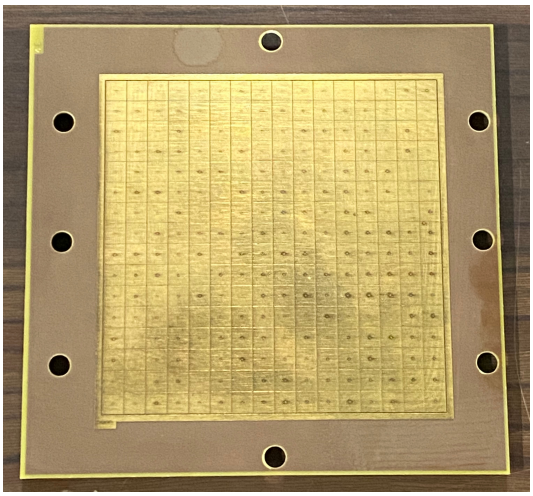

Figure 3.6: Picture of a GEM anode with a square pattern of 256 pads.

with independent channels for voltage distribution, rather than employing a more common resistor voltage divider, is particularly useful for the high rate applications. In this context, the intense signal causes a high current to flow in the circuit, leading to difficulties in keeping the voltage levels (and thus the gain values) stable when using a divider. The use of separate voltage generators for each channel assures better control of the system, as documented in a similar context in [Heifets and Margulis, 2012].

3.2.2 Anodes and readout

The collection anode of a Triple-GEM detector is commonly a printed circuit board (PCB), copper layered on one side, with a pattern of chequered pads or orthogonal strips to collect the electrons on the other. Figure 3.6 shows an image of the most common geometry employed: a square pattern of 256 pads, each with a 6 mm side. Different anode structures will be shown and commented in chapter 4.

The signal at the anode is produced by the charge induced by the electrons moving in the induction region of the detector (for more details, refer to chapter 6 of [Sauli, 2023]). The signal duration is thus dependent on the width of the induction region itself, the intensity of the field applied, and the properties of the fill gas in terms of electron mobility. With the typical values employed in this work, the resulting signal length is of about 100 ns. The anode is connected to a readout system, based on the combination of an Application-Specific Integrated Circuit (ASIC) called GEMINI, and a custom-made Field Programmable Gate Array (FPGA), developed in collaboration with Nuclear Instruments.

GEMINI is a fully-integrated analog front-end electronic system, custom

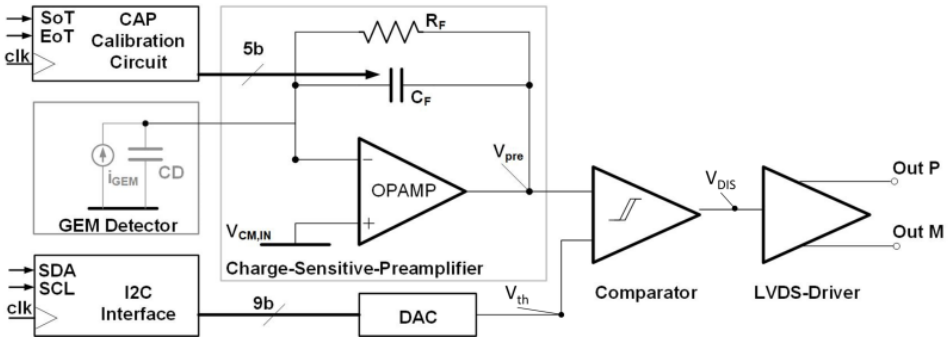

Figure 3.7: Schematic representation of a GEMINI channel. [Muraro et al., 2019]

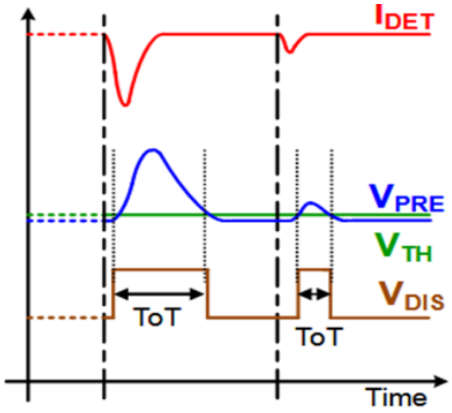

Figure 3.8: Relationship among the input channel current, the pre-amplified and the threshold voltages, and the digital output of the comparator. [Muraro et al., 2019]

developed for GEM-based detectors, in 0.18 µm CMOS technology. [Pezzotta et al., 2015] It is composed of 16 channels, each with a low-noise Charge-Sensitive Preamplifier (CSP), responsible for the charge collection, a built-in hysteresis comparator, which compares the voltage signal with a fixed threshold, and a dedicated driver for conversion into Low Voltage Differential Signal (LVDS) standard. Figure 3.7 shows a schematic of the channel structure, while Figure 3.8 displays the relationship among the input channel current, the pre-amplified and the threshold voltages, and the digital output of the comparator.

The output signal of the GEMINI ASIC is routed to the FPGA, the firmware of which is based on a series of Time to Digital Converters (TDC), sampling the input with a frequency of 2 GHz. For each signal collected on a channel, the FPGA records the information about the Time of Arrival (ToA) and the Time over Threshold (ToT) of the signal (an indirect measure of the charge), as well as the channel number (from which the position of the signal on the anode can be inferred). The data is packed in a 64-bit word structure,

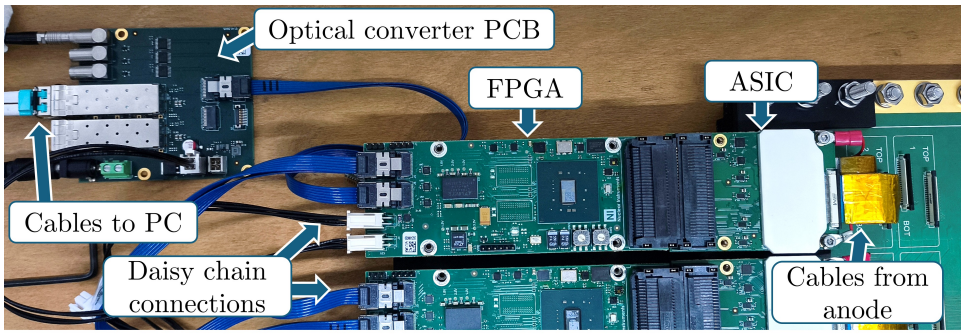

Figure 3.9: Picture of the components of the acquisition chain used for the GEM detectors in this work.

and sent to the data acquisition system through means of an optical fibre.

A picture of the physical components of the system is shown in Figure 3.9, presenting the GEMINI ASIC, the FPGA and their connections to both the anode and the PCB for optical conversion of the signals and routing to the PC. Multiple FPGAs can be connected in daisy chain layout, with each one managing the signal from 64 channels of the collection anode.

3.2.3 Applications

As mentioned above, the capabilities of GEM detectors in terms of temporal, spatial and energy resolution, together with their ability to be used in harsh radiation conditions, make them appealing for different applications in various context and environments.

Traditionally GEM detectors find their main employment in the field of High Energy Physics, as for example different experiments at CERN, such as COMPASS [Ketzer et al., 2002] and CMS [Hong, 2025]. In these applications, GEM detectors are used mainly in the context of charged particle tracking. During the years, GEM detector have found also application in other fields, such as medical imaging [Amaldi et al., 2011, Leidner et al., 2021].

GEM detectors have also been employed more recently in applications regarding soft X-ray diagnostics for nuclear fusion, finding applications on various machines as JET [Rzadkiewicz et al., 2013], MAST-U [Celora et al., 2025], KSTAR [Pacella et al., 2013] and WEST [Mazon et al., 2022], and being designed for future uses in different machines as DTT [Malinowski et al., 2021] and DEMO, where they are planned for the measurement of radiated power as well [Chernyshova et al., 2022].

The combination of a GEM detector with a suitable converter allows it to be used as a neutron detector. Neutrons, which are neutral particles that would not produce direct ionization in the gas, can be detected by means of a converter, with interactions producing charged particles. These are then detected by the GEM detector, which can provide information about the

position and the energy of the original neutron. GEM detectors have been successfully employed for the study of thermal neutrons, where the converter is made mainly of boron and the charged particles produced are alphas and lithium ions [Albani et al., 2020, Muraro et al., 2021]. They have found their use also in the study of fast neutrons, where the converter is made of plastic material and protons are produced by means of elastic (n, p) reactions on hydrogen and detected [Muraro et al., 2016].

GEM detectors have been also proposed and employed for the detection of photons, through the use of a different converter. In particular, Cherenkov detectors have been designed with the combination of GEM technology and UV-sensitive photo-cathodes as caesium iodide (CsI) [Meinschad et al., 2004, Azmoun et al., 2019, Putignano et al., 2023].

3.3 The data analysis software

The data produced by the acquisition system of the GEM detectors has its own format, which is not directly compatible with the standard data analysis tools used for other diagnostics. A new software named GEM-GUI was thus developed to allow for easy access to the data, their visualization and analysis of the results. The software was mainly developed in Python, exploiting the PyQt5 library as basis for its Graphical User Interface, and the NumPy and SciPy libraries for the main operations of data analysis. The software also comprises some C++ scripts, called through wrappers, for the operations of pre-processing needed on the raw data. The GEM-GUI software is developed to run on Linux distributions, but there have been also adaptation for its use on the Windows operative systems.

As previously mentioned, the information coming from the acquisition chain of the GEM detector is composed by 64-bit words, one for each time a channel of the anode collects charge above the threshold. The single piece of data contains information about the Time of Arrival and Time-over-Threshold of the event, together with a univocal ID for identifying the channel itself. From this data it is possible, considering detector calibration and data pre-processing, to derive the time and space distribution of the incoming radiation events and their energies. In the following, the structure of the data and the way they can be treated are described in more detail, for what concerns the two main aspects of the software: clusterization and visualization of the data. The process of calibration for the detectors is described in the next chapter.

3.3.1 Event clusterization

The use of a segmented anode in the acquisition of a detector implies an additional challenge with respect to other kinds of charge collection systems. The interaction of a single particle in the detector volume (later referred

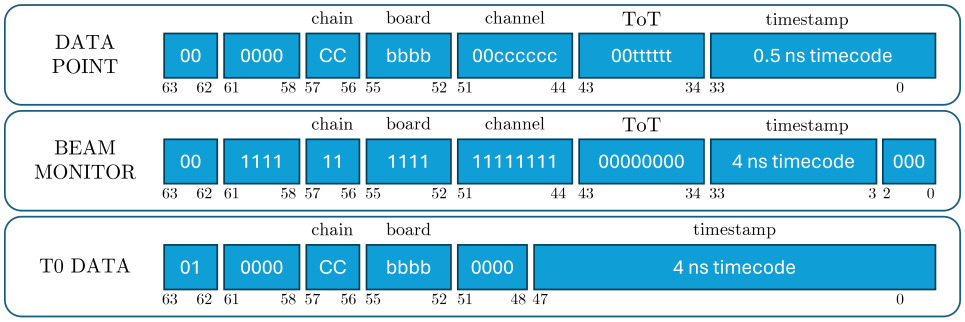

Figure 3.10: Bitwise representation of raw data produced by the GEM acquisition system.

to as "event") may cause charge collection instances (later defined "hits") in more than one channel. This implies that the original piece of information has to be reconstructed from multiple single packets. This process is commonly referred to as "clusterization", and it represents one of the main pre-processing functionalities performed on the raw data coming from the GEM detector acquisition system. It is implemented in the software with a custom C++ shared library, compiled beforehand and executed from the Python code through a wrapper from the ctypes library.

Before the clusterization process takes place, the algorithm first decrypts the 64-bit words coming from the acquisition system, recovering the information about the ToA, the ToT and the channel ID for each hit. The composition of the words is presented in Figure 3.10. The time of arrival is indicated as "timestamp", and the channel ID is derived from a combination of the "chain", "board" and "channel" information. The first 6 bits of each word are used to discriminate between charge collection events, beam monitor events (used in different tracking experiments), and ticks of the clock of the readout (indicated as "T0 DATA"). The latter are used as time references to avoid overflows in the timestamp fields.

After the data incoming from the acquisition system has been decrypted, the hits are sorted by ToA, and any spurious event is removed by the arrays. The algorithm then iterates through the list of hits, selecting the ones that could pertain the same event and combining their information together to produce the array of the particle interaction events. This is achieved by checking the hits following the first one against both a temporal and a spatial window, user defined. In most of the cases of study considered in this work, the maximum time difference between two hits to be considered part of the same event is 50 ns, and the hits need to pertain channels adjacent to each other.

The best values for the windows in time and space depend on the dimensions of the drift region and the electron mobility. Tests have been performed during the characterization processes of the detectors to verify the suitability

of the choices. As was expected, keeping the rates around 1 kHz to 10 kHz, no influence was observed from changes in the time window in the range from 20 ns to 100 ns. Other tests addressed the possibility of having some channels non-functional, so the clusterization was performed increasing the maximum spatial distance between hits up to 3 pads (about 10 mm) and, again, no significant changes were observed for the counting rates used in lab.

The final events obtained as output from the clusterization process are assigned properties calculated from the single hits. The timestamp corresponds to the one of the first hit, the charge is the sum of the charges collected by the single channels, and the channel to which the event is assigned is the one that received the most charge in the interaction. Additionally, the event has an attribute defining the number of hits that it was composed by. The clusterized list of events is saved to disk in custom binary format and is then readable from the other applications of the GEM-GUI software to display information about the data.

The clusterization algorithm is open source and can be updated, fixing issues encountered during experimental campaigns, and making it suitable for different uses and conditions.

3.3.2 Data visualization

The GEM-GUI software has been mainly developed with the aim of being a user-friendly tool, giving the ability to access and visualize data coming from the GEM detector. Through the main window of its graphical user interface (Figure 3.11), the user can access four main kinds of plot for the experimental sessions: time traces, heatmaps, energy spectra and spectrograms.

Time traces (Figure 3.12) are histograms displaying the number of events detected for a certain unit of time. Since the acquisition is asynchronous among channels, there is not a fixed time resolution for the display, but instead the time binning for the plot is chosen by the user, down to the limit of tens of nanoseconds. Heatmaps (Figure 3.13) are images of the spatial distribution of the events integrated on user-chosen time frames. The channels are displayed on a grid and each one is coloured on the basis of the number of events that it recorded. The energy spectra (Figure 3.14) are histograms of the number of events in a time frame, integrated over energy bins, again with a choice from the user for what concerns the binning. Spectrograms (Figure 3.15) are a 2D distribution of the events in terms of both time and energy binning.

The software is designed to allow, for each plot, different filters on the events, on the basis of their timestamps, energy, or on the number of hits composing the events themselves. All of these features are accessible with buttons and checkboxes, and for every plot the data can be exported to CSV files (in the case of the heatmaps, a video of the sequence of frames

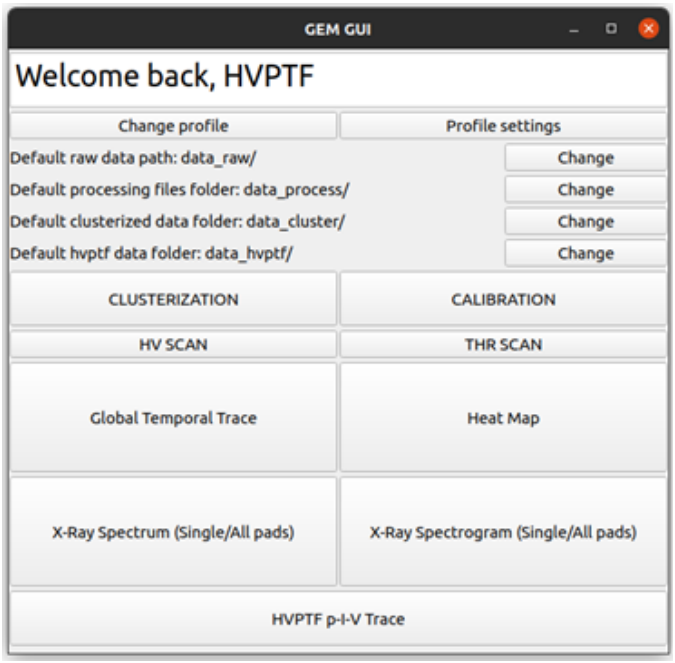

Figure 3.11: Main window of the GEM-GUI software.

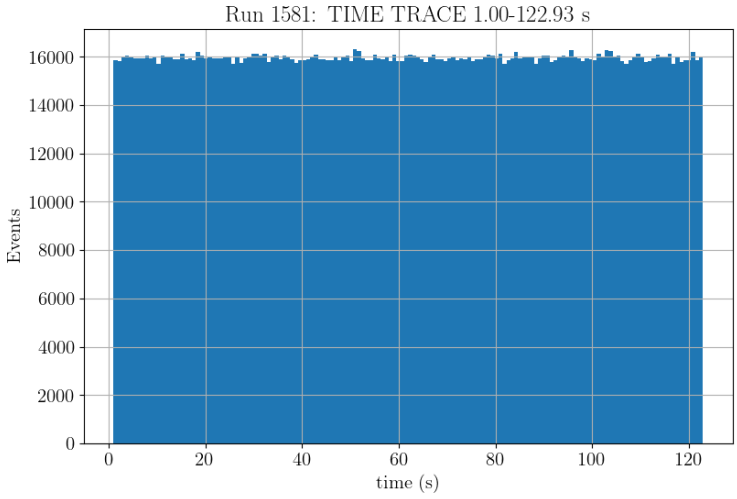

Figure 3.12: Example of time trace displayed by the GEM-GUI software.

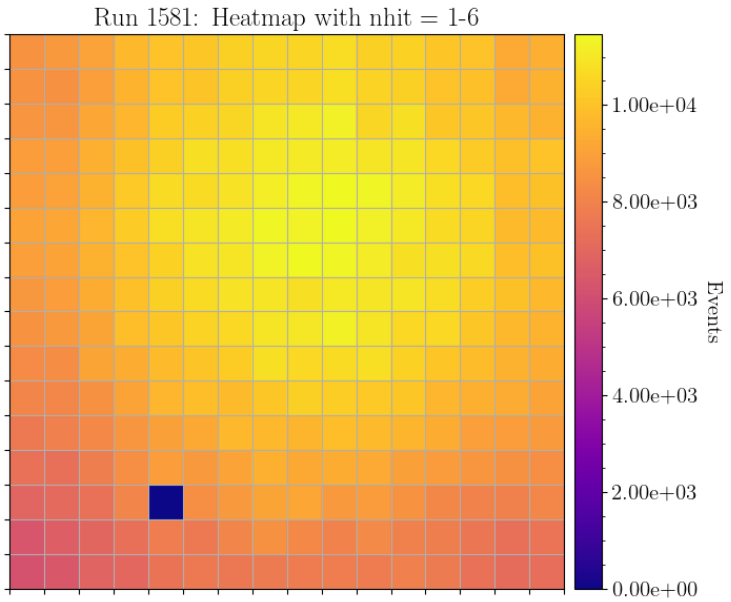

Figure 3.13: Example of heatmap displayed by the GEM-GUI software.

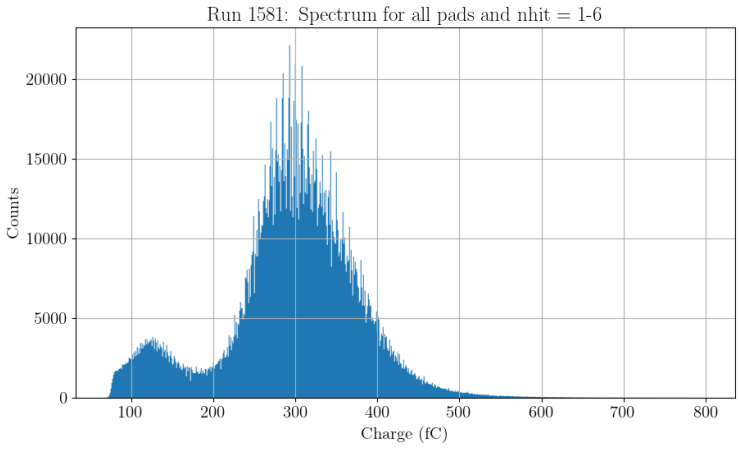

Figure 3.14: Example of energy spectrum displayed by the GEM-GUI software.

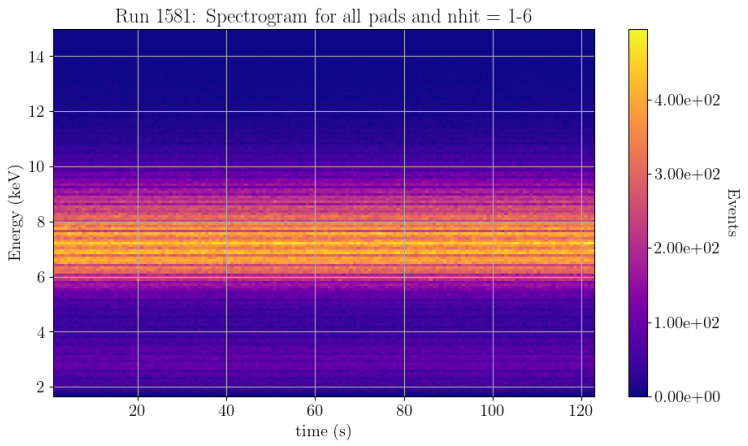

Figure 3.15: Example of spectrogram displayed by the GEM-GUI software.

can be produced as well). Additionally, different aspect of visualization are available, as the selection between linear and logarithmic scales for the axes or the possibility to switch between the absolute number of events and the count rate. The software also manages autonomously the cases in which the data to display would be too much for the plots to process, taking into account a fixed maximum number of events and subdividing the visualization in multiple time frames whenever it is surpassed, to guarantee fluid response as much as possible. For every plot, clicking on a point gives information about the data at that position, it being the number of events and corresponding event rate for a bin of the time trace, for a channel of the heatmap, for a bin of the spectrum or for one of the spectrogram.

All the different plots are interlinked via software. For example, cursor selection of one or more channels in a heatmap can produce, on a new window, the corresponding energy spectrum or time trace for those channels with the same parameters. Also, a range selector on the time traces allows to visualize the spatial or the energy distribution of the detected radiation for that period, with additional possible frame subdivision, and so on. All of these functionalities help in the data analysis processes, allowing to compare directly plots generated with different visualization parameters.

The GEM-GUI software has been used extensively in the activities of this work, but also on other projects of the research group. For this, in addition to the main functionalities described above, additional capabilities have been developed and implemented, to be used in the specific cases of different kinds of GEM detectors or different experiments. For example, in the cases of different anode geometries the heatmaps are built differently to represent correctly the spatial distribution of the channels. In the cases of applications for soft X-ray detection on tokamaks, instead, the fast Fourier

transform spectrogram plot has been added. For the analysis of data in the HVPTF experiments, an additional graph allows the display of the X-ray signal detected by the GEM detectors together with the signals coming from other diagnostics, mainly the current, voltage and pressure collected by the analog system. Also, an algorithm has been implemented to cross-correlate the signals, achieving an approximate temporal synchronization for a more correct visualization and comparison between the time traces of the different instruments.

Chapter 4

Experimental Activities

During the last years, many studies have been performed in different electrode configurations at the HVPTF facility. One of the main focuses has been the analysis of the X-ray radiation coming from the chamber at the occurrence of electric discharges in conditioning experiments, which was correlated with the voltage and current signals of the power supplies. For the analysis of the radiation, LYSO and $LaBr_3(Ce)$ scintillators were used initially. These detectors offer high detection efficiency and spectroscopic capabilities with a good energy resolution.

Gas Electron Multiplier detectors have been added to the HVPTF set of diagnostics to offer a complementary measurement focused on the flux of soft X-rays, with an acquisition resolved in time, space and energy altogether. Different GEM-based detectors have been developed, tested and used for data collection. This chapter documents the main developments and results of the experimental activities throughout the years, both in laboratory tests and at the facility.

Three different detector models in particular have been employed, with the characteristics described in Table 4.1. For each one of them, the peculiarities in development and the installation and uses are described.

Identifier	GEM coating	Channels	Channel structure
XR-GEM-1	aluminium	256	6 mm sided pads
XR-GEM-2	copper	512	X-Y strips
XR-GEM-3	copper	384	3 mm and 6 mm sided pads

Table 4.1: Details of the different GEM detectors installed and used in HVPTF.

4.1 Detector characterization

The first aspect to consider in the development of a detector, after its design and assembly, is characterization. For every detector described in the following, the procedure of calibration of each channel follows the same concept, so it is described just once, with later references to the changes implemented in specific cases. The calibration process allows to link the Time-over-Threshold information of each event to the correspondent value of charge collected at the anode, which is then related to the energy deposited by the particle in the gas volume of the detector. The empirical relationship between ToT and charge (q) is in the form:

$$ToT(q) = a + b \cdot q - \frac{c}{q - d} \tag{4.1}$$

Which is the combination of a linear trend for high charge values and a non-linear asymptotic component for $q \sim d$, a value related to the voltage threshold imposed on the Time-over-Threshold circuit (V_{TH} in Figure 3.8) [Cancelli et al., 2022]. The charge value obtained from this equation can be related to the energy loss of the incoming photon through:

$$q(E) = G(HV) \cdot \frac{E_x}{W_i} \cdot 1.6 \cdot 10^{-19} C \tag{4.2}$$

Where W_i is the average energy necessary to produce an electron-ion pair in the gas (see section 3.1.2), about 28 eV for the common Ar-CO_2 70-30% mixture. G is the gain factor, a function of the cumulative voltage difference set among the GEM foils HV. The values of this function can be experimentally measured (see details in chapter 7 of [Sauli, 2023]), but they are often taken from reference look-up tables, depending on the detector geometrical configuration and gas mixture. The function $G(HV)$ employed for the detectors of this work is plotted in Figure 4.1.

The calibration procedure aims at finding, for each channel, the values of the four free parameters a, b, c and d, through a best fit of experimental data obtained for peaks of known energy.

Conventional calibration procedures for radiation detectors rely on the use of multiple radioactive sources emitting at different energy values, spanning over the range of interest, in order to interpolate a continuous curve. In the case of the GEM detectors developed in this work, however, a different principle is exploited to give equivalent results with a limited number of materials.

A portable X-ray gun, the Amptek Mini-X2 X-ray tube [MiniX2, 2025], is used to direct a beam of Bremsstrahlung photons to a solid target (as for example titanium, copper or molybdenum), which produces quasi-monochromatic characteristic fluorescence emission in response. The detector is placed to

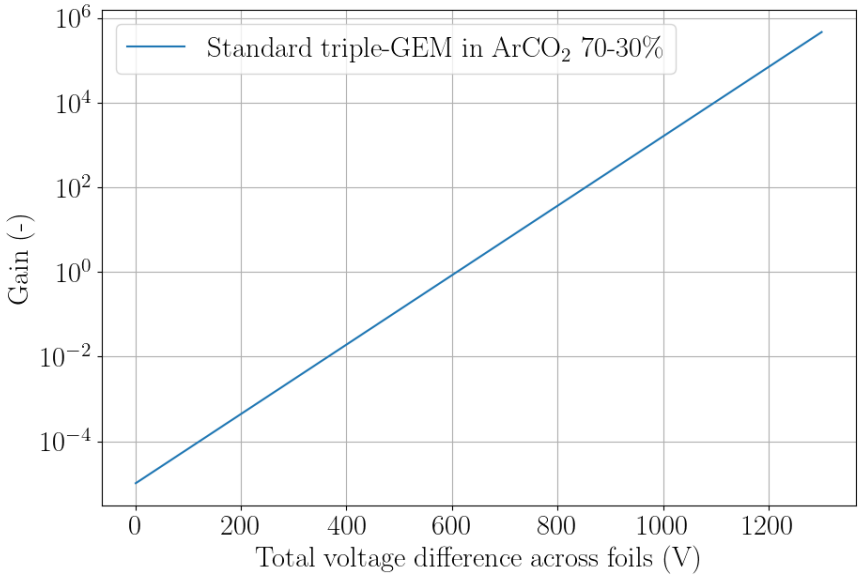

Figure 4.1: Tabulated values of gain as a function of voltage difference for the triple-GEM with the geometrical configuration used in this work.

collect this quasi-monochromatic beam, without being influenced by the primary beam coming from the Mini-X2, as sketched in Figure 4.2.

The high voltage applied to the foils is varied, modifying the gain ratio of the detector (factor G of Equation 4.2), thus obtaining different values of collected charge (and ToT) at the channels for incoming photons of the same energy. An example of the shift to higher values of ToT with increasing voltage differences is displayed in Figure 4.3.

Each channel of the detector must be calibrated independently. Using low energy X-rays that have a high chance to interact through photoelectric effect in the gas (releasing all of their energy, as explained in section 3.1.1), the probability of producing small clusters of electrons is also maximized, leading to the collection of the whole charge from a single channel of the anode. Thus, by considering only the events that are clusterized from a single hit, Equations 4.2 and 4.1 can be applied.

The calibration algorithm is designed to collect data from consecutive measurements at different values of high voltage and fit Gaussian curves on the fluorescence peaks of the ToT spectra for each channel. Particular care is taken to correct for possible experimental issues in this procedure, as for example the influence of electrical noise on any channel. The calibration algorithm implemented in the GEM-GUI software is able to discern the correct position of the photoelectric interaction peak even in presence of the intense signal at low energies characteristic of noise, as shown in Figure 4.4.

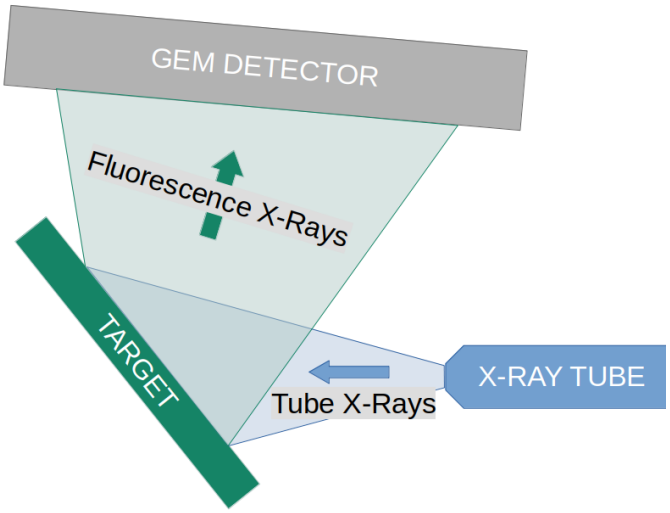

Figure 4.2: Sketch of a top-down view of the fluorescence setup for detector calibration. [Caruggi et al., 2023]

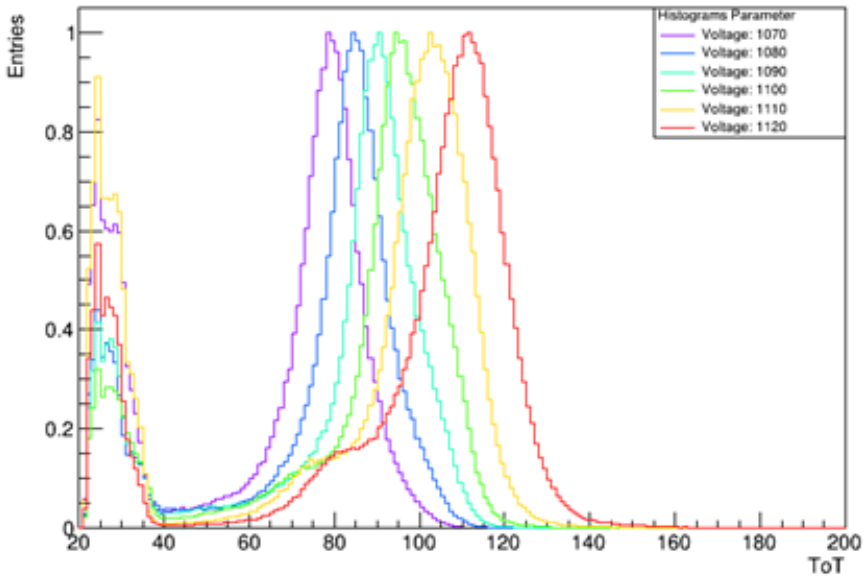

Figure 4.3: Example of ToT shift for the same energy peak for the GEM detector at the variation of high voltage on the foils. [Caruggi et al., 2023]

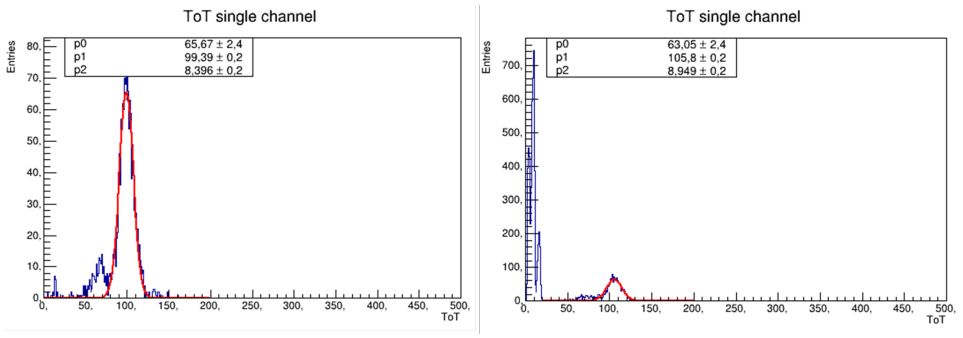

Figure 4.4: Examples of Gaussian fit of the ToT peaks used for calibration. On the left, the example of a channel with little to no noise issues, on the right the example of a particularly noisy channel.

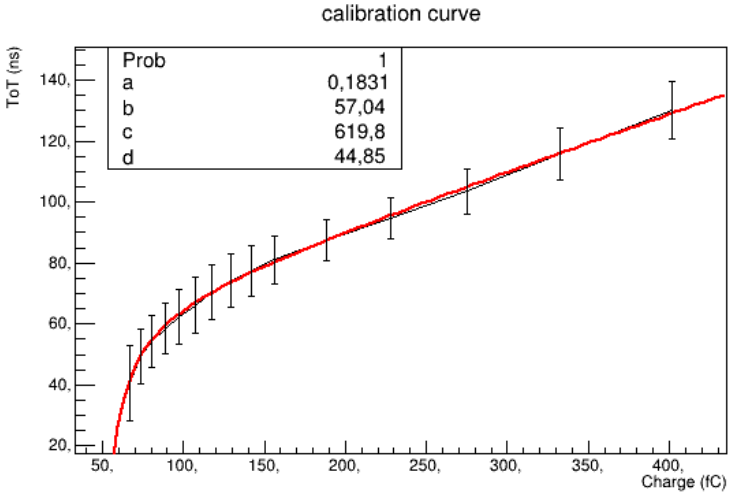

Figure 4.5: Example of a fitted calibration curve for a channel. [Caruggi et al., 2023]

The mean value of the interpolated Gaussian peak is then compared with the expected charge value, which depends on the detector gain. The resulting points are fitted on a ToT-charge graph following the formula of Equation 4.1, to find the best values for the free parameters for each channel. The resulting ToT-charge curve for a single channel is presented in Figure 4.5.

The GEM-GUI software calibration algorithm is also equipped with routines to automatically check the quality of the experimental points obtained for the curve and to verify the final result as well. Experimentally, other fluorescence materials with different characteristic energy can be used after calibration to confirm that the measurements still fit the expected results.

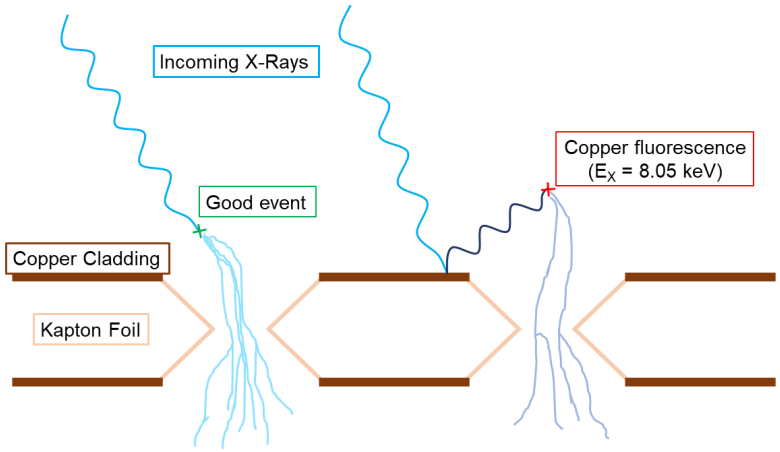

Figure 4.6: Sketch of the phenomenon of copper fluorescence induced noise in conventional GEM detectors. [Caruggi et al., 2023]

4.1.1 Characterization of Al-coated GEM foils

The first GEM detector employed at HVPTF, as presented above, uses foils coated in aluminium instead of the more traditional copper. Standard GEM detectors present a peculiar issue when employed for the analysis of soft X-ray radiation (in the range from 2 keV to 20 keV), in the sense that the copper used for coating (and other components of the detector as well) can be the source of a non-negligible background signal. Copper has a characteristic fluorescence emission with K_α line at 8.05 keV, which can occur in case of interaction of higher energy X-rays with it. These characteristic X-rays may then be collected as an external event by the detector, acting as a source of unwanted noise on the measurements, as sketched in Figure 4.6.

The use of another metal, for example aluminium, as coating can help in removing the background signal in the energy range of interest, since its K_α emission line is located at 1.5 keV. Prototypes of Al-coated foils were produced in collaboration with CERN, using a DC magnetron sputtering machine for vacuum deposition. The initial thickness of the coating was about 10 µm, later reduced to 5 µm by chemical etching. The manufacturing of Al-coated foils is also different for the fact that it does not require the placement of a chromium substrate between kapton and metal coating, which is needed in traditional foils. This absence actually avoids another potential source of unwanted background, since the K_α emission of chromium is at 5.411 keV, still in the region of interest.

The performance of a detector with Al-coated foils has been tested in laboratory against a conventional one with Cu-coated ones. Having verified that the operational working parameters were sufficiently close between the two, the comparison was made on their spectral response to the characteristic

fluorescence emission of different materials, with the same setup described above for detector calibration. The resulting plots, for fluorescence of titanium ($K_\alpha = 4.5\,\mathrm{keV}$), copper ($K_\alpha = 8.05\,\mathrm{keV}$), and molybdenum ($K_\alpha = 17.4\,\mathrm{keV}$) are shown in Figure 4.7.

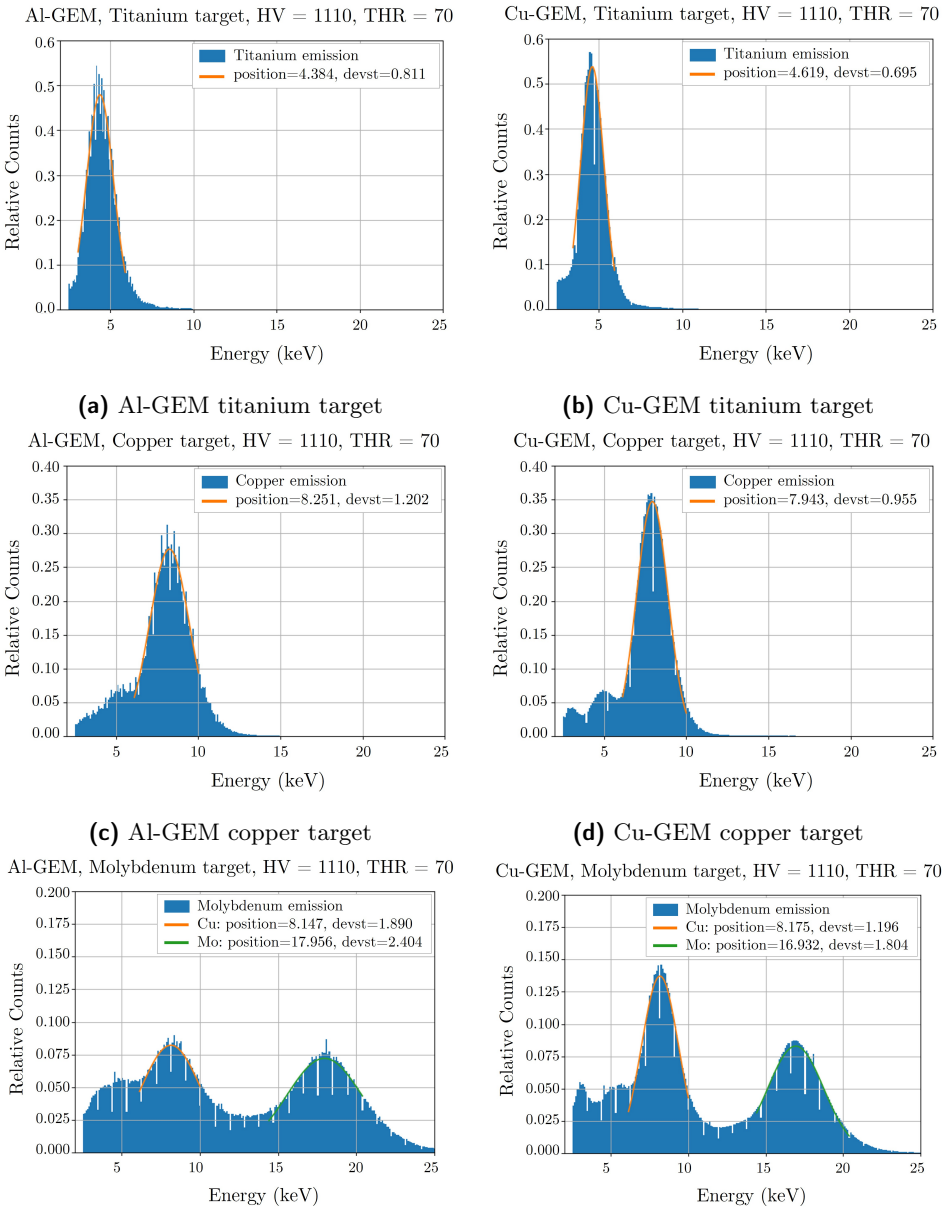

(a) Al-GEM titanium target

(b) Cu-GEM titanium target

(c) Al-GEM copper target

(d) Cu-GEM copper target

(e) Al-GEM molybdenum target

(f) Cu-GEM molybdenum target

Figure 4.7: Energy spectra of fluorescence peaks, with interpolation of Gaussian peaks. Left: Al-GEM, right: Cu-GEM. Adapted from [Caruggi et al., 2023]

Figure 4.8: Picture of the XR-GEM-1 detector as installed at HVPTF.

4.2 The XR-GEM-1 detector

4.2.1 Installation

The first GEM-based detector to be installed at the High Voltage Padova Test Facility was an Al-coated triple-GEM setup, equipped with a 256-pad collection anode as the one shown in Figure 3.6. As mentioned above, each pad measures 6x6 mm^2, and is treated by the acquisition system as a stand-alone channel for data collection.

The detector was mounted on the side of the vacuum vessel of the facility, as depicted in Figure 4.8, on supports that allowed for movement on the radial direction of the vessel itself.

The line of sight of the detector was defined by the position of a CF40 flange and a lead collimator mounted on its front, constituting a pinhole optical geometry (Figure 4.9).

The flange was equipped with a Beryllium window, 25 µm thick and with a diameter of 13 mm, to allow for the passage of low energy X-rays outside the chamber. This setup implies that the range of view of the detector inside the chamber is enlarged or narrowed depending on the distance between the detector and the flange window, allowing for more or less of a magnification effect of the objects in view, with a related higher or lower average count rate of the detector. Some preliminary measurements had thus to be performed not only to define the correct operational parameters for the detector, but

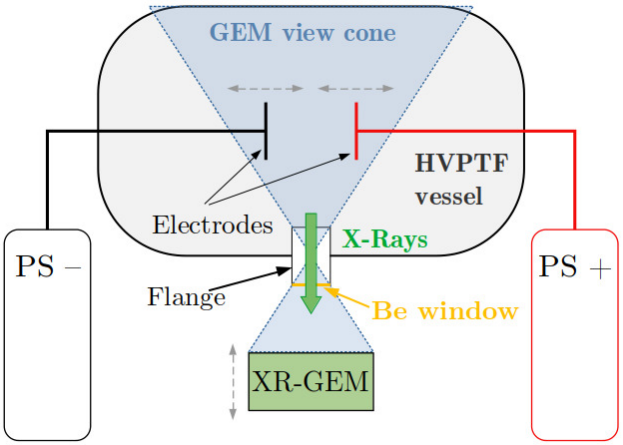

Figure 4.9: Schematic representation of the installation of the GEM detector at HVPTF.

also to choose its position on the line of sight, with a trade-off between the level of detail of the view and the statistical accuracy of the data collected.

4.2.2 Preliminary tests on insulators

The first experimental sessions of HVPTF after the installation of the XR-GEM-1 detector were a series of electrical tests of a set of ceramic insulators designed for the MITICA facility (the full-scale prototype for the ITER neutral beam injector). The measurements were aimed at testing their ability to withstand the electrical load necessary for their application on MITICA, resulting in the ability to keep the required voltage for long times with small leak currents [Marcuzzi et al., 2015]. Pictures of the insulators mounted on the supports of the vacuum chamber, and as seen from the window of the GEM line of sight, are shown in Figure 4.10.

During the experiments, electric discharges were expected, with a quasi-uniform distribution of X-ray emission from the middle of the chamber. This could be used as reference profile to define the correct working parameters for the XR-GEM-1 detector. The analysis also helped in showcasing the innovations that the GEM-based detectors introduced in the set of diagnostics of HVPTF. The ability to produce maps of the spatial distribution of the incoming radiation can enable tomographic reconstruction of the emissivity profile in the chamber. Also, the better temporal resolution with respect to the previously available scintillator allows to follow the fast transient and gain new insight on the dynamics of the phenomena on shorter time scales.

Multiple experimental sessions were performed, with data collection from the XR-GEM-1 detector, with varying values for HV (thus signal gain) and

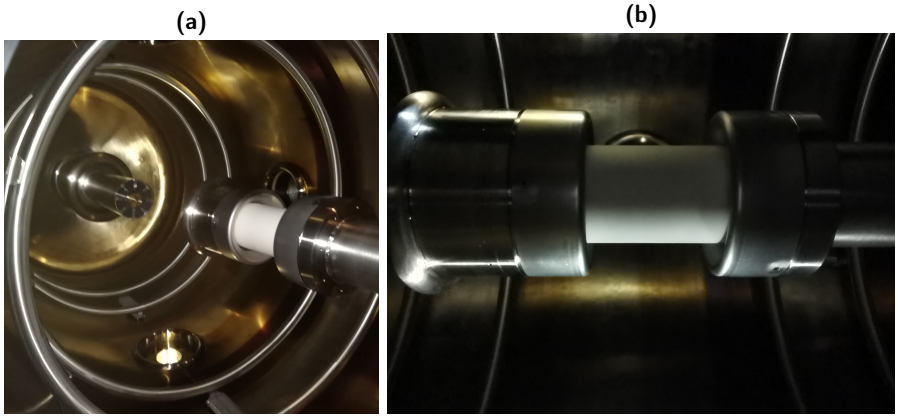

Figure 4.10: Pictures of the installation in the HVPTF vessel of an alumina insulator prototype for MITICA. (a) Photo of the open vessel with the insulator on one support. (b) Photo of the view from the window at the GEM detector line of sight.

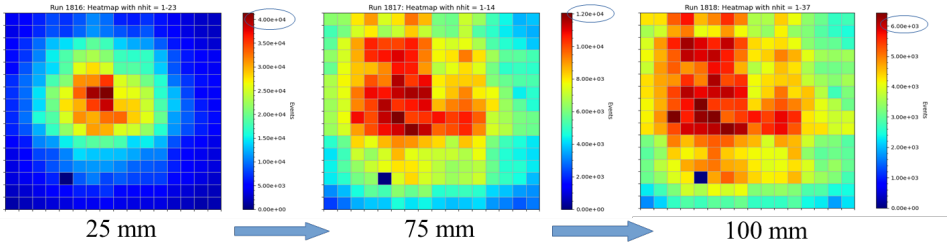

Figure 4.11: Images of the X-ray emission of the same object taken at three different distances (25, 75 and 100 mm), to highlight the change in the range of view of the GEM detector.

distance between detector and window. The data showed confirmation of the magnification effect expected, as can be seen in Figure 4.11, with a set of three images taken in the same configuration of the experiment but at three different positions.

The preliminary tests resulted in a fixed value of HV, translating in a gain factor of about $5 \cdot 10^3$ that would be kept for the following experiments. The values used for the next detectors were then close to the same. The detector was fixed at a 20 cm distance from the window, focusing the analysis on the emissivity from the space between the electrodes at small distances.

4.2.3 Needle-plane configuration

After the tests on the insulator, the XR-GEM-1 detector collected data during the conditioning experiments of a set of needle-plane electrodes (shown

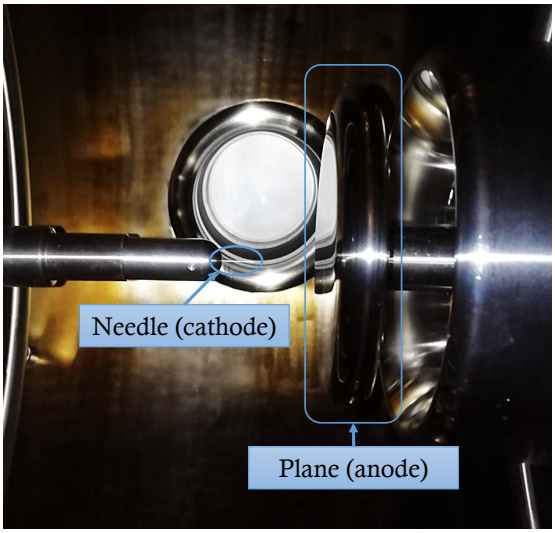

Figure 4.12: Picture of the needle-plane electrodes inside the HVPTF chamber studied in the experimental sessions with the XR-GEM-1 detector.

in Figure 4.12) on single polarity (i.e. with only the needle electrode brought to negative voltage, and the planar one kept at ground), with a gap length of 36 mm.

Unfortunately, one of the FPGAs connected to the system sustained some damage during the first measurements at the facility, thus preventing acquisition of data from one quarter of the detector. The line of sight was adjusted as well as possible to account for this fact, capturing the emission coming from the electrodes with the functioning parts of the acquisition chain.

The conditioning procedure of the electrodes followed the scheme described in section 2.4. The observation of the temporal evolution of the X-ray emission collected by the detector started first with reference to the current and voltage signals coming from the analog readout of the power supplies.

The conditioning ramp profiles already displayed in chapter 2 are reported again in Figure 4.13a, with a closer look at a subsection of the ramp in Figure 4.13b. As already described, the X-ray emission is absent at the beginning of the conditioning, until the threshold for field emission is reached, after which an almost steady-state signal value is detected. The reference spatial profile collected by the GEM detector is presented in Figure 4.14, with a sketch indicating the location of the electrodes in the range of view.

As it can be seen from the plots of Figure 4.13, the quasi-steady dark current signal is interspersed with spikes, both in current and in X-ray signal, linked to drops in voltage. These are the micro-discharges described in chapter 1, and a strong correlation can be seen between the electrical sig-

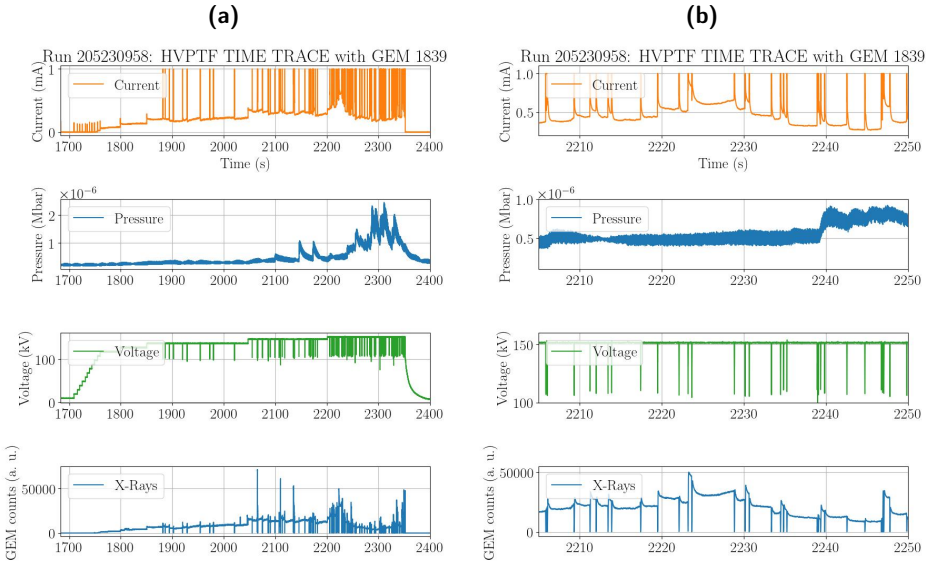

Figure 4.13: Time evolution of analog and X-ray signals during the experimental session studied. (a) View of the signals during the full conditioning ramp of 700 s. (b) Zoom of the graph in (a) from 2205 s to 2250 s.

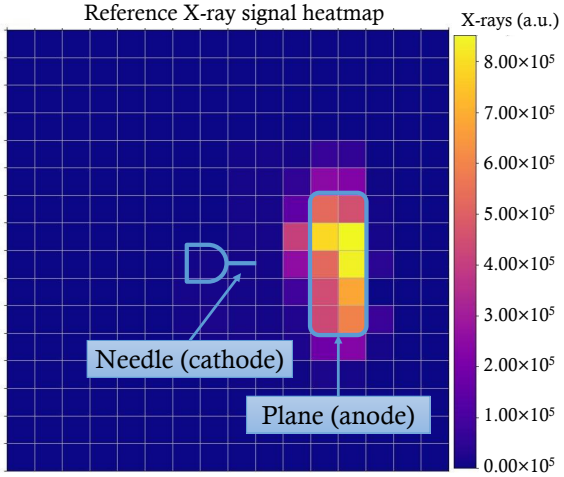

Figure 4.14: Heatmap of the radiation observed with the XR-GEM-1 detector for the dark current signal in the needle-plane electrode configuration, with indications for the positioning and size of the electrodes expected from geometrical considerations.

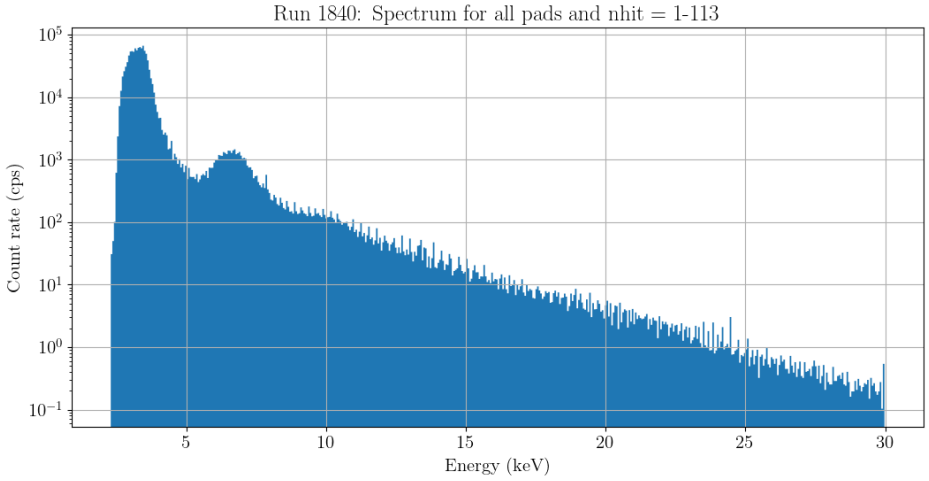

Figure 4.15: Spectrum of the radiation observed with the XR-GEM-1 detector, integrated over all the detection area and the whole conditioning ramp.

nals and the X-ray emission, as mentioned above in relation also to different works. [Spagnolo et al., 2021, Kushoro et al., 2022].

The correlation between measurements can be justified considering that the majority of the X-rays observed by the detectors are those produced by Bremsstrahlung radiation of the electrons involved in both the field emission and the discharges. In the following, more details on the studies of the X-ray emission collected with the XR-GEM-1 are presented, for what concerns both the general characteristics of radiation during the conditioning ramps and the detailed analysis of the single micro-discharges.

Observations on energy spectra

The first analysis performed on the data was focused on the energy spectrum of the radiation collected by the GEM detector, and its comparison with the data collected by the other X-ray diagnostics. All the channels were considered together in this case, producing an integrated spectrum of the total detection area. The spectrum integrated in time for a whole conditioning ramp is shown on a logarithmic scale in Figure 4.15, for energies up to 30 keV.

As it can be seen, the spectrum exhibits the characteristic shape of the Bremsstrahlung radiation recorded with the scintillator detectors (see section 2.3), even in the small range of energies relevant for a GEM detector. In addition to the Bremsstrahlung radiation, however, an emission located between 5 keV and 8 keV is present. This contribution was identified as a possible characteristic emission of AISI 304 (of which a plot is presented in Figure 4.16), which the electrodes and chamber are made of.

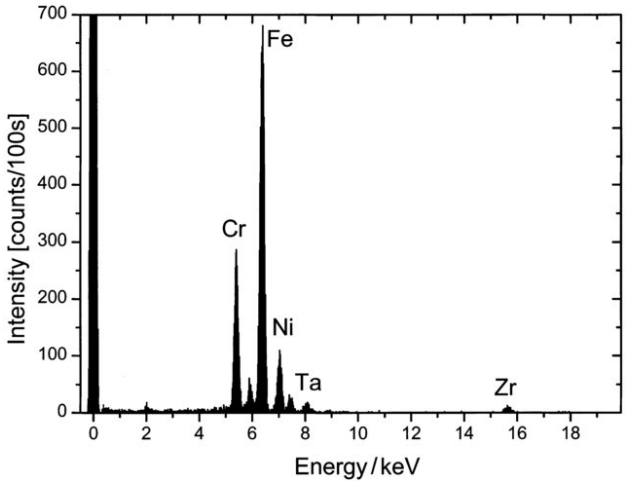

Figure 4.16: Characteristic X-ray fluorescence spectrum of AISI304 stainless-steel [Kawai et al., 2004].

This hypothesis was later confirmed by comparison with a spectrum collected by a commercial silicon drift detector (SDD) in an experimental setup similar to that of HVPTF. The distance between electrodes of this second experiment was smaller, and the voltage difference involved was lower (which was instrumental for the chance to use an SDD without paralysing it), but the materials were the same. The spectrum collected by the SDD is shown in Figure 4.17, with clear peaks at energy values around the same region of the emission observed with the GEM detector.

Further studies on the energy spectrum focused on the endpoint variation as a function of the voltage difference between electrodes. The hypothesis was that, even by having a detector with significant efficiency only for soft X-rays, the characteristics of the energy spectrum could still be indicative of the maximum energy of the Bremsstrahlung electrons.

Figure 4.18 shows the sequence of four spectra, integrated on time intervals corresponding to different values of voltage difference between electrodes, with indication of the linear fits performed to calculate the spectrum endpoint on each one.

The high-energy end of a Bremsstrahlung spectrum should follow:

$$N(E) = A \cdot e^{-kE} \tag{4.3}$$

Where $N(E)$ is the number of photons detected at energy E, k is related to the maximum energy of the electrons producing the Bremsstrahlung radiation and A is a normalization constant. Taking the natural logarithm of both sides, the relationship becomes linear:

$$\ln(N(E)) = \ln(A) - kE = b + mE \tag{4.4}$$

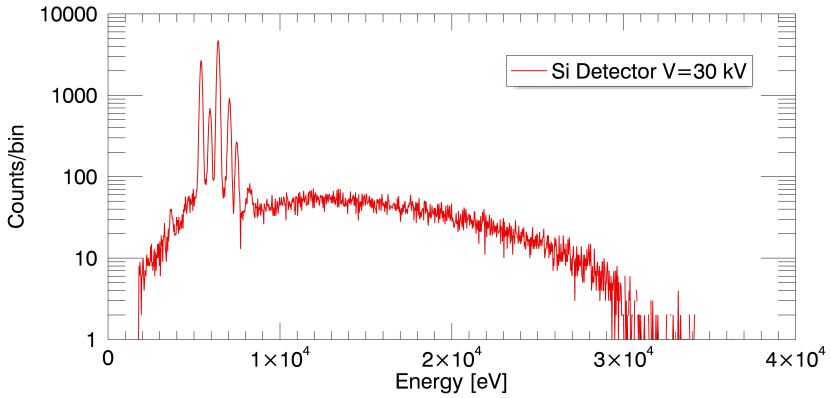

Figure 4.17: X-ray spectrum collected with a silicon drift detector on experimental conditions similar to those of HVPTF.

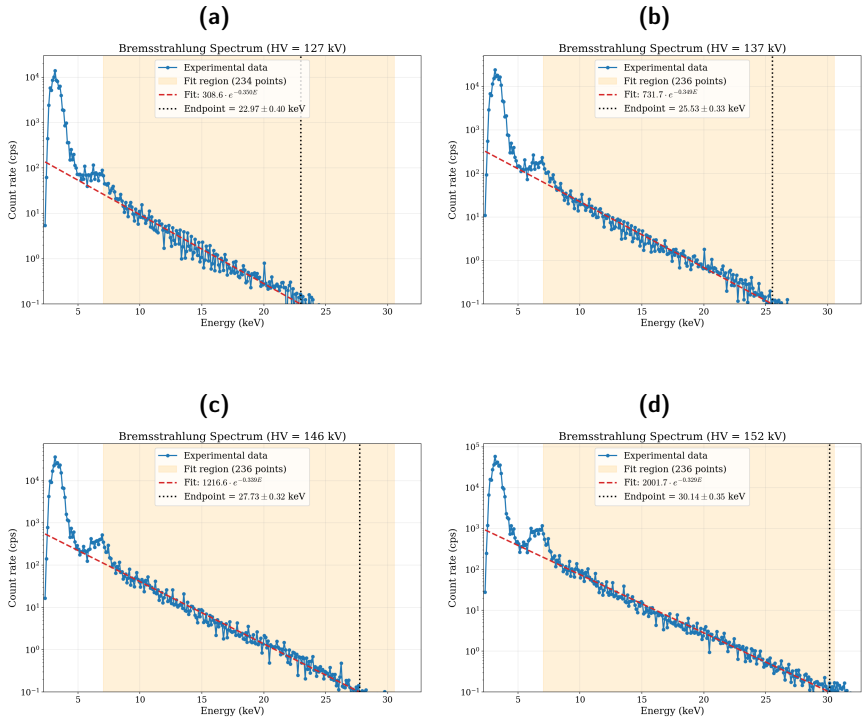

Figure 4.18: Spectra of the radiation observed with the XR-GEM-1 detector, integrated over all the detection area at different electrode voltage difference. (a) Spectrum taken at 127 keV. (b) Spectrum taken at 137 keV. (c) Spectrum taken at 146 keV. (d) Spectrum taken at 152 keV.

Voltage difference	Calculated endpoint
(127 ± 1) keV	(22.967 ± 0.401) keV
(137 ± 1) keV	(25.529 ± 0.327) keV
(146 ± 1) keV	(27.726 ± 0.324) keV
(152 ± 1) keV	(30.144 ± 0.348) keV

Table 4.2: Endpoints calculated for the XR-GEM-1 spectra at different values of voltage difference between electrodes.

Interpolation was thus performed using a linear fit on the data points of the logarithmic spectra, considering only a reduced energy range. The first 12.5% of data points were excluded, in order to take into account only the high-energy tail and neglecting the effects of possible noise and background. The last 20% of data points for each spectrum were also excluded for the low count rates they represented and the related high statistical uncertainty. After finding the coefficients b and m of the linear fit, the endpoint of the spectrum was calculated as the energy value for which the linear fit falls lower than 0.1 counts per second:

$$E_0 = \frac{\ln(0.1) - b}{m} \tag{4.5}$$

The resulting endpoints for the four spectra are summarized in Table 4.2, with errors defined by uncertainty propagation.

An additional linear fit was then performed to derive a relationship between the GEM spectrum endpoint value and the value of the voltage difference between electrodes. The result is shown in Figure 4.19, with the coefficients of the linear fit shown in the legend.

This analysis proved that even if the GEM-based detectors are only sensitive to low energy X-rays, the characteristics of the spectrum that they collect in these experimental conditions can still be used to derive information about the Bremsstrahlung radiation produced by the electrons accelerated in the high voltage gap, allowing for more accurate considerations in the following studies.

Observations on spatial distribution

After considering the energy spectra collected over the entirety of the detector, the focus was shifted to the analysis of the signals in relation to their spatial locations, discriminating among different regions of the range of view as sources. The heatmaps and histograms in Figure 4.20 show that the previously mentioned emission around 5 keV to 8 keV, attributed to characteristic fluorescence of AISI304, is prominent only in the spectrum recorded by channels that have a direct line of sight pointing to the plane electrode, and it is

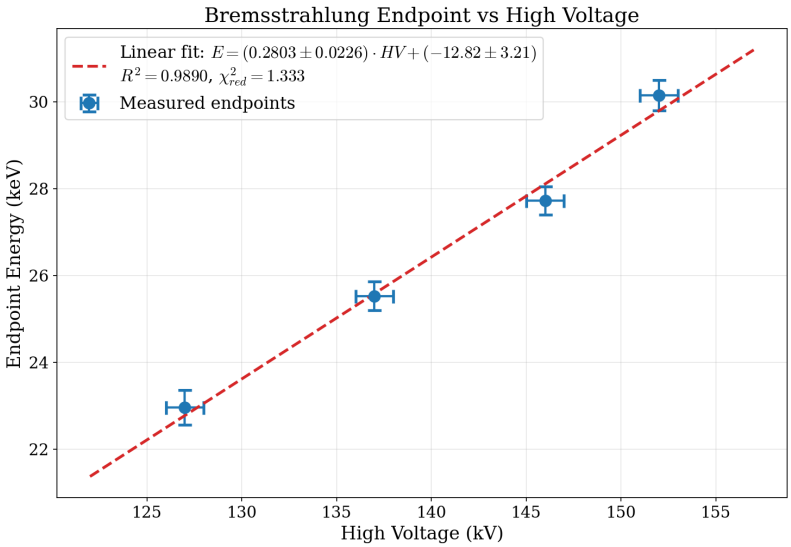

Figure 4.19: Linear fit of the endpoint value for the XR-GEM-1 spectra depending on the value of voltage difference between electrodes.

relatively lower for channels pointing at other sections of the chamber.

An additional consideration on this emission was possible after new experimental sessions, that were performed at higher pressures, making use of the injection systems that can introduce different gases in the chamber. The pressure level was raised to the value foreseen for the conditions in MITICA during beam operations, of about 10^{-4} mbar, in order to observe any possible change in the breakdown voltage.

The resulting experimental data for the XR-GEM-1 showed that the stainless-steel characteristic emission from the plane electrode was greatly reduced. In particular, a filtering operation was implemented in the GEM-GUI software, to produce heatmaps displaying on the ratio, for each channel, between the events in a certain range of energy and the total recorded:

$$channel\ events = \frac{\text{counts between 5 keV and 9 keV}}{\text{total channel counts}} \tag{4.6}$$

Figure 4.21 shows the resulting heatmaps with the filtering option active, comparing the measurements of a session at 10^{-7} mbar and one with the argon atmosphere at 10^{-4} mbar. The heatmap on the left shows clearly that the emission in the range around 5 keV to 9 keV is important on the region of the plane for the case of chamber kept at lower pressure, while it is much reduced from the same region in the case of argon insertion, shown on the right.

Following the observations reported here, new experimental tests can be planned, in order to study more accurately the effect of gas insertion in the

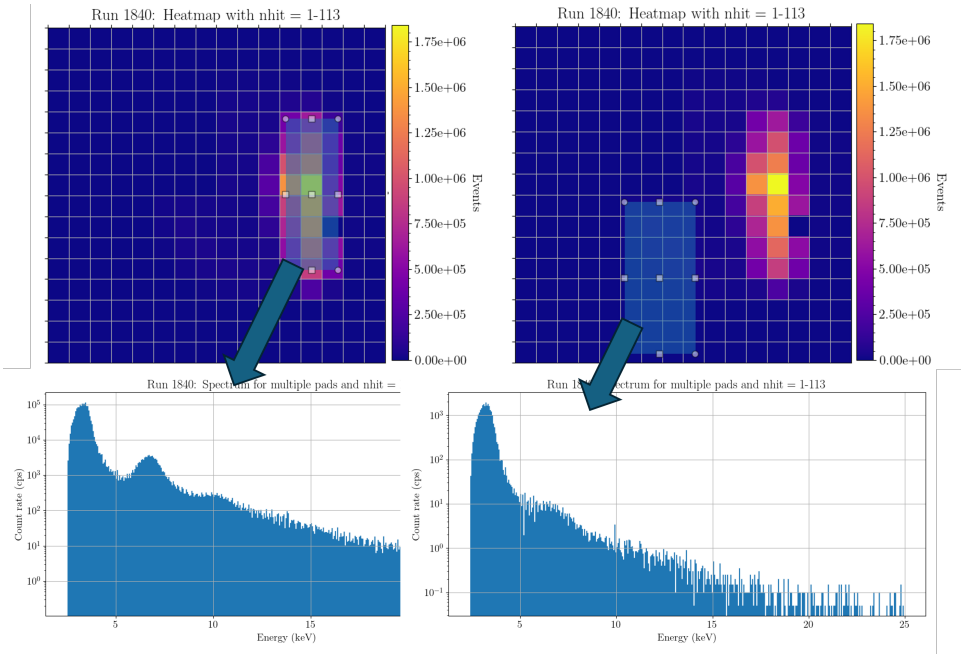

Figure 4.20: Comparison of heatmaps and corresponding energy spectra for the X-rays collected by the XR-GEM-1 detector, between pixels with a line of sight on the electrode (on the left) and pixels with lines of sight on the chamber (on the right).

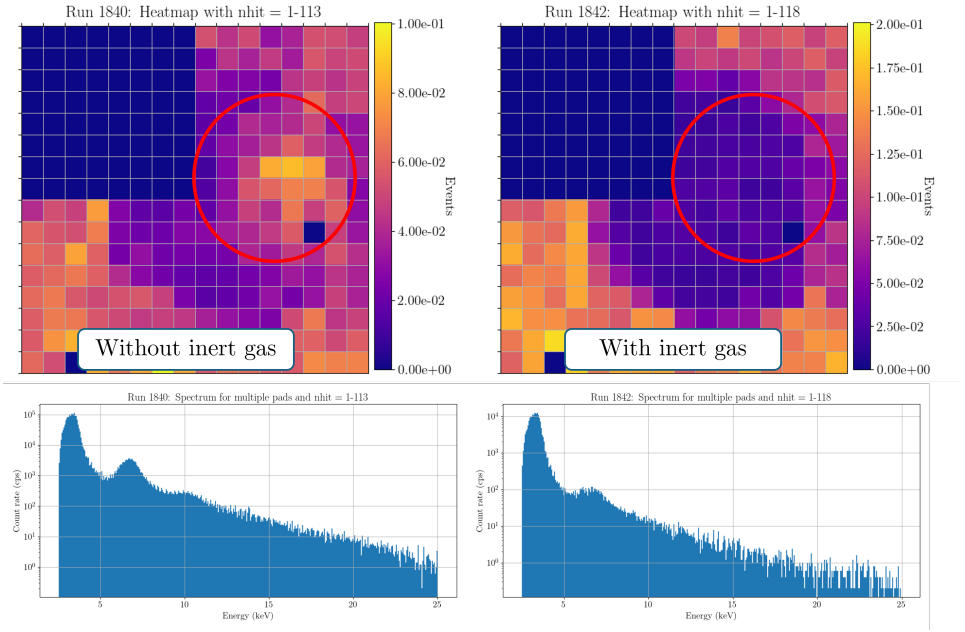

Figure 4.21: Comparison of heatmaps with filtering option and corresponding energy spectra for the X-rays collected by the GEM detector, between a run in vacuum (on the left) and one with argon insertion (on the right).

chamber during the conditioning sessions. Additionally, a more in-depth analysis of the characteristic emission could be performed by collecting data from conditioning of electrodes of different materials.

Study on breakdown precursors

Other studies performed on the data acquired by the GEM detector were focused on the search of breakdown precursors in the micro-discharge patterns, with the long-term aim of finding some method to foresee the occurrence of breakdowns and mitigate or prevent completely their effects. The main approach for this analysis was to find a transformation of the collected data that could be translated to a Figure of Merit (FoM) for the micro-discharge observation and the breakdown prediction.

The idea behind this study is that detection of X-rays in almost instantaneous, and a quantity based on the measurements of the GEM detector can be derived and monitored in real-time, identifying micro-discharge or breakdown occurrence ahead of standard electrical measurements. Different combinations of data were thus tested, with different integration times and on different runs. The most promising candidate that was pursued was the measurement of the ratio between the intensity of the X-ray signal coming from between the electrodes, with respect to the one coming from the plane electrode itself:

$$FoM = \frac{\text{cps between electrodes}}{\text{cps from plane}} \tag{4.7}$$

This quantity can be calculated directly as the ratio between the number of events of two sets of pixels in the chosen time frame (in this example, the green and orange regions on the reference heatmap of Figure 4.22). The simple arithmetic basis of this measurement would allow to easily implement the calculations on a real-time system as for example a FPGA.

The Figure of Merit chosen qualitatively presents correlations with the evolution of current and pressure measurements (as shown in Figure 4.23) and, thanks to the temporal resolution of the GEM detector, it could be calculated on shorter timescales with respect to the analog measurements (as portrayed in Figure 4.24).

The search of the precursors, and the definition of a suitable Figure of Merit based on X-ray data collection, could not be developed in detail due to the lack of synchronization among the diagnostic systems installed at HVPTF. Defining whether a quantity changes before or after another is dependent on their data being based on the same time definition. Additional studies on the matter have thus been held off to focus on the development and installation of a system for synchronization of the diagnostics, as described in section 4.5. Future experimental sessions featuring this system will allow for more detailed and conclusive studies on the search for breakdown precursors.

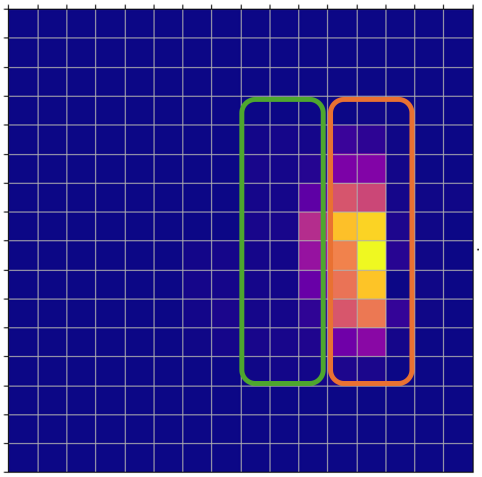

Figure 4.22: Sketch of the regions used in the heatmaps for the calculation of the Figure of Merit. Green region corresponds to the emission from the space between the electrodes. Orange region corresponds to the emission coming from the plane electrode.

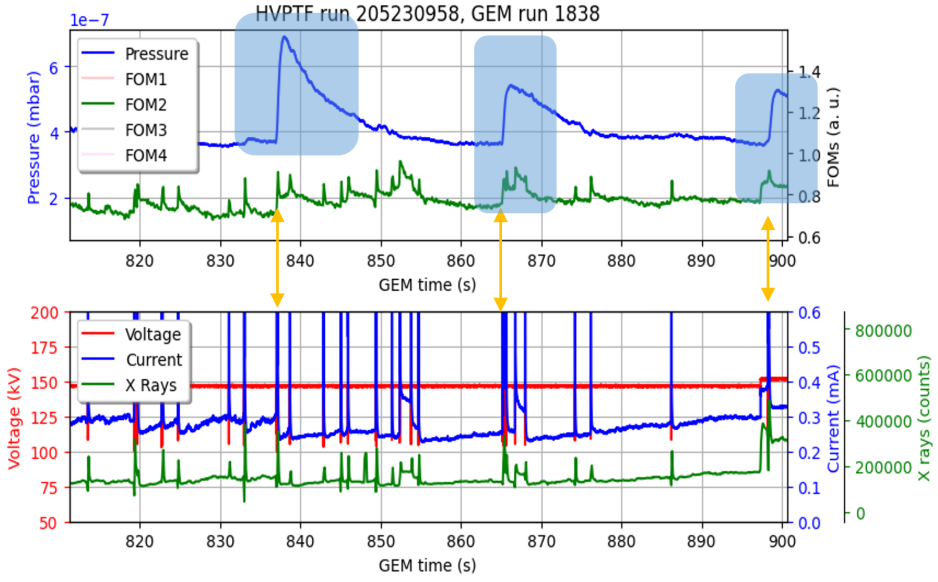

Figure 4.23: Observation of correlations between the FoM time trace and the current measurements, on a large timescale.

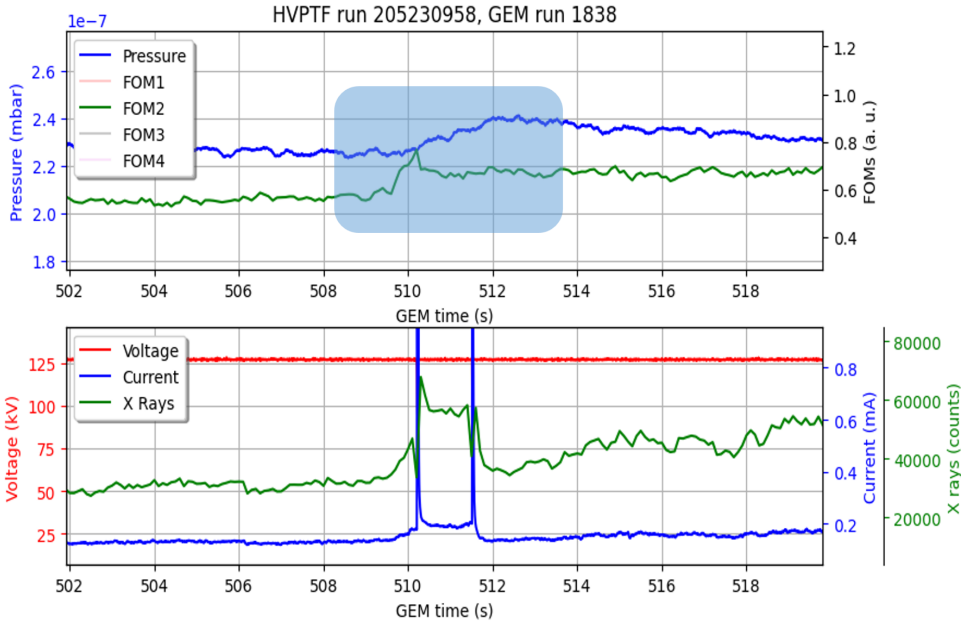

Figure 4.24: Observation of the FoM signal preceding the rise in pressure registered by the analog system, on a small timescale.

Micro-discharge fine analysis

Other studies on the data collected with the XR-GEM-1 detector, as mentioned before, were aimed at a finer characterization of the micro-discharge phenomenology. An algorithm was developed in order to automatically extract small temporal slices of signals around each micro-discharge from the full data of the experimental sessions. This was done by sampling the X-ray signal with a binning of 10 ms and searching for peaks above a fixed threshold. The timestamps of the peaks were used as reference to isolate the current, voltage and X-ray data contained in a time window of about 0.15 s around each one of them.

Details of current, voltage and X-ray trends on a smaller timescale than before are shown in Figure 4.25, which presents data recorded over a single micro-discharge time window.

This graph suggests that each micro-discharge event, appearing in the plots of Figure 4.13 as a single point spike, may have a finer structure beneath. The current signal shows two consecutive rising features, with the second one being interpreted as the reaction of the system to recover the voltage level after its drop.

The plot shows also why the readings of the analog diagnostic system are not sufficient for detailed studies, as both the full scale and the sampling frequency of the measurements are limiting or impeding the possibility of deriving meaningful data about the dynamics of the micro-discharges. Looking

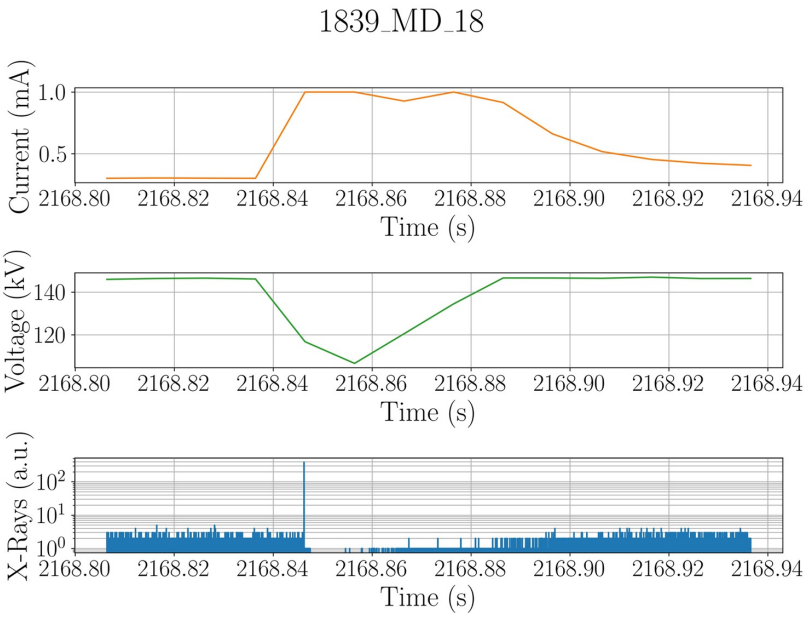

Figure 4.25: Time evolution of X-ray signal in a single micro-discharge with about a 0.15 s window.

at the X-ray signal plot instead, which has a denser binning, more features about the emission can be observed. It can be seen that the intensity of the signal during the micro-discharge is orders of magnitude higher than during the field emission, and also that following the spike the emission is absent for some time, until the voltage is brought back to nominal value.

Considering only the data collected by the GEM detector, the sampling time can be reduced further and the finer structure of the time evolution can be studied. In this context, some preliminary studies showed that the counting rate during the discharges was so high that, even with the good performances of a GEM-based detector, saturation was reached. This implies that the detector, for the duration of the more intense discharges, was paralysed (i.e. some events were lost) or, more probably, suffered from event pile-up (i.e. multiple events were recorded and clusterized as a single one).

As a result of this, the further analyses presented in this section have been performed with no clusterization of the data, meaning that the events plotted in the graphs correspond to the charge collection from each individual channel. The occurrence of pile-up may also cause overflow errors in the acquisition chain for the Time-over-Threshold measurements, preventing an accurate conversion of the ToT to charge and energy values. Because of this, the study on the micro-discharge events was limited to the time traces and heatmaps of the radiation, without considering the energy spectra.

A plot of the evolution of the X-ray signal with a sampling time of 100 ns,

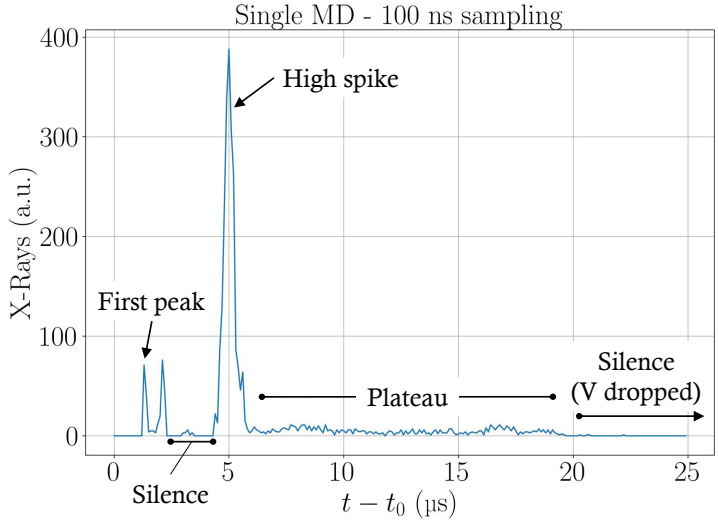

Figure 4.26: Time evolution of X-ray signal in a single micro-discharge, with reference to an arbitrary t_0 chosen as start of the discharge itself.

is presented in Figure 4.26. The plot shows firstly a peak of small intensity, bifurcated, lasting for about 1 µs, followed by some silence (i.e. absence of counts at the detector) with a duration of approximately 2 µs, and then the true high-intensity spike of the micro-discharge. The maximum point observable is about 400 units, that would correspond to 4 Gcps over the digital acquisition chain, further indicating a saturation condition for the system, rather than the real value that should have been recorded. After the spike, the plot shows a lower intensity plateau, lasting for about 15 µs, followed by another drop to zero counts. This last region is the absence of emission corresponding to the drop in the voltage of the electrodes, which has a duration of about 20 ms, orders of magnitude longer with respect to the whole dynamics of the micro-discharge itself.

The evolution of the observed data during few microseconds after the start of a discharge was found to be highly consistent, both during a single conditioning ramp and across multiple experimental sessions. The time bins of every micro-discharge were aligned with reference to the features found in the time trace described above, in particular the high spike, and the counts could be summed up for each bin without changes in the features of the plot and obtaining features in the spatial distribution of the summed counts that were similar to the single micro-discharges. This allowed for derivation of more statistically sound data.

A combined study of the distribution of the events in both space and time was thus performed. Gathering together the channels with the same signal features, three main groups were discerned, represented with coloured

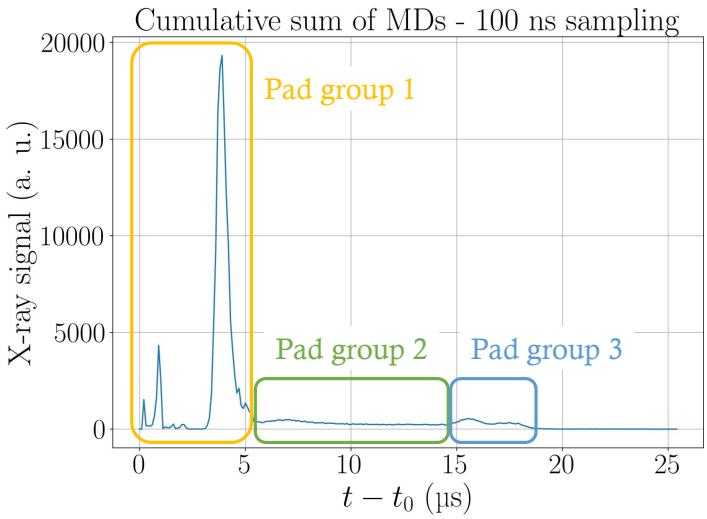

Figure 4.27: Reference time evolution of all micro-discharges, with the groups distinguishable by colours.

borders both in the sketched reference time trace of Figure 4.27 and in the reference heatmap of Figure 4.28. The first group of pads, that have signal only during the first 5 µs of the discharge approximately, as shown in Figure 4.29, are those that do not have a direct line of sight towards the electrodes, and thus receive signal mainly due to emission coming from the chamber walls. The channels looking at the plane electrode instead, which are the ones collecting signal for the field emission during the rest of the experimental run, actually exhibit no counts during the spikes of the micro-discharge, and contribute to the signal only on the plateau after the 5 µs mark. In particular, the signal collected until 15 µs from the start of the event comes from the pixels that have lines of sight pointing at the space around the plane electrode, as shown in Figure 4.30, while the ones that look to the centre of it show counts only in the end of the micro-discharge development (see Figure 4.31).

The increase in the statistics achieved with the sum of the different micro-discharges allowed also to produce heatmaps of consecutive frames, 100 ns each in length, of the cumulative time dynamics plot. The reference time trace is shown once again in Figure 4.32. The distinct regions are now four instead of the previous three, since the bifurcated spike has a different observable dynamic evolution with respect to the high spike. Figure 4.33 shows the evolution of the emission during the first peaks of signal of the plot, Figure 4.34 shows the X-ray distribution during the high spike of signal, Figure 4.35 refers to the evolution up to the 15 µs mark, and finally Figure 4.36 presents the evidence of the emission returning to the source it

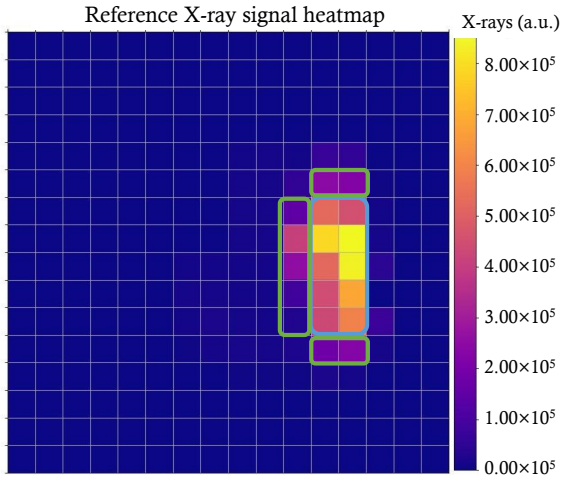

Figure 4.28: Heatmap of radiation for the micro-discharges, with groups distinguishable by colours (the orange group comprises all the pads external to the green and blue lines).

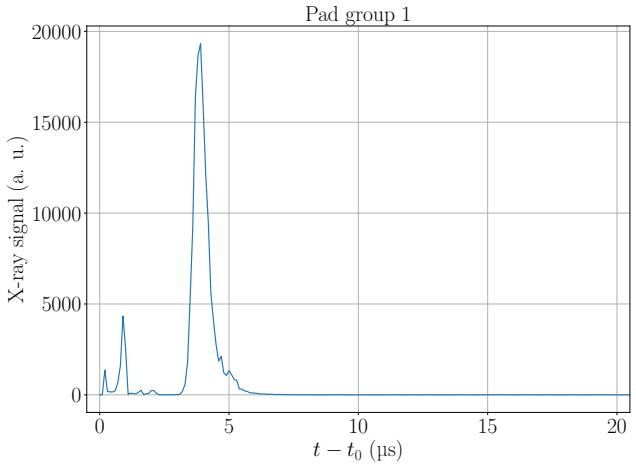

Figure 4.29: Time evolution of X-ray signal for the chamber pads for the cumulative MDs.

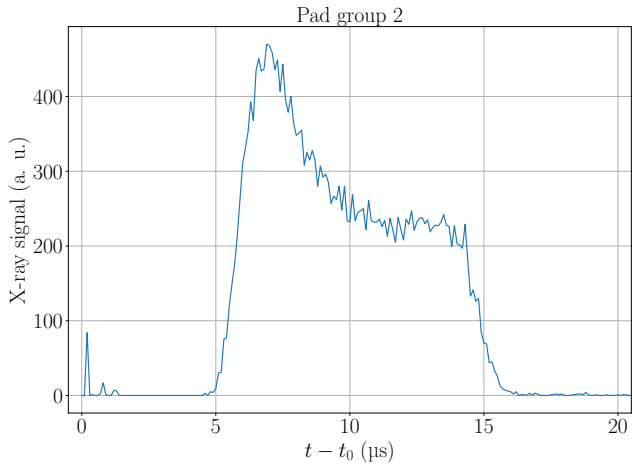

Figure 4.30: Time evolution of X-ray signal for the around-plane pads for the cumulative MDs.

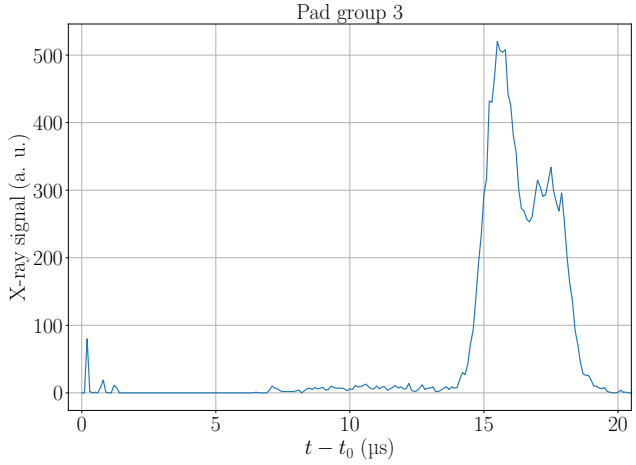

Figure 4.31: Time evolution of X-ray signal for the center-plane pads for the cumulative MDs.

has for the dark current during the rest of the experimental session.

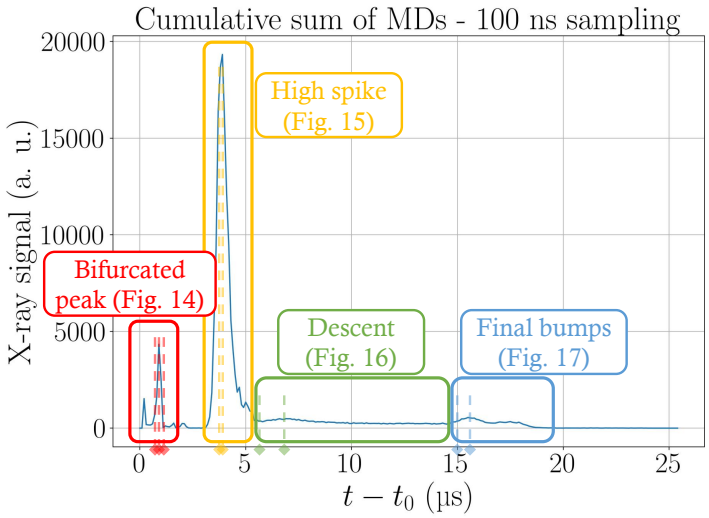

Figure 4.32: Reference time evolution of all micro-discharges with the 4 groups distinguishable by colours, and reference to Figures 4.33 to 4.36. Dashed lines with arrows correspond to the temporal marks of the frames selected for the heatmaps.

The results obtained with the XR-GEM-1 detector were instrumental in the characterization of the microscale dynamics of the emission of X-rays during the micro-discharge phenomena in HVPTF, but they also served to highlight some potential areas of improvement with the experimental setup.

Firstly, the extreme counting rate experienced by the single channels was high enough that saturation was reached even with this detector, and the true count of events was not well known. Secondly, while the images obtained corresponded to the expected view on the basis of the geometry of the setup, the details were minimal. A detector with better spatial resolution (thus with more numerous and smaller channels) could help both in limiting the number of events per channel and in allowing for better imaging capabilities. New prototypes were thus developed and installed, as described in the next sections. Unfortunately, due to shortage of components and an issue with the production of aluminium GEM foils, the other detectors had to rely on the use of more conventional copper coated foils.

Additionally, the data analysis performed with the first GEM detector exposed the need for the development of a system for the synchronization of the data acquisition procedures of the different diagnostics, in order to allow for direct comparison among various signals and easier study of the correlations and of the time sequence of the processes involved in the discharge phenomena. The development of this system, both in its hardware and corresponding software components, is described in section 4.5.

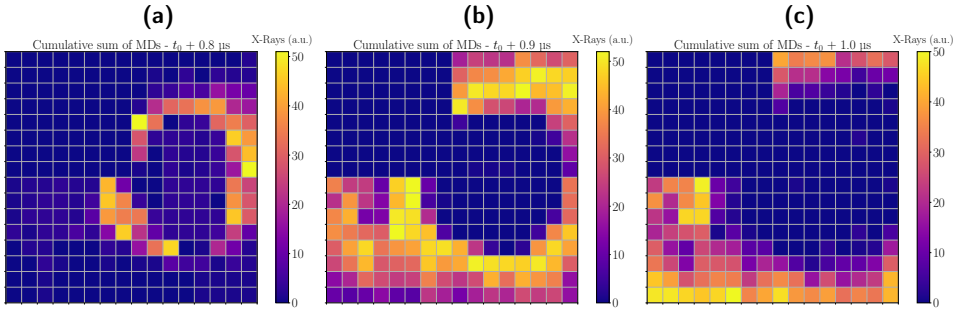

Figure 4.33: Spatial distribution of the detected radiation during the bifurcated peak of the micro-discharge. (a) Frame taken at 0.8 µs. (b) Frame taken at 0.9 µs. (c) Frame taken at 1 µs.

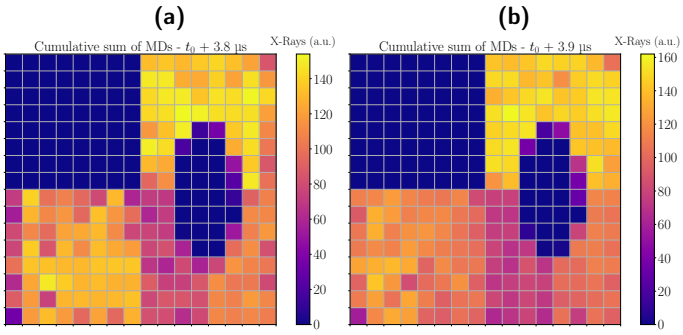

Figure 4.34: Spatial distribution of the detected radiation during the high spike of the micro-discharge. (a) Frame taken at 3.8 µs. (b) Frame taken at 3.9 µs.

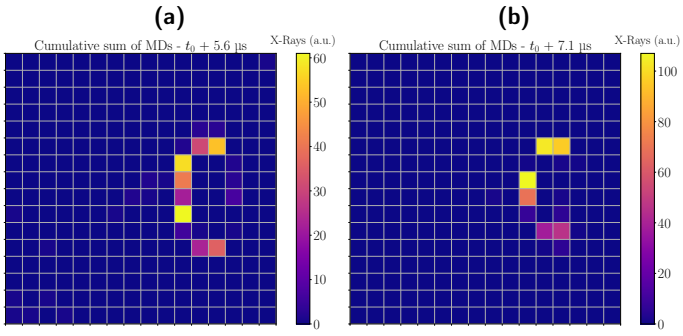

Figure 4.35: Spatial distribution of the detected radiation during the descent of the micro-discharge. (a) Frame taken at 5.6 µs. (b) Frame taken at 7.1 µs.

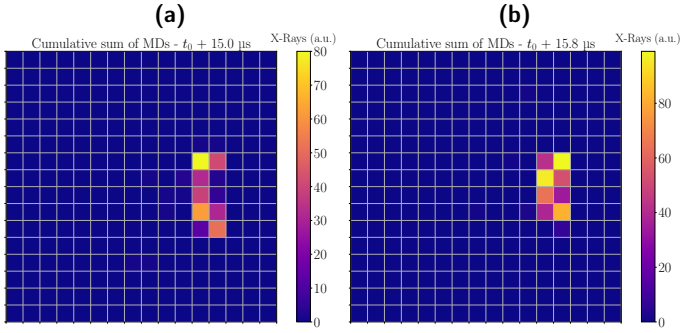

Figure 4.36: Spatial distribution of the detected radiation during the final bumps of the micro-discharge. (a) Frame taken at 15 µs. (b) Frame taken at 15.8 µs.

Finally, the innovative observations made on the data collected from the XR-GEM-1 detector sparked the interest in developing a simulation model that could justify the experimental findings. The description of this software tool is presented in chapter 5.

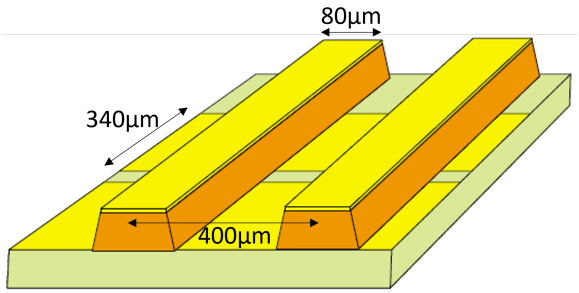

Figure 4.37: Diagram of the X-Y strip structure with indication of the dimensions.

4.3 The XR-GEM-2 detector

The second GEM-based detector developed to be installed at HVPTF differed from the previous one for the use of a X-Y strip structure for the collection anode. The structure of these strips is shown in Figure 4.37. The size of the strips is designed for equal charge sharing between the two directions. [Ketzer et al., 2002]

The detector was assembled employing a conventional triple-GEM structure and Cu-coated foils (due to the procurement issues of Al-coated ones mentioned above). The electronic readout system was the same as the previous detector, with the addition of new FPGAs, due to the increase of the total number of independent channels to be read up to 512, with 256 strips in the X direction and 256 strips in the Y direction. The collection anode still covered approximately the same surface area of the previous detector (about 10x10 cm^2).

4.3.1 Counting rate characterization

The use of a two-coordinate readout structure introduced the need for additional pre-processing routines in the GEM-GUI software, keeping into account the identification of coincidence events among the strips to localize them in the X-Y plane. The reconstruction of the events is done with the charge centroid method (for details see [Lavezzi et al., 2017]). The clusterization algorithm follows firstly the same logic described in section 3.3.1 for the X and the Y strips separately. Having reconstructed single X and Y value for each event, a merging operation is then performed between the two sets in order to localize the events on the plane.

This software routine imposes an additional operational limit on the high-rate capabilities of the detector, due to the chance of production of artefacts in the reconstructed image when multiple events happen within a single merging time window. An example of this phenomenon is sketched in Figure 4.38. Considering a charge collection event located at the crossing point of green lines and another one located at the crossing point of the orange lines

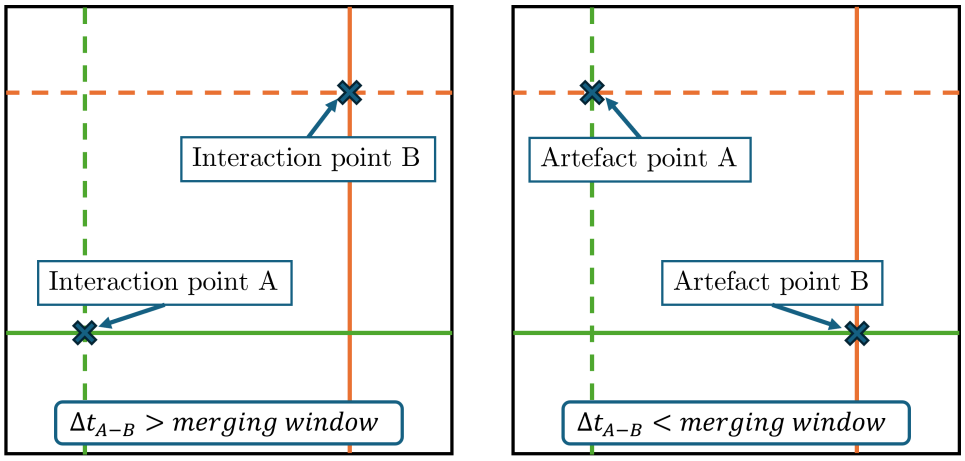

Figure 4.38: Sketch of the events leading to the production of artefacts in the location of events on the X-Y strip plane.

(interaction points A and B of the picture on the left), the events recorded at the corresponding X and Y strips can be correctly paired without issues when there is a time difference between them higher than the merging window. If the charge collection events from the four strips fall in the same window, however, it may be possible to pair the two solid lines for one event and the two dashed lines for the other, leading to the production of the artefact points of the picture on the right.

During the characterization of the strip detector, thus, operation at high rates was tested in consideration of this aspect. Stainless-steel masks with different numbers and distributions of holes were placed in front of the detector during a fluorescence measurement session.

An example of the results can be seen in Figure 4.39, with the comparison of two heatmaps. The one on the left was taken with the detector registering an average count rate of 6.81×10^5 Hz, and the two diagonal holes of the mask can be clearly seen, with the absence of additional features. The image on the right was reconstructed from a measurement with the same mask, but with an average rate of 4.29×10^6 Hz, and it can be clearly seen that the algorithm has wrongly matched any X and Y events, leading to the introduction of two additional holes as artefacts, located at the opposite angles of the real ones, just as shown in the sketch above.

It is worth to point out that, in addition to this, the strip readout imposed another change in the characterization procedure for the XR-GEM-2 detector. In particular, each channel could not be calibrated independently on the full value of charge collected for the photons. To account for the fact that each event is shared at least between two strips (one in the X direction and one in the Y direction), two approaches were considered: either calibrating the single strips on half of the charge value each, or calibrating each

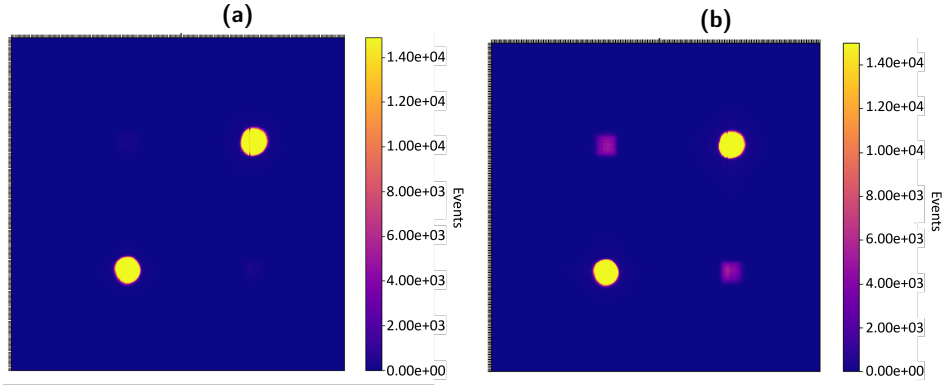

Figure 4.39: Example of production of artefacts by the reconstruction algorithm used for the strip detector. (a) Heatmap of a run with average rate of 6.81×10^5 Hz. (b) Heatmap of a run with average rate of 4.29×10^6 Hz.

crossing of strip pairs as if it was a pad of a conventional readout anode. The latter solution has been chosen, as the accuracy of the charge sharing could not be verified in laboratory tests. Thus, the calibration was performed independently on the $256 \cdot 256$ crossings of the strip channels. Other than this, the algorithm followed the exact same procedure described at the beginning of the chapter, with the addition of the merging among X and Y events in the clusterization mentioned above.

4.3.2 Imaging characterization

Additional tests were performed during the characterization of the XR-GEM-2 detector, to verify the improvements of its application in terms of spatial resolution. X-ray transmission imaging was performed on bone mock-ups. The experimental setup of the measurement is shown in Figure 4.40. The specimens were placed between the detector and the X-ray tube, which was operated at a voltage of 10 kV and a current of 5 µA. Acquisition time was kept under 10 s for each sample.

Various bone structures were employed, among which the mock-up of an ankle, one of a broken femur (with a fracture about 0.5 mm wide), and one of a metallic implant inserted in a radius. The corresponding comparisons between pictures and reconstructed images are shown in Figure 4.41.

These images show qualitatively the improvement of spatial resolution that was achieved with the new detector prototype, which gave the chance to distinguish structures smaller than a millimetre.

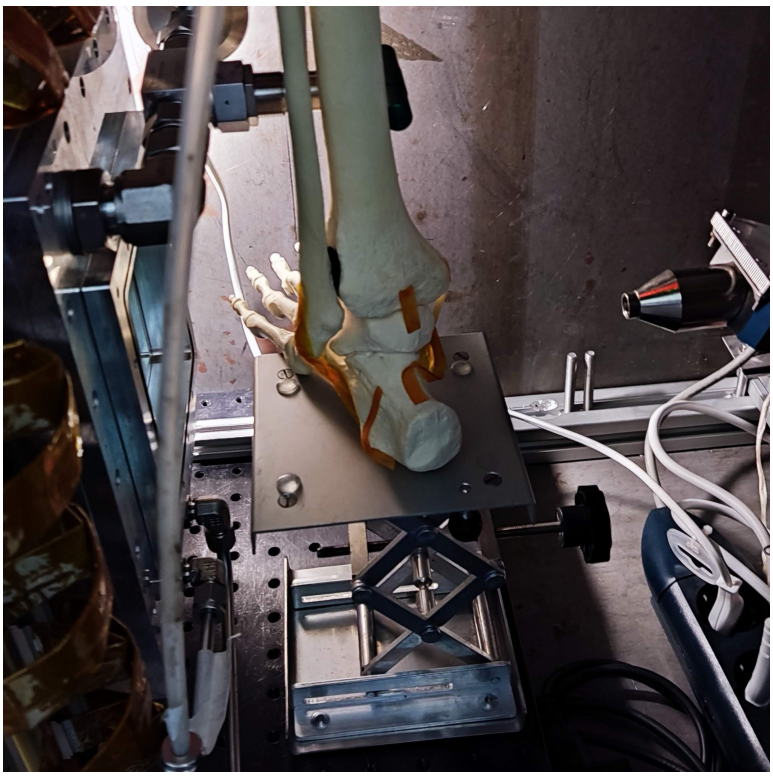

Figure 4.40: Picture of the setup for bone mock-up imaging.

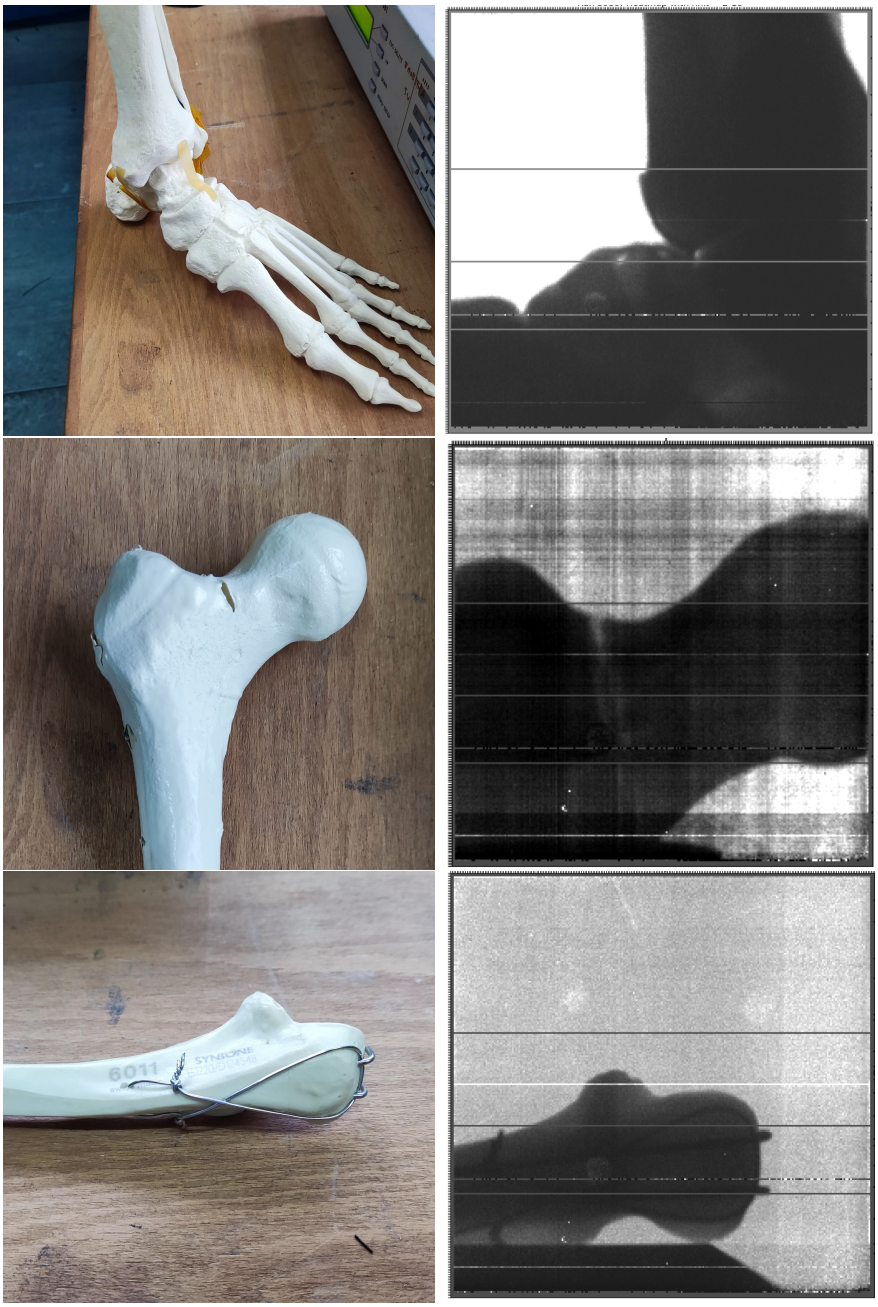

Figure 4.41: On the left, picture of the bone mock-ups used for measurements. On the right, corresponding heatmaps of data captured with the strip GEM detector.

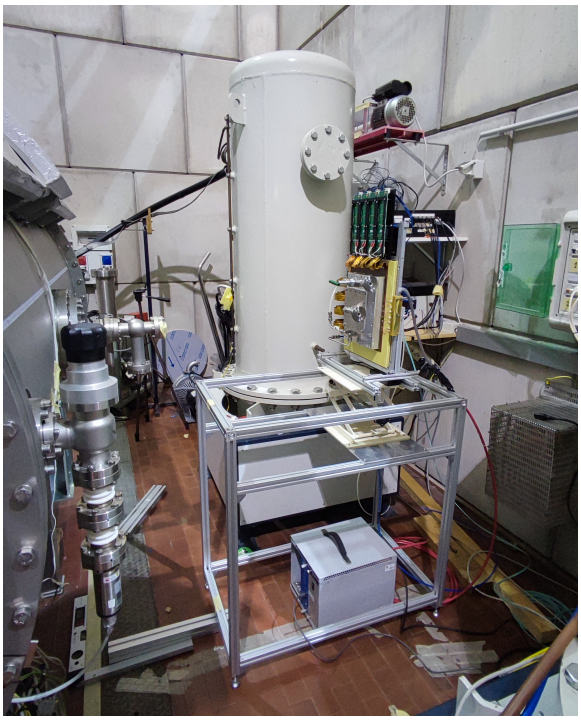

Figure 4.42: Picture of the strip GEM detector as installed at HVPTF, with its own stand-alone support structure.

4.3.3 Installation and use at HVPTF

After characterization, the detector was brought to HVPTF and installed on the same line of sight of the previous one. A new stand-alone support structure was designed and built to allow for a more stable positioning of the detector, as shown in Figure 4.42.

The XR-GEM-2 detector was used for data collection during new conditioning experiments, still with a needle-plane electrode configuration, but in a double polarity condition (i.e. with both electrodes brought to high voltage, one of them positive and the other negative). Unfortunately, unforeseen issues related to electrical grounding arose when employing the positive electrode power supply together with the negative one. This lead to the presence of high intensity noise in the data collected, preventing additional studies on the micro-discharge characterization.

Some data was still reconstructed via software exploiting an additional functionality developed for the GEM-GUI named "transmission mode". This works by plotting, for each channel on the heatmap, the ratio of the number of events of two runs, both normalized by their acquisition time. This method allows to filter out unwanted noise, or to make comparisons when testing similar experimental conditions with small variations. In this case,

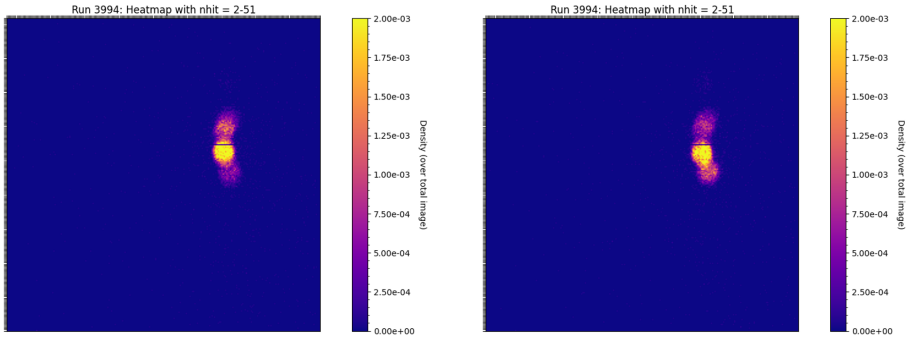

Figure 4.43: Reconstructed heatmap of the radiation observed with the XR-GEM-2 detector for the dark current signal in the needle-plane electrode configuration.

the functionality was used to observe the signal collected for the dark current emissions, while filtering out the noise, taken as reference from acquisitions performed with the power supplies on, but low voltage applied to the electrodes.

Examples of the best reconstructed data obtained with the strip readout, showing emission coming from the plane electrode, are shown in Figure 4.43. The round-shaped distributions of counts that are apparent in the images are thought to be other kinds of possible artefacts from the clusterization software, but no further study was advanced on them because the detector was considered not employable in the noise conditions of the experiment and was dismissed, to be potentially upgraded and brought back in future studies.

The results obtained with the XR-GEM-2 detector, while not instrumental in advancing the characterization of the micro-discharge emissions, were useful in confirming that a better spatial resolution was useful in the management of the signal intensity per channel. They also helped in understanding the need for a more electrically stable readout system, which was then addressed in the development of the following detector prototype, described in the next section.

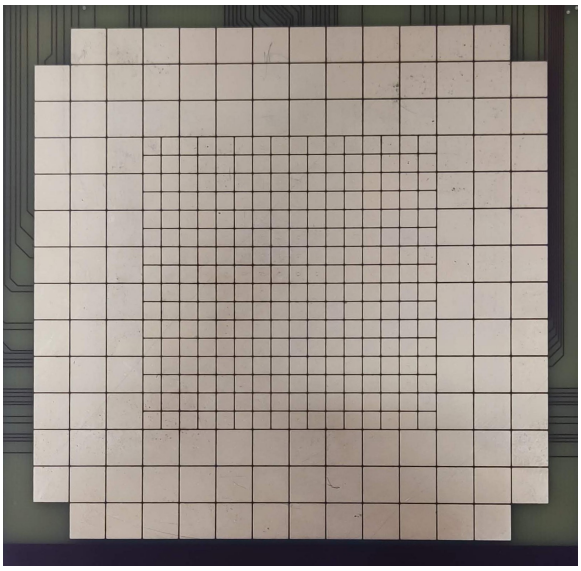

Figure 4.44: Picture of the XR-GEM-3 detector collection anode.

4.4 The XR-GEM-3 detector

The new GEM-based detector developed for HVPTF, and currently installed at the facility, is designed similarly to the previous ones, in that it still employs a triple-GEM structure, with copper coating on the foils. The collection anode, in this case, is composed by 384 independent channels, with 256 of them arranged in a central square and having a side of 3 mm, and the remaining 128 placed around to form a larger square structure, and each with a side of 6 mm, as shown in Figure 4.44.

The detector is also designed to be encased in a metal structure, with better grounding connections, in order to reduce the unwanted noise in the experimental setup that was experienced with the XR-GEM-2 detector. In addition to the improvements in the detector design, to account for the previously experienced grounding issues, the clock and trigger signals for the readout electronics are carried from the acquisition PC with sets of transceivers, forming an optical bridge in order to obtain electric decoupling between the two parts of the system. The combination of these factors allows for a significant reduction of noise, resulting in a much cleaner signal to be acquired, so that the detector can be used more extensively.

The detector was recently installed at the facility, on the same line of sight of the previous ones, employing the same stand-alone support structure as before, as shown in Figure 4.45.

Preliminary data has been collected with the XR-GEM-3 during new experimental sessions, mainly the observation of spark-gap electrodes designed for the MITICA facility, and in the conditioning experiments with a sphere-

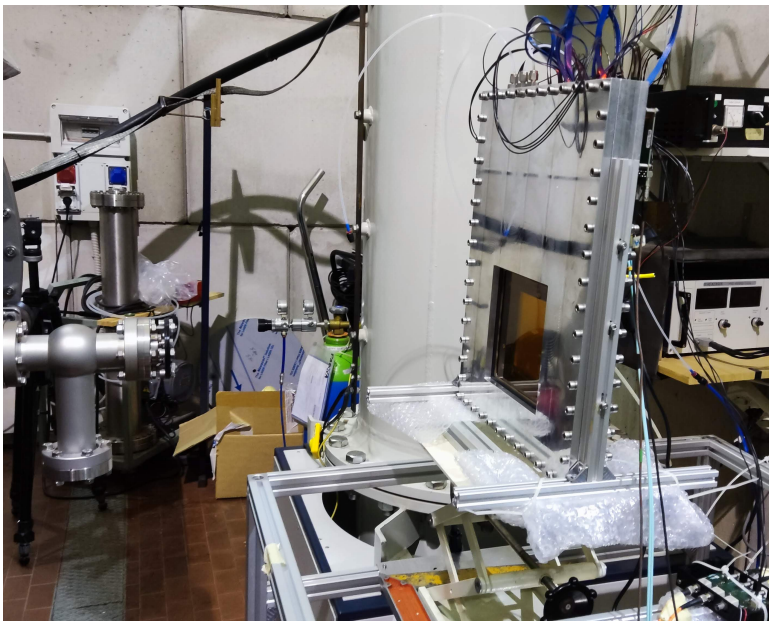

Figure 4.45: Picture of the XR-GEM-3 detector as installed at HVPTF.

plane electrode configuration. These data sets were used as benchmark to verify the solutions implemented for grounding issues and to test the correct operation of the synchronization system. The detector will be ready to collect data in the next experimental sessions of the facility, to serve for further studies on the characterization of the micro-discharge emissions.

4.5 The synchronization system

The measurements performed at HVPTF with the first GEM detector, as mentioned in the previous sections, highlighted the need to have temporal synchronization of the signals collected by the various diagnostics of the facility. This is of paramount importance in any experiment to make both comparisons and to develop multi-approach analyses for the solution of the problems at hand. In a good operational environment, all the data collection instruments should have a common external reference clock signal, and they should have the same physical reference as starting time of the measurements. Additionally, the automation of the data acquisition processes for the different diagnostics is preferable, so that the operator can control and monitor all the relevant data from a central hub.

This section presents the development of a system to generate clock and trigger signals for the instruments installed at HVPTF, and the development of a software to control and monitor the data acquisition systems remotely.

4.5.1 The hardware and firmware setup

The main hardware components used for the development of the synchronization system for HVPTF are a RFSoC4x2 board and a series of electro-optical converters for the signals. The RFSoC4x2 is a development board from AMD-Xilinx, developed by the PYNQ team in partnership with Real Digital, designed around the Zynq Ultrascale+ Radio Frequency System-on-Chip (RFSoC) device. A picture of the board is presented in Figure 4.46.

The board features both a programmable logic (FPGA) component and a processing system (ARM core), combining them with high-accuracy ADCs and DACs operating at giga samples per second and a series of other I/O interfaces, making it suitable for numerous applications, as for example high-speed data acquisition and digital signal processing. The corresponding block diagram is shown in Figure 4.47. Particular attention was put on the PMOD channels, two sets of eight pins each (named PMOD-A and PMOD-B) that act as I/O interfaces and are controlled by the programmable logic components of the board.

The board also features the capability to load overlays, pre-packed designs that bridge the connection between the programmable logic components and the processing system, while also giving the chance to externally interact with the system to change parameters and monitor the board activities. In the case of application of HVPTF, a custom overlay has been built. This instructs the firmware of the programmable logic components to scale the internal clock produced from the oscilloscope of the processing system to the values necessary to operate the acquisition systems of the different diagnostics. A scheme of the block diagram of the overlay firmware is presented in Figure 4.48.

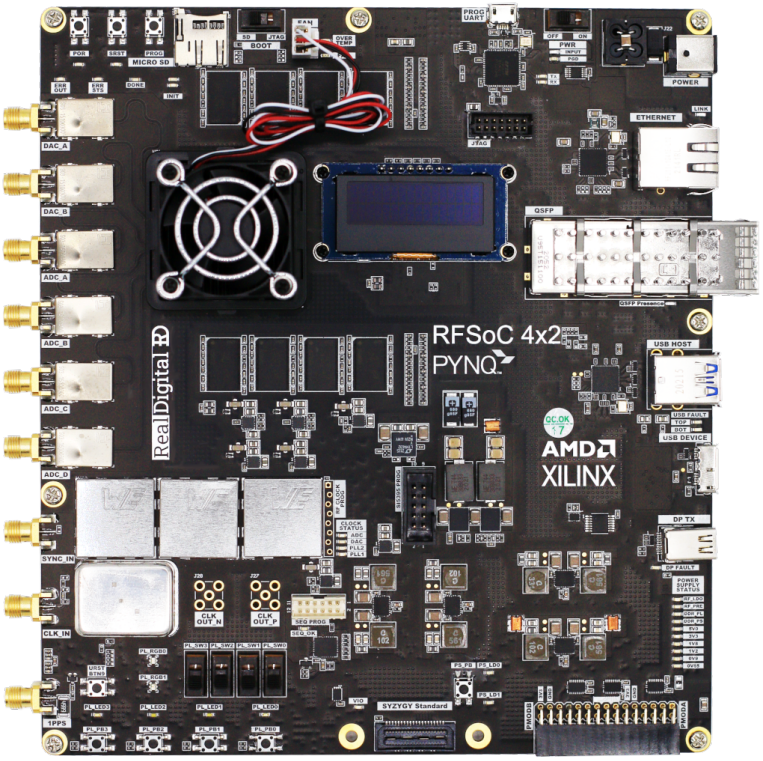

Figure 4.46: Picture of the RFSoC4x2 board used for the synchronization system of HVPTF.

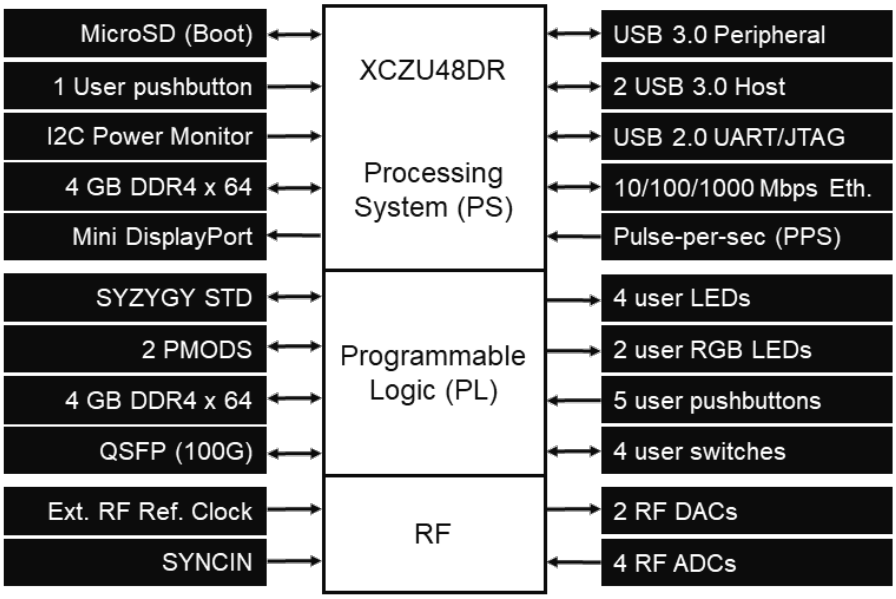

Figure 4.47: Block diagram of the RFSoC4x2 board.

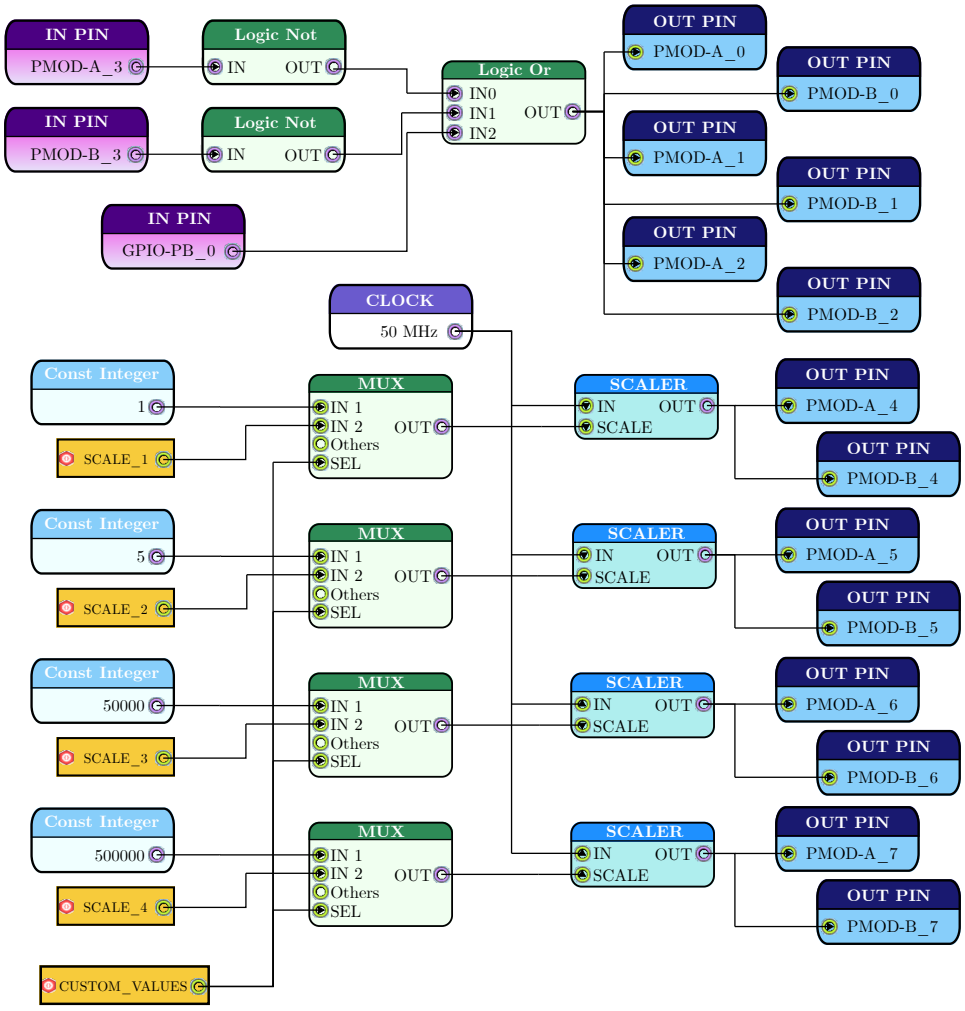

Figure 4.48: Block diagram of the firmware overlay developed on the RFSoC4x2 board for the synchronization system of HVPTF.

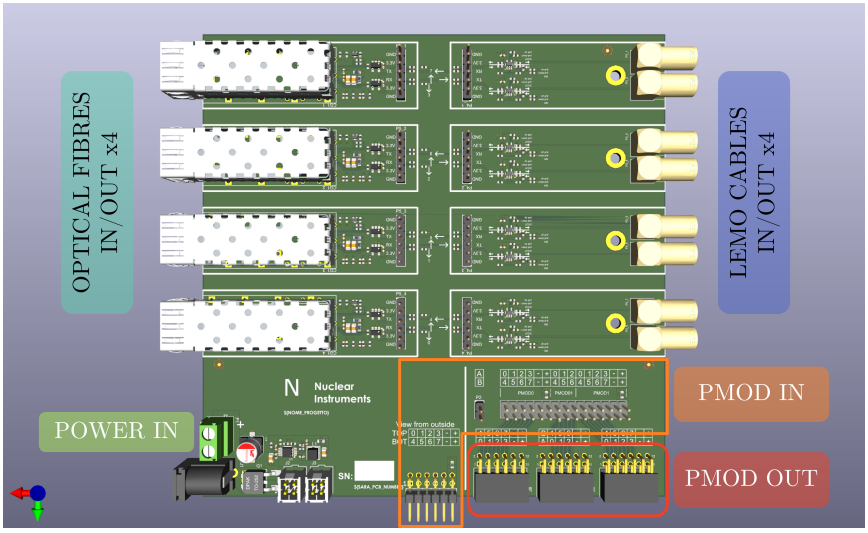

Figure 4.49: Rendering of the electro-optical converter board developed for the synchronization system of HVPTF.

As it can be seen, the main components of the system act so that the base asynchronous 50 MHz clock signal coming from the processing system is scaled down by either fixed factors or user-defined custom values, read from a register file. The resulting slower clocks are dished out from the PMOD pins (from both A and B sets) with numbers from 4 to 7. Additionally, a custom trigger logic is developed, which outputs a high signal from PMOD pins 0, 1 and 2 when a button is pressed on the board. This trigger signal is also raised when a low signal is fed in input to a PMOD pin 3. This is justified by the use of a passive external switch button, connected to the PMOD pin 3 and the ground of the PMOD ports. Closing the switch lowers the signal in input and raises the output trigger consequently.

The electric clock and trigger signals coming from the RFSoC4x2 board can be connected directly to the different diagnostic systems in HVPTF, but this could cause serious grounding issues and there is the risk of damaging the equipment in the occurrence of electric surges. In order to preserve electric insulation among the different instruments, the signals have to be converted to optical, transmitted through fibres, and then converted back to electric with different components, each sharing the ground with its dedicated diagnostics. Electro-optical converter boards were thus developed, in collaboration with Nuclear Instruments. The converter boards are based on the use of transceivers to be used both ways (for the conversion from electrical to optical and the other way around), coupled with an electrical circuit for stabilization of the signals and removal of noise. A render of the board layout is shown in Figure 4.49.

The complete system was tested in lab before installation at the facility.

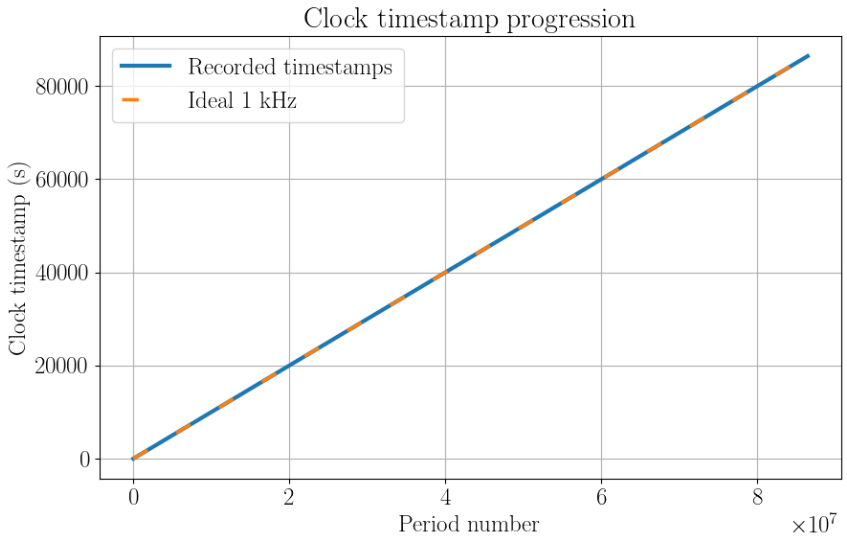

Figure 4.50: Plot of the consecutive timestamps recorded for the 1 kHz clock, with comparison to the exact curve.

The voltage levels of the signals were tuned to the needs of each acquisition system, verifying their correct implementation for the diagnostics.

An additional test was performed to check for the possible presence of issues in the clock signals coming from the system. A clock with a frequency of 1 kHz produced by the RFSoC board was fed to an input channel of a CAEN DT5730SB digitizer (the same model used for acquisition of the scintillator signals in HVPTF), and the period of the cycles was sampled for a total of 24 h. Figure 4.50 shows the trend of the timestamps sampled as a function of their number. The fact that the curve is rectilinear and does not change steepness shows the absence of drifting effects during the acquisition time, further confirmed by the coincidence with the "ideal 1 kHz" line, drawn by simply dividing the number of sample by 1000. Figure 4.51 presents a histogram of the time difference recorded between consecutive events, in logarithmic scale for the y axis, with the zero value referred to the exact 1 ms difference. The plot shows two full bins around the center (the fact that it is not a single one is due to rounding errors in the calculation of the timestamps), and two other bins on either side, representing the occurrence of jittering, the intensity of which is limited to approximately 2 ns (0.002 µs) either way (positive or negative).

4.5.2 The synchronization software

The physical synchronization of the clock and trigger signals for the diagnostics of HVPTF, as mentioned above, was accompanied by the development

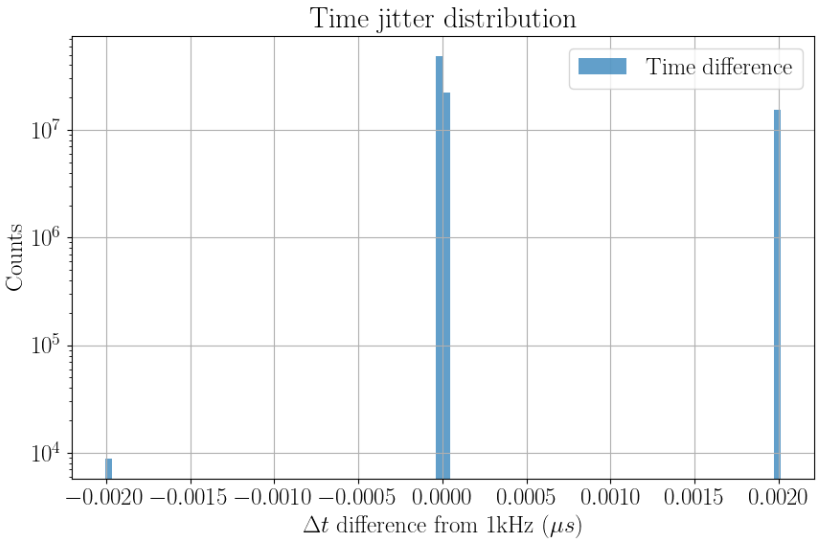

Figure 4.51: Histogram of the time difference between consecutive events of the 1 kHz clock, referred to the exact value.

of a software to manage and control simultaneously the various data acquisition software running on each of the diagnostic computers. The algorithm was written in Python, with a combination of finite state machine structure, a server-client logic for the computers, and an asynchronous messaging protocol for network communication.

The code is based on the use of the libraries pysm and pyzmq to achieve the functionalities just mentioned, in combination with custom Application Programming Interfaces (APIs) and process spawning features to interact with the specific data acquisition software suites.

The role of server computer is assigned to the machine in control of the main interface of the HVPTF system, i.e. the supervisor system described in section 2.3, with a platform based on a LabVIEW interface. When the synchronization algorithm is started, it uses the ZeroMQ messaging functionalities provided by the pyzmq library to connect to the network, bind the IP address of the machine, listen to the messages incoming from the supervisor on a predefined port, and broadcast correspondent instructions on the network to the connected clients. The other computers run the client version of the algorithm, which tries to establish connection to the server, and goes on to receive the instructions coming over the network and acting appropriately, in a manner dependent on the specific diagnostic system connected to the computer. The first development has been focused on the connection of the main HVPTF system with the scintillator diagnostics, that make use of a CAEN DT5730SB digitizer for signal collection, and the GEM detector, which has its own data acquisition system described in the previous chapter.

The CAEN digitizer is controlled from the acquisition computer of the scintillators with the use of the ABCD software, a distributed Data Acquisition (DAQ) framework developed in C/C++ by researchers of the European Joint Research Center (JRC), with the aim of acquiring data from signal digitizers in Nuclear Physics experiments [ABCD, 2025]. The term distributed refers to the fact that, in this framework, each task related to the DAQ runs in a separate process. The software can be controlled with a web-based user interface, but there are also external communication APIs, which are invoked by the finite state machine algorithm, mainly by calling a custom startup script and then interacting with the same socket interface which is the base of the communication among processes in ABCD.

The GEM detector acquisition software runs similarly to ABCD, in the sense that it also has an underlying C/C++ code running multiple processes simultaneously, with the choice between a web-based user interface or communication via sockets for its interaction and control. It is thus easy to follow the same logic for both the client-side algorithms, with only small changes in the details of the API calls, to obtain solid results.

Chapter 5

Modelling and Simulation

The experimental observations based on the data collected with the XR-GEM-1 detector, described in the previous chapter, motivated the search for a model to try and justify the considerations derived about the phenomena observed. In particular, the analysis of the X-ray emission during the micro-discharges on the short temporal scale presented in section 4.2.3, sparked the interest to develop simulation tools that could reproduce phenomena similar to what was observed in the experiments.

This chapter presents the development of such a model, composed of a combination of different parts and developed across multiple software, that can act as a full framework for analysis and validation of the phenomenology and dynamics of the micro-discharges in vacuum of HVPTF.

5.1 Theoretical basis

The model considered in this work is based on the concept of an interchange of electrons, ions and photons between cathode and anode. [Trump and Van De Graaff, 1947]. Electrons are emitted from the cathode in the vacuum gap between the electrodes, they are accelerated by the electric field, and can produce secondary emission upon their collisions with the anode. The species extracted from the surface are mainly photons or ionized heavy atoms of the material constituting the electrode. These can then be directed back towards the cathode (especially the ions, under the influence of the electric field), where they impinge and may produce other electrons, advancing the process in time and leading to potential avalanche occurrences. The discharge, in the hypothesis followed here, can occur when the number of secondary electrons produced in the system diverges to high values.

A sketch of the condition described by this model, for the ideal case of two parallel planar electrodes, is shown in Figure 5.1, where the quantities Γ represent fluxes of particles, with the subscript referring to the particle species and the superscript referring to the electrode at which the flux is

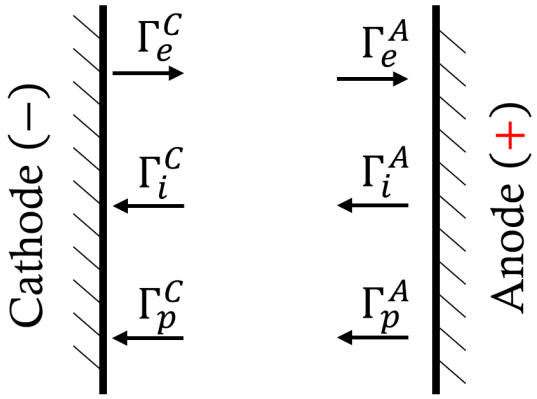

Figure 5.1: Sketch of the theoretical model describing the interchange of charged particles and photons between electrodes in vacuum.

observed. The directions of the arrows define the sign conventions for the the model.

With reference to the sketch, the fluxes of particles going towards and leaving each electrode can be related, introducing some coefficients representing the production of secondaries. Letting A be the number of ions extracted in average by an electron impinging on the anode, for example, the relation between the flux of electrons impinging on the anode and the flux of ions leaving it can be written as:

$$\Gamma_i^A = A \cdot \Gamma_e^A \tag{5.1}$$

Similar relations can be written for all species by implementing other coefficients. Thus, B is defined as the average number of electrons extracted at the cathode per incident ions, C corresponds to the average number of photons produced at the anode per incident electron, and D is the average number of electrons produced at the cathode by an incident photon.

Other physical aspects of the system can be introduced to make it more realistic. A fixed term of production of electrons at the cathode is added, corresponding to the contribution of the Fowler-Nordheim current described in section 1.2.2, here indicated as Γ_{FN}, and written with an explicit dependence on the electric field. The simplest set of equations that describes the system can be written as follows:

$$\begin{cases} \Gamma_e^C = B \cdot \Gamma_i^C + D \cdot \Gamma_p^C + \Gamma_{FN}(E_C) \\ \Gamma_i^A = A \cdot \Gamma_e^A \\ \Gamma_p^A = C \cdot \Gamma_e^A \\ \Gamma_i^C + \Gamma_e^C = \Gamma_i^A + \Gamma_e^A \end{cases} \tag{5.2}$$

Where the last equation is a balance expressing the conservation of charge

between anode and cathode in the ideal system. For the real case of study of HVPTF, additional considerations have to be made to take into account other phenomena occurring in the system. In particular, the process of gas desorption from the surfaces of electrodes can play an important role in the matter. [Diamond, 1998] The presence of additional molecules, even if in small number, in the interspace between the electrodes, can lead to a multiplication of the electrons in their path, producing at the same time additional positive ions that can travel towards the cathode and augment the processes described above. In addition to this, past experimental observations at HVPTF have shown that the electric discharges occurring in the system can involve the walls of the vacuum vessel too, since the latter can act as a third fixed voltage level in the system. This means that the charge balance written above needs an additional term to account for the current flowing towards the walls of the chamber.

The equations of the ideal system are thus modified with the introduction of a coefficient F, that represents the average number of electron-ion pairs generated by each electron travelling between the electrodes. This coefficient depends on the quantity of molecules desorbed from the surfaces and available to be ionized. One final consideration to be made is that, in general, photons travelling from one electrode to the other could incur in reactions with the other species present in the space. This can be taken into account with the introduction of a last coefficient G, representing the average effect of any occurrence of photon multiplication. The system of equations describing the case of study thus becomes:

$$\begin{cases} \Gamma_e^C = B \cdot \Gamma_i^C + D \cdot \Gamma_p^C + \Gamma_{FN}(E_C) \\ \Gamma_i^A = A \cdot \Gamma_e^A \\ \Gamma_p^A = C \cdot \Gamma_e^A \\ \Gamma_i^C = \Gamma_i^A + F \cdot \Gamma_e^C \\ \Gamma_e^A = (1+F) \cdot \Gamma_e^C \\ \Gamma_p^C = G \cdot \Gamma_p^A \\ (\Gamma_i^C + \Gamma_e^C) - (\Gamma_i^A + \Gamma_e^A) = (\Gamma_i^{chamber} + \Gamma_e^{chamber}) \end{cases} \tag{5.3}$$

The coefficients defined to model the terms of production of secondaries are summed up in Table 5.1.

This set of equations contains terms that interact with one another and may not be easy to calculate or deduce directly. The approach for a solution in this work is thus to break up the problem in smaller parts, finding the values of the coefficients needed to describe the system, and to combine all the effects afterwards in a single framework modelling the remaining phenomena not solved for, as explained in the following sections.

Coefficient	Physical term
A	Number of ions extracted per electron at the anode
B	Number of electrons extracted per ion at the cathode
C	Number of photons extracted per electron at the anode
D	Number of electrons extracted per photon at the cathode
F	Number of electron-ion pairs produced in the gas
G	Multiplication factor for travelling photons

Table 5.1: Definition of the coefficients for the model equations.

5.2 Single phenomena simulations

As mentioned above, the full problem to be solved was segmented in parts, and single aspects of the system were modelled and simulated with dedicated software. In particular, the coefficients corresponding to the average production of secondary particles from the interactions of primaries (coefficients A, B, C and D of Equation 5.3), were retrieved with the Monte Carlo codes Geant4 and TRIM. In addition to this, the profiles of pressure in space and time deriving from outgassing of the surfaces were calculated with the Molflow software. This section presents the assumptions performed, the development of the single code simulations, and the results obtained.

5.2.1 Geant4 simulations

Geant4 is a Monte Carlo based toolkit for the simulation of the passage of particles through matter. It is applied in various areas of study, mainly for high energy, nuclear and accelerator physics [Agostinelli et al., 2003, Allison et al., 2006, Allison et al., 2016].

The simulations have been developed with the simplest approach possible: a beam of particles in vacuum, impinging on a solid surface, at different energies and angles, with no external electric field applied. The surface is modelled as a wall of stainless steel, 5 cm thick and 10 m wide on the other two dimensions. A sketch of the geometry is shown in Figure 5.2.

The beam is defined as a general particle source, with $1e8$ primaries, emitted from a planar square surface posed at 1 cm from the wall. Beam energies and angles of incidence span the range from 10 keV to 300 keV at steps of 10 keV, and from 0° to 80° at steps of 5°. The physics list for the simulations was built with a modular constructor, including the G4EmLivermorePhysics and G4DecayPhysics libraries.

The simulations have been performed for beams of both electrons and photons, collecting as result the number of particles coming back out from the stainless-steel wall into the vacuum, grouped by kind (photons, electrons, ions). In this way, both the coefficients C and D (respectively, photons ex-

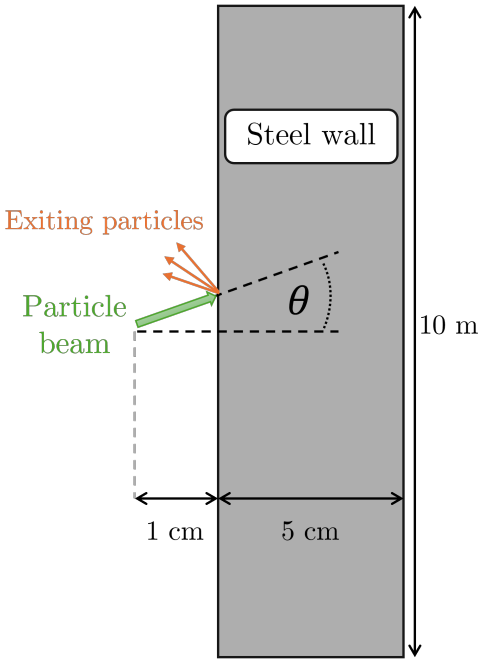

Figure 5.2: Sketch of the geometry used for simulations in Geant4, with indications of the components. The angle of incidence of the beam is θ. (image not to scale)

tracted per incident electron and electrons extracted per incident photons) could be retrieved, as well as coefficient A (ions extracted per incident electron). The resulting values, plotted as function of energy of the primary beam, are shown in Figure 5.3 and Figure 5.4, for a few angles of incidence as an example.

For what concerns coefficient A, the simulations performed in the energy and angle ranges considered never lead to any event of ion extraction by the impinging electron beams. For the purposes of the model, consequently, it is assumed to have a value lower than $1e-8$ and thus be negligible.

The results obtained with the Geant4 simulations are of the order of $1e-3$ for both coefficients C and D, with the exceptional case of gamma rays impinging at grazing angles on the surfaces. Since the aim of this study is ultimately to find the conditions for which the process of electron production diverges (in order to achieve an avalanche phenomenon), it has been concluded that these processes of production of secondaries is not influential, and it has been thus neglected from the combined simulations that are described below. The model has been developed to be flexible, however, so that in future studies the simulations can be easily repeated with different ranges and materials involved, potentially finding conditions for which these processes are major contributors in the development of a discharge.

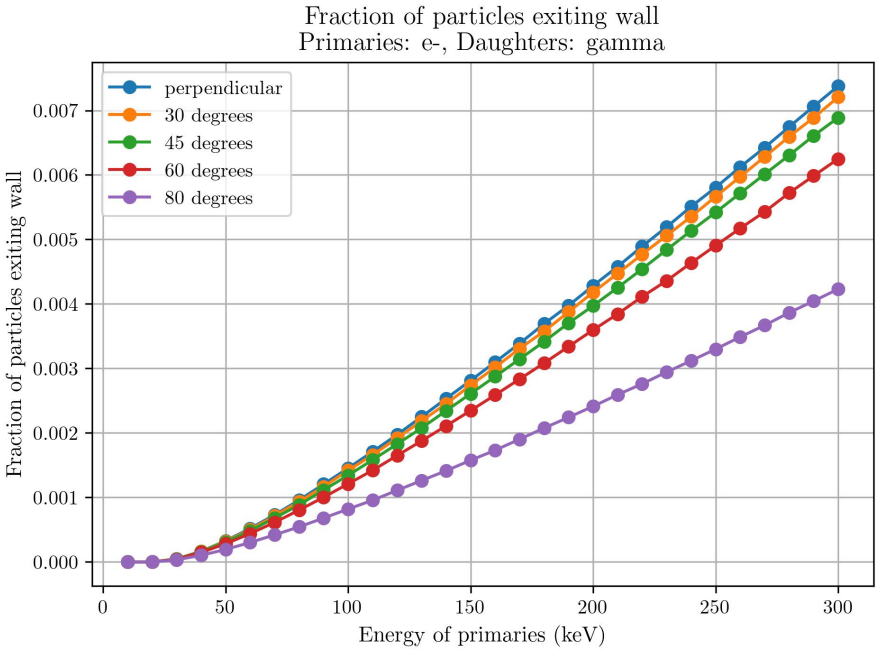

Figure 5.3: Plot of coefficient C obtained from Geant4 simulations, as a function of primary beam energy, for different angles of incidence.

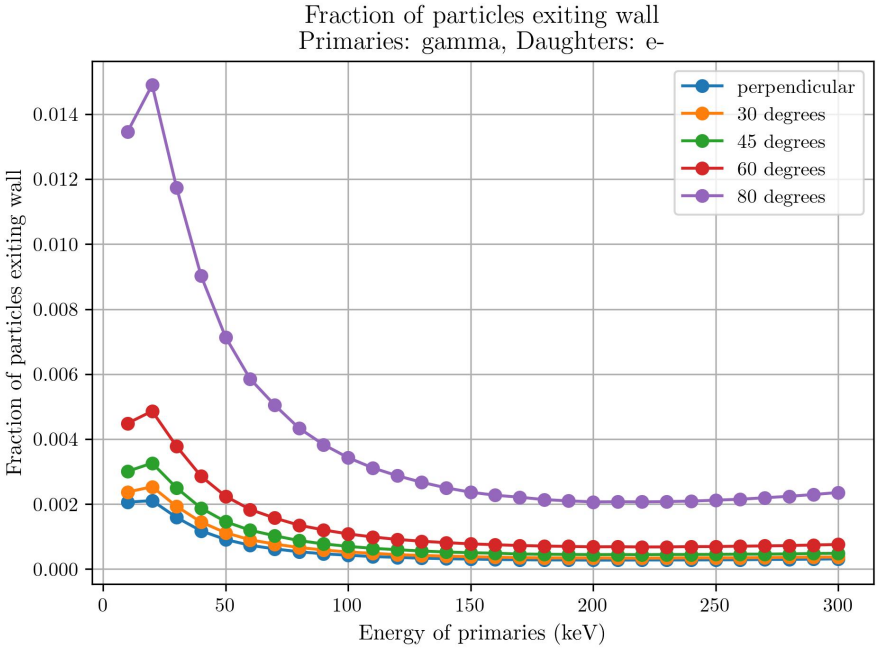

Figure 5.4: Plot of coefficient D obtained from Geant4 simulations, as a function of primary beam energy, for different angles of incidence.

5.2.2 TRIM simulations

The average number of electrons extracted from the stainless-steel wall by the incident ions, corresponding to coefficient B of Equation 5.3, was calculated with the Transport of Ions in Matter (TRIM) software. It uses a quantum mechanical treatment of ion-atom collisions to model the interactions of impinging ions on a surface, calculating the resulting 3D distribution of the ions and simulating the phenomena associated with the energy loss of the ion, as target damage, sputtering, ionization and phonon production [Ziegler et al., 2010].

The simulations were again developed following the simplest approach possible: single atom ion beams were fired at a stainless-steel surface, spanning ranges of energy and angle of incidence. The results for the total ionization energy deposition as a function of depth were collected. For what concerns the impinging ions considered, it is expected that the outgassing process from the surfaces in HVPTF involves both atmospheric gases as nitrogen and oxygen, and organic residuals (hydrocarbons) derived from surface cleaning. This assumption is confirmed by the experimental readings of the residual gas analyser installed at the facility. The simulations were thus performed in this preliminary stage of development for ion beams of hydrogen, carbon, nitrogen and oxygen. The choice of values for energy and angle of incidence was the same as for the Geant4 simulations (10 keV to 300 keV at steps of 10 keV and 0° to 80° at steps of 5°).

For the calculation of coefficient B, the approach presented in [Kireeff Covo et al., 2006] was followed. The ionization energy released by the impinging ions (E_{TRIM}) was divided by the average energy to free an electron inside the material (J), and the contributions from each unit of depth were summed, weighting them with an exponential model of radiation transport in matter to account for the chance of the electrons to reach the surface and be extracted. The production of electrons in the material was considered isotropic, so the probability for the emitted electrons to be directed back towards the surface rather than deeper in the material (P) has been fixed at 0.5. An additional factor was also introduced to account for the processes involved in the interactions of impinging ions heavier than hydrogen (C_{HI}). Coefficient B was thus calculated as:

$$B = C_{HI} \cdot P \cdot \sum_{x=0}^{d} \frac{E_{TRIM}(x)}{J} e^{-x/L} \tag{5.4}$$

Where d and L represent the depth of the electron escape layer and the mean attenuation length for electrons in metals. They were fixed, respectively, at 20 Å and 10 Å. The values for coefficient B resulting from the formula are shown, for some atoms and angles as example, in Figure 5.5.

The species considered in this study are expected to be ionized in their molecular form rather than as single atom ions. Thus, entire molecules

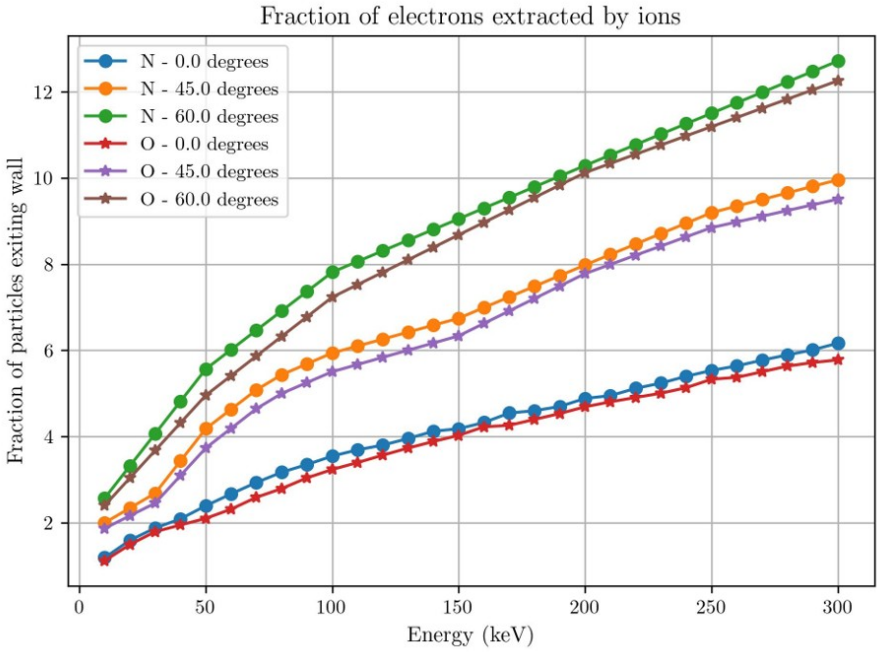

Figure 5.5: Plot of coefficient B for single atoms obtained from the simulations, as a function of primary beam energy, for different angles of incidence.

should be modelled as particles impinging on the surfaces. However, for the energy ranges considered it is safe to assume that, upon striking the metal, molecules dissociate in their atomic components. Therefore, the B coefficient for molecules may be calculated as the weighted sum of the ones for the single atoms, based on the relative mass of each atom in the molecule. As an example, the resulting values of B for the CO_2 and the H_2O molecules are plotted in Figure 5.6.

It can be seen from the plot that these resulting values are more significant than what found for coefficients A, C and D above. In particular, being above unity, coefficient B could be one of the major contributors to the development of discharges, leading to multiplication of the electrons involved in the system. The values obtained for the different molecules were thus exported to be used for the complete simulation model described in the following.

5.2.3 Molflow simulations

Molflow is a Monte Carlo software, developed at CERN, which allows the calculation of pressure in an arbitrarily complex geometry in vacuum conditions, where the molecular flow is to be considered. The code uses the test-particle Monte Carlo method, in which virtual gas molecules are gener-

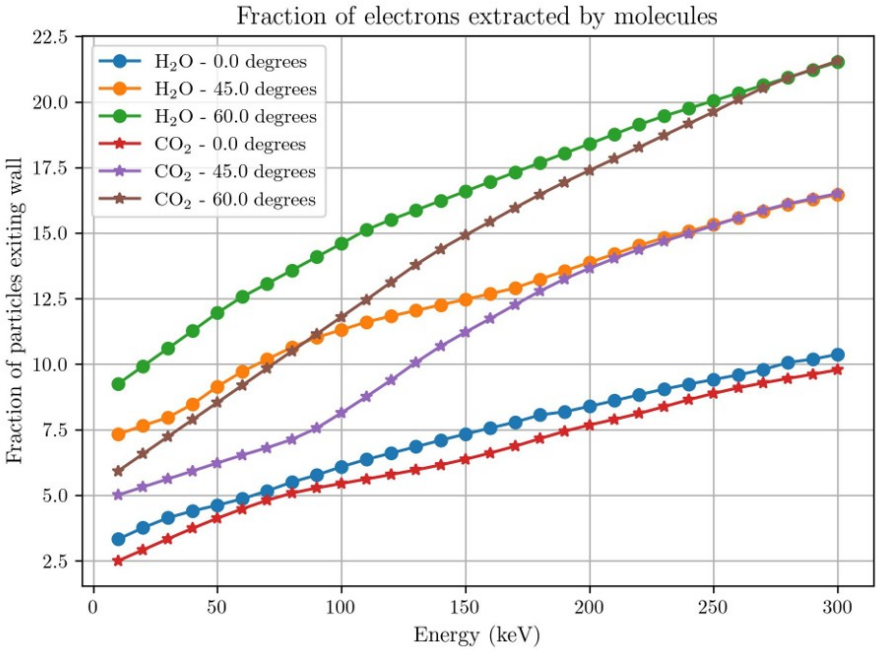

Figure 5.6: Plot of coefficient B for molecules obtained from the simulations, as a function of primary beam energy, for different angles of incidence.

ated from a source and tracked to absorption. Physical quantities such as pressure, density and impingement rates can be calculated on the basis of the number of hits between the virtual molecules and geometrical polygons defined in the environment [Kersevan and Ady, 2019].

The HVPTF vessel has been modelled geometrically in the software, for the needle-plane electrode configuration with a distance of 36 mm, starting from a simplified CAD section of the chamber, with the addition of two regions for the pump and the main pressure sensor respectively. The resulting geometry is shown with a wireframe structure in Figure 5.7.

Two separate sets of simulations have been performed. The first regarded steady-state conditions, referring to the average value of pressure in the chamber in operational conditions. The second set of simulations concerned with the evolution in time of the pressure profile in the chamber, following the emission of a quantity of gas from the planar electrode. This is meant to represent the phenomenon of desorption of gas from the surface of the electrode during conditioning experiments, as mentioned in section 1.2.3.

Steady-state simulations

Steady-state simulations have been performed considering a fixed outgassing rate from all the internal surfaces of the HVPTF vessel. To reproduce the

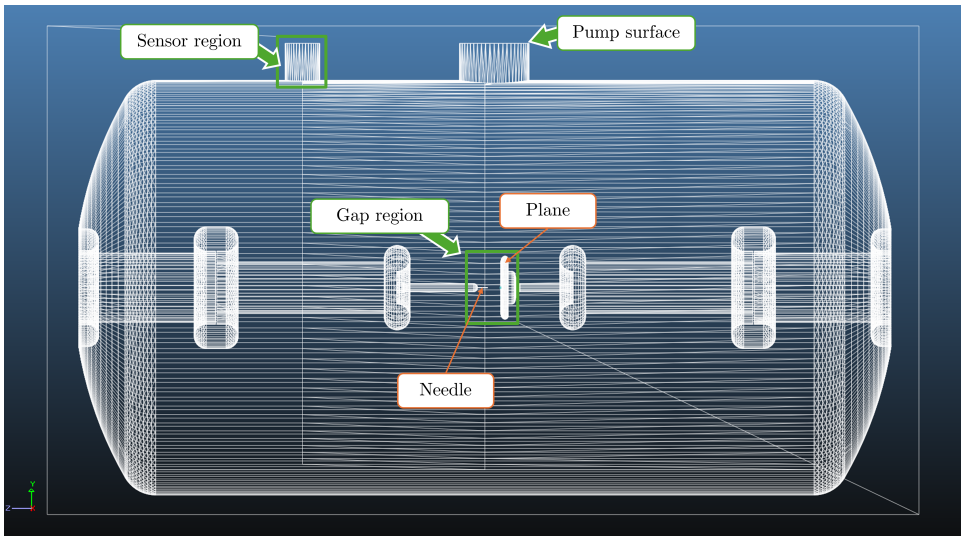

Figure 5.7: Plot of the geometry of HVPTF as reconstructed in Molflow, with indications of the electrodes and the regions mentioned in the text.

value of the average pressure observed during the experimental sessions, which was about 2×10^{-7} mbar, considering a pumping speed of $500\,\mathrm{L\,s^{-1}}$, and a surface area of about $11.8\,\mathrm{m^2}$, the outgassing rate has been calculated as:

$$\phi_{og} = \frac{p \cdot \Gamma_{pump}}{S} = 8.475 \times 10^{-10}\,\mathrm{mbar\,L\,s^{-1}\,cm^{-2}} \tag{5.5}$$

The resulting value is reasonable for AISI304L after cleaning and polishing [Fedchak et al., 2021]. The steady-state simulations verified that the resulting value of average pressure in the chamber is in accordance with the experimental measurements, and that pressure is evenly distributed across the volume.

Time dependent simulations

The time dependent simulations have been set to calculate the evolution in time of the pressure profile following an outgassing burst from the surface of the plane electrode. The hypothesis at the basis of this approach, as mentioned above, is that, during the conditioning experiments at HVPTF, the electric discharges between electrodes are caused by an increment of molecules available for ionization in the gap, with a magnitude sufficient to cause electrons to multiply and produce an avalanche discharge. The emission of gas is confirmed by the experimental measurements of the pressure level inside the chamber and the readings from the residual gas analyser. The source of gas is considered the plane electrode, subjected to a combination of phenomena: vacuum and thermal outgassing, electron bombardment, and

Desorption rate	Pulse duration
$7.5\,\mathrm{mbar\,L\,s^{-1}}$	10 µs
$10\,\mathrm{mbar\,L\,s^{-1}}$	7.5 µs
$12.5\,\mathrm{mbar\,L\,s^{-1}}$	6 µs
$15\,\mathrm{mbar\,L\,s^{-1}}$	5 µs
$20\,\mathrm{mbar\,L\,s^{-1}}$	3.75 µs
$37.5\,\mathrm{mbar\,L\,s^{-1}}$	2 µs
$75\,\mathrm{mbar\,L\,s^{-1}}$	1 µs

Table 5.2: Details of different desorption pulses considered for the Molflow simulations.

outgassing due to high voltage levels can all contribute to produce the onset of gas release, as described in [Diamond, 1998]. The aim of the simulation work is not to justify the origin of the gas, but only to model what are the conditions deriving from a defined burst.

The magnitude of the outgassing burst was fixed at $7.5 \times 10^{-5}\,\mathrm{mbar\,L}$, after some preliminary trial-and-error simulations, to get a resulting profile for the sensor region consistent with the data recorded experimentally from the pressure sensor. The number of particles released was calculated from the integral value of the pulse (which corresponds to the product of pressure and volume), following the ideal gas equation, at standard temperature (293.15 K):

$$N_p = \frac{pV}{kT} = \frac{\int_t pulse}{kT} = 1.85 \cdot 10^{15} \tag{5.6}$$

Considering that the gas is emitted from a surface of approximately $81\,\mathrm{cm^2}$, this value corresponds to about 2% of a monolayer of adsorbed gas (about $10^{15}\,\mathrm{molecules/cm^2}$ per monolayer [Diamond, 1998]).

The simulations have been performed considering different combinations of values for the intensity and duration of the gas injection, as shown in Table 5.2, keeping constant the pulse integral value. This allowed to observe the influence of the free parameters on the results of the simulations without affecting the long-term average pressure profile in time of the chamber.

The simulations were performed with a custom incremental sequence of time steps, spanning over multiple orders of magnitude, as reported in Table 5.3, so that the full dynamics of the phenomena could be represented and understood.

The case with an pulse of $15\,\mathrm{mbar\,L\,s^{-1}}$ lasting 5 µs is considered as reference for further considerations. Figure 5.8 shows the evolution of the pressure profile in time as seen qualitatively in Molflow, for successive time steps, with coloured tiles on the relevant positions of measurement.

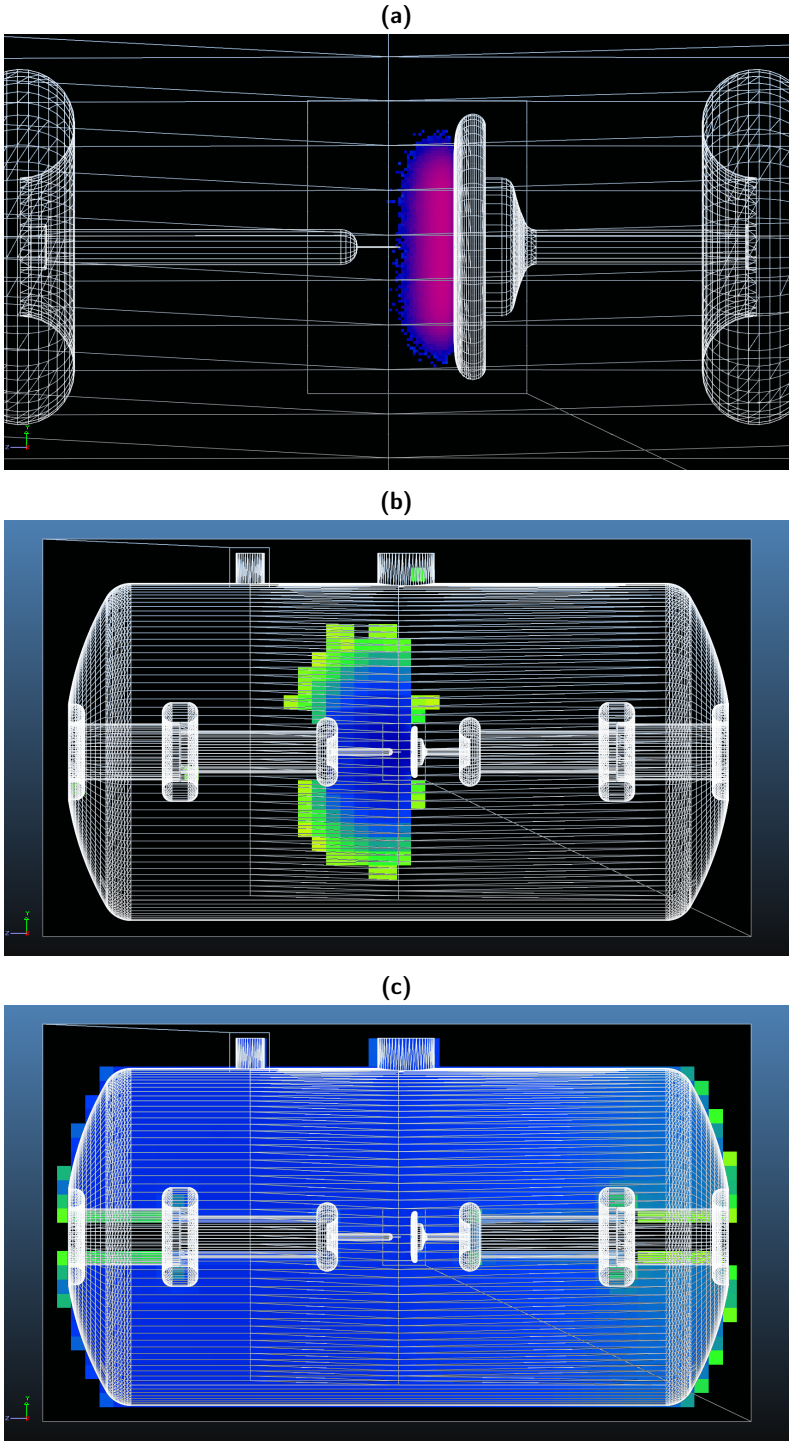

Figure 5.8: Resulting pressure profile in Molflow with the example gas desorption pulse. (a) Pressure profile after 30 µs (zoom near the electrodes). (b) Pressure profile after 300 µs. (c) Pressure profile after 3 ms.

Range start	Range step	Range end	Integration half-window
0 µs	1 µs	20 µs	500 ns
30 µs	10 µs	150 µs	5 µs
200 µs	100 µs	1000 µs	50 µs
2 ms	1 ms	10 ms	500 µs
20 ms	10 ms	100 ms	5 ms
200 ms	100 ms	1000 ms	50 ms
2 s	1 s	10 s	500 ms
20 s	10 s	100 s	5 s

Table 5.3: Sequence of time steps considered for the Molflow simulations.

The evolution in time of the average pressure has been calculated separately for the entire geometry, for the region between electrodes, and for the region of the pressure sensor, considering also the background pressure found with the steady-state simulations. The resulting graph is reported in Figure 5.9.

As it can be seen from the plot, the distance between the sensor region and the middle of the chamber implies that there are delays in the response of the system to the outgassing bursts, as the sensor region registers a change from the steady-state background pressure value only about 1 ms after the pulse, when the average pressure in the gap region has already diminished by orders of magnitude. This also implies that a small variation of pressure at the sensor can be related to a much more intense change between the electrodes, encouraging the hypothesis that the discharges may develop as classical avalanches due to the presence and ionization of enough gas extracted from the electrodes.

As mentioned before, different values for the intensity and the time duration of the gas desorption pulse have been tested, keeping constant the total number of particles produced (the integral of the pulse curve). The profiles resulting from the set of simulations, for the sensor region only, are shown in Figure 5.10.

As it can be seen from the plot, the differences in shape (height and length) of the outgassing pulse cause no change in the profile for the sensor region.

Figure 5.11a presents the profiles of the average pressure in the inter-electrode gap region for the different pulse shapes, showing that the long-term behaviour is again the same for all simulations. Figure 5.11b, instead, highlights that the short-term trend of the curves depends on the characteristics of the pulse. The numerical results, in terms of peak pressure values and corresponding timestamps, are reported in Table 5.4.

The results obtained with this set of simulations imply that reproducing the experimental measurements for the pressure sensor does not fully deter-

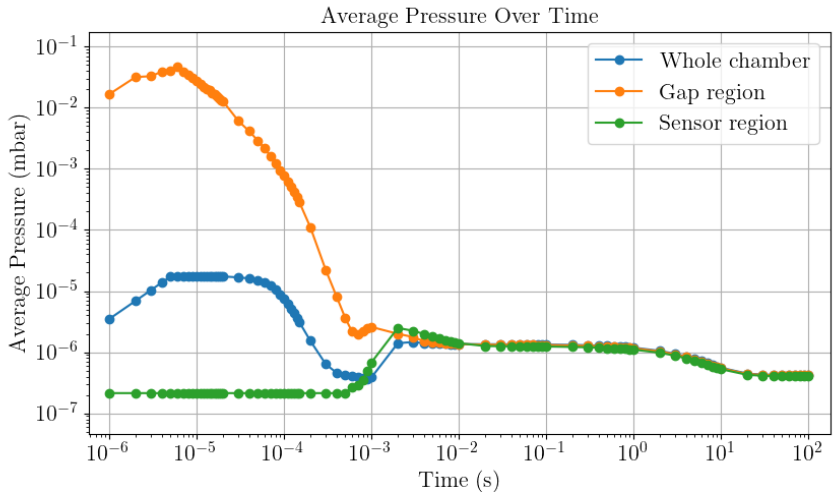

Figure 5.9: Plot of the evolution in time of the average pressure calculated with Molflow, for the entire chamber, the space between the electrodes and the sensor region, with a single pulse shape.

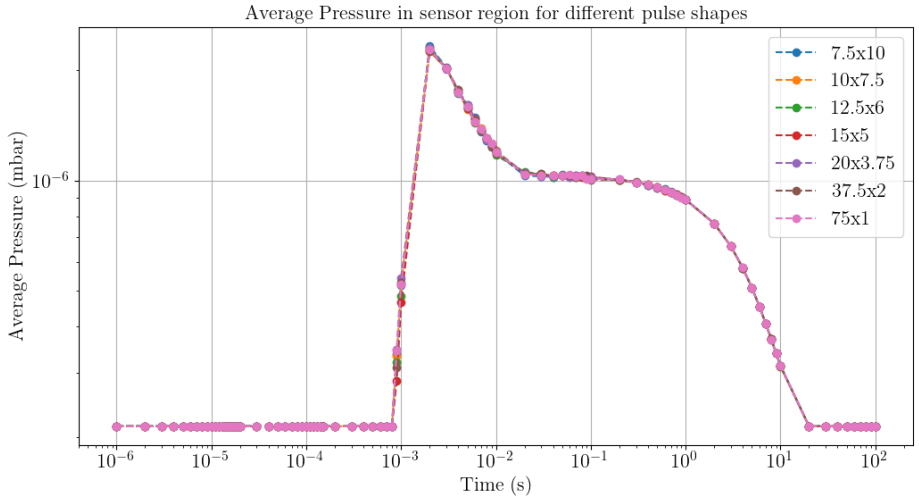

Figure 5.10: Plot of the evolution in time of the average pressure calculated with Molflow, for the sensor region, for different pulse shapes.

(a)

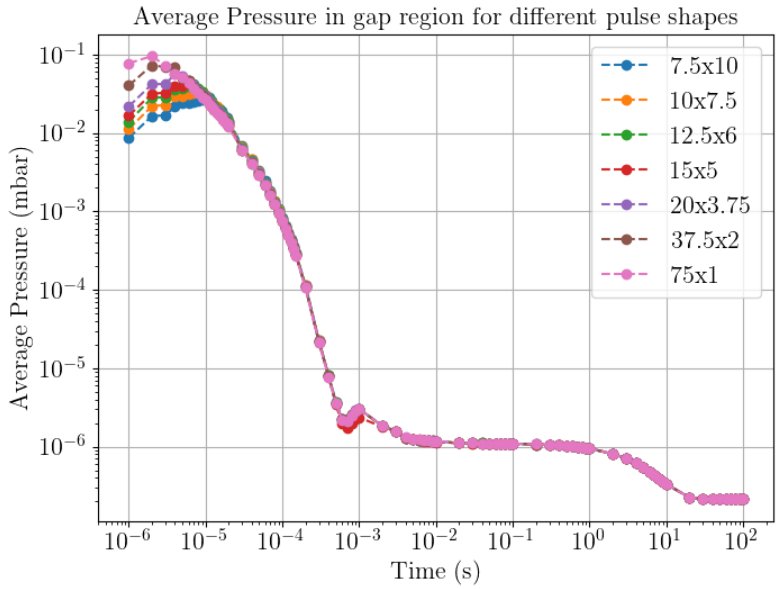

(b)

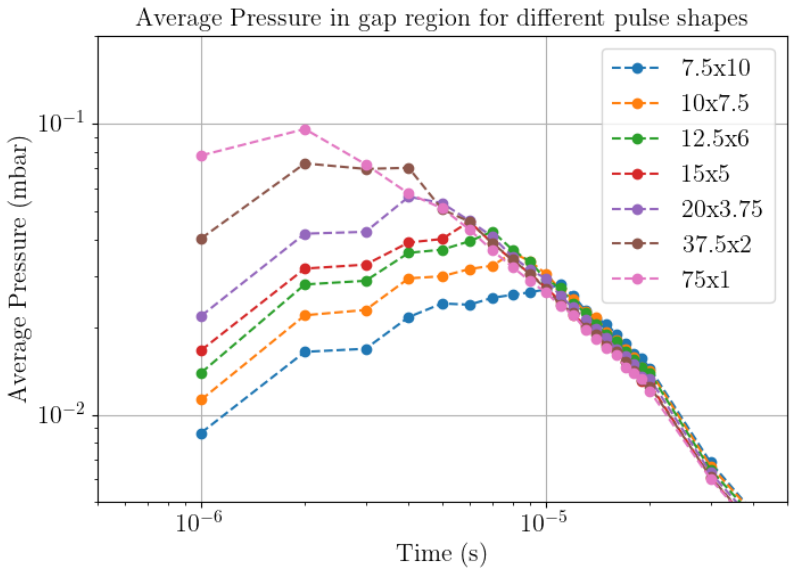

Figure 5.11: Plot of the evolution in time of the average pressure calculated with Molflow, for the inter-electrode gap region, for different pulse shapes. (a) Plot of the profile for the full length of the simulations. (b) Zoom on the initial region of the plot

Desorption rate	Pulse duration	Peak pressure	Peak timestamp
$7.5\,\mathrm{mbar\,L\,s^{-1}}$	10 µs	0.0280 mbar	11 µs
$10\,\mathrm{mbar\,L\,s^{-1}}$	7.5 µs	0.0360 mbar	8 µs
$12.5\,\mathrm{mbar\,L\,s^{-1}}$	6 µs	0.0425 mbar	7 µs
$15\,\mathrm{mbar\,L\,s^{-1}}$	5 µs	0.0461 mbar	6 µs
$20\,\mathrm{mbar\,L\,s^{-1}}$	3.75 µs	0.0560 mbar	4 µs
$37.5\,\mathrm{mbar\,L\,s^{-1}}$	2 µs	0.0729 mbar	2 µs
$75\,\mathrm{mbar\,L\,s^{-1}}$	1 µs	0.0957 mbar	2 µs

Table 5.4: Peak pressures reached for different pulse parameters in the Molflow simulations.

mine the phenomenology of gas desorption in the microscale for time and space. That is instead more influenced by the peak pressure value reached on the short-term time trends, as detailed in the next section.

5.3 Integrated simulations

Once the simulations of single phenomena performed with the various codes described above produced their results and the necessary information were retrieved, a full model was built to account for all the contributions, simulating the motion of electrons and ions in the environment of the HVPTF vacuum chamber. The software of choice for this complete model was COMSOL, a multiphysics finite element simulation tool developed for engineering and physics applications. In the following, the components of the model are presented and explained.

The model has been built as a 2D axisymmetric domain. The geometry of the transverse section of the HVPTF chamber is the same as for section 5.2.3, without the pump and sensor regions. It is directly imported from a CAD design, with default repair tolerance. The geometrical plot is shown in Figure 5.12.

The geometry is composed by a solid volume, corresponding to the vacuum environment, and multiple boundaries, representing the electrodes, their supports and the external walls of the chamber. Materials "Air" and "304L [solid, polished]" were chosen from the library for the volume and the boundaries respectively, setting all the properties needed for electrical studies.

An interpolated function was defined to account for the B coefficient calculated from the results obtained with SRIM (the nitrogen molecule curve has been considered for preliminary studies), depending on the energy and the angle of incidence of the particle colliding with the surface. The values of coefficients A, C and D retrieved from Geant4, as mentioned before, were considered too small to be of real significance in the simulated conditions,

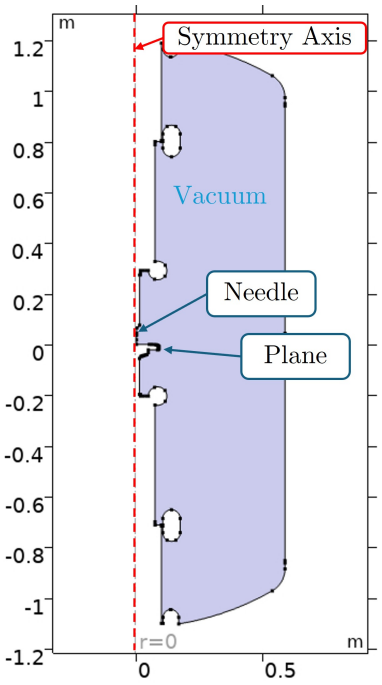

Figure 5.12: Plot of the geometry imported in COMSOL for the HVPTF vessel, with indications of the main components.

and they were neglected. The pressure profile in space and time found with Molflow was interpolated in COMSOL as well. It was defined just as an external function with no direct physical meaning, in order to be used only in the relevant context of calculations. Implementing a full modelling of the corresponding pressure field, which is the more rigorous approach, would have lead to additional complications in the definition of the simulation.

Two more functions were defined for the COMSOL model, to account for the other phenomena considered. A random function is used to assign the value of angle of incidence to the incoming particles when modelling secondary electron extraction from ion impingement on the walls. This is done because, without it, all charged particles in the simulation would always hit the metal surfaces of the boundaries perpendicularly. In the real case of the experiments this is not completely true, as the roughness of the surfaces may cause the particles, travelling at high velocities, to hit the existing microscopic defects and protrusions at different angles. The random function simulates this stochastic behaviour as a first approximation. The last function defined in the model is used to account for the dependence of the ionization cross-section of the gases on the energy of the travelling electrons. It has been interpolated on the basis of the data gathered from the main libraries found on the open-access website LXCat [Carbone et al., 2021]. The databases considered for this study were: Morgan [LXCat -

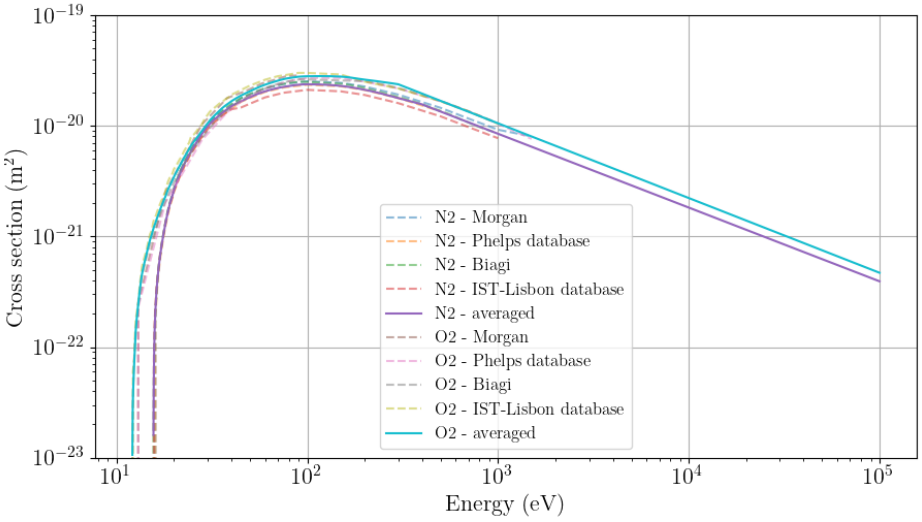

Figure 5.13: Plot of the interpolated curve for the ionization cross section of the electrons to be used in the COMSOL simulations.

Morgan, 2025], Phelps [LXCat - Phelps, 2025], Biagi [LXCat - Biagi, 2025] and IST-Lisbon [LXCat - IST-Lisbon, 2025], which are the more widely employed. The cross-section values were interpolated, as first approximation, for a mixture of nitrogen and oxygen with atmospheric percentages, and extrapolated following a $1/E$ trend up to the energies of interest of the electrons in the HVPTF environment. The plot of the resulting curves is shown in Figure 5.13.

The physical processes considered in the model are defined in two modules taken from the COMSOL library: Electrostatics and Charged Particle Tracing. The former solves Gauss' Law for the electric field using the scalar electric potential as the dependent variable, in order to compute the electric field and other quantities of interest in the domain. Axial symmetry and charge conservation are included in the formulation by default. Initial and boundary conditions are defined in order to set a fixed voltage level on the two electrodes (in particular, $-150\,\mathrm{kV}$ on the needle cathode and ground on the planar anode), and fixed ground on the chamber walls. The resulting voltage map, with streamlines representing the electric field, is shown in Figure 5.14.

The second module, Charged Particle Tracing, is responsible for the simulation of the movement of the electrons and ions in the domain, based on the solution of the corresponding equations of motion. In this work, two species of particles are defined: electrons, which have default properties for mass and charge, and gas molecules. For the definition of the latter, the mass is calculated as weighted average of air molecules ($4.81 \times 10^{-26}\,\mathrm{kg}$), and

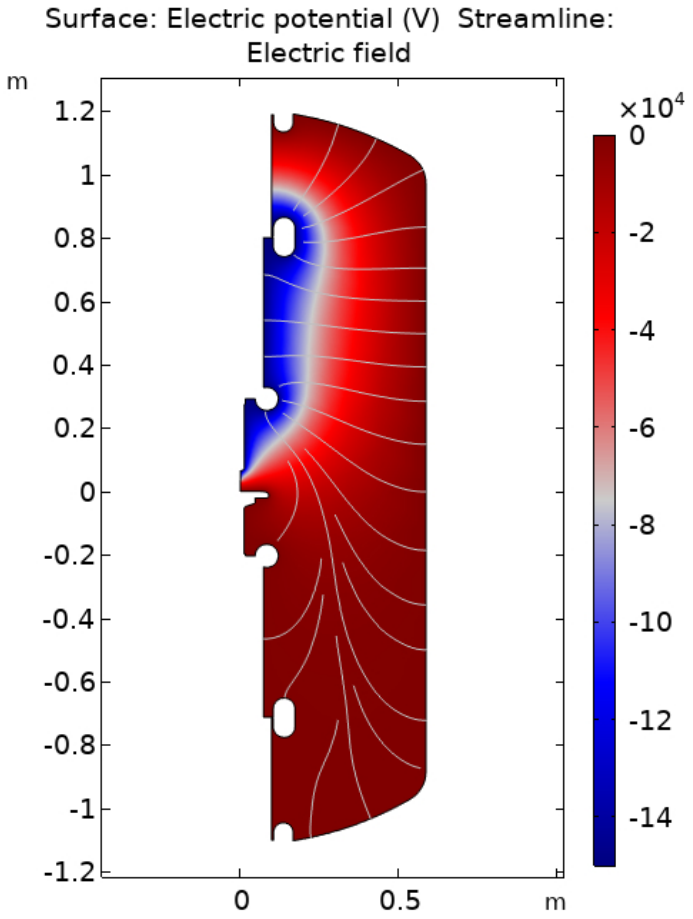

Figure 5.14: Plot of the voltage map calculated with COMSOL for the HVPTF geometry, with grey streamlines indicating the electric field.

unitary positive charge is considered as first approximation.

For the wall boundaries of the geometry, the freeze condition is employed (i.e. particles stop on their tracks but keep their final speed value), in order to visualize the impact point of the particles at the end of the simulation. Additionally, a secondary emission feature is defined to simulate the extraction of electrons from the surfaces upon ion impingement. The secondary emission is enabled only for positively charged incoming particles, and the number of secondary electrons extracted is sampled from the interpolated function corresponding to the B coefficient calculated from TRIM, accounting for a randomness of the angle of incidence as mentioned above.

Primary electrons are introduced in the simulation with an inlet boundary, located at the tip of the needle cathode. Due to the way that the simulation of particle currents is handled in COMSOL, it was preferred to have electrons released as single particles and at fixed timestamps, in order to approximate the behaviour of the system at different conditions of pressure distribution in the volume. Many electrons are released each time, to derive statistically relevant results from each simulation. This approach implies that the effects of space-charge density have to be neglected, and the electric field cannot be influenced by the presence of the particles. Considering the small experimental values of currents in HVPTF and the high electric fields calculated, however, this was considered a justified approximation.

Electric force is applied to all the particles in the domain, based on the calculations of the Electrostatics module. Particle-particle interactions are considered as well, with Coulomb interaction forces being included in the simulation. Finally, collisions of the electrons with the background gas are implemented as well, considering the average molar mass of air ($28.96\,\mathrm{g\,mol^{-1}}$) and a temperature of $293.15\,\mathrm{K}$ as parameters. The density of the molecules in the domain is calculated on the basis of a pressure distribution interpolated from the results of Molflow, following the ideal gas law. Particle counters help in keeping track of the number of primaries introduced from the inlet boundary and the number of secondaries produced in time from the interactions modelled.

A free triangular mesh, generated with the default options for the modules considered in the simulations, was applied to the geometry. An additional refinement was performed in the space between the electrodes, and another one to further increase the density of the elements near the tip of the needle electrode, where the electric field is expected to be most intense, leading to abrupt accelerations for the electrons moving in the vacuum.

The first simulations showed that the physical aspects were modelled consistently with what expected. Figure 5.15 show the electrons (green dots), being injected from the needle cathode point, moving in the space between the electrodes, following the field lines, and producing ions (magenta dots) through ionization of the gas desorbed from the front of the plane electrode.

The positive ions were then observed moving back towards the cath-

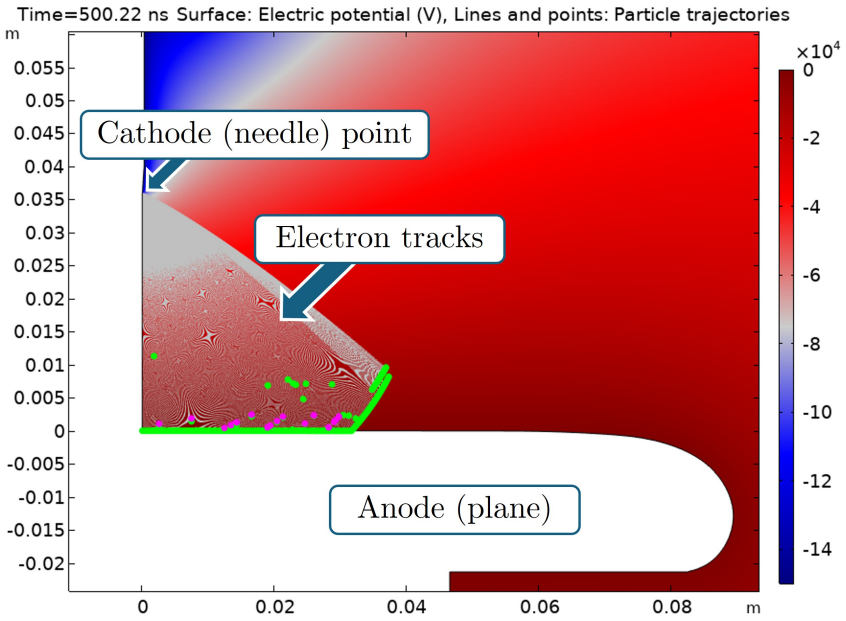

Figure 5.15: Plot of the electrons (green) travelling from cathode to anode and producing ions (magenta) from the gas, as modelled in COMSOL. Electron tracks are plotted in grey and appear different from single lines due to limited COMSOL visualization capabilities.

ode again, impinging on the surfaces and extracting secondary electrons, as shown in Figure 5.16.

The main result collected from the simulations was, for each injection timestamp, the ratio between the number of secondary electrons produced and the primaries generated, with the divergence condition (and thus the possible onset of an electric discharge) defined as this ratio being greater than unity. Preliminary analysis of the simulations assessed that the probability of divergence was maximized around the time when the value of pressure in the region between the electrodes reached its maximum, as could be expected. Consequently, the simulations were focused on the timestamps surrounding the pressure peak of each pulse shape, reported in Table 5.4.

The main influencing factor for the results of the simulations is the ionization process occurring for the electrons travelling in the gap between the electrodes. This, as stated above, is handled by COMSOL with a Monte Carlo approach. As a consequence, the number of secondaries produced can vary a lot for the same simulation due to the randomness in the system. This was taken into account in the study by running multiple simulations with the same parameter values and averaging the results. Figure 5.17 shows, as an example of this concept, the plot of the ratio between secondaries and primaries as a function of injection timestamp for the case of the burst of

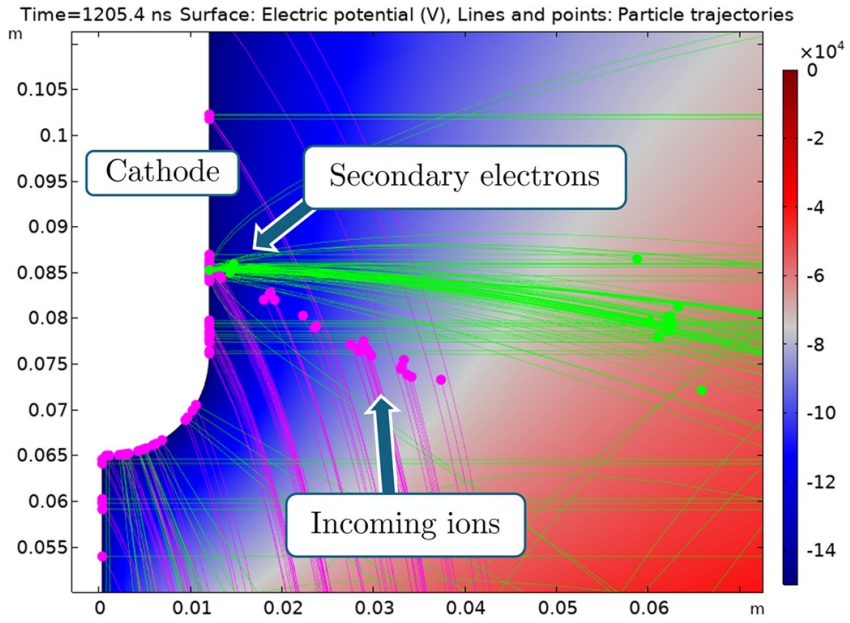

Figure 5.16: Plot of the ions (magenta) travelling from anode to cathode and producing secondary electrons (green) upon impact, as modelled in COMSOL.

duration 1 µs.

The results obtained by these simulations lead to two main considerations. Firstly, it was confirmed that the maximum ratio of production of secondaries is obtained for the timestamps around the maximum value of pressure found with the Molflow analysis, allowing to carry on the studies focusing only on those frames. However, as it can be seen from the plot, the very low values of ratio indicated that the pressure field directly interpolated from Molflow is not intense enough to approach the divergence condition and thus justifying an electron avalanche.

A custom multiplying factor was thus introduced in the model, to be implemented in the calculations of gas density in the domain carried on by the ionization module. This parameter could in principle be varied to model a higher magnitude of outgassing, to find the parameters needed to reach the divergence conditions without having to repeat the simulations in Molflow, which are more time-consuming with respect to the ones run in COMSOL. The use of the multiplication factor can be justified by the fact that the relevant time scales to be modelled are short, and the crucial factor is the maximum pressure established in the gap between the electrodes, as shown above. This was confirmed practically by comparison between two simulations in COMSOL, one run with the standard Molflow field and a multiplying factor of 10, and the other considering the pressure field obtained by a Molflow simulation with 10 times the outgassing burst intensity. The

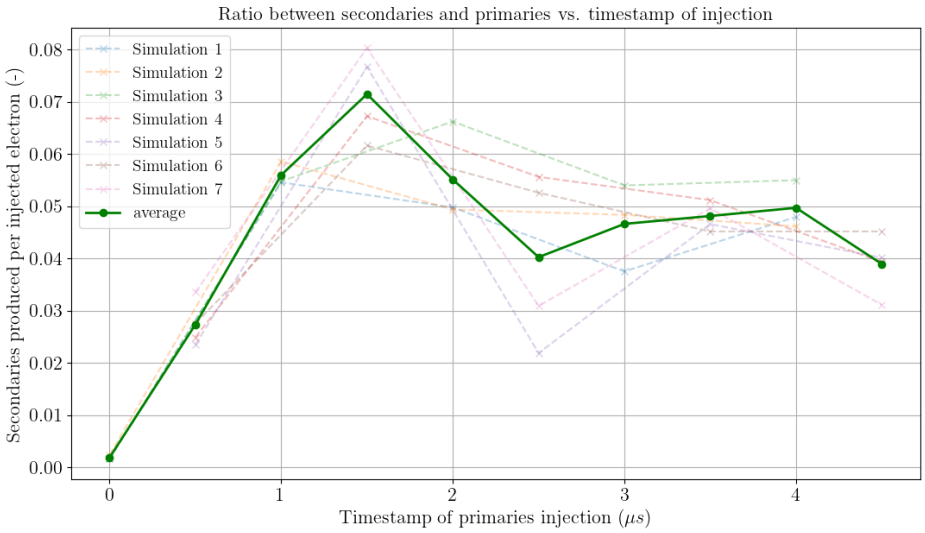

Figure 5.17: Plot of the trend of the ratio between secondaries and primaries, as a function of injection timestamp. The data from single simulations is plotted to highlight the variance in results, together with the final average.

two simulations produced results in accordance with each other.

A plot of the results of the COMSOL simulations as function of the multiplying factor is shown in Figure 5.18, for few of the different outgassing pulse shapes defined previously. The plot has been produced by considering the maximum value of ratio in each simulation, and averaging the results of the multiple simulations run for every set of parameters, as mentioned above. The full range of multiplying factor values was simulated only for one reference pulse shape, and the following simulations focused only on the relevant region of the range (between 8 and 10).

As it can be seen, the ratio of production of secondaries in the system increases with increasing multiplying factor, up to the point where the divergence condition previously defined is met. With the current setup for the simulations, the factor has to be set to a value of about 9 to 10 in most of the cases of study, with only small difference depending on the choice of outgassing pulse profile. The following section presents detailed considerations about these results and an outlook on future and improved works on the matter.

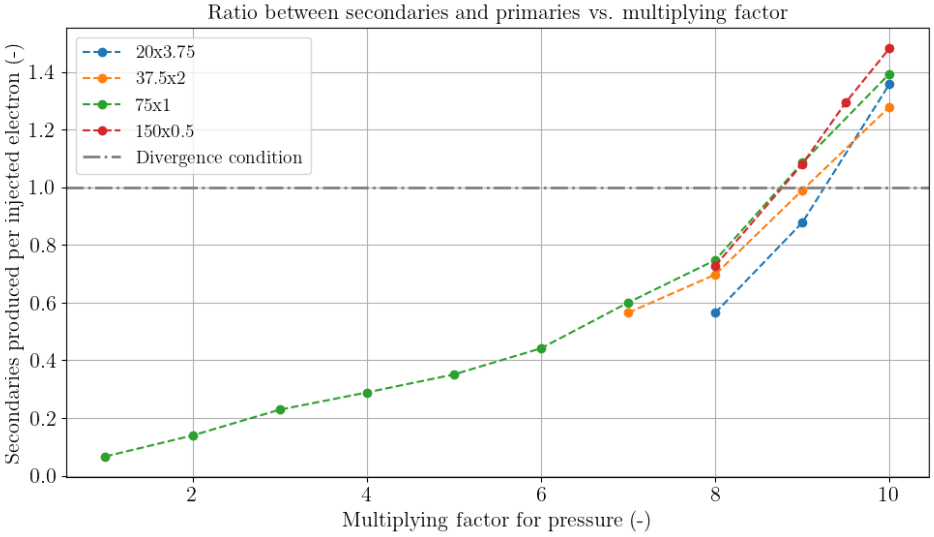

Figure 5.18: Plot of the trend of the ratio between secondaries and primaries, as a function of multiplying factor, for different outgassing pulse shapes.

5.4 Considerations and outlook

This chapter presented the development of a simulation tool based on a very simplified model, which contains many approximations and takes into account only a fraction of the many concurring physical aspects of the dynamics of the discharges. The results show that the simulations managed to reach the divergence condition, defined as the production of a number of secondaries larger than the primaries injected in the system. This is surely an important preliminary achievement, confirming the soundness of the theory behind the model. However, in order to reach the desired outcome, a value of at least 9 of multiplying factor was needed to be applied to the pressure profile. This fact highlights the need for additional improvements and considerations, both in the single phenomena analyses and in the integrated model, before arriving at definitive conclusions.

The calculations performed with the Geant4 and TRIM software, in their simple context, should be already representative of the phenomena they try to replicate, but more details could be included in the respective models. In combination with this, new experimental tests could be planned in order to better analyse and verify the results obtained for the single processes.

The pressure profile calculations performed with Molflow would probably benefit the most from a refinement of the geometry, in particular with more realistic representations of the pressure sensor and the pump regions. In this case as well, definition of a new set of experiments in a test bed environment, with better control of the conditions and easier to reproduce, could help in achieving validation of the single aspects involved in the desorption and diffusion of the gases in the chamber. Another aspect involves the outgassing burst. For the study presented here, the desorption process involved the whole front surface of the plane electrode. Future works could expand on this, modelling desorption from a reduced area, in order to see if the same divergence conditions can be met with a lower quantity of particles desorbed and thus lower pressures overall.

One of the main issues of the COMSOL simulations is probably the fact that they considered ionization caused only by the electrons travelling in the gap between the electrodes, with a single possible ionization state for the background gas. Future work on the matter may focus, for example, on the inclusion of the ionization processes caused by the positively charged ions as well, or the production of different ionization states and ions with charge values higher than unity. This could help in reaching the divergence conditions at lower pressure values with respect to what used in the analysis presented in this work. In addition to this, the model takes into account for now just a single gaseous specie with properties calculated as weighted average of atmospheric gases. Improvements of the simulations could focus also on the representation of multiple different gases in the mixture, potentially implementing the experimental data coming from the residual gas

analyser to measure their ratio. In the same context, the secondary emission of electrons from ion bombardment could also be improved by the definition of different components to consider the separate effect of the various species that take part in the process.

In conclusion, the work presented in this chapter constitutes the first step towards a complete and modular simulation framework for the study of micro-discharges in the HVPTF facility. By combining the use of different tools for the simulation of single processes to be considered, the integrated model yielded preliminary quantitative results that are already of significance. While further refinements of the model and experimental validation of the calculations are required to reach more relevant conclusions, the framework has been built as flexible and can be extended and improved by further studies. It will work as a good first basis to plan new experimental campaigns and gain new insight, with the ultimate aim of characterizing and reproducing completely the micro-discharge phenomena in vacuum.

Conclusions and perspectives

The realization of the ITER reactor prototype is currently the main focus of the research for nuclear fusion power production of the European community. Its aim of achieving power production with a gain factor of 10 is one of the fundamental steps for the advancement of the overall research plans. One of the main systems to provide the external heating necessary for the fusion reaction is the Neutral Beam Injector, based on the extraction and acceleration of a negative deuterium ion beam, followed by its neutralization and injection in the plasma. The full-scale prototype of the NBI, the MITICA experiment, is facing the criticalities in the development of the system, among which high voltage insulation is one of the most important. The High Voltage Padova Test Facility has been developed to study the electric discharge phenomena that may occur in MITICA, focusing mainly on conditioning experiments and on the study of micro-discharges and breakdowns. In recent years, the analysis of X-ray emissions in this context has proven to be particularly instrumental in the progress for the characterization and understanding of the discharge phenomenology.

The development of X-ray GEM-based detectors for the analysis of micro-discharges in HVPTF has been presented in this thesis. The data collected by the first prototype, the XR-GEM-1 detector, allowed for accurate analysis of the spatial and temporal characteristics of the X-ray emission during discharges, leading to innovative insights on the processes involved and proving the additional capabilities that this kind of instruments adds to the diagnostic set of the facility. Development of new and improved prototypes, the XR-GEM-2 and XR-GEM-3 detectors, has helped to further add to the quality of the studies, highlighting different areas of improvement for the experimental setup. Chapter 4 presented also the development and installation of a synchronization system for data acquisition of the diagnostics at HVPTF, based on the combination of hardware and software components. Its implementation will allow for more accurate and easier analysis of the comparisons and correlations among the different signals, leading to improvements in the analyses already performed and in understanding of the discharge phenomena.

In combination with the experimental activities, a simulation model for the micro-discharge phenomenology in HVPTF has been developed, as de-

scribed in chapter 5. The model, based on the combined use of Monte Carlo codes and of finite element analysis software, allows for the reproduction of the motion of the charged particles in the electric field of the domain, considering also the effects of collisions with the gas desorbed by the surfaces during the discharges. The results obtained with the model have shown agreement with the experimental data, but also implied the need for additional improvements in order to better reproduce the phenomenology observed. The model will be further developed in the future, including more physical processes and refining the definition of the current ones, in order to improve its accuracy and obtain a better understanding of the discharge dynamics.

The activities presented in this thesis represent a first step in the development of new diagnostic and modelling tools for the studies at the High Voltage Padova Test Facility, achieving important preliminary results and leaving room for new developments and further improvements. Both the diagnostic tools and the simulation model will be implemented in future studies at the facility, which may focus on new aspects of the discharge phenomenology to gain new insights on the discharge phenomena. This will ultimately aid in the design and operation of the MITICA system and in the development of the Neutral Beam Injector for the ITER tokamak.

Bibliography

[ABCD, 2025] ABCD (2025). Abcd documentation. `https://abcd-docs.readthedocs.io/en/latest/`. Accessed: October 2025.

[Agostinelli et al., 2003] Agostinelli, S., Allison, J., Amako, K., Apostolakis, J., Araujo, H., Arce, P., Asai, M., Axen, D., Banerjee, S., Barrand, G., Behner, F., Bellagamba, L., Boudreau, J., Broglia, L., Brunengo, A., Burkhardt, H., Chauvie, S., Chuma, J., Chytracek, R., Cooperman, G., Cosmo, G., Degtyarenko, P., Dell'Acqua, A., Depaola, G., Dietrich, D., Enami, R., Feliciello, A., Ferguson, C., Fesefeldt, H., Folger, G., Foppiano, F., Forti, A., Garelli, S., Giani, S., Giannitrapani, R., Gibin, D., Gómez Cadenas, J., González, I., Gracia Abril, G., Greeniaus, G., Greiner, W., Grichine, V., Grossheim, A., Guatelli, S., Gumplinger, P., Hamatsu, R., Hashimoto, K., Hasui, H., Heikkinen, A., Howard, A., Ivanchenko, V., Johnson, A., Jones, F., Kallenbach, J., Kanaya, N., Kawabata, M., Kawabata, Y., Kawaguti, M., Kelner, S., Kent, P., Kimura, A., Kodama, T., Kokoulin, R., Kossov, M., Kurashige, H., Lamanna, E., Lampén, T., Lara, V., Lefebure, V., Lei, F., Liendl, M., Lockman, W., Longo, F., Magni, S., Maire, M., Medernach, E., Minamimoto, K., Mora de Freitas, P., Morita, Y., Murakami, K., Nagamatu, M., Nartallo, R., Nieminen, P., Nishimura, T., Ohtsubo, K., Okamura, M., O'Neale, S., Oohata, Y., Paech, K., Perl, J., Pfeiffer, A., Pia, M., Ranjard, F., Rybin, A., Sadilov, S., Di Salvo, E., Santin, G., Sasaki, T., Savvas, N., Sawada, Y., Scherer, S., Sei, S., Sirotenko, V., Smith, D., Starkov, N., Stoecker, H., Sulkimo, J., Takahata, M., Tanaka, S., Tcherniaev, E., Safai Tehrani, E., Tropeano, M., Truscott, P., Uno, H., Urban, L., Urban, P., Verderi, M., Walkden, A., Wander, W., Weber, H., Wellisch, J., Wenaus, T., Williams, D., Wright, D., Yamada, T., Yoshida, H., and Zschiesche, D. (2003). Geant4—a simulation toolkit. *Nuclear Instruments and Methods in Physics Research Section A: Accelerators, Spectrometers, Detectors and Associated Equipment*, 506(3):250–303.

[Albani et al., 2020] Albani, G., Perelli Cippo, E., Croci, G., Muraro, A., Hall-Wilton, R., Höglund, C., Menelle, A., Grosso, G., Murtas, F., Rebai, M., Robinson, L., Schmidt, S., Svensson, P.-O., Tardocchi, M., and Gorini, G. (2020). High-rate measurements of the novel band-gem technology

for thermal neutron detection at spallation sources. *Nuclear Instruments and Methods in Physics Research Section A: Accelerators, Spectrometers, Detectors and Associated Equipment*, 957:163389.

[Allison et al., 2006] Allison, J., Amako, K., Apostolakis, J., Araujo, H., Arce Dubois, P., Asai, M., Barrand, G., Capra, R., Chauvie, S., Chytracek, R., Cirrone, G., Cooperman, G., Cosmo, G., Cuttone, G., Daquino, G., Donszelmann, M., Dressel, M., Folger, G., Foppiano, F., Generowicz, J., Grichine, V., Guatelli, S., Gumplinger, P., Heikkinen, A., Hrivnacova, I., Howard, A., Incerti, S., Ivanchenko, V., Johnson, T., Jones, F., Koi, T., Kokoulin, R., Kossov, M., Kurashige, H., Lara, V., Larsson, S., Lei, F., Link, O., Longo, F., Maire, M., Mantero, A., Mascialino, B., McLaren, I., Mendez Lorenzo, P., Minamimoto, K., Murakami, K., Nieminen, P., Pandola, L., Parlati, S., Peralta, L., Perl, J., Pfeiffer, A., Pia, M., Ribon, A., Rodrigues, P., Russo, G., Sadilov, S., Santin, G., Sasaki, T., Smith, D., Starkov, N., Tanaka, S., Tcherniaev, E., Tome, B., Trindade, A., Truscott, P., Urban, L., Verderi, M., Walkden, A., Wellisch, J., Williams, D., Wright, D., and Yoshida, H. (2006). Geant4 developments and applications. *IEEE Transactions on Nuclear Science*, 53(1):270–278.

[Allison et al., 2016] Allison, J., Amako, K., Apostolakis, J., Arce, P., Asai, M., Aso, T., Bagli, E., Bagulya, A., Banerjee, S., Barrand, G., Beck, B., Bogdanov, A., Brandt, D., Brown, J., Burkhardt, H., Canal, P., Cano-Ott, D., Chauvie, S., Cho, K., Cirrone, G., Cooperman, G., Cortés-Giraldo, M., Cosmo, G., Cuttone, G., Depaola, G., Desorgher, L., Dong, X., Dotti, A., Elvira, V., Folger, G., Francis, Z., Galoyan, A., Garnier, L., Gayer, M., Genser, K., Grichine, V., Guatelli, S., Guèye, P., Gumplinger, P., Howard, A., Hřivnáčová, I., Hwang, S., Incerti, S., Ivanchenko, A., Ivanchenko, V., Jones, F., Jun, S., Kaitaniemi, P., Karakatsanis, N., Karamitros, M., Kelsey, M., Kimura, A., Koi, T., Kurashige, H., Lechner, A., Lee, S., Longo, F., Maire, M., Mancusi, D., Mantero, A., Mendoza, E., Morgan, B., Murakami, K., Nikitina, T., Pandola, L., Paprocki, P., Perl, J., Petrović, I., Pia, M., Pokorski, W., Quesada, J., Raine, M., Reis, M., Ribon, A., Ristić Fira, A., Romano, F., Russo, G., Santin, G., Sasaki, T., Sawkey, D., Shin, J., Strakovsky, I., Taborda, A., Tanaka, S., Tomé, B., Toshito, T., Tran, H., Truscott, P., Urban, L., Uzhinsky, V., Verbeke, J., Verderi, M., Wendt, B., Wenzel, H., Wright, D., Wright, D., Yamashita, T., Yarba, J., and Yoshida, H. (2016). Recent developments in geant4. *Nuclear Instruments and Methods in Physics Research Section A: Accelerators, Spectrometers, Detectors and Associated Equipment*, 835:186–225.

[Amaldi et al., 2011] Amaldi, U., Bianchi, A., Chang, Y.-H., Go, A., Hajdas, W., Malakhov, N., Samarati, J., Sauli, F., and Watts, D. (2011). Construction, test and operation of a proton range radiography system. *Nuclear Instruments and Methods in Physics Research Section A: Accel-*

erators, Spectrometers, Detectors and Associated Equipment, 629(1):337–344.

[Azmoun et al., 2019] Azmoun, B., Dehmelt, K., Hemmick, T. K., Majka, R., Nguyen, H. N., Phipps, M., Purschke, M. L., Ram, N., Roh, W., Shangase, D., Smirnov, N., Woody, C., and Zhang, A. (2019). Results from a prototype combination tpc cherenkov detector with gem readout. *IEEE Transactions on Nuclear Science*, 66(8):1984–1992.

[Cancelli et al., 2022] Cancelli, S., Muraro, A., Perelli Cippo, E., Abba, A., Corradi, G., Grosso, G., Gorini, G., Kushoro, M., Murtas, F., Putignano, O., Scionti, J., Tagnani, D., Tardocchi, M., and Croci, G. (2022). Electronic readout characterisation of a new soft x-ray diagnostic for burning plasma. *Journal of Instrumentation*, 17(08):C08028.

[Carbone et al., 2021] Carbone, E., Graef, W., Hagelaar, G., Boer, D., Hopkins, M. M., Stephens, J. C., Yee, B. T., Pancheshnyi, S., van Dijk, J., and Pitchford, L. (2021). Data needs for modeling low-temperature non-equilibrium plasmas: The lxcat project, history, perspectives and a tutorial. *Atoms*, 9(1).

[Caruggi et al., 2023] Caruggi, F., Cancelli, S., Celora, A., Guiotto, F., Croci, G., Tardocchi, M., Murtas, F., de Oliveira, R., Perelli Cippo, E., Gorini, G., Grosso, G., and Muraro, A. (2023). Performance of a triple gem detector equipped with al-gem foils for x-rays detection. *Nuclear Instruments and Methods in Physics Research, Section A: Accelerators, Spectrometers, Detectors and Associated Equipment*, 1047.

[Celora et al., 2025] Celora, A., Caruggi, F., Putignano, O., Cancelli, S., Claps, G., Cordella, F., Garzotti, L., Gorini, G., Grosso, G., Guiotto, F., Lazzaro, E., Nocente, M., Pacella, D., Perelli Cippo, E., Rigamonti, D., Rose, E., Sarwar, R., Scannell, R., Scioscioli, F., Tardocchi, M., Croci, G., and Muraro, A. (2025). Assessment of a space and energy resolved diagnostic based on gem technology on mast-u. *Measurement Science and Technology*, 36(1).

[Chernyshova et al., 2022] Chernyshova, M., Dobrut, M., Jablonski, S., Malinowski, K., and Fornal, T. (2022). Multi-chamber gem-based concept of radiated power/sxr measurement system for use in high radiation environment of demo. *Journal of Instrumentation*, 17:C05013.

[Conde, 2020] Conde, L. (2020). Introduction to electric discharges. In *An Introduction to Plasma Physics and its Space Applications, Volume 2*, 2053-2563, pages 4–1 to 4–12. IOP Publishing.

[Corradi et al., 2007] Corradi, G., Murtas, F., and Tagnani, D. (2007). A novel high-voltage system for a triple gem detector. *Nuclear Instruments*

and Methods in Physics Research Section A: Accelerators, Spectrometers, Detectors and Associated Equipment, 572(1):96–97. Frontier Detectors for Frontier Physics.

[De Lorenzi et al., 2011] De Lorenzi, A., Pilan, N., Lotto, L., Fincato, M., Pesavento, G., and Gobbo, R. (2011). Hvptf—the high voltage laboratory for the iter neutral beam test facility. *Fusion Engineering and Design*, 86(6):742–745. Proceedings of the 26th Symposium of Fusion Technology (SOFT-26).

[De Lorenzi et al., 2013] De Lorenzi, A., Pilan, N., and Spada, E. (2013). Progress in the validation of the voltage holding prediction model at the high-voltage padova test facility. *IEEE Transactions on Plasma Science*, 41(8):2128–2134.

[Diamond, 1998] Diamond, W. T. (1998). New perspectives in vacuum high voltage insulation. ii. gas desorption. *Journal of Vacuum Science & Technology A*, 16(2):720–735.

[Farrall, 1990] Farrall, G. A. (1990). Electrical breakdown in vacuum. In Schaefer, G., Kristiansen, M., and Guenther, A., editors, *Gas Discharge Closing Switches*, pages 193–250. Springer US, Boston, MA.

[Fedchak et al., 2021] Fedchak, J. A., Scherschligt, J. K., Avdiaj, S., Barker, D. S., Eckel, S. P., Bowers, B., OĆonnell, S., and Henderson, P. (2021). Outgassing rate comparison of seven geometrically similar vacuum chambers of different materials and heat treatments. *Journal of Vacuum Science & Technology B*, 39(2):024201.

[Fowler and Nordheim, 1928] Fowler, R. H. and Nordheim, L. (1928). Electron emission in intense electric fields. *Proceedings of the Royal Society of London. Series A, Containing Papers of a Mathematical and Physical Character*, 119(781):173–181.

[GEM, 2025] GEM (2025). Gem general. `https://gdd.web.cern.ch/sites/default/files/oldGDD/www/gemgeneral.html`. Accessed: October 2025.

[Heifets and Margulis, 2012] Heifets, M. and Margulis, P. (2012). Fully active voltage divider for pmt photo-detector. In *2012 IEEE Nuclear Science Symposium and Medical Imaging Conference Record (NSS/MIC)*, pages 807–814.

[Hemsworth et al., 2017] Hemsworth, R. S., Boilson, D., Blatchford, P., Palma, M. D., Chitarin, G., de Esch, H. P. L., Geli, F., Dremel, M., Graceffa, J., Marcuzzi, D., Serianni, G., Shah, D., Singh, M., Urbani, M., and Zaccaria, P. (2017). Overview of the design of the iter heating neutral beam injectors. *New Journal of Physics*, 19(2):025005.

[Hong, 2025] Hong, Y. (2025). Gem detectors for the cms endcap muon system: status of three detector stations. *Journal of Instrumentation*, 20(04):C04022.

[Huxley and Crompton, 1974] Huxley, L. and Crompton, R. (1974). *The Diffusion and Drift of Electrons in Gases*. Wiley series in plasma physics. Wiley.

[ITER, 2025] ITER (2025). Iter - the way to new energy. `https://www.iter.org`. Accessed: October 2025.

[Kawai et al., 2004] Kawai, J., Yamada, T., and Fujimura, H. (2004). Portable x-ray fluorescence spectrometer with an electric battery. *Bunseki Kagaku*, 53.

[Kersevan and Ady, 2019] Kersevan, R. and Ady, M. (2019). Recent Developments of Monte-Carlo Codes Molflow+ and Synrad+. In *Proc. 10th International Particle Accelerator Conference (IPAC'19), Melbourne, Australia, 19-24 May 2019*, number 10 in International Particle Accelerator Conference, pages 1327–1330, Geneva, Switzerland. JACoW Publishing.

[Ketzer et al., 2002] Ketzer, B., Altunbas, M., Dehmelt, K., Ehlers, J., Friedrich, J., Grube, B., Kappler, S., Konorov, I., Paul, S., Placci, A., Ropelewski, L., Sauli, F., Schmitt, L., and Simon, F. (2002). Triple gem tracking detectors for compass. *IEEE Transactions on Nuclear Science*, 49(5):2403–2410.

[Kireeff Covo et al., 2006] Kireeff Covo, M., Molvik, A. W., Friedman, A., Westenskow, G., Barnard, J. J., Cohen, R., Seidl, P. A., Kwan, J. W., Logan, G., Baca, D., Bieniosek, F., Celata, C. M., Vay, J.-L., and Vujic, J. L. (2006). Beam energy scaling of ion-induced electron yield from k^+ impact on stainless steel. *Phys. Rev. ST Accel. Beams*, 9:063201.

[Knoll, 2010] Knoll, G. (2010). *Radiation Detection and Measurement (4th ed.)*. John Wiley, Hoboken, NJ.

[Kunhardt, 1990] Kunhardt, E. E. (1990). Electrical breakdown in gases in electric fields. In *Gas Discharge Closing Switches*, pages 15–44. Springer US, Boston, MA.

[Kushoro et al., 2022] Kushoro, M., Croci, G., Mario, I., Muraro, A., Rigamonti, D., Cancelli, S., Lorenzi, A. D., Fincato, M., Fontana, C., Gobbo, R., Grosso, G., Lotto, L., Cormack, O. M., Putignano, O., Pino, F., Spada, E., Spagnolo, S., Tardocchi, M., and Pilan, N. (2022). Characterization of vacuum hv microdischarges at hvptf through x-ray bremsstrahlung spectroscopy. *Journal of Instrumentation*, 17(01):C01054.

[Lavezzi et al., 2017] Lavezzi, L., Alexeev, M., Amoroso, A., Ferroli, R. B., Bertani, M., Bettoni, D., Bianchi, F., Calcaterra, A., Canale, N., Capodiferro, M., Carassiti, V., Cerioni, S., Chai, J., Chiozzi, S., Cibinetto, G., Cossio, F., Ramusino, A. C., De Mori, F., Destefanis, M., Dong, J., Evangelisti, F., Farinelli, R., Fava, L., Felici, G., Fioravanti, E., Garzia, I., Gatta, M., Greco, M., Leng, C., Li, H., Maggiora, M., Malaguti, R., Marcello, S., Melchiorri, M., Mezzadri, G., Mignone, M., Morello, G., Pacetti, S., Patteri, P., Pellegrino, J., Pelosi, A., Rivetti, A., Rolo, M. D., Savrié, M., Scodeggio, M., Soldani, E., Sosio, S., Spataro, S., Tskhadadze, E., Verma, S., Wheadon, R., and Yan, L. (2017). Performance of the microtpc reconstruction for gem detectors at high rate. In *2017 IEEE Nuclear Science Symposium and Medical Imaging Conference (NSS/MIC)*, pages 1–5.

[Leidner et al., 2021] Leidner, J., Murtas, F., and Silari, M. (2021). Medical applications of the gempix. *Applied Sciences*, 11(1).

[LXCat - Biagi, 2025] LXCat - Biagi (2025). Biagi database, lxcat. `https://www.lxcat.net/Biagi`. Retrieved on September 2025.

[LXCat - IST-Lisbon, 2025] LXCat - IST-Lisbon (2025). Ist-lisbon database, lxcat. `https://www.lxcat.net/IST-Lisbon`. Retrieved on September 2025.

[LXCat - Morgan, 2025] LXCat - Morgan (2025). Morgan database, lxcat. `https://www.lxcat.net/Morgan`. Retrieved on September 2025.

[LXCat - Phelps, 2025] LXCat - Phelps (2025). Phelps database, lxcat. `https://www.lxcat.net/Phelps`. Retrieved on September 2025.

[Malinowski et al., 2021] Malinowski, K., Chernyshova, M., Jabłoński, S., and Casiragi, I. (2021). Optimization of gem-based detector readout electrode structure for sxr imaging of tokamak plasma. *Journal of Instrumentation*, 16(11):C11014.

[Marcuzzi et al., 2015] Marcuzzi, D., Agostinetti, P., Dalla Palma, M., De Muri, M., Chitarin, G., Gambetta, G., Marconato, N., Pasqualotto, R., Pavei, M., Pilan, N., Rizzolo, A., Serianni, G., Toigo, V., Trevisan, L., Visentin, M., Zaccaria, P., Zaupa, M., Boilson, D., Graceffa, J., Hemsworth, R. S., Choi, C. H., Marti, M., Roux, K., Singh, M. J., Masiello, A., Froeschle, M., Heinemann, B., Nocentini, R., Riedl, R., Tobari, H., de Esch, H. P. L., and Muvvala, V. N. (2015). Final design of the beam source for the mitica injector. *Review of Scientific Instruments*, 87(2):02B309.

[Mazon et al., 2022] Mazon, D., Chernyshova, M., Jardin, A., Peysson, Y., Król, K., Malard, P., Czarski, T., Wojeński, A., Malinowski, K., Colette, D., Poźniak, K., Kasprowicz, G., Zabołotny, W., Krawczyk, R., Kolasiński, P., Gąska, M., Linczuk, P., Bielecki, J., Scholz, M., Dworak, D., and the WEST Team (2022). First gem measurements at west and perspectives for fast electrons and heavy impurities transport studies in tokamaks. *Journal of Instrumentation*, 17(01):C01073.

[Meinschad et al., 2004] Meinschad, T., Ropelewski, L., and Sauli, F. (2004). Gem-based photon detector for rich applications. *Nuclear Instruments and Methods in Physics Research Section A: Accelerators, Spectrometers, Detectors and Associated Equipment*, 535(1):324–329. Proceedings of the 10th International Vienna Conference on Instrumentation.

[Miller, 1990] Miller, H. (1990). Electrical discharges in vacuum 1877-1979. *IEEE Transactions on Electrical Insulation*, 25(5):765–860.

[MiniX2, 2025] MiniX2 (2025). Amptek mini-x2 x-ray tube. `https://www.amptek.com/internal-products/obsolete-products/mini-x2-x-ray-tube`. Accessed: October 2025.

[MITICA, 2025] MITICA (2025). Mitica - consorzio rfx. `https://www.igi.cnr.it/ricerca/negative-ion-neutral-beam-injection/mitica/`. Accessed: October 2025.

[Muraro et al., 2019] Muraro, A., Claps, G., Croci, G., Cordella, F., Gorini, G., Grosso, G., Hu, Z., Mangiagalli, L., McCormack, O., Murtas, F., Nocente, M., Cippo, E. P., Panontin, E., Pedroni, M., Rebai, M., Rigamonti, D., Tardocchi, M., and Pacella, D. (2019). Development and characterization of a new soft x-ray diagnostic concept for tokamaks. *Journal of Instrumentation*, 14(08):C08012.

[Muraro et al., 2021] Muraro, A., Claps, G., Croci, G., Lai, C.-C., Oliveira, R., Altieri, S., Cancelli, S., Gorini, G., Hall-Wilton, R., Hoglund, C., Cippo, E., Robinson, L., Svensson, P., and Murtas, F. (2021). Mbgem: a stack of borated gem detector for high efficiency thermal neutron detection. *The European Physical Journal Plus*, 136.

[Muraro et al., 2016] Muraro, A., Croci, G., Albani, G., Claps, G., Cavenago, M., Cazzaniga, C., Dalla Palma, M., Grosso, G., Murtas, F., Pasqualotto, R., Perelli Cippo, E., Rebai, M., Tardocchi, M., Tollin, M., and Gorini, G. (2016). Performance of the full size ngem detector for the spider experiment. *Nuclear Instruments and Methods in Physics Research Section A: Accelerators, Spectrometers, Detectors and Associated Equipment*, 813:147–152.

[Nordheim, 1928] Nordheim, L. (1928). The effect of the image force on the emission and reflexion of electrons by metals. *Proceedings of the Royal Society of London. Series A, Containing Papers of a Mathematical and Physical Character*, 121(788):626–639.

[Ollegott et al., 2020] Ollegott, K., Wirth, P., Oberste-Beulmann, C., Awakowicz, P., and Muhler, M. (2020). Fundamental properties and applications of dielectric barrier discharges in plasma-catalytic processes at atmospheric pressure. *Chemie Ingenieur Technik*, 92(10):1542–1558.

[Pacella et al., 2013] Pacella, D., Gabellieri, L., Romano, A., Causa, F., Murtas, F., Claps, G., Lee, S., Hong, J., Jang, J., and Choe, W. (2013). Gem-based energy resolved x-ray tangential imaging system on kstar. *40th EPS Conference on Plasma Physics, EPS 2013*, 2:1314–1317.

[Pezzotta et al., 2015] Pezzotta, A., Corradi, G., Croci, G., Matteis, M. D., Murtas, F., Tagnani, D., Gorini, G., and Baschirotto, A. (2015). Gemini, a cmos 180 nm mixed-signal 16-channel asic for triple-gem detectors readout. *2015 IEEE SENSORS - Proceedings*.

[Pilan et al., 2024] Pilan, N., Agostini, M., Caruggi, F., Chitarin, G., Cordaro, L., Croci, G., Deamborsis, S., Fincato, M., Franchin, L., Guiotto, F., Lotto, L., Marconato, N., Mario, I., Muraro, A., Patton, T., Pino, F., Spada, E., Serianni, G., Spagnolo, S., and De Lorenzi, A. (2024). Role of electron stimulated desorption in the initiation of hvdc vacuum arc. *Vacuum*, 224:113109.

[Pilan et al., 2022] Pilan, N., Cavenago, M., Chitarin, G., De Lorenzi, A., Fontana, C. L., McCormack, O., Gobbo, R., Fincato, M., Lotto, L., Pesavento, G., Pino, F., Spada, E., Spagnolo, S., and Zuin, M. (2022). Prebreakdown phenomena between vacuum insulated electrodes: The role of accumulation points in the onset of microdischarges. *IEEE Transactions on Plasma Science*, 50(9):2695–2699.

[Pilan et al., 2020] Pilan, N., Deambrosis, S., Lorenzi, A. D., Fincato, M., Fontana, C., Gobbo, R., Lotto, L., Martines, E., Cormack, O. M., Pasqualotto, R., Patton, T., Pesavento, G., Pino, F., Spada, E., Spagnolo, S., and Zuin, M. (2020). Study of high dc voltage breakdown between stainless steel electrodes separated by long vacuum gaps. *Nuclear Fusion*, 60(7):076010.

[Pilan et al., 2015] Pilan, N., Marcuzzi, D., Rizzolo, A., Grando, L., Gambetta, G., Rosa, S. D., Kraemer, V., Quirmbach, T., Chitarin, G., Gobbo, R., Pesavento, G., De Lorenzi, A., Lotto, L., Rizzieri, R., Fincato, M., Romanato, L., Trevisan, L., Cervaro, V., and Franchin, L. (2015). Electrical and structural r&d activities on high voltage dc solid insulator in

vacuum. *Fusion Engineering and Design*, 96-97:563–567. Proceedings of the 28th Symposium On Fusion Technology (SOFT-28).

[Pilan et al., 2010] Pilan, N., Veltri, P., and De Lorenzi, A. (2010). Voltage holding prediction in multi-electrode multi-voltage systems insulated in vacuum. In *24th ISDEIV 2010*, pages 15–18.

[Pilan et al., 2011] Pilan, N., Veltri, P., and Lorenzi, A. D. (2011). Voltage holding prediction in multi electrode-multi voltage systems insulated in vacuum. *IEEE Transactions on Dielectrics and Electrical Insulation*, 18(2):553–560.

[Pinto, 2013] Pinto, S. D. (2013). Gem applications outside high energy physics. *Modern Physics Letters A*, 28(13):1340025.

[Putignano et al., 2023] Putignano, O., Croci, G., Muraro, A., Cancelli, S., Caruggi, F., Gorini, G., Grosso, G., Kushoro, M. H., Marcer, G., Nocente, M., Cippo, E. P., Rebai, M., Rigamonti, D., and Tardocchi, M. (2023). Conceptual design of a gem (gas electron multiplier) based gas cherenkov detector for measurement of 17 mev gamma rays from t(d, γ)5he in magnetic confinement fusion plasmas. *Review of Scientific Instruments*, 94(1):013501.

[Rzadkiewicz et al., 2013] Rzadkiewicz, J., Dominik, W., Scholz, M., Chernyshova, M., Czarski, T., Czyrkowski, H., Dabrowski, R., Jakubowska, K., Karpinski, L., Kasprowicz, G., Kierzkowski, K., Pozniak, K., Salapa, Z., Zabolotny, W., Blanchard, P., Tyrrell, S., and Zastrow, K.-D. (2013). Design of t-gem detectors for x-ray diagnostics on jet. *Nuclear Instruments and Methods in Physics Research Section A: Accelerators, Spectrometers, Detectors and Associated Equipment*, 720:36–38. Selected papers from the 2nd International Conference Frontiers in Diagnostic Technologies (ICFDT2).

[Sauli, 2016] Sauli, F. (2016). The gas electron multiplier (gem): Operating principles and applications. *Nuclear Instruments and Methods in Physics Research Section A: Accelerators, Spectrometers, Detectors and Associated Equipment*, 805:2–24. Special Issue in memory of Glenn F. Knoll.

[Sauli, 2023] Sauli, F. (2023). *Gaseous Radiation Detectors: Fundamentals and Applications*. Cambridge Monographs on Particle Physics, Nuclear Physics and Cosmology. Cambridge University Press.

[Spagnolo et al., 2021] Spagnolo, S., Pilan, N., Lorenzi, A. D., Fontana, C., McCormack, O., Muraro, A., Croci, G., Gobbo, G., Gorini, G., Grosso, G., Fincato, M., Lotto, L., Martines, E., Pino, F., Rigamonti, D., Rossetto, F., Spada, E., Tardocchi, M., and Zuin, M. (2021). Characterization of x-ray events for a vacuum high voltage holding experiment. In *2020*

29th International Symposium on Discharges and Electrical Insulation in Vacuum (ISDEIV), pages 58–61.

[Toigo et al., 2017] Toigo, V., Piovan, R., Bello, S. D., Gaio, E., Luchetta, A., Pasqualotto, R., Zaccaria, P., Bigi, M., Chitarin, G., Marcuzzi, D., Pomaro, N., Serianni, G., Agostinetti, P., Agostini, M., Antoni, V., Aprile, D., Baltador, C., Barbisan, M., Battistella, M., Boldrin, M., Brombin, M., Palma, M. D., Lorenzi, A. D., Delogu, R., Muri, M. D., Fellin, F., Ferro, A., Fiorentin, A., Gambetta, G., Gnesotto, F., Grando, L., Jain, P., Maistrello, A., Manduchi, G., Marconato, N., Moresco, M., Ocello, E., Pavei, M., Peruzzo, S., Pilan, N., Pimazzoni, A., Recchia, M., Rizzolo, A., Rostagni, G., Sartori, E., Siragusa, M., Sonato, P., Sottocornola, A., Spada, E., Spagnolo, S., Spolaore, M., Taliercio, C., Valente, M., Veltri, P., Zamengo, A., Zaniol, B., Zanotto, L., Zaupa, M., Boilson, D., Graceffa, J., Svensson, L., Schunke, B., Decamps, H., Urbani, M., Kushwah, M., Chareyre, J., Singh, M., Bonicelli, T., Agarici, G., Garbuglia, A., Masiello, A., Paolucci, F., Simon, M., Bailly-Maitre, L., Bragulat, E., Gomez, G., Gutierrez, D., Mico, G., Moreno, J.-F., Pilard, V., Kashiwagi, M., Hanada, M., Tobari, H., Watanabe, K., Maejima, T., Kojima, A., Umeda, N., Yamanaka, H., Chakraborty, A., Baruah, U., Rotti, C., Patel, H., Nagaraju, M. V., Singh, N. P., Patel, A., Dhola, H., Raval, B., Fantz, U., Heinemann, B., Kraus, W., Hanke, S., Hauer, V., Ochoa, S., Blatchford, P., Chuilon, B., Xue, Y., Esch, H. P. L. D., Hemsworth, R., Croci, G., Gorini, G., Rebai, M., Muraro, A., Tardocchi, M., Cavenago, M., D'Arienzo, M., Sandri, S., and Tonti, A. (2017). The prima test facility: Spider and mitica test-beds for iter neutral beam injectors. *New Journal of Physics*, 19(8):085004.

[Townsend, 1910] Townsend, S. J. (1910). *The theory of ionization of gases by collision*. London, Constable, 1910.

[Trump and Van De Graaff, 1947] Trump, J. G. and Van De Graaff, R. J. (1947). The insulation of high voltages in vacuum. *Journal of Applied Physics*, 18(3):327–332.

[Von Engel, 1955] Von Engel, A. (1955). *Ionized Gases*. Clarendon Press.

[Ziegler et al., 2010] Ziegler, J. F., Ziegler, M., and Biersack, J. (2010). Srim – the stopping and range of ions in matter (2010). *Nuclear Instruments and Methods in Physics Research Section B: Beam Interactions with Materials and Atoms*, 268(11):1818–1823. 19th International Conference on Ion Beam Analysis.

List of Publications

During my Ph.D. I co-authored the following papers.

- Caruggi F., et al. Performance of a triple GEM detector equipped with Al-GEM foils for X-rays detection. *Nuclear Instruments and Methods in Physics Research Section A*, 1047 (2023). doi:10.1016/j.nima.2022.167855.
- Caruggi F., et al. Development of a data analysis software for the XR-GEM installed at HVPTF and preliminary results. *Proceedings of IS-DEIV*, 2023-June, 29–32 (2023). doi:10.23919/ISDEIV55268.2023.10199827.
- Caruggi F., et al. Development of a Triple-GEM detector with strip readout and GEMINI chip for X rays and neutron imaging. *Journal of Instrumentation*, 19(2) (2024). doi:10.1088/1748-0221/19/02/C02015.
- Caruggi F., et al. Analysis of micro-discharges fine dynamics via x-ray detection on the high voltage Padova test facility experiment. *High Voltage*, 10(4), 1043–1052 (2025). doi:10.1049/hve2.70042.
- Cancelli S., et al. Characterisation of N2-GEM: a beam monitor based on Ar-N2 gas mixture. *Journal of Instrumentation*, 18(5) (2023). doi:10.1088/1748-0221/18/05/C05005.
- Cancelli S., et al. Characterisation of a medium-size-area high-rate multi-layer boron-coated GEM detector for thermal neutrons. *European Physical Journal Plus*, 139(11) (2024). doi:10.1140/epjp/s13360-024-05790-z.
- Cancelli S., et al. Development of a multi-layer high-efficiency GEM-based neutron detector for spallation sources. *Scientific Reports*, 14(1) (2024). doi:10.1038/s41598-024-74958-5.
- Celora A., et al. A multipurpose numerical method for imaging studies and tomographic reconstruction. *Journal of Instrumentation*, 19(3) (2024). doi:10.1088/1748-0221/19/03/C03032.
- Celora A., et al. Analysis of neutron related background of the SXR GEM diagnostic on MAST-U. *Journal of Instrumentation*, 20(5) (2025). doi:10.1088/1748-0221/20/05/C05010.

- Celora A., et al. Assessment of a space and energy resolved diagnostic based on GEM technology on MAST-U. *Measurement Science and Technology*, 36(1) (2025). doi:10.1088/1361-6501/ad8cfb.

- Chomiczewska A., et al. Impurity study in the dimensionless and dimensional isotope identity experiment between JET Deuterium and Tritium L-mode plasmas. *Nuclear Fusion*, 65(1) (2025). doi:10.1088/1741-4326/ad9758.

- Griener M., et al. Characterization of the I-phase regime at TCV. *Nuclear Fusion*, 65(1) (2025). doi:10.1088/1741-4326/ad96cb.

- Guiotto F., et al. Data Analysis and Tomographic Reconstruction via X-Ray Measurements With a GEM Detector at the High-Voltage Padova Test Facility. *IEEE Transactions on Plasma Science*, 52(9), 4450–4461 (2024). doi:10.1109/TPS.2024.3406776.

- Guiotto F., et al. REVOLT-Upgrade: a software tool for fast, energy-resolved simulations of soft x-ray detectors in nuclear fusion experiments. *Measurement Science and Technology*, 36(7) (2025). doi:10.1088/1361-6501/ade465.

- Joffrin E., et al. Overview of the EUROfusion Tokamak Exploitation programme in support of ITER and DEMO. *Nuclear Fusion*, 64(11) (2024). doi:10.1088/1741-4326/ad2be4.

- Kong M., et al. 3D MHD modelling of plasmoid drift following massive material injection in a tokamak. *Nuclear Fusion*, 65(1) (2025). doi:10.1088/1741-4326/ad96ca.

- Luís R., et al. Neutronics Simulations for DEMO Diagnostics. *Sensors*, 23(11) (2023). doi:10.3390/s23115104.

- Marocco D., et al. Design status of the neutron and gamma-ray diagnostics for the Divertor Tokamak Test facility. *Fusion Engineering and Design*, 202 (2024). doi:10.1016/j.fusengdes.2024.114308.

- Perelli Cippo E., et al. Towards the use of SDD as an absolute detector for high-energy neutron measurements. *Journal of Instrumentation*, 18(5) (2023). doi:10.1088/1748-0221/18/05/C05019.

- Pilan N., et al. Role of Electron Stimulated Desorption in the initiation of HVDC vacuum arc. *Vacuum*, 224 (2024). doi:10.1016/j.vacuum.2024.113109.

- Putignano O., et al. Conceptual design of a GEM (gas electron multiplier) based gas Cherenkov detector for measurement of 17 MeV gamma rays from T(D, γ)5He in magnetic confinement fusion plasmas. *Review of Scientific Instruments*, 94(1) (2023). doi:10.1063/5.0101761.

- Verhaegh K., et al. Divertor shaping with neutral baffling as a solution to the tokamak power exhaust challenge. *Communications Physics*, 8(1) (2025). doi:10.1038/s42005-025-02121-1.

During my Ph.D. I presented the following contributions to conferences and workshops.

- Abstract and poster at the 7th Conference on Micro Pattern Gaseous Detectors (MPGD 2022), titled "Preliminary analyses of X-Rays from vacuum discharges during HV conditioning experiments at HVPTF with a GEM detector".

- Abstract and oral presentation at the 30th International Symposium on Discharges and Electrical Insulation in Vacuum (ISDEIV 2023), titled "Development of a data analysis software for the XR-GEM installed at HVPTF and preliminary results".

- Abstract and poster at the International Workshop on IMAGING (IMAGING 2023), titled "Development of a Triple-GEM detector with strip readout and GEMINI chip for X rays and neutron imaging".

- Abstract and oral presentation at the 11th International Workshop on the Mechanisms of Vacuum Arcs (MeVArc 2024), titled "Analysis of the micro-scale dynamics of X-Ray emission profiles collected with a GEM detector in needle-plane experiments at HVPTF".

- Abstract and oral presentation at the 12th International Workshop on the Mechanisms of Vacuum Arcs (MeVArc 2025), titled "Simulations for the study of micro-discharges in conditioning experiments at HVPTF".

- Abstract, poster and short oral at the International Conference on Diagnostics For Fusion Reactors: the Burning Plasma Era (ICFRD 2025), titled "Study of in-vacuum discharges with Xrays at the High Voltage Padova Test Facility".

- Abstract and oral presentation at the 31st International Symposium on Discharges and Electrical Insulation in Vacuum (ISDEIV 2025), titled "Simulations of micro-scale dynamics of discharges in conditioning experiments at the High Voltage Padova Test Facility".

Publications attached to this thesis

In the following pages we report the full version of the papers relevant for this Ph.D. thesis.

- Caruggi F., et al. Performance of a triple GEM detector equipped with Al-GEM foils for X-rays detection. *Nuclear Instruments and Methods in Physics Research Section A*, 1047 (2023). doi:10.1016/j.nima.2022.167855.
- Caruggi F., et al. Development of a data analysis software for the XR-GEM installed at HVPTF and preliminary results. *Proceedings of ISDEIV*, 2023-June, 29–32 (2023). doi:10.23919/ISDEIV55268.2023.10199827.
- Caruggi F., et al. Development of a Triple-GEM detector with strip readout and GEMINI chip for X rays and neutron imaging. *Journal of Instrumentation*, 19(2) (2024). doi:10.1088/1748-0221/19/02/C02015.
- Caruggi F., et al. Analysis of micro-discharges fine dynamics via x-ray detection on the high voltage Padova test facility experiment. *High Voltage*, 10(4), 1043–1052 (2025). doi:10.1049/hve2.70042.

Nuclear Inst. and Methods in Physics Research, A 1047 (2023) 167855

Contents lists available at ScienceDirect

Nuclear Inst. and Methods in Physics Research, A

journal homepage: www.elsevier.com/locate/nima

Performance of a triple GEM detector equipped with Al-GEM foils for X-rays detection

Federico Caruggi [a,b,*], Stephanie Cancelli [a,c], Agostino Celora [a], Federico Guiotto [a], Gabriele Croci [a,b,c], Marco Tardocchi [b,c], Fabrizio Murtas [d], Rui de Oliveira [e], Enrico Perelli Cippo [b], Giuseppe Gorini [a,b,c], Giovanni Grosso [b], Andrea Muraro [b]

[a] Dipartimento di Fisica "G. Occhialini", University of Milano-Bicocca, Piazza della Scienza 3, Milano, 20125, Italy
[b] Istituto per la Scienza e Tecnologia dei Plasmi, CNR, Via Cozzi 53, Milano, 20125, Italy
[c] INFN, Sezione Milano-Bicocca, Piazza della Scienza 3, Milano, 20125, Italy
[d] INFN, Laboratori Nazionali di Frascati, Via Enrico Fermi 40, Frascati, 00044, Italy
[e] European Organization for Nuclear Research (CERN), Geneva, Switzerland

ARTICLE INFO

Keywords:
Micropattern Gaseous detectors
Gas electron multiplier
X-ray detectors

ABSTRACT

The study of Soft X-ray emission can be a source of fundamental information, particularly for what concerns tokamaks and plasma diagnostics, but also in general in the fields of high energy and nuclear physics. Detection systems based on Gas Electron Multipliers (GEM) technology can be of particular use in the context of X-ray analyses, being relatively low cost while maintaining good spatial and temporal resolution and capability to sustain high counting rates (up to MHz/mm^2). The development of these new and improved detectors is thus of interest, especially in the research about diagnostic and control of machines for fusion energy. In this work, the performance of a new triple-GEM detector, characterized by an aluminum metallic coating on both layers of the GEM foils, is presented and a comparison is made with the more conventional design employing copper coating. The performances of an aluminum-coated GEM (Al-GEM) detector and of a standard copper-coated GEM (Cu-GEM) detector in revealing quasi-monochromatic X-ray beams coming from different fluorescence materials are compared. The Al-GEM detector is shown to less suffer the issue of unwanted background on the signal caused by the presence of copper inside the detector itself. The suppression of this noise source encourages the use of Al-GEM detectors to perform spectroscopy in harsh environments, such as tokamak machines, where soft X-rays are useful probes to control different plasma properties and parameters.

1. Introduction

The measurement of Soft X-ray (SXR) radiation is nowadays fundamental for many applications, especially in the context of plasma diagnostics and magnetic fusion devices [1,2]. In this environment, the analysis of this kind of emission, in the energy range between 2 and 20 keV, is a unique source of information, allowing for the study of various plasma parameters and for equilibrium control during tokamak operation [3]. For this task, detectors with high count rate capability, good temporal and spatial resolution and, most importantly, stability and radiation hardness are required. The Gas Electron Multiplier (GEM) [4] detector, one of the most widely employed Micro-Pattern Gaseous Detectors, is a gas proportional counter that exploits the ionization of a noble gas by the incident radiation photons, and the subsequent multiplication of the liberated electrons, through high-intensity electric fields. The GEM detector described in this paper is coupled with an Application Specific Integrated Circuit (ASIC) called GEMINI (GEM INtegrated Interface) and a custom made FPGA (Field Programmable Gate Array) board. The system can be used for both neutron (if a suitable converter is employed) [5–8] and SXR detection [9,10]. The key-points of this GEM-based detection system, for the SXR case, are good spatial resolution (few mm) and timing resolution (sub-ms), excellent rate capability (up to MHz/mm^2), intrinsic insensitivity to gamma and neutron radiation and relatively low cost.

1.1. The GEM detector

A standard GEM foil is a thin (50 μm) foil of kapton (a plastic insulator), metal-coated on both sides with a 5 μm layer of copper. A high-density pattern of bi-conical micro-holes (140 μm apart) is produced on the foil by chemical etching. A voltage difference of a few hundreds Volts is applied to the metal faces, which therefore behave as electrodes, generating a high electric field inside the holes. Electrons

* Corresponding author at: Dipartimento di Fisica "G. Occhialini", University of Milano-Bicocca, Piazza della Scienza 3, Milano, 20125, Italy.
E-mail address: federico.caruggi@unimib.it (F. Caruggi).

https://doi.org/10.1016/j.nima.2022.167855
Received 30 September 2022; Received in revised form 3 November 2022; Accepted 19 November 2022
Available online 5 December 2022

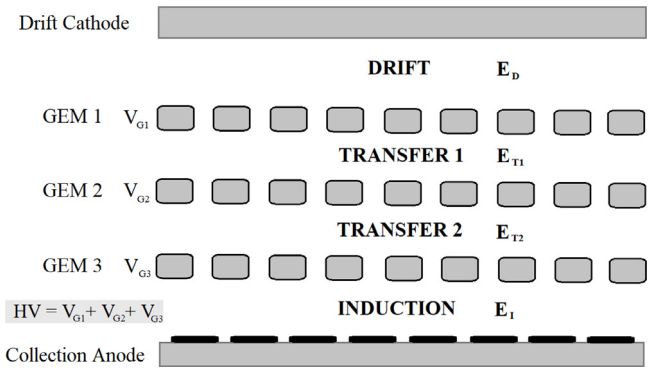

Fig. 1. Schematics of a triple-GEM detector.

are thus accelerated in their passage through the holes and the number of charge carriers is multiplied. Multiple GEM foils can be arranged in a cascade layout, to obtain higher overall gain values with lower voltage differences on each electrode, reducing the risks of discharges which could damage the detector. [4]

The configuration for SXR detection described in this work is the triple-GEM detector, made up of three GEM foils aluminum-coated, as shown in Fig. 1. The photoelectric interaction of the impinging photons and the first gas ionization occur in the drift zone between the cathode (which consists of a thin aluminized Mylar window) and the first GEM foil. The number of electron-ion pairs generated is proportional to the energy of the incoming radiation [11]. The primary electrons, carried by the electric field, drift towards the GEM foils, traverse the holes, and are multiplied in each of the three stages of the cascade. In the final induction region they are carried to a padded anode, made of 256 gold-coated copper pads of 6×6 mm^2, producing a detectable signal for each original incoming photon. The voltage difference (HV) on each GEM foil is set independently with a custom designed High Voltage module called HVGEM [12]. Fig. 2 shows a single GEM foil and the padded anode employed for the detector.

1.2. The readout system

The GEMINI ASIC is a fully-integrated analog front-end electronic system, custom developed for GEM detectors, in 0.18 μm CMOS technology [13]. It features 16 channels, each one with the architecture of Fig. 3. The current signal coming from the detector anode (i_{GEM}) is collected by the feedback capacitance (C_F) of a low-noise charge-sensitive preamplifier (CSP). The voltage output (V_{pre}) is fed to a small built-in hysteresis comparator. The comparison is made with a fixed threshold (V_{th}) coming from a R-2R Digital to Analog Converter (DAC), and set through an I^{2}C interface, which defines the minimum detectable charge for a given configuration (in terms of gain) of the detector. The digital output of the comparator (V_{DIS}) is then converted by a dedicated driver into LVDS (Low Voltage Differential Signal) standard. The output signal contains information about the Time of Arrival (ToA) of the event and its duration over V_{th}, called "Time-over-Threshold" (ToT), the latter being proportional to the input charge. An example of this principle of operation is shown in Fig. 4.

The signals coming from the GEMINI ASICs are read by a custom made FPGA board, able to collect information from a total of 256 GEMINI channels. The firmware of the board is made of a series of Time to Digital Converters (TDC), sampling the input with a frequency of 2 GHz (time resolution of 0.5 ns). For each signal, the ToA and the ToT information and the channel ID of the event are registered and packed in a 64-bit word routed to the board output. The DAQ PC is connected to the FPGA through an optical fiber, which has a theoretical bandwidth of about 10 Gbit/s, limiting the maximum rate on the detector to about 125 MHz [14].

Table 1
Characteristics of the two detectors. The width of the different regions is given going from top to bottom with reference to Fig. 1, so it corresponds to the order: DRIFT, Transfer 1 (T1), Transfer 2 (T2), INDUCTION.

	Al-GEM	Cu-GEM
GEM foil coating:	Aluminum	Copper
Width of regions (mm):	4, 1, 2, 1	4, 1, 2, 1
Number of pads at anode:	256	256
Dimensions of single pad:	6×6 mm^2	6×6 mm^2
Gas mixture (% vol):	Ar–CO_2 70–30	Ar–CO_2 70–30

1.3. Issues with standard copper GEM foils for SXR detection

While being suitable for various applications due to their many aforementioned qualities, the standard GEM detectors present a particular issue in being used for analysis of SXR radiation, in the energy range 2 to 20 keV. The copper used for the coating of a standard GEM foil, in fact, can be the source of a non-negligible background signal, because of the possibility that the incoming X-rays pass through the drift region without interaction with the gas and cause excitation of the Cu atoms instead, with subsequent emission of their characteristic K_α fluorescence X-ray at 8.05 KeV (see Fig. 5). This value of energy lays in the band of interest for the analysis of the SXRs, thus introducing a unwanted source of noise on the otherwise clean signal.

To overcome the issue, a new type of triple GEM detector is studied in this work, following the same concept proposed in [15]. The difference with respect to conventional GEM detectors is that the metallic coating of the foils is not made of copper, but of aluminum instead. The use of Al as coating should not generate a background signal in the band of interest, since the Al K_α emission line is located at an energy of 1.5 KeV. The aluminum coating is obtained by vacuum deposition using a DC magnetron sputtering machine. The initial thickness is in the range of 10 μm, reduced later on at 5 μm by soft phosphoric acid chemical etching. The aluminum coating is also void of the chromium substrate which is placed between kapton and copper for traditional GEM foils, avoiding another potential source of unwanted background (Cr K_α line is at 5.411 keV). The performance of the new detector (identified as Al-GEM) is tested against a conventional copper-coated GEM detector (referred as Cu-GEM). The parameters of the two systems are reported in Table 1.

2. The experimental setup

Both detectors operate with a flowing Ar–CO_2 mixture at atmospheric pressure, and the composition of the mixture is controlled by two digital thermal mass flow controllers [16]. The voltage difference for each GEM foil is controlled by the HVGEM module. The same electronic readout configuration is used for both detectors.

The two detectors are studied and compared in their response to the fluorescence radiation emitted by different metallic targets. Titanium is used at first to find suitable working conditions for the detectors (in terms of voltages and thresholds), and to perform the calibration of the detector responses. Copper and molybdenum are then used for testing and comparison of the results. The X-ray tube [17] produces a continuum bremsstrahlung emission superimposed with Ag K-lines at 22 keV and 25 keV. The X-ray beam is directed onto the target, from which fluorescence X-ray lines are emitted, resulting in a quasi-monochromatic radiation with an energy depending only on the chosen material for the target, which can be used as a reference. Fig. 6 shows a picture of the setup, together with a sketch of the process.

3. Detector characterization

3.1. High Voltage scan and Threshold scan

The characterization of the detectors to find the right working conditions is performed through the "threshold (THR) scan" and the "High Voltage (HV) scan".

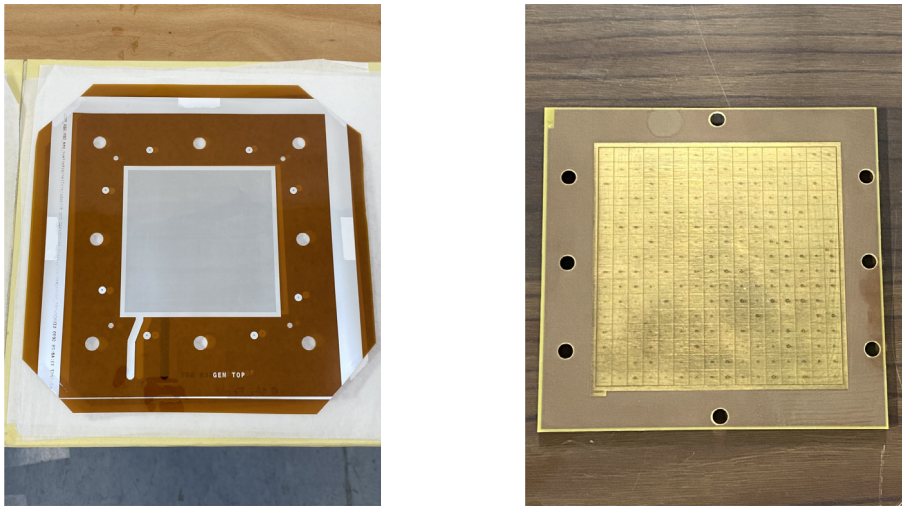

(a) (b)

Fig. 2. (a): Picture of a GEM foil covered with aluminum. (b): The detector anode made of 256 pads.

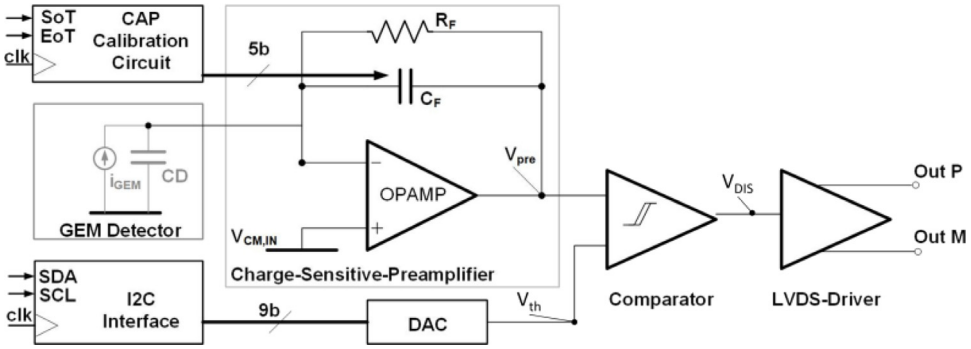

Fig. 3. Schematics of a single GEMINI channel. [9].

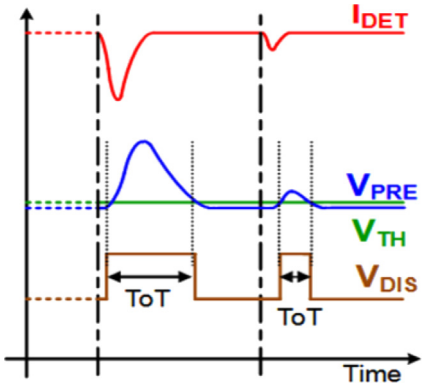

Fig. 4. Principle of operation of a single GEMINI channel [9].

The goal of the first procedure is to find a suitable threshold value (V_{th} of Fig. 4) for the ASICs: the value must be high enough to stop excessive background noise from being detected, while being low enough not to lose the actual signal. The setup features the following values of electric field (with reference to Fig. 1): 1 kV/cm for the drift region (E_D), 3 kV/cm for both the transfer regions (E_{T1} and E_{T2}) and 5 kV/cm for the induction region (E_I). Using the titanium target for fluorescence (K_α = 4.5 keV), the rate of detection is recorded and plotted versus V_{th} (see Fig. 7), while keeping fixed the potential difference on each GEM foil, all set to 370 V (the detector gain corresponds to a voltage of 1110 V in total). As it can be seen, the curve begins with a sharp drop, representing the cut on the background noise, followed by a plateau, which represents the threshold range for which the incoming signal is being cleanly detected. A minor downward slope indicates that, as expected, increments of the threshold cause some signal loss. The operational V_{th} is set to the value of 70 LSB for both detectors.

The HV scan aims at finding a good value of cumulative voltage difference (and thus gain) for the GEM foils. This value must be high enough to make sure that all the incoming particles of relevant energy produce a readable signal, while being kept low enough not to incur in risk of discharges or spurious signals. The procedure consists again in irradiating the detector using the titanium target for fluorescence, while the same values of electric field are employed, but this time a fixed value of threshold is set for the ASICs, while varying the voltage applied to the GEM foils. Fig. 8 shows the trends of counting rates as function of this variation of HV. A plateau is clearly visible for each curve, representing the conditions of full charge collection and thus the suitable operative ranges for the detectors. The operational value of HV for both detectors is chosen at 1110 V.

The pictures of both the THR and the HV scan show some little differences between the detectors. In particular, for what concerns the HV scan, it seems that the Al-GEM needs a voltage higher of about 20 V to reach the same counting plateau of the Cu-GEM. This difference could be accounted for by use of different voltage-gain relationships for the two detectors, but as better explained below it is preferred to keep the differences on the HV value since it is an operational parameter easier to correct.

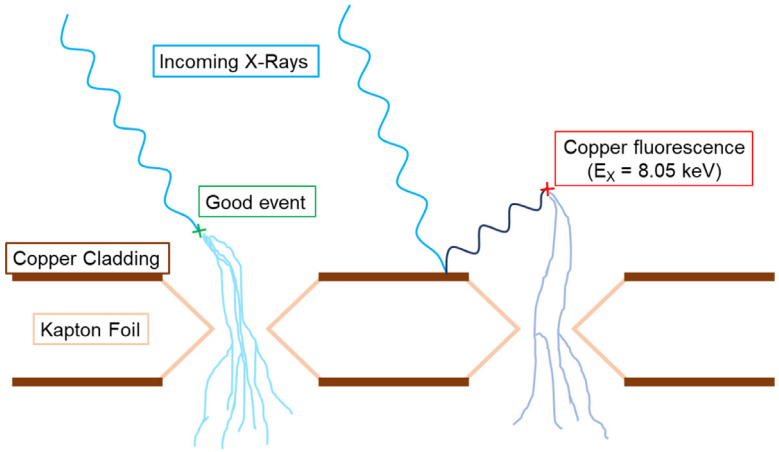

Fig. 5. Sketch of Cu excitation effect on conventional GEM detectors.

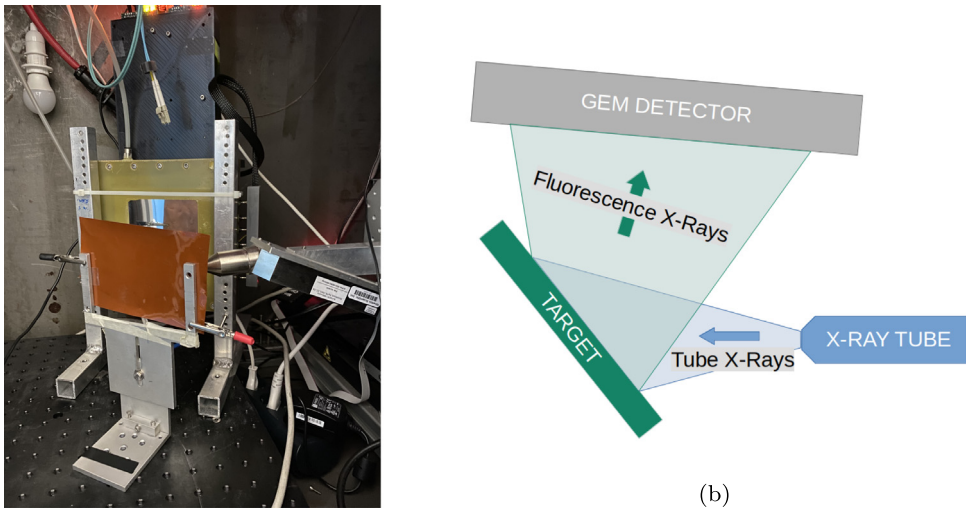

(a) (b)

Fig. 6. (a): The experimental setup of the GEM detector inside the X-ray chamber. The Al-GEM detector, the X-ray source and copper target for fluorescence are visible. (b) Simple sketch of a top-down view of the fluorescence setup.

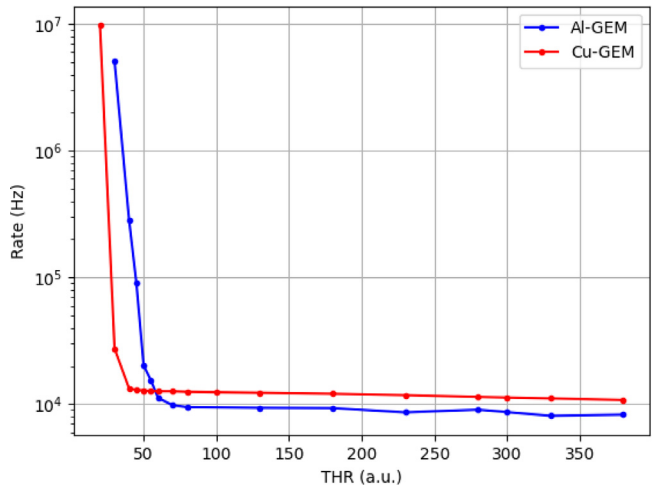

Fig. 7. THR scan comparison: Titanium target, Total voltage on GEM foils = 1110 V.

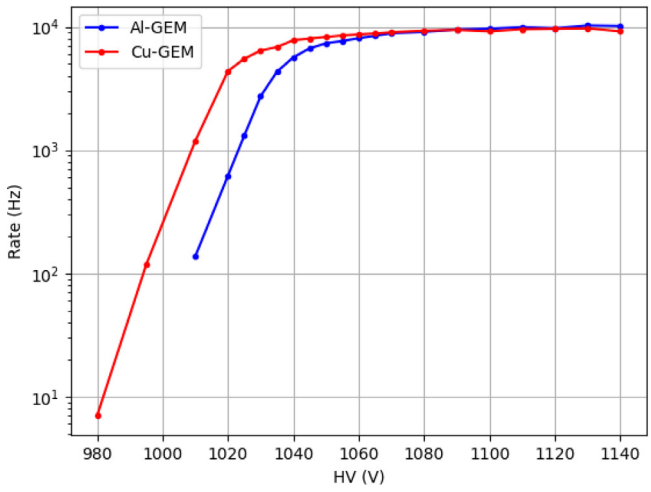

Fig. 8. HV scan comparison of Al-GEM (blue line) and Cu-GEM (red line), performed with a Titanium target and V_{th}= 70 LSB.

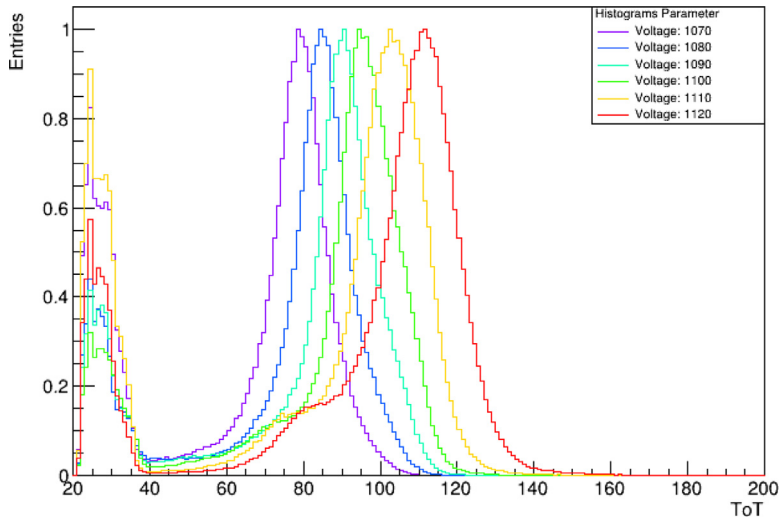

Fig. 9. Example of the peak shift in the Titanium ToT spectra of the Al-GEM detector.

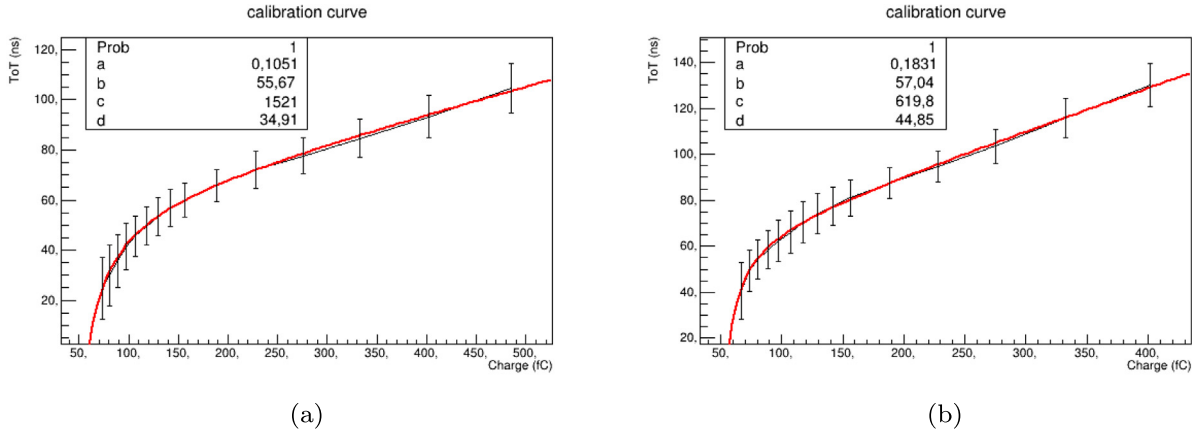

Fig. 10. Examples of fitted calibration curves for a single channel, with resulting parameters. (a) Al-GEM (b) Cu-GEM. In black, experimental points and straight lines connecting them. In red, fitted curves.

4. Detector calibration and analysis

As mentioned above, the raw output of the detection system consists of 64-bit words containing information about the ToA, the ToT and the channel ID for the incoming signals. In order to obtain the value of charge (which can then be related to the energy) deposited on the pads for each event, the detector response has to be calibrated. The relation between ToT and deposited charge q is

$$ToT\ (q) = a + b \cdot q - \frac{c}{q-d} \tag{1}$$

The calibration procedure aims at finding the values of the free parameters a, b, c and d for each individual pad, by fitting experimental data on a reference fluorescence peak. The calibration curve has a linear trend for high values of charge, while it is non-linear in the lower region, where $q \sim d$. More details on the process of calibration can be found in [9]

4.1. Calibration procedure

The experimental setup is the same illustrated for the HV scan. The titanium target is exploited again for fluorescence, and the counting rate is recorded for a variation of the value of HV (and thus the gain) applied to the GEM foils, while keeping constant the threshold value and the magnitude of the electric fields between them. The energy deposited by the incoming X-rays in the drift and conversion gap is fixed, so the variation of gain influences linearly the deposited charge on the pads, following

$$q(E) = Gain \cdot \frac{E}{W_i} \cdot 1.6 \cdot 10^{-19}\mathrm{C} \tag{2}$$

where W_i is the average energy required to create an electron-ion pair in the gas (about 28 eV for the chosen mixture), so that E/W_i is the number of primary electrons produced. The conversion factor from HV to detector gain is taken from previously published data [18]. As briefly mentioned above, the voltage-gain relationship is in principle different for each GEM detector, and new proper curves should be calculated and employed. However, gain measurements are harder to perform than HV scans. Thus, on the basis of the hypothesis that the functional form of the voltage-gain relationship is the same, an alternative approach is to shift the focus on changing, for different detectors, the operational conditions easier to control (i.e. the HV value). This choice will result in different calibration curves, which should take already into account the effect, allowing to use the same voltage-gain relationship in the different detectors. The impact of this approximation will be studied in the future, after a full characterization of the gain of the two detectors is done.

Following the experimental procedure described above, the ToT peak corresponding to full X-rays energy deposition will be shifted

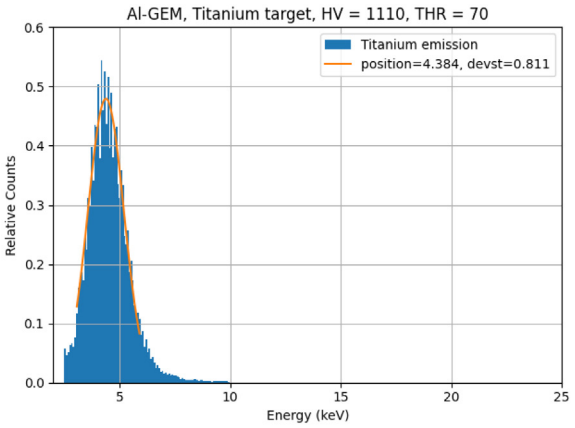

(a) Al-GEM titanium target

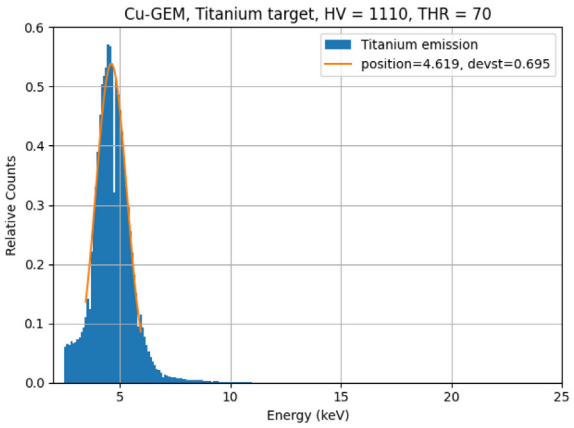

(b) Cu-GEM titanium target

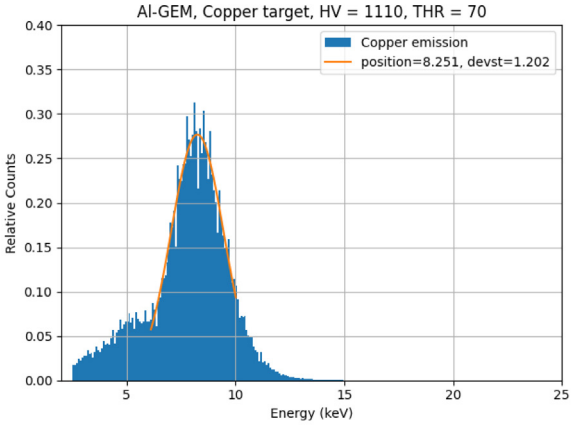

(c) Al-GEM copper target

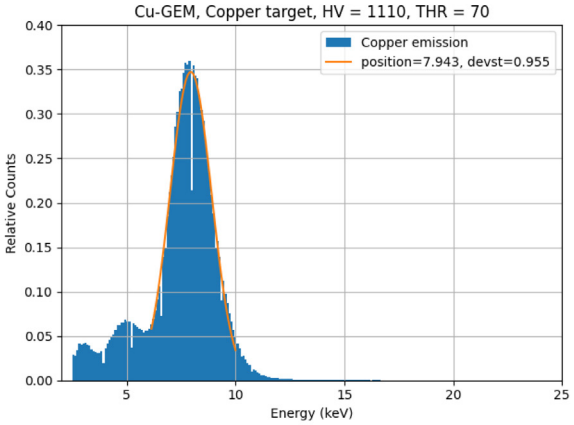

(d) Cu-GEM copper target

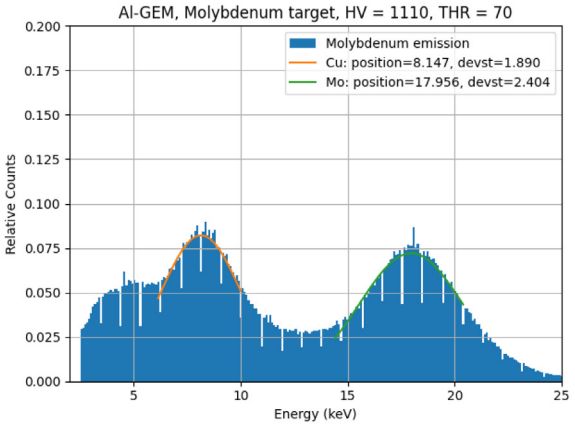

(e) Al-GEM molybdenum target

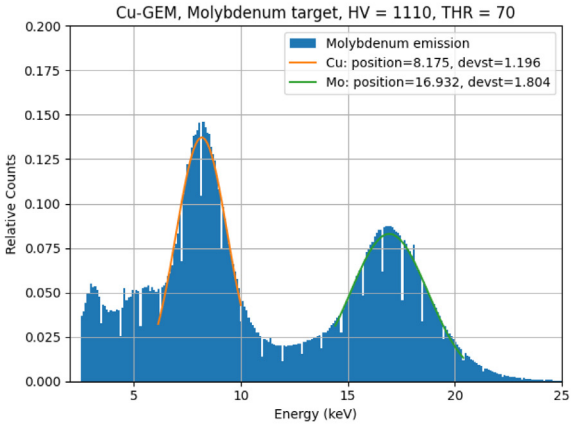

(f) Cu-GEM molybdenum target

Fig. 11. Energy spectra of different fluorescence peaks for the two detectors (Al-GEM on the left and Cu-GEM on the right).

as a function of HV, as displayed in Fig. 9, since the number of produced secondary electrons varies with the gain for the same number of primaries. Knowing the theoretical energy value of the target K_α fluorescence peak, experimental data can be fitted using Eq. (1), finding the required parameters for each pad. An example of fitted calibration curve for the same pad on the two different detectors is shown by the red lines in Fig. 10, clearly displaying the transition from the non-linear behavior at low values of charge to the linear trend at the higher ones. The error bars on the points represent the sigma parameter (which is related to the standard deviation) of the fitted Gaussian peaks for the titanium fluorescence in the ToT spectra.

4.2. Energy spectra of different targets

After the calibration procedure, the ToT values read from the detectors can be converted to charge and energy signals, giving the possibility to directly analyze energy spectra of the incoming radiation for all the anode pads. Different fluorescence targets are thus used to compare the overall response of the two detectors. A copper target (K_α

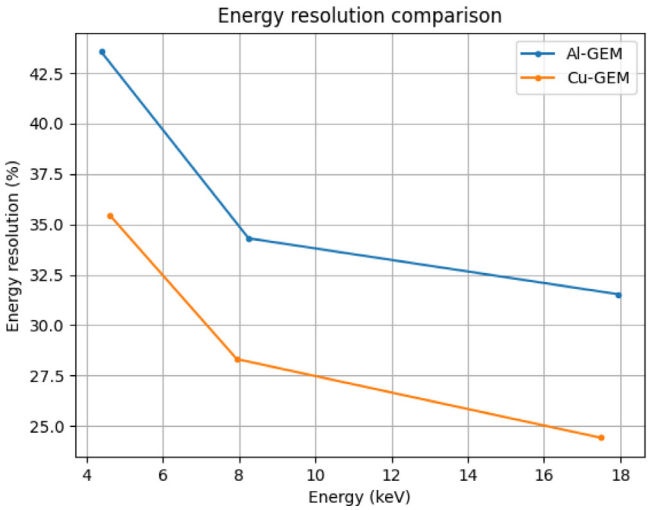

Fig. 12. Comparison of energy resolution between the two detectors.

= 8.05 keV) and a molybdenum target (K_α = 17.4 keV) are used, in order to analyze the full range of study for SXR radiation and to put in evidence the differences between the two detectors. The spectra, resulting from the counts collected over the whole GEM surfaces (from the entirety of the pads), are shown in Fig. 11. All the energy peaks have been fitted with a standard Gaussian shape, with mean value and standard deviation reported in the legend. The y-axis label, relative counts, refers to the fact that the number of events for each bin has been divided for the total number of events in the spectrum, so that the integral of the full spectrum gives one.

5. Comparison between Al-GEM and standard Cu-GEM detector

From the first two graphs (Figs. 11(a) and 11(b)) it can be seen that the calibration procedure allows now to convert the ToT signal of the titanium peak to the right energy value (K_α = 4.5 keV), within acceptable statistical errors and without significant differences in the comparison between the two detectors. The same can be said for Figs. 11(c) and 11(d), where the copper peak (K_α = 8.05 keV) is shown. The last two graphs (Figs. 11(e) and 11(f)), resulting from the molybdenum target fluorescence (K_α = 17.4 keV), are key to highlight the main difference between the two detectors. The high energy of the X-rays coming from the target allows to clearly discern two separate peaks in the pictures, one corresponding to the molybdenum emission itself and another one, which can be referred again to a copper fluorescence. This second peak is generated from the presence of Cu components inside or outside the detector (e.g. surrounding chamber and read-out electronics), and it represents a source of background on the signal, to be kept as low as possible for a clean readout of the incoming radiation.

The study of the detector response to the molybdenum emission, thanks to the presence of these two separated peaks, can be useful for different reasons. First of all, a calculation of the ratio of the positions of the fitted Gaussian curves can be an additional indicator of the success of the calibration, giving the possibility to check that the procedure was effective over all the energy range of interest. This was done for all the single pads of both detectors, and the result, in terms of average value, is shown in Table 2, together with the comparison with the true value, $K_{\alpha,Mo}/K_{\alpha,Cu}$. Following this, the relative intensity of the two peaks has been taken into account. Due to the differences in the fitted peak positions and standard deviations, a common set of energy values has been arbitrarily chosen for both the detectors, identifying the copper peak in the energy range 6.0–10.0 keV, and the molybdenum one in the range 13.5–21.5 keV. These values are not to be taken as representative of a physical phenomenon, but rather as convenient boundaries to perform a comparison between the spectra. Figs. 11(c) and 11(e) already act as indicators of the results: the copper peak registered by the Al-GEM appears visually of almost half intensity with respect to the one calculated from the Cu-GEM. The average of the analytical results calculated separately for each pad of the detectors are reported in Table 2. The comparison indicates thus clearly that the X-ray emissions from the copper cladding of the Cu-GEM has a non-negligible effect on the spectrum, as it is responsible of almost doubling the intensity of the background noise seen by the Al-GEM detector in the same conditions.

An additional aspect of comparison of the two detectors is presented in Fig. 12 , where a plot of the energy resolution values (calculated as ratio between FWHM and position of the fitted peaks) is displayed as function of energy. As it can be seen, the resolution of the Cu-GEM detector is better for all three comparison points. This fact could be of importance in the choice of the detector to employ for a specific use, with a trade-off between lower background signal and worse energy resolution.

A last analysis was performed on both the detectors, to see what is the result of applying a correction on the energy spectra seen, depending on the variable efficiency that the detector presents over the full range of interest. Seeing as the intensity of the radiation on the detector is about uniform, the length of the drift zone is taken as representative of the average thickness that the incoming particles traverse (in the real case there are particles coming from different angles and traveling longer or shorter than this in the gas, and other not stopping at all). The correction is thus calculated on the basis of the stopping power of the gaseous mixture employed for the detector, following:

$$correction(E) = \frac{1}{efficiency(E)} = \frac{1}{1 - e^{-\mu(E)\cdot l_D}} \tag{3}$$

where μ is the X-ray attenuation coefficient of the gaseous mixture (which is a function of energy), and l_D is the length of the drift zone.

The correction is applied simply by multiplication of the counts detected for each value of energy and the results, for both the molybdenum spectra studied above, is shown in Fig. 13. As clearly visible, the correction is quite relevant, modifying the spectrum considerably and the height of the molybdenum peak increases, making it predominant with respect to the copper one (for the case of the Al-GEM, the ratio between the heights of the peaks goes from less than 1 to about 7). Again, the difference between the detectors, in terms of integrated counts of molybdenum and copper emissions, was calculated, with the results reported in Table 2.

6. Conclusions

The new type of GEM detector employed in this work, with aluminum coating on the foils (Al-GEM), is shown to provide results compatible with the ones given by the more traditional Cu-GEM design, demonstrating also the validity of previously exploited methods (as the calibration procedure) on the new different design. The comparison between the two instruments, performed with reference to a molybdenum fluorescence energy spectrum, puts in evidence in particular the unwanted amplification of the copper background in the Cu-GEM response, arising from the interaction of the incoming X-rays directly with the metallic cladding of the GEM foils. The same background, even if still present, is greatly reduced in the Al-GEM spectrum. The new detector prototype is thus a good candidate to be used in the detection and analysis of SXR emission, particularly for plasma diagnostics. The results of the application of the efficiency correction, at the end, show also that it is possible to reconstruct a more realistic energy spectrum of the incoming radiation, based solely on the data gathered by the GEM detector and on the knowledge of the operational parameters of the instrument. Future studies on this matter could aim at a validation of the final results obtained, by comparison with a different detection system, possibly one more accurate in terms of energy resolution.

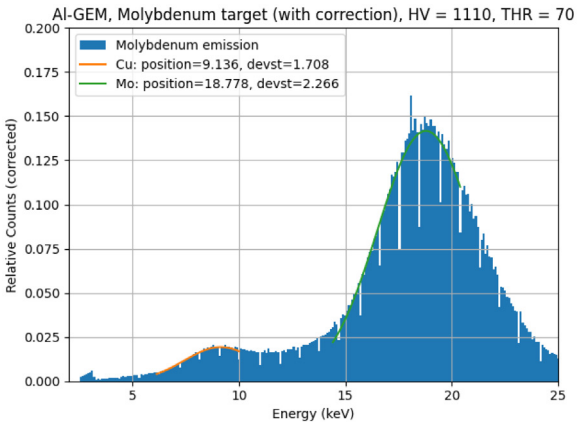

(a) Al-GEM molybdenum target, corrected

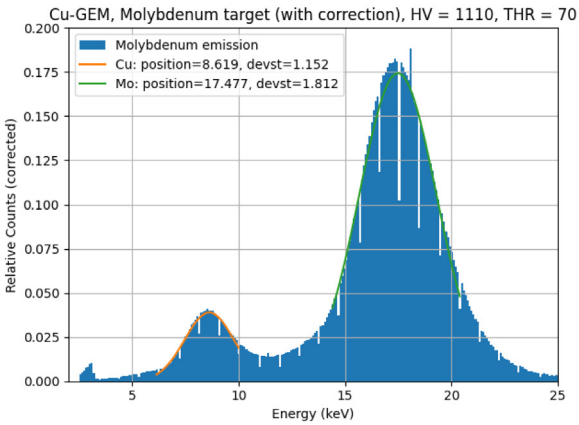

(b) Cu-GEM molybdenum target, corrected

Fig. 13. Energy spectra of molybdenum fluorescence peaks, corrected for the detector efficiency (Al-GEM on the left and Cu-GEM on the right).

Table 2
Results of the comparison between detectors, based on the molybdenum emissions of Fig. 11.

Quantity	Al-GEM	Cu-GEM	
$K_{\alpha,Mo}/K_{\alpha,Cu}$	2.367 ± 0.543	2.053 ± 0.292	Expected value: 2.161
I_{Cu}/I_{Mo}	0.674 ± 0.125	1.007 ± 0.147	Ratio: 0.669
(With efficiencyenergy correction)	0.075 ± 0.013	0.129 ± 0.021	Ratio: 0.581

Declaration of competing interest

The authors declare that they have no known competing financial interests or personal relationships that could have appeared to influence the work reported in this paper.

Data availability

Data will be made available on request.

Acknowledgments

This work has been carried out within the framework of the EUROfusion consortium. The views and opinions expressed herein do not necessarily reflect those of the European Commission.

References

[1] D. Mazon, A. Jardin, P. Malard, M. Chernyshova, C. Coston, P. Malard, M. O'Mullane, T. Czarski, K. Malinowski, F. Faisse, F. Ferlay, J. Verger, A. Bec, S. Larroque, G. Kasprowicz, A. Wojenski, K. Pozniak, SXR measurement and W transport survey using GEM tomographic system on WEST, J. Instrument. 12 (11) (2017) C11034, http://dx.doi.org/10.1088/1748-0221/12/11/C11034.

[2] L.F. Delgado-Aparicio, J. Maddox, N. Pablant, K. Hill, M. Bitter, J.E. Rice, R. Granetz, A. Hubbard, J. Irby, M. Greenwald, E. Marmar, K. Tritz, D. Stutman, B. Stratton, P. Efthimion, Multi-energy SXR cameras for magnetically confined fusion plasmas, Rev. Sci. Instrum. 87 (11) (2016) 11E204, http://dx.doi.org/10.1063/1.4964807.

[3] J. Wesson, Tokamaks, third ed., Oxford University Press, 2004.

[4] F. Sauli, The gas electron multiplier (GEM): Operating principles and applications, Nucl. Instrum. Methods Phys. Res. A 805 (2016) 2–24, http://dx.doi.org/10.1016/j.nima.2015.07.060.

[5] S. Cancelli, A. Muraro, E.P. Cippo, G. Romanelli, A. Abba, Y. Chen, G. Grosso, G. Gorini, Z. Hu, C.-C. Lai, O.M. Cormack, L. Robinson, P.-O. Svensson, M. Tardocchi, R. Hall-Wilton1, Y. Xie, S. Zhijia, J. Zhou, X. Zhou, G. Croci, Development of a ceramic double thick GEM detector for transmission measurements at the VESUVIO instrument at ISIS, J. Instrum. 16 (2021) http://dx.doi.org/10.1088/1748-0221/16/06/P06003.

[6] A. Muraro, G. Claps, G. Croci, C.C. Lai, R.D. Oliveira, S. Altieri, S. Cancelli, G. Gorini, R. Hall-Wilton, C. Höglund, E.P. Cippo, L. Robinson, P. Svensson, F. Murtas, MBGEM: A stack of borated GEM detector for high efficiency thermal neutron detection, Eur. Phys. J. Plus 136 (2021) 1–14, http://dx.doi.org/10.1140/epjp/s13360-021-01707-2.

[7] G. Croci, G. Claps, M. Cavenago, M.D. Palma, G. Grosso, F. Murtas, R. Pasqualotto, E.P. Cippo, A. Pietropaolo, M. Rebai, M. Tardocchi, M. Tollin, G. Gorini, NGEM fast neutron detectors for beam diagnostics, Nucl. Instrum. Methods Phys. Res. A 720 (2013) 144–148, http://dx.doi.org/10.1016/j.nima.2012.12.014.

[8] E.P. Cippo, G. Croci, A. Muraro, A. Menelle, G. Albani, M. Cavenago, C. Cazzaniga, G. Claps, G. Grosso, F. Murtas, M. Rebai, M. Tardocchi, G. Gorini, A GEM-based thermal neutron detector for high counting rate applications, J. Instrum. 10 (2015) http://dx.doi.org/10.1088/1748-0221/10/10/P10003.

[9] A. Muraro, G. Claps, G. Croci, F. Cordella, G. Gorini, G. Grosso, Z. Hu, L. Mangiagalli, O. McCormack, F. Murtas, M. Nocente, E.P. Cippo, E. Panontin, M. Pedroni, M. Rebai, D. Rigamonti, M. Tardocchi, D. Pacella, Development and characterization of a new soft X-ray diagnostic concept for tokamaks, J. Instrum. 14 (2019) C08012, http://dx.doi.org/10.1088/1748-0221/14/08/C08012.

[10] M. Chernyshova, T. Czarski, K. Malinowski, E. Kowalska-Strzęciwilk, J. Król, K.T. Poźniak, G. Kasprowicz, W. Zabołotny, A. Wojeński, R.D. Krawczyk, P. Kolasiński, I.N. Demchenko, Y. Melikhov, Development of GEM detector for tokamak SXR tomography system: Preliminary laboratory tests, Fusion Eng. Des. 123 (2017) 877–881, http://dx.doi.org/10.1016/j.fusengdes.2017.03.107.

[11] G. Knoll, Radiation Detection and Measurement, Wiley, 2010.

[12] G. Corradi, F. Murtas, D. Tagnani, A novel high-voltage system for a triple GEM detector, Nucl. Instrum. Methods Phys. Res. A 572 (1) (2007) 96–97, http://dx.doi.org/10.1016/j.nima.2006.10.166, Frontier Detectors for Frontier Physics.

[13] A. Pezzotta, G. Corradi, G. Croci, M.D. Matteis, F. Murtas, D. Tagnani, G. Gorini, A. Baschirotto, GEMINI, a CMOS 180 nm mixed-signal 16-channel ASIC for triple-GEM detectors readout, in: 2015 IEEE SENSORS - Proceedings, Institute of Electrical and Electronics Engineers Inc., 2015, http://dx.doi.org/10.1109/ICSENS.2015.7370468.

[14] S. Cancelli, A. Muraro, E.P. Cippo, A. Abba, G. Corradi, G. Grosso, G. Gorini, M. Kushoro, F. Murtas, O. Putignano, J. Scionti, D. Tagnani, M. Tardocchi, G. Croci, Electronic readout characterisation of a new soft X-ray diagnostic for burning plasma, J. Instrum. 17 (2022) C08028, http://dx.doi.org/10.1088/1748-0221/17/08/C08028.

[15] M. Chernyshova, K. Malinowski, T. Czarski, E. Kowalska-Strzęciwilk, P. Linczuk, A. Wojeński, R.D. Krawczyk, Y. Melikhov, Advantages of al based GEM detector aimed at plasma soft-semi hard X-ray radiation imaging, Fusion Eng. Des. 146 (2019) 1039–1042, http://dx.doi.org/10.1016/j.fusengdes.2019.01.153, SI:SOFT-30.

[16] Bronkhorst, F-201CV, EL-Flow select mass flow controller - 0,16…25000 mln/min [cited 2022-11-02], 2022, URL https://www.bronkhorst.com/int/products/gas-flow/el-flow-select/f-201cv/.

[17] Amptek, Mini-X2 X-Ray tube system for XRF [cited 2022-11-02], 2019, URL https://www.amptek.com/products/mini-x2-x-ray-tube.

[18] M. Alfonsi, G. Bencivenni, P.D. Simone, F. Murtas, M.P. Lener, W. Bonivento, A. Cardini, C. Deplano, D. Raspino, D. Pinci, High-rate particle triggering with triple-GEM detector, Nucl. Instrum. Methods Phys. Res. A 518 (2004) 106–112, http://dx.doi.org/10.1016/j.nima.2003.10.035.

30th International Symposium on Discharges and Electrical Insulation in Vacuum

Development of a data analysis software for the XR-GEM installed at HVPTF and preliminary results

Federico Caruggi
Dipartimento di fisica
Università di Milano-Bicocca
Milano, Italy
f.caruggi@campus.unimib.it

Gabriele Croci
Dipartimento di fisica
Università di Milano-Bicocca
Milano, Italy

Antonio De Lorenzi
Consorzio RFX
Padova, Italy

Giovanni Grosso
Istituto per la Scienza e Tecnologia dei Plasmi, CNR
Milano, Italy

Federico Guiotto
Dipartimento di fisica
Università di Padova
Padova, Italy

Matteo Hakeem Kushoro
Dipartimento di fisica
Università di Milano-Bicocca
Milano, Italy

Luca Lotto
Consorzio RFX
Padova, Italy

Isabella Mario
Consorzio RFX
Padova, Italy

Agostino Celora
Dipartimento di fisica
Università di Milano-Bicocca
Milano, Italy

Nicola Pilan
Consorzio RFX
Padova, Italy

Silvia Spagnolo
Consorzio RFX
Padova, Italy

Andrea Muraro
Istituto per la Scienza e Tecnologia dei Plasmi, CNR
Milano, Italy

Abstract*—The MITICA experiment, under construction at Consorzio RFX (Padova, Italy), is the full-scale prototype for the Neutral Beam Injector (NBI) of the ITER tokamak. One of the critical aspects for the ion beam accelerator is high voltage holding over long vacuum gaps (up to 1 MV from the ion source to the enclosing vessel), with the main issue being the occurrence of discharge events, which could severely damage the machine. To study this phenomenology, with the aim of prevention of discharges, the High Voltage Padova Test Facility (HVPTF) experiment is in operation. The setup of HVPTF consists in a cylindrical vacuum vessel, with stable pressure control, in which two replaceable electrodes are mounted with an adjustable gap width. The electrodes are powered by independent power supplies, allowing for a total voltage difference up to 800kV. Current and voltage of the power supplies, as well as the pressure and the gas composition inside the chamber are monitored at a sampling rate of 100 Hz. Additionally, the bremsstrahlung X-ray emission produced by the accelerated electrons during discharges is monitored by means of scintillators at higher rates (up to 1 MHz). Data from past experimental campaigns have been analyzed and correlations between the current/voltage signals and the X-ray emission have been highlighted. Recently, a new detector, based on the Gas Electron Multiplier (GEM) and optimized for X-ray detection, has been installed at HVPTF. The detector acts as a very fast single photon counting system (with rates up to about 125 MHz), allowing for real-time measurement of the X-ray emission rate, which could be used as basis for the development of a feedback control system for the prevention of discharges. The aim of this work is to illustrate the development of a new data analysis software, tailored on the data read by the GEM detector, displaying some of the first results obtained from the recent experimental campaigns. Future perspectives will also be drawn, for the next steps to take towards the realization of the breakdown prevention system.

Keywords—ITER, MITICA, HVPTF, X-Ray Detection, Gas Electron Multiplier

I. INTRODUCTION

The MITICA (Megavolt ITER Injector and Concept Advancement) experiment, currently under construction at Consorzio RFX in Padova (Italy) [1], represents the full-scale prototype of the Neutral Beam Injector (NBI) system for the ITER tokamak, i.e. an external heating apparatus able to provide power to the plasma through injection of a neutral beam with an energy of 1 MeV, and energy transfer through collisions. This is achieved through the extraction, acceleration, and neutralization of a beam of negative ions [2], using a multi-aperture, multi-grid system in vacuum. One of the major challenges for the MITICA experiment is to maintain the required high voltage differences over long vacuum gaps between the acceleration grids, with the main issue in this context being the occurrence of "discharge events", i.e., spikes in current flowing between electrodes (combined with drops of the applied voltage difference). These occurrences are commonly distinguished in "microdischarges", events characterized by fast timescales and small values of current, and "breakdowns", disruptive events longer in time and with higher currents, which could damage the instruments. Microdischarges are potentially precursors of breakdown events, thus the study of these shorter phenomena can be of great interest in the efforts for the prevention of breakdowns and the mitigation of their damage. In this framework, the High Voltage Padova Test Facility (HVPTF) experiment has been developed, for the analysis of the phenomenology of in-vacuum discharges between electrodes up to voltage differences of 800 kV [3] [4]. Discharges are characterized by a flow of electrons stripped from the cathode and accelerated towards the anode, incurring in collisions and emitting bremsstrahlung X-rays. The analysis of the HVPTF experiment is thus performed with a focus on this kind of emission.

II. The HVPTF Experiment

The experimental setup of HVPTF consists of a cylindrical vacuum vessel of AISI 304 stainless steel, with a diameter of 1200 mm and 2400 mm length. Through the use of suitable vacuum pumps, the internal pressure of the chamber can be stably controlled in the range 10^{-2}-10^{-7} mbar. Two stainless-steel electrodes are installed inside the vessel, separated by an adjustable gap which can be regulated from a few mm up to 250 mm. The electrodes are replaceable, so that different geometries can be tested (e.g., sphere, plane, needle). Two independent Cockroft-Walton power supplies feed the electrodes, allowing for a voltage difference up to 800 kV_{DC}, with the vessel walls kept at ground. Current and voltage outputs of the power supplies, together with the pressure inside the chamber, are sampled at a frequency of 100 Hz. A picture of the experimental setup, comprising also additional instruments, is shown in Fig. 1.

X-ray emissions can be read by two scintillators, installed behind glass windows, at a distance of about 2 m from the electrodes: an enhanced Lanthanum Bromide ($LaBr_3$) [5] and a LYSO crystal [6], both manufactured by Saint-Gobain. Previous studies have already demonstrated the presence of correlations between analog signals (current and voltage) and X-ray emissions [7] [8], but some limitations have been discovered, with pile-up issues occurring in case of discharge events at high voltages, where the emission intensity increases drastically. Recently, a new detector, based on the Gas Electron Multiplier technology and tailored on X-ray detection (XR-GEM), has been installed at HVPTF (shown in Fig. 2). The instrument is placed on a movable tray, so that its distance from the electrodes can be adjusted, with a direct line of sight to the center of the chamber through the beryllium window of a pinhole collimator. The detector is equipped with a digital acquisition setup, so that it can be used as a very fast single photon counting system, so that even in the case of discharges with the higher values of voltage, pile-up effects are not a relevant issue.

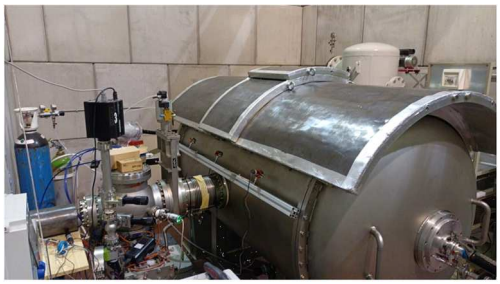

Fig. 1. HVPTF experimental setup.

Fig. 2. XR-GEM detector installed at HVPTF.

III. The XR-GEM Detector

The Gas Electron Multiplier (GEM) [9] is one of the most widely employed kinds of Micro-Pattern Gaseous Detectors. It is a gas proportional counter, exploiting ionization of a noble gas, and acceleration and multiplication of the extracted electrons with high-intensity electric fields. GEM-based detection systems have been employed for detection of both neutrons (with the usage of converter materials) [10] [11] [12] and X-rays [13] [14]. The XR-GEM, tailored for the detection of Soft X-Rays (especially in the range 2-20 keV) can achieve good spatial and temporal resolutions, maintaining excellent rate capabilities and relatively low cost, and being intrinsically insensitive to incoming gamma and neutron radiations. Details about the detector characterization can be found in [15].

A. Gas Electron Multiplier

Fig. 3 displays the schematic of a triple-GEM detector. The incoming radiation interacts in the drift region, ionizing the gas and producing primary particles (electron-hole pairs). The multiplication of the signal carriers (i.e., the electrons) is obtained in the transfer regions by passage through multiple subsequent GEM foils. Each foil is a sheet of plastic insulator (kapton) 50 µm thick, metal-coated on both sides by a thin (5 µm) layer of aluminum, and chemically etched to obtain a high-density pattern of bi-conical micro-holes (140 µm apart). Applying a voltage difference of few hundred Volts between the metal faces generates a high electric field inside the holes, allowing for acceleration and multiplication of the passing electrons. The multi-step cascade arrangement of 3 GEM foils allows for high gains without too high potential differences on each electrode, reducing the risks of damage to the instrument. Finally, the electrons are carried in the induction region towards a padded anode, composed by 256 individual 6x6 mm^2 pads. A module called HVGEM [16] allows for independent setting of the voltage difference on each foil (V_{G1}, V_{G2}, V_{G3}).

B. Readout system

The readout system of the GEM detector exploits a combination of GEMINI (GEM Integrated Interface) ASICs and FPGA (Field Programmable Gate Array) boards. The former is a fully integrated analog front-end electronic system, developed in 0.18 µm CMOS technology for GEM systems

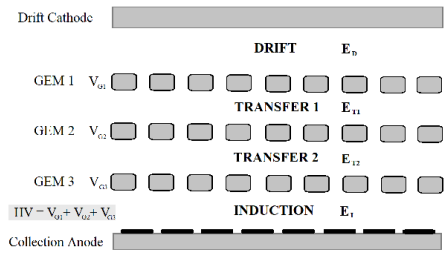

Fig. 3. Schematics of a triple GEM detector.

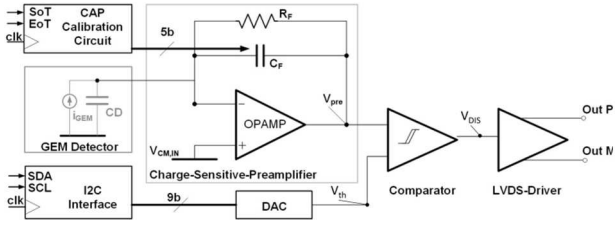

Fig. 4. Schematics of a single GEMINI channel

[17]. In each channel, as shown in Fig. 4, the feedback capacitance (C_F) of a low-noise charge-sensitive preamplifier (CSP) collects the signal incoming from the anode of the detector (i_{GEM}). The output voltage (V_{pre}) is compared with a fixed threshold (V_{th}) by means of a small built-in hysteresis comparator. The threshold represents the minimum detectable signal for a given voltage (and thus gain) of the detector foils. The final output, V_{DIS}, is converted into Low Voltage Differential Signal standard and contains information about the Time of Arrival (ToA) and the "Time-over-Threshold" (ToT) of each event. The latter, as shown in Fig. 5, is the length of time where the signal stays over V_{th}, and it is proportional to the charge deposited by the primary radiation.

Data coming from the ASICs are sent to a series of custom-made FPGA boards. Their firmware is composed by a series of Time to Digital Converters (TDC), sampling the input at a frequency of 2 GHz. Each signal received by the boards is registered and packed in a 64-bit word containing the ToA, the ToT and the channel ID of the event, to be then routed to the DAQ PC by means of optical fiber. The theoretical bandwidth of the latter, of about 10 Gbit/s, limits in the end the maximum detectable rate on the detector to about 125 MHz. [18].

C. *Data analysis software*

To analyze the data coming from the GEM detector, a new software is under development. The code is mainly written in Python, it is provided with a graphical user interface (GUI), and it exploits C++ routines for pre-processing functionalities. It focuses on various different aspects of data visualization, e.g. the temporal evolution, 2D imaging, and energy spectra of the incoming X-rays. The GUI allows to interact with the graphs, displaying additional information, or giving the possibility to perform quick analyses, e.g. event filtering, rate calculations, spectra endpoints and integrals or curve fitting. One functionality in particular used for the analyses on the HVPTF experiment is “heatmap filtering”. It allows, the user to display an heatmap representing, for each pad, the percentage of events (out of the total events registered) falling in a user-defined energy window. This helps highlighting the presence of spatially localized signals of defined energy ranges, as for example the characteristic X-ray emissions of particular materials. In addition to the data analysis software, a spatial reconstruction algorithm is being developed, in order to exploit the spatial resolution of the detector to obtain, starting from the intensity of radiation detected, the reconstruction of X-ray emissivity of the source.

IV. Analyses and Discussion

Data coming from a few experimental sessions of HVPTF have already been studied with the newly developed software. One of the most important innovations that the use of a GEM-based detector offers is the possibility of spatial localization of the radiation, and thus 2D imaging. The range of view of the detector, when placed in front of a collimator, is bi-conical, as portrayed in Fig. 6. This configuration allows also to obtain different levels of magnification (zoom) of the incoming image, just by varying the distance between detector and collimator. This effect was made evident in the analysis of an experimental session performed for tests on an insulator, during which the detector distance was changed between every run. The result is shown in Fig. 7, for three different values of distance. The magnification is enhanced when the detector is moved away from the collimator, making possible to discern more details of the same picture. This advantage, however, comes intrinsically with the drawback of a worsening of the statistics: moving the detector farther lowers the count rate obtained in the same conditions.

Further analyses were conducted on a series of experimental sessions with needle-plane electrodes. Being a commonly studied case, this can be the starting point for various considerations about the characterization of the discharge phenomenology. Unfortunately, during these experimental sessions, a component of the readout electronics of the detector was damaged. Thus, all the heatmaps have a quarter of the detector with no counts at all. As it can be seen from Fig. 8, the localization of the radiation registered by the GEM detector seems to suggest that the main source of X-ray emission of the chamber is concentrated in proximity of the electrodes, particularly the plane. Preliminary results of the emissivity spatial reconstruction code mentioned above seem to confirm this observation.

In Fig. 9, an heatmap with the filtering functionality described in the previous section allows to identify the presence of an emission in the energy range around 7.5 keV, localized only in the direct neighborhood of the electrodes, while the surrounding regions, and in particular the volume behind the needle electrode (corresponding to the supporting structure) is void of the emission itself. The result is confirmed by looking at the spectra produced for pads from different regions of the detector, as displayed in Fig. 10, where each spectrum is shown besides the heatmap with the rectangle selector placed on the corresponding pads. This emission could be caused by the fluorescence of sputtered material coming from the electrodes. Future studies on the matter, combined with more developed and accurate spatial reconstruction processes, will be aimed at confirming or denying this theory.

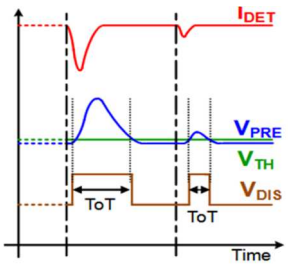

Fig. 5. Principle of operation of a single GEMINI channel

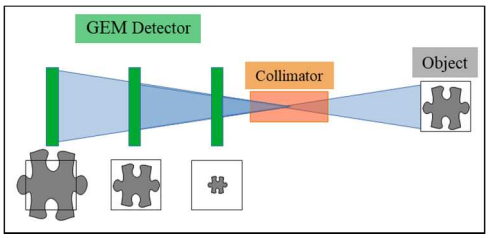

Fig. 6. Sketch of the view range of the GEM detector, with magnification effect.

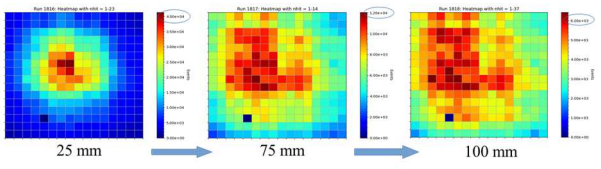

Fig. 7. Result of the magnification effect on a series of GEM

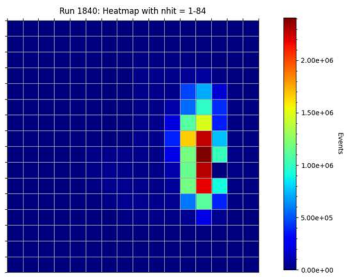

Fig. 8. 2D image of needle-plane emission obtained with GEM.

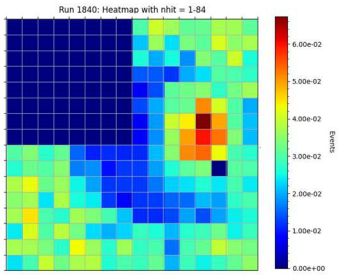

Fig. 9. 2D heatmap with filtering in range 6.5-8.5 keV.

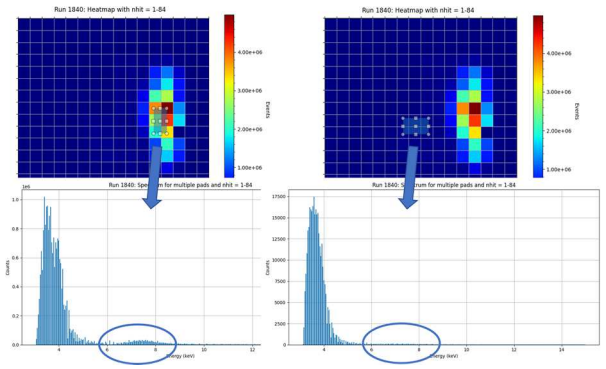

Fig. 10. Comparison of spectra from the plane electrode and chamber.

V. Future Perspectives and Conclusion

The use of the GEM-based detector for the analysis of X-ray emissions can be appealing for the case of study of HVPTF. The possibility of 2D imaging, combined with the algorithm of spatial reconstruction and the good energy resolution of the detector, can give new insights on the physics of the discharges. The excellent rate capabilities of the GEM can also be exploited as the basis for the future implementation of a feedback control system, for prevention and mitigation of the discharges. Future perspectives for the use of the XR-GEM diagnostics feature the analyses of data coming from the next experimental campaigns, in parallel with further development of the data analysis software. The development and installation of an additional GEM detector, on a line of view orthogonal with respect to the current one has been proposed, aiming at the possibility of a full 3D reconstruction of the X-ray emissivity within the vacuum chamber.

Acknowledgments

This work has been carried out within the framework of the EUROfusion consortium, funded by the European Union via the Euratom Research and Training Programme (Grant Agreement No 101052200 – EUROfusion). Views and opinions expressed are however those of the author(s) only and do not necessarily reflect those of the European Union or the European Commission. Neither the European Union nor the European Commission can be held responsible for them.

This work has been carried out within the framework of the ITER RFX Neutral Beam Testing Facility (NBTF) Agreement and has received funding from the ITER Organization. The views and opinions expressed herein do not necessarily reflect those of the ITER Organization.

References

[1] V. Toigo et al., “The PRIMA test facility: SPIDER and MITICA test-beds for ITER neutral beam injectors”, New Journal of Physics, vol. 19 (8), August 2017.

[2] R. S. Hemsworth et al., “Overview of the design of the ITER heating neutral beam injectors”, New Journal of Physics, vol. 19 (2), February 2017.

[3] A. De Lorenzi, N. Pilan, L. Lotto, M. Fincato, G. Pesavento and R. Gobbo, “HVPTF-The high voltage laboratory for the ITER neutral beam test facility”, Fusion Engineering and Design, vol. 86 (6), 2011 [proceedings of the 26th Symposium of Fusion Technology (SOFT-26)].

[4] N. Pilan et al., “Study of high DC voltage breakdown between stainless steel electrodes separated by long vacuum gaps”, Nuclear Fusion, vol. 60 (7), June 2020.

[5] S. Gobain, “Lanthanum bromide, standard enhanced | crystals” (2022), available at *https://www.crystals.saint-gobain.com/radiation-detection-scintillators/crystal-scintillators/lanthanum-bromide-labr3* [accessed 2023-02-15].

[6] S. Gobain, “LYSO scintillation crystals | crystals” (2022), available at *https://www.crystals.saint-gobain.com/radiation-detection-scintillators/crystal-scintillators/lyso-scintillation-crystals* [accessed 2023-02-15].

[7] S. Spagnolo et al., “Characterization of x-ray events for a vacuum high voltage holding experiment”, proceedings of the 29th International Symposium on Discharges and Electrical Insulation in Vacuum (ISDEIV), 2021.

[8] M. H. Kushoro et al., “Characterization of vacuum HV microdischarges at HVPTF through x-ray bremsstrahlung spectroscopy”, Journal of Instrumentation, vol. 17 (1), January 2022.

[9] F. Sauli, “The gas electron multiplier (GEM): operating principles and applications”, Nucl. Instrum. Methods Phys. Res. A, vol. 805, pp. 2-24, January 2016.

[10] G. Croci et al., “nGEM fast neutron detectors for beam diagnostics”, Nucl. Instrum. Methods Phys. Res. A, vol 720, pp. 144-148, August 2013.

[11] S. Cancelli et al., “Development of a ceramic double thick GEM detector for transmission measurements at the VESUVIO instrument at ISIS”, Journal of Instrumentation, vol. 16, June 2021.

[12] A. Muraro et al., “MBGEM: a stack of borated GEM detector for high efficiency thermal neutron detection”, European Physical Journal Plus, vol. 136, pp. 1-14, July 2021.

[13] M. Chernyshova et al., “Development of GEM detector for tokamak SXR tomography system: preliminary laboratory tests”, Fusion Engineering and Design, vol. 123, pp. 877-881, November 2017.

[14] A. Muraro et al., “Development and characterization of a new soft x-ray diagnostic concept for tokamaks”, Journal of Instrumentation, vol. 14 (8), August 2019.

[15] F. Caruggi et al., “Performance of a triple GEM detector equipped with Al-GEM foils for x-rays detection”, Nucl. Instrum. Methods Phys. Res. A, vol. 1047, February 2023.

[16] G. Corradi, F. Murtas and D. Tagnani, “A novel high-voltage system for a triple GEM detector”, Nucl. Instrum. Methods Phys. Res. A, vol. 572, pp. 96-97, March 2007.

[17] A. Pezzotta et al., “GEMINI, a CMOS 180 nm mixed-signal 16-channel ASIC for triple-GEM detectors readout”, 2015 IEEE SENSORS, pp. 1-4, December 2015.

[18] S. Cancelli et al., “Electronic readout characterisation of a new soft x-ray diagnostic for burning plasma”, Journal of Instrumentation, vol. 17, August 2022.

Published by IOP Publishing for Sissa Medialab

Received: *October 25, 2023*
Accepted: *December 11, 2023*
Published: *February 2, 2024*

International Workshop on Imaging
Varenna (Lake Como), Italy
26–29 September 2023

Development of a Triple-GEM detector with strip readout and GEMINI chip for X rays and neutron imaging

F. Caruggi[a,b,*] **A. Celora**[a] **S. Cancelli**[a,b] **G. Gorini**[a,b,c] **G. Grosso**[c] **F. Guiotto**[d] **A. Muraro**[c] **E. Perelli Cippo**[c] **M. Petruzzo**[a] **O. Putignano**[c] **M. Tardocchi**[b,c] **L.S. Giarratana**[e] **and G. Croci**[a,b,c]

[a] *Dipartimento di Fisica "G. Occhialini", University of Milano-Bicocca, Piazza della Scienza 3, Milano, Italy*
[b] *INFN Sezione Milano-Bicocca, Piazza della Scienza 3, Milano, Italy*
[c] *Istituto per la Scienza e Tecnologia dei Plasmi, CNR, via Cozzi 53, Milano, Italy*
[d] *Dipartimento di Fisica, Università di Padova, via F. Marzolo 8, Padova, Italy*
[e] *Ospedale dei Bambini "Vittore Buzzi", ASST Fatebenefratelli Sacco, via Castelvetro 32, Milano, Italy*

E-mail: f.caruggi@campus.unimib.it

Abstract: Thermal neutron imaging can be a useful tool in the study of the internal structure of an object. The different attenuation properties of the materials with respect to X rays give rise to different interactions and the result is a complementary non-destructive analysis, which can provide important additional information. This technique has been successfully employed in different areas of work, especially in material science and cultural heritage studies. This paper describes the development of a new detection system and its characterization performed with X ray emissions. The system features the use of a gaseous detector, based on the Gas Electron Multiplier technology, and a fully digital electronic readout, with a combination of custom-made ASICs (called GEMINI) and FPGA boards, enabling fast single photon counting. The detector can be thus used directly for X ray imaging, while the addition of a suitable converter in its active volume will allow for detection of neutrons and for reconstruction of their tracks. The readout system is based on a x-y strip structure and features the reconstruction of single events through the center of mass methodology, allowing for accurate tomography, with sub-mm spatial resolution, in combination with sub-ms time resolution and high rate capabilities (up to MHz/mm^2).

Keywords: Inspection with neutrons; Inspection with x-rays; Micropattern gaseous detectors (MSGC, GEM, THGEM, RETHGEM, MHSP, MICROPIC, MICROMEGAS, InGrid, etc); CMOS readout of gaseous detectors

*Corresponding author.

https://doi.org/10.1088/1748-0221/19/02/C02015

Contents

1 **Introduction** 1

2 **STRIP-GEM detector** 1

3 **Detector characterization** 2

4 **Bone imaging** 3

5 **Conclusions and perspectives** 5

1 Introduction

Imaging techniques have become widespread and much useful in various fields of study, allowing for non-destructive investigation of different samples, especially in material science [1] and cultural heritage [2, 3] studies. In this context, both X-rays and neutrons are employed, giving complementary information about the observed objects. The research for faster and more accurate radiation detectors, together with the development of new and better data analysis software and reconstruction techniques are needed for the betterment of imaging studies. In this framework, detectors based on the Gas Electron Multiplier (GEM) principle can be employed, both for X-rays and neutrons (exploiting suitable converters). This kind of detectors features great temporal resolution, high-rate capabilities and radiation hardness, combined with good spatial and energy resolution altogether. In the following, the description of the system and its working principle will first be presented, to then describe the characterization, as well as preliminary results of X ray imaging on different samples. Perspectives for the upgrade of the system for neutron detection will be presented as well.

2 STRIP-GEM detector

The gaseous detector developed in this work is based on the interaction of incoming X-rays with a mixture of Ar-CO2 (70–30%) in the active volume, with ionization and production of electrons. Gas Electron Multiplier (GEM) foils are sheets of kapton, 50 µm thick, metal-coated on both sides (5 µm layer of Copper), with a high-density pattern of biconical holes etched inside. [4] A microscope image of the hole patterns is shown on the left in figure 1. The application of a voltage difference between the two metal sides of the foil produces concentrated dipole electric fields in the holes, accelerating and multiplying the electrons in their passage. The use of multiple GEM foils in a cascade setup allow for high gains without too high voltage differences on the single foil. A scheme of the detector structure can be seen on the right in figure 1.

The signal is formed at the charge collection anode, featuring two perpendicular sets of 256 strips, with a pitch of 400 µm and separated by polymer ridges of 50 µm. The different width of the X and Y strips is optimized to obtain equal charge sharing on the two axes for each event. A scheme of the strip structure is shown in figure 2. The active area of the detector is approximately $10{\times}10\,\mathrm{cm}^2$.

2024 JINST 19 C02015

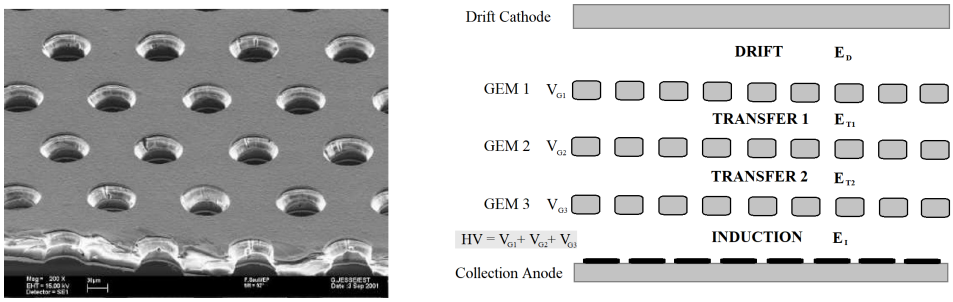

Figure 1. On the left, microscope image of the GEM foil hole pattern. On the right, schematics of the Triple-GEM detector.

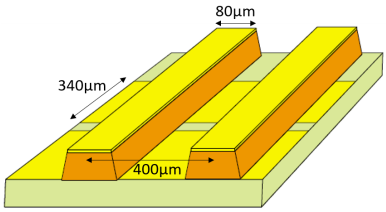

Figure 2. Schematics of the XY-strip structure of the anode.

The readout electronics is a fully digital chain composed of a combination of custom-made GEMINI ASICs [5] and FPGA boards, registering time of arrival, channel and time-over-threshold (ToT) for each event. The detector is a very fast and accurate single photon counter. Upon calibration, the information about ToT of each event can be translated in charge (and energy) of the incoming X-rays.

The application of a suitable converter, either deposited on the GEM foils [6] or in the active volume gas mixture [7], would allow for the detection of neutrons through the products of their conversion, with the same detector concept. The same system presented in this work will be modified to be employed for neutron imaging, following the same concept illustrated in [6].

3 Detector characterization

The optimal value for the detector parameters, namely the cumulative voltage difference across the foils (HV) and the threshold for each channel, have been found by analysis of the detector response in terms of counting rates. The HV parameter has been optimized to obtain full charge deposition of the incoming events (see [8] for details on the procedure), and the thresholds have been adjusted on the basis of the suppression of noise in the experimental environment. Charge calibration has been performed observing a single photo-emission peak (Ti fluorescence was used, with an energy of 4.5 keV), based on the variation of ToT values depending on the HV value applied, as described in [9].

Reconstruction of the single events is done through center-of-gravity method, with separate analyses of X and Y strips followed by event merging. This procedure imposes an operational limit on the high-rate capabilities of the detector, due to the production of artefacts in the image caused by the algorithm. Operation at high-rates has been studied with the use of stainless-steel masks. The detector was irradiated by X-rays, with covers on the window having different numbers of holes drilled at various locations. As an example, figure 3 shows the comparison of the image obtained

2024 JINST 19 C02015

at an average count rate on the detector of $6.81 \cdot 10^5$ Hz (on the left), where the two diagonal holes in the mask can be clearly seen with no other features in the 2D map, with respect to another image taken with the same mask at an average rate of $4.29 \cdot 10^6$ Hz (on the right). The software algorithm is not fully capable of reconstructing all events in the right places, and some X and Y events are wrongly matched, leading to the appearance of two additional holes in the opposite angles of the real ones. Additional dedicated studies will be focused on the algorithm to understand if it is possible to correct for these artefacts in some way.

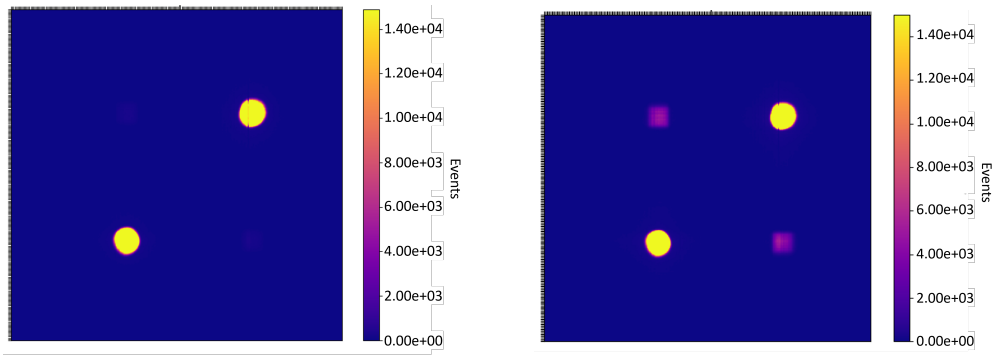

Figure 3. Example of production of artefacts in the reconstruction algorithm, with comparison of images taken at different rates ($6.81 \cdot 10^5$ Hz on the left, $4.29 \cdot 10^6$ Hz on the right).

4 Bone imaging

In order to demonstrate the capabilities of the new detector developed in this work, X-ray transmission imaging was performed on bone mock-ups. The experimental setup of the measurement can be seen in figure 4. The specimens were put in between the detector and the X-ray source. The X-ray tube was operated at a voltage of 10 kV and with a current of 5 µA. Irradiation lasted less than 10 seconds for each sample.

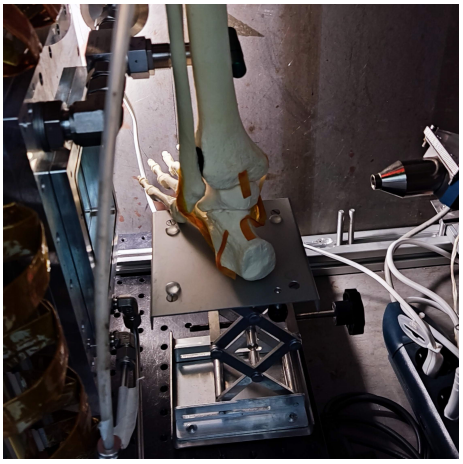

Figure 4. Experimental setup of the bone transmission measurements.

2024 JINST 19 C02015

Different bone-like structures were observed. Figure 5 shows the resulting images, obtained by plotting directly the data coming from the detector, with a simple normalization to the empty beam image (i.e. the count rate obtained without samples in between the X-ray gun and the detector). The color scales of the images were adjusted to obtain a visually pleasing results and were not result of contrast optimization or other post-processing operation.

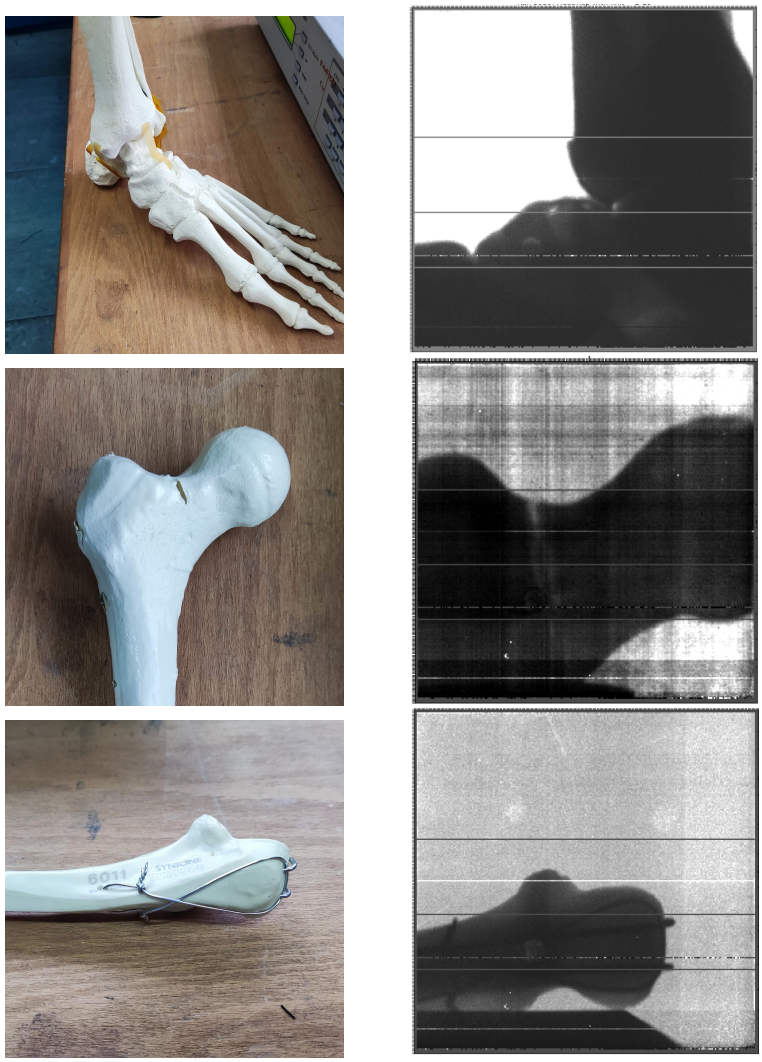

Figure 5. On the left, picture of the observed bone mock-ups. On the right, corresponding images captured with the detector.

The images show qualitatively the good spatial resolution that can be achieved with the use of the XY-strip anode structure, being able to distinguish structures smaller than a millimeter. It is to be noted that the measurement was only a preliminary observation: the parameters of the setup, namely voltage and current of the X-ray gun, as well as distance and position of the sample and the detector, can be subject to optimization to lead to better results. Additional dedicated studies will be also performed to quantify more accurately the spatial resolution obtainable.

2024 JINST 19 C02015

5 Conclusions and perspectives

In this work, the development of a new GEM-based detector with a XY-strip anode pattern was presented. The properties of this kind of detector offer good perspectives for the analysis of different samples through X-ray and neutron imaging techniques. The characterization of the detector was presented, and a first demonstration of its capabilities was shown.

Future perspectives include the possibility of advanced studies on high-rate measurements and optimized imaging experiments. In addition, the upgrade of the system with the addition of a suitable converter, to be used for neutron imaging, is under way.

References

[1] N. Kardjilov, I. Manke, A. Hilger, M. Strobl and J. Banhart, *Neutron imaging in materials science*, *Mater. Today* **14** (2011) 248.

[2] D.D. Martino et al., *A neutron diffraction and imaging study of ancient iron tie rods*, 2018 *JINST* **13** C05009.

[3] M. Dinca and D. Mandescu, *Thermal neutron tomography for cultural heritage at inr*, *Phys. Procedia* **69** (2015) 646.

[4] F. Sauli, *The gas electron multiplier (GEM): Operating principles and applications*, *Nucl. Instrum. Meth. A* **805** (2016) 2.

[5] A. Pezzotta et al., *GEMINI, a CMOS 180 nm mixed-signal 16-channel ASIC for Triple-GEM detectors readout*, in the proceedings of the *IEEE SENSORS 2015*, Busan, Republic of Korea (2015), p. 1–4 [DOI:10.1109/ICSENS.2015.7370468].

[6] A. Muraro et al., *Mbgem: a stack of borated gem detector for high efficiency thermal neutron detection*, *Eur. Phys. J. Plus* **136** (2021) 1.

[7] S. Cancelli et al., *Characterisation of N2-GEM: a beam monitor based on Ar-N_2 gas mixture*, 2023 *JINST* **18** C05005.

[8] F. Caruggi et al., *Performance of a triple GEM detector equipped with Al-GEM foils for X-rays detection*, *Nucl. Instrum. Meth. A* **1047** (2023) 167855.

[9] A. Muraro et al., *Development and characterization of a new soft x-ray diagnostic concept for tokamaks*, 2019 *JINST* **14** C08012.

2024 JINST 19 C02015

Received: 10 July 2024 | Revised: 1 November 2024 | Accepted: 16 December 2024

High Voltage

DOI: 10.1049/hve2.70042

国家电网 STATE GRID 中国电力科学研究院有限公司 CHINA ELECTRIC POWER RESEARCH INSTITUTE

The Institution of Engineering and Technology

WILEY

ORIGINAL RESEARCH

Analysis of micro-discharges fine dynamics via x-ray detection on the high voltage Padova test facility experiment

Federico Caruggi[1,2] | Gabriele Croci[1,2,3] | Stephanie Cancelli[1,2,3] | Agostino Celora[1] | Antonio De Lorenzi[4] | Michele Fincato[4] | Giuseppe Gorini[1,2,3] | Giovanni Grosso[3] | Federico Guiotto[5,6] | Enzo Lazzaro[3] | Luca Lotto[7] | Nicola Pilan[5] | Oscar Putignano[3] | Silvia Spagnolo[4,5] | Marco Tardocchi[1,3] | Andrea Muraro[2,3]

[1]Department of Physics "G. Occhialini", University of Milano-Bicocca, Milan, Italy

[2]INFN, Sezione Milano-Bicocca, Milan, Italy

[3]Istituto per la Scienza e Tecnologia dei Plasmi, CNR-ISTP, Milan, Italy

[4]Istituto per la Scienza e Tecnologia dei Plasmi, CNR-ISTP, Padova, Italy

[5]Consorzio RFX (CNR, ENEA, INFN, Università di Padova, Acciaierie Venete SpA), Padova, Italy

[6]Centro Ricerche Fusione (CRF) - University of Padova, Padova, Italy

[7]Dipartimento di Ingegneria Industriale – DII, Università di Padova, Padova, Italy

Correspondence
Federico Caruggi.
Email: f.caruggi@campus.unimib.it

Associate Editor: Zhiyuan Liu

Funding information
EUROfusion, Grant/Award Number: 101052200

Abstract

The high voltage Padova test facility (HVPTF) is an experiment set in Padova, Italy, operating in the framework of the Neutral Beam Test Facility project of the International Thermonuclear Experimental Reactor (ITER). One of the purposes of HVPTF is to study the phenomenology of discharge events occurring between electrodes at high voltage differences over long vacuum gaps, which is crucial in the development of the neutral beam injector foreseen for ITER. The facility hosts a cylindrical vacuum vessel with stable pressure control, where two electrodes of different possible geometries can be mounted. Two independent power supplies allow for total voltage differences up to 800 kV_{DC} with adjustable gap widths up to 250 mm. Among the diagnostics, a gas electron multiplier (GEM) detector is installed for acquisition of x-ray emission on a radial line of sight of the vessel. This paper presents a study of the experimental sessions featuring stainless-steel needle-plane electrodes. The analysis is based on the GEM data, in relation to the information on current and voltage of the two power supplies. The events are characterised in terms of both temporal and spatial evolution, providing sequential emission profiles with spatial resolution of tens of millimetres on timescales of the order of hundreds of nanoseconds.

1 | INTRODUCTION

In the framework of the research for nuclear fusion power production, the International Thermonuclear Experimental Reactor (ITER) is under construction in Cadarache, France. The aim for this device is to demonstrate the feasibility of energy production through magnetically confined nuclear fusion reactions with a Q-value of 10. Among the external heating systems needed by the plasma, the use of neutral beam injectors (NBI) is foreseen. The device is designed to perform acceleration of a negative ion beam with a current of 40 A up to energies of 1 MeV, followed by its neutralisation and direct

injection in the plasma, where energy can be transferred through collisions. ITER requires two NBIs, each one to deliver 16.7 MW power for up to 3600 s [1].

In the context of the Neutral Beam Test Facility, the programme responsible for the research and development of the NBI, the megavolt ITER injector concept advancement (MITICA) experiment is under commissioning in Padova, Italy [2]. It consists of a full-scale prototype of the NBI, featuring the use of five accelerating grids in vacuum (each gap with 200 kV voltage difference) to obtain the high beam energies required. A representation of the device is displayed in Figure 1.

One of the major challenges in its operation is thus high voltage holding capabilities over long vacuum gaps. The main issue in this context is the occurrence of electrical discharges, phenomena observable as spikes of current concurrent with voltage drops that can prevent the system correct operation. In this work, discharges are classified either as micro-discharges, which are those from which the system can recover autonomously, or breakdowns, more violent occurrences where the system fully switches off, and manual intervention is needed to restore operation. Events of the latter kind can cause serious damage to the equipment as well. The study of micro-discharges and breakdown precursors can be of help in the design of a control system for breakdown prevention and safe operation of the MITICA accelerator.

In order to gain a better understanding of the phenomenology of discharges, the high voltage Padova test facility (HVPTF) experiment has been set up in support of MITICA operations [3]. It consists of a large vacuum vessel (about 2.4 m^3) in which two electrodes are mounted. Electrodes of various shapes can be used to study different configurations, and their distance can be varied up to 250 mm. Two independent power supplies provide voltage differences up to 800 kV_{DC} with the possibility to use single or double polarity. Current and voltage of both power supplies are monitored with a sampling frequency of 100 Hz together with the pressure inside the chamber (measured by different instruments located in multiple positions around the wall of the vacuum vessel). Additional diagnostics feature a residual gas analyser for the composition of the gas mixture going out of the chamber and multiple cameras for various light spectrum regions and with various sampling rates. During operation, the vessel is also characterised by emission of x-rays, mainly produced by Bremsstrahlung radiation of the electrons extracted and accelerated in the discharges. These are monitored as well, with the combined use of inorganic scintillators and, since 2022, gas electron multiplier (GEM)-based detectors. A picture of the rear of the HVPTF vessel with the scintillators is shown in Figure 2. Correlations between the dynamics of the power supply currents and the x-rays have been observed in the past already [4, 5]. Because of the higher speed of the signal, a more detailed analysis of the emitted radiation can be of help in the search for breakdown precursors, and real-time analysis of the emission profiles can possibly aid in the design of a feedback-loop control system for the experiment with the aim of granting safe operative conditions in the context of the MITICA experiment and the ITER NBI as well.

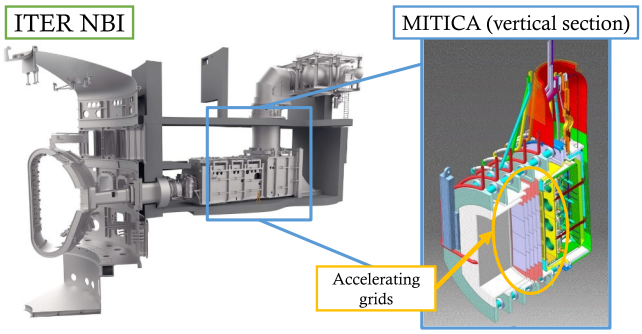

FIGURE 1 View of a 3D rendering of the ITER NBI and section of MITICA. ITER NBI, International Thermonuclear Experimental Reactor neutral beam injector and MITICA, megavolt ITER injector concept advancement.

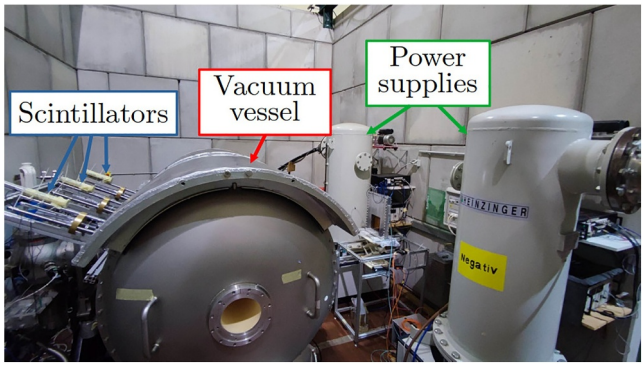

FIGURE 2 Picture of the high voltage Padova test facility vacuum vessel and setup.

2 | GEM DETECTORS

A GEM foil [6] is a thin sheet of kapton (50 μm thick), with both sides covered by a layer of metal coating (commonly Cu, 5 μm thick but Al can be the choice as well [7]), in which a series of micro-holes is etched with a high density pattern. The application of a voltage difference between the two metal faces produces high dipole fields in the holes. This property can be exploited for electron multiplication and signal amplification.

A GEM detector is a gaseous detector in which the signal is generated by the gas ionisation in the drift region of the active volume caused by the incoming radiation (x-rays in this case). The extracted electrons are accelerated towards the foils by the electric field and are multiplied as they traverse the holes. Multiple foils in cascade are commonly employed in order to achieve high gain levels without having to apply too high voltage differences across a single foil. The signal is collected by a pixelated anode at the end, providing information about the spatial distribution of the incoming radiation. A schematic representation of the detector is shown in Figure 3, referencing three GEM foils which delimit four volumetric regions, and the different values of voltage imposed on each channel of the HV module. The detector employed in this work consists of a

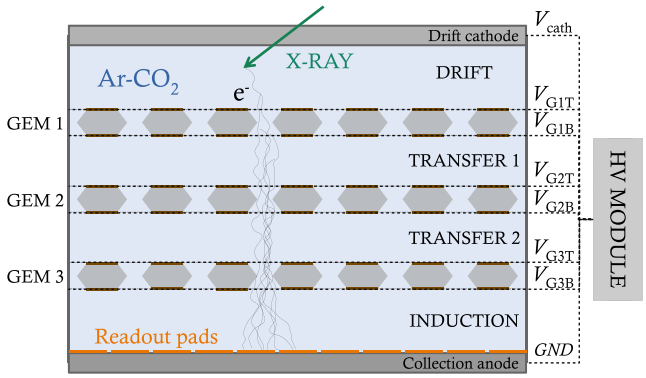

FIGURE 3 Schematic representation of a triple GEM detector. GEM, gas electron multiplier.

stack of three foils metal-coated with Cu. It contains a mixture of Ar-CO_2 70%–30% and the collection anode is composed by 256 pads, 6 × 6 mm^2 each with a total active area of 100 cm^2.

The detector is coupled with a digital readout chain made by the combination of custom-made application-specific integrated circuits (ASICs) named GEM integrated interface (GEMINI) [8] and field programmable gate arrays, able to record, for each event, the timestamp, the incidence position on the anode (each pixel, or pad, correspond to one channel) and some information about energy through the use of the time-over-threshold measurement (more details can be found in Muraro et al. and Cancelli et al. [9, 10]). The detector can be thus used for fast and accurate single photon counting. The system features both great temporal resolution (< 1 ms) and good spatial resolution (in the order of few mms), together with a decent energy resolution (20% at 6 keV).

GEM-based detectors are especially useful for charged particle tracking and x-ray detection, for various applications [11, 12], but with the use of suitable converters they can also be adapted for fast or thermal neutron detection [13–15].

It must be mentioned that unfortunately one of the ASICs connected to the detector was damaged during the experimental runs, thus the images of the spatial distribution of the radiation reported in the following sections have always one-quarter (the top left one) void of counts.

2.1 | Data clusterisation

In common practice, the analysis of data collected from a pixelated anode, as the one used in the GEM detector, foresees a process called clusterisation. The passage of a single photon in the active volume produces generally more than one electron, so that multiple channels collect charge for the same event. The clusterisation process consists in the aggregation of the signals of the single pads, depending on timestamps and position, to reduce them to a single event corresponding to the photon with its total deposited charge. A first analysis of the data collected in this work, however, showed signs that the detector reached counting saturation during the discharges, so that it got paralysed (meaning that it lost some events) or, more probably, it reached the conditions of pile-up on the events (meaning that multiple events are recorded as a single one). Because of this, the analyses presented in the following were performed without clusterisation of the data, meaning that for each time a pixel collected charge, a separate event was recorded. The intensity of the x-ray signal in the time traces of this text will thus be represented as arbitrary units instead of number of incoming x-rays. The pile-up issue can additionally cause overflow of the time-over-threshold measurements, so that the information cannot be converted accurately to charge and energy values. For this reason, in the following analyses, the radiation spectra were not taken into account.

3 | DATA COLLECTION AND ANALYSIS

During the experimental sessions considered, the detector was installed on a radial line of sight of the HVPTF vacuum vessel, behind a Beryllium window which allows passage of the x-rays. The flange has a support for a Pb collimator to be mounted in order to reduce the incoming flux of particles on the detector but for the data collected for this work the full flange width was used (13 mm diameter). A schematic of the configuration is displayed in Figure 4, and a picture of the setup in Figure 5. Moveable components (represented in the scheme by the double dashed grey arrows) of the GEM support allowed for a variation of the range of view, depending on the distance between the detector and the collimator (the further away the detector is placed, the more restricted is the view range and the more magnified the objects are seen).

A stainless steel needle, 29 mm long, was used as cathode, whereas the anode was a plane of 108 mm diameter, also made of stainless steel. The distance between the electrodes was fixed at 36 mm. A picture of the electrodes mounted inside the chamber is shown in Figure 6. During the experimental sessions examined, single polarity was used, which means that the cathode was brought at negative voltages and the anode was kept at ground.

The experimental procedure consisted in the application of successive voltage steps in order to achieve what is called electrode conditioning, which refers to the development of the capabilities of the electrodes themselves to sustain high voltage differences without breakdowns (a more detailed description of the process can be found in Pilan et al. [16]). In this instance, the GEM detector was able to observe the emission of Bremsstrahlung x-ray radiation produced by the electrons extracted during the discharges and impinging on solid obstacles, giving information about the dynamics of the phenomena. A needle was chosen as cathode in order to have more favourable conditions for electron extraction (because of the strongly divergent electric field), hence the occurrence of micro-discharges, mainly with the aim of obtaining large datasets in relatively short time for extensive analyses. Examples of additional results obtained for the same experimental sessions, not mentioned in this work, were presented in Caruggi et al. [17]. All the studies described here were performed with the use of a custom data analysis software developed by

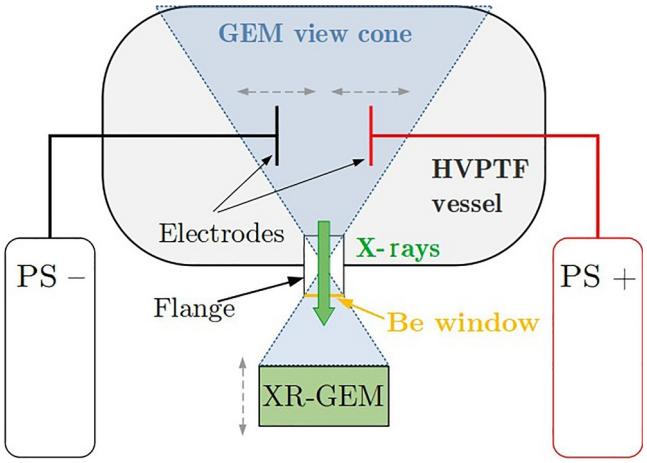

FIGURE 4 Schematic representation of the GEM detector setup on HVPTF. GEM, gas electron multiplier and HVPTF, high voltage Padova test facility.

FIGURE 5 Picture of the gas electron multiplier detector installation.

the authors, tailored for the display of GEM detector data and for the comparison with the analogue signals of HVPTF.

3.1 | Time traces

The first analysis was performed on the temporal evolution of the x-ray emission collected by the detector with reference to

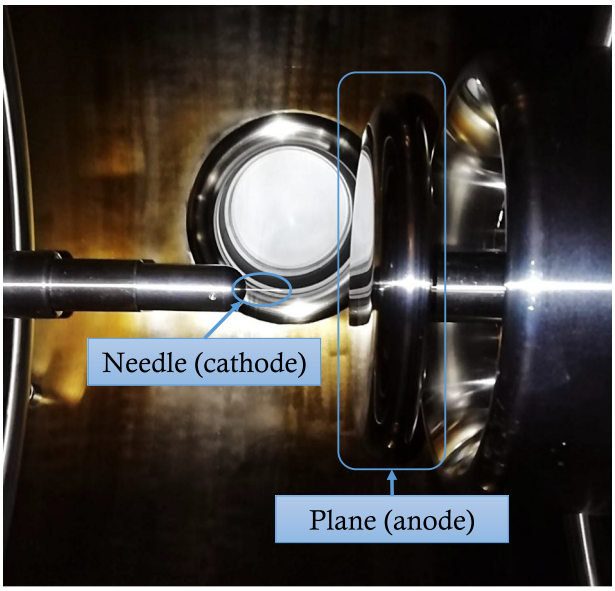

FIGURE 6 Picture of the electrodes inside the high voltage Padova test facility vessel.

the current and voltage signals coming from the analogue readout of the power supplies. A first view of a full conditioning ramp is displayed in Figure 7a, displaying current, pressure, voltage and x-ray signals. As can be seen, at the beginning of the steps the x-ray emission is absent, and it starts to be detected after reaching a high enough value of voltage on the negative electrode, approximately 120 kV. Following that, a continuous background of counts is recorded by the detector, interspersed with signal spikes, occurring in correspondence of spikes in the current signal and drops of voltage. These are the micro-discharges mentioned above, superimposed, for what concerns the x-ray signal, to the continuous dark current emission developing between the electrodes (i.e. the Fowler–Nordheim emission current), a phenomenon analogous to what is described in Spada et al. [18].

A more detailed view is shown in Figure 7b which better highlights the strong correlation between the analogue and x-ray signals, in the sense that, for each current peak and voltage drop, there is a corresponding structure on the x-ray emission profile (a fact that can be seen here more clearly with respect to the full-ramp picture). As previously mentioned, these correlations were already observed in the past (see e.g. [4, 5]) and they can be justified considering that the majority of the x-rays observed come from Bremsstrahlung radiation of the electrons involved in the discharges.

In the final section of the ramp, the voltage value is kept constant to try and reach stability in the system (ideally the aim is a situation where micro-discharges are absent), and after the last voltage step the breakdown happens, meaning that the voltage drops too much for the system to recover, and the system itself shuts down. From the figures, we can also see that the system experiences an increase of pressure at the end of the conditioning ramp, where the micro-discharges are more frequent. This is possibly caused by gas desorption from

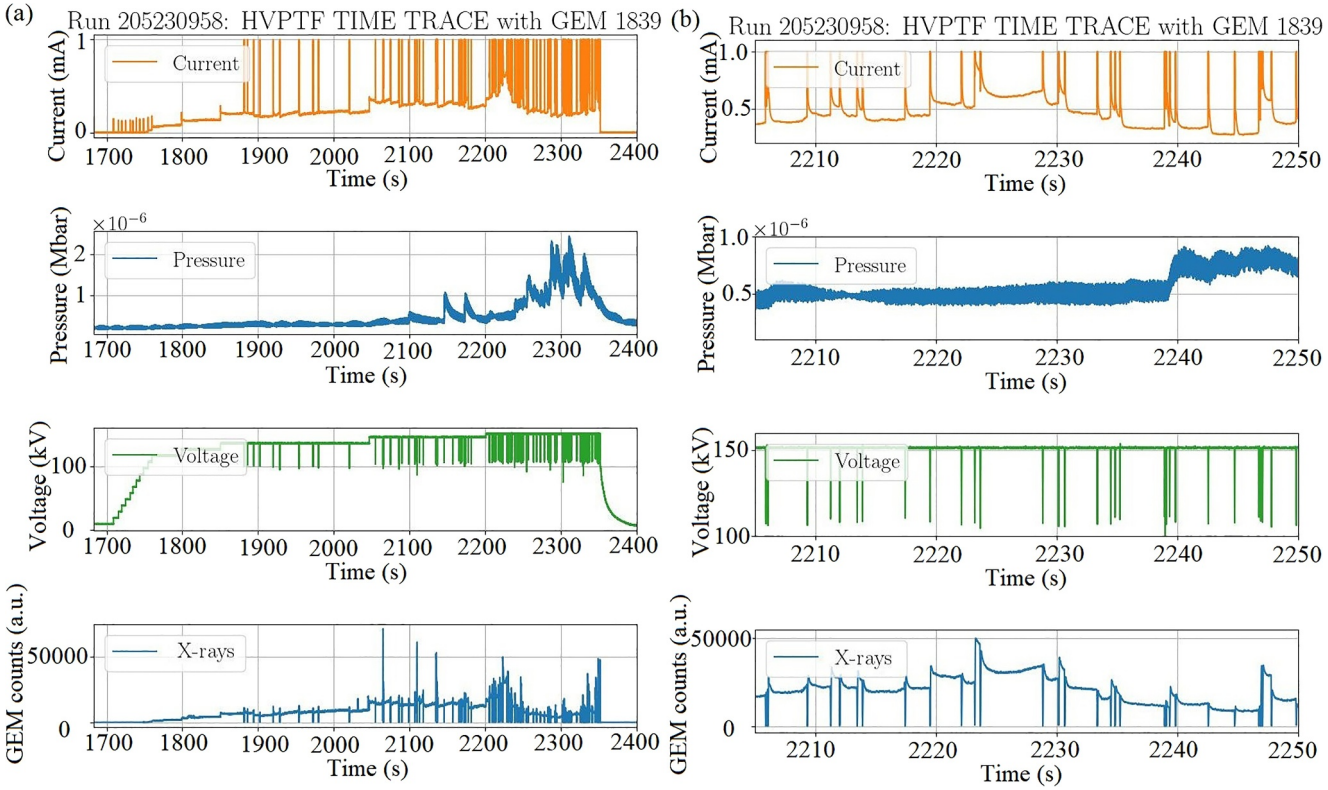

FIGURE 7 Time evolution of analogue and x-ray signals during the experimental session studied. (a) View of the signals during the full 700 s ramp. (b) Zoom of the graph in (a) from 2205 to 2250 s.

the electrode surfaces caused by the discharges themselves [19].

Details on an even smaller timescale are shown in Figure 8, with plots showing current and voltage signals from the analogue system and x-ray signal from the GEM detector, during a single micro-discharge (over a 0.14 s time window).

Firstly, we can see that the micro-discharge, appearing in Figure 7 as a single point spike, has more structure underneath: the current signal shows two rising features, one right after another. Here, it is assumed that the first one corresponds to the micro-discharge spike itself, whereas the other is intrinsically produced by the system, needing to feed current to increase the voltage after its drop. It can be also seen that the analogue system alone is not enough to perform a detailed analysis of the phenomena, because of the limited full scale of the current measurement which caps at 1 mA and the sampling frequency which is quite low (100 Hz). Additionally, the fact that the current is measured at the power supplies implies that the signal is not really representative of what happens between the electrodes, because of the presence of additional elements in the interposed electrical circuit with their own contributions. Because of these issues, it becomes unfeasible to derive meaningful data about the dynamics of the micro-discharge from the analogue measurement alone. Analysis of the x-ray signal plot instead, with a denser binning, shows more features about the emission. The continuous background already

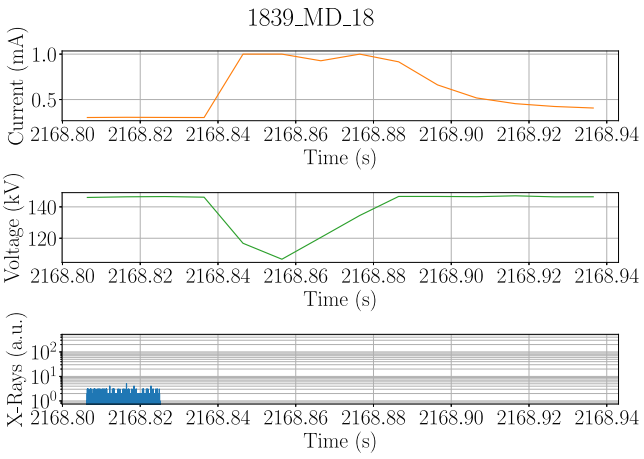

FIGURE 8 Time evolution of x-ray signal in a single micro-discharge with a 0.14 s window.

mentioned before is still present, but we can see that its intensity is much lower in relation to the signal spike during the micro-discharge. The latter appears again as a single short spike, after which the emission switches off until the voltage is brought back up to nominal value. The capability of the GEM detector to measure the spatial distribution of the incoming radiation can be also firstly exploited, as shown in Figure 9, to see that the continuous background (the picture shows the

cumulative events of a 10 s window) comes from a region where we expect to monitor radiation coming directly from the plane anode (a reference schematic is superimposed to show the expected positions of the electrodes in the view range of the GEM detector).

We can exploit the great temporal resolution capabilities of the GEM detector to have much lower sampling times and again look at the dynamics underneath what appears, on larger timescales, as a single spike. Figure 10a shows a plot of the evolution in time of x-ray radiation detected for a single micro-discharge with a sampling time of 100 ns, and new details appear. The plot shows firstly a peak with small intensity, bifurcated, which lasts for about 1 μs. This is followed by some silence (absence of counts of the detector), with a duration of approximately 2 μs, and then the real spike of high intensity. Here the limit of the detector can be seen, since the peak is not a single point but a capped rising feature. The maximum reached is about 400 units, corresponding to 4 Gcps for the digital acquisition chain. After the spike, we can see from the plot a lower intensity plateau, lasting for about 15 μs, followed by again absence of counts. This is the silence caused by the drop in system voltage and has a duration of about 20 ms, orders of magnitude longer with respect to the micro-discharge itself, as seen from the previous plot of Figure 8.

This observed dynamics is heavily consistent across all the micro-discharges analysed, so that the counts per bin can be summed up to have more statistics on the data taken into account. The resulting graph of the cumulative counts in time for a full conditioning ramp is shown in Figure 10b, and it can be seen that all the features just observed are still recognisable with a smoother plotted curve. The consistency was found also across the various conditioning ramps taken into account for this study, even if only a single set of data is presented here in detail for the sake of simplicity. Multiple consecutive conditioning ramps, among which the detector distance was changed, still showed the same dynamics in the time evolution of the signal, with the only difference being in the spatial distribution of the radiation (as mentioned before, with the view range and level of magnification depending on the position of the detector on the supports).

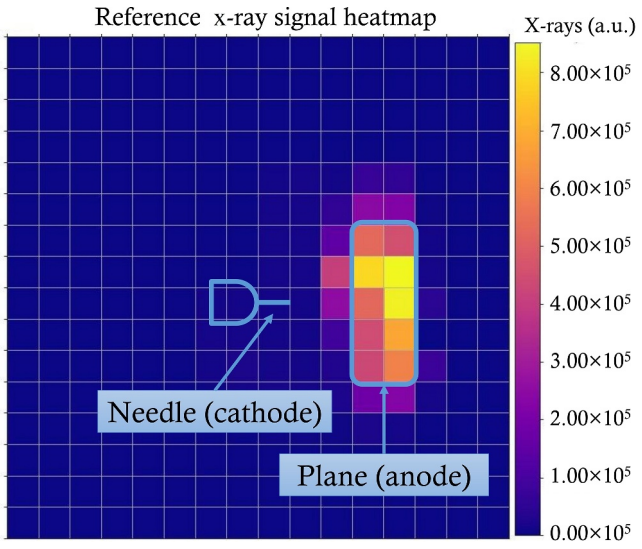

FIGURE 9 Heatmap of the x-ray detected for dark current signal (with a 10 s sampling window), with schematic representation of the expected placement of the electrodes.

3.2 | Space-time analyses

Following the first analysis, the capabilities of the GEM detector were exploited to perform a combined study of the distribution of events in both space and time, looking at the time dynamics of the signal collected by each channel and grouping together pads with the same evolution. Again, the counts from all the micro-discharges of a conditioning ramp are summed to achieve better statistics. The analysis shows the presence of three of these groups, the characteristic dynamics of which are illustrated in the following. Figure 11a displays the reference time trace with the three regions highlighted in different colours, and Figure 11b shows the reference image of the dark current counts to identify the position of the pads in

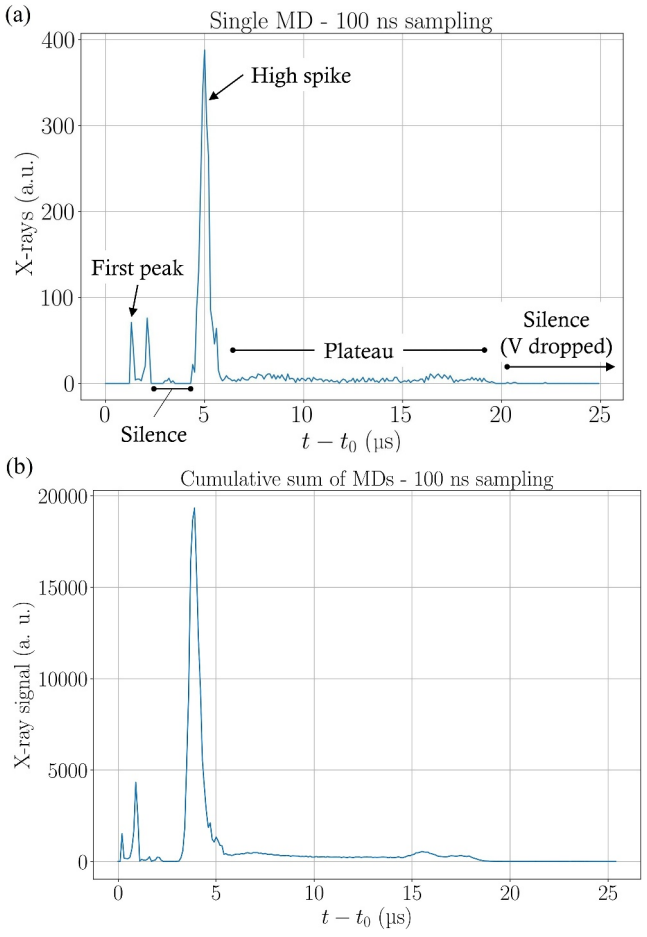

FIGURE 10 Time evolution of x-ray signal in the micro-discharges, with reference to an arbitrary t_0 chosen as start of the discharge itself. (a) Single micro-discharge view. (b) Cumulative signal across all micro-discharges.

the GEM view range, with the same colour code for the groups as the former (the yellow pad group is made of all the pads that have no coloured border).

The pixels that have a line of sight towards the chamber walls (surrounding the space where the electrodes are placed) show signal only during the first 5 μs approximately, contributing only to the first bifurcated peak and the full spike (Figure 12a). The pixels looking at the plane electrode instead, which are the ones detecting the continuous background of counts (dark current signal) during the whole run, exhibit no signal during the spikes, and they have counts only after the 5 μs mark. The apparent plateau of the previous subsection is shown instead as a gradual descent (Figure 12b), pertaining only to some pads that have a line of view of the space immediately around the plane. Two final increments of counts can be seen on the time trace of the pixels looking directly at the centre of the plane electrode (Figure 12c).

The consistency of the time dynamics across all the micro-discharges mentioned before also allows to have enough statistics to produce the images of the single frames corresponding to the cumulative time dynamics plot. The reference time trace is shown once again in Figure 13, with regions highlighted similarly to the previous analysis. In this case, there are four distinct colours as the first bifurcated spike shows a different dynamics with respect to the high peak. Figures 14–17 show the sequences of frames for the different regions of the time trace, calculated for the time values

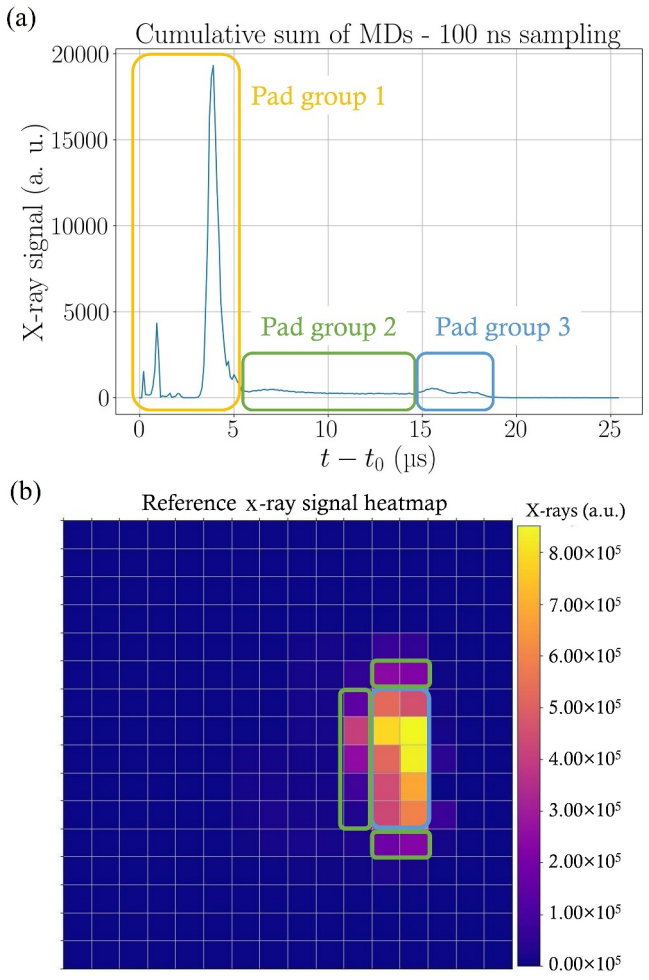

FIGURE 11 Space-time analysis of the micro-discharges. (a) Reference time evolution of all micro-discharges. (b) Heatmap of incoming radiation, with the groups distinguishable by colours.

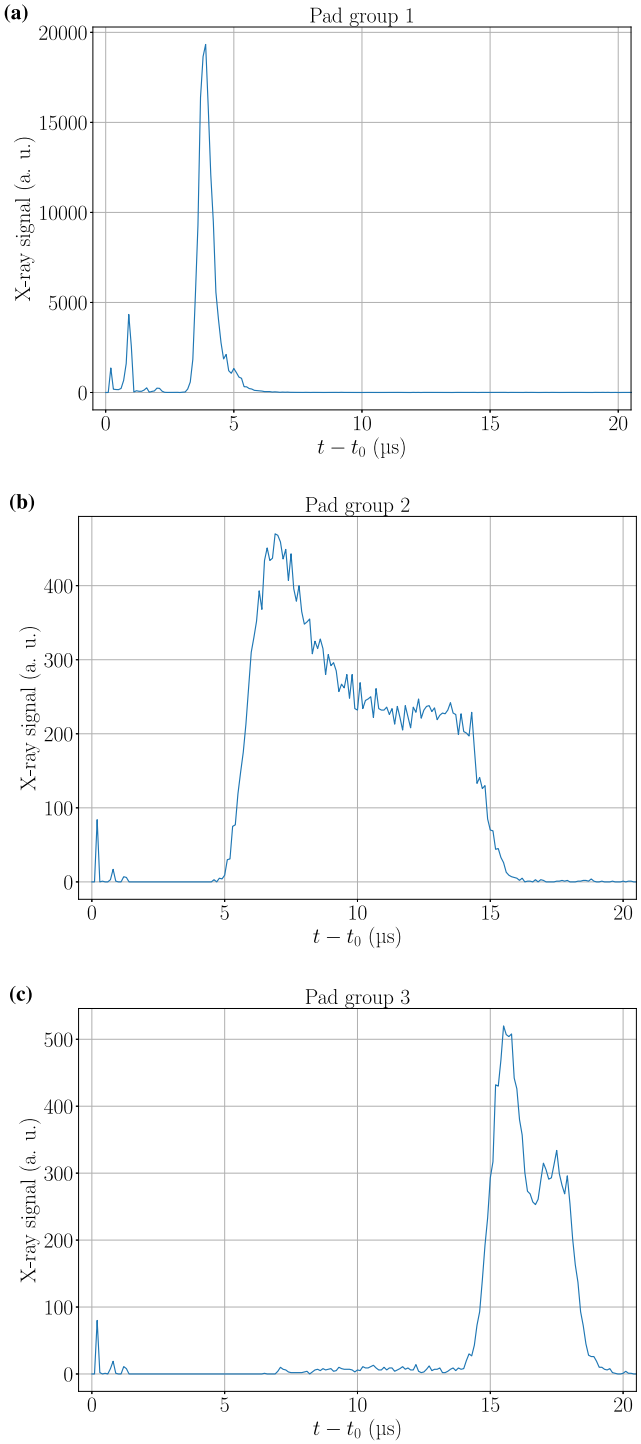

FIGURE 12 Time evolution of x-ray signal for the three pad groups for the cumulative micro-discharges. (a) Chamber pads. (b) Around-plane pads. (c) Centre-plane pads.

indicated by the dashed lines in the main picture, and with borders of the corresponding colour. In particular, Figure 14, corresponding to the bifurcated spike, shows that the emission of x-rays, initially located around the anode, diverges outward to the edges of the detector view range. This phenomenon can be interpreted as the fact that the electrons which emit Bremsstrahlung radiation are deviated from their path towards the anode to go towards the chamber walls and surroundings.

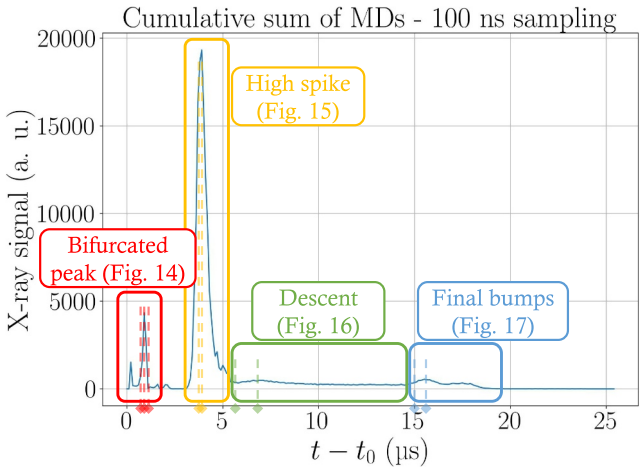

FIGURE 13 Reference time evolution of all micro-discharges with the four groups distinguishable by colours, and reference to Figures 14–17. Dashed lines with arrows correspond to the temporal marks of the frames selected for the heatmaps.

This is observed twice, in correspondence to the two bifurcations of the spike. Figure 15, taken from frames in the high peak, shows contribution to the signal from all the pixels except for those looking at the plane electrode. During the descent, as mentioned before and as shown in Figure 16, only the pads with lines of sight around the plane have counts, as if the electrons were hitting a different larger surface around it. After the 15 µs mark, as presented in Figure 17, the radiation is back on the pixels receiving signals from the central part of the plane, as is the case of the dark current signal, just before the micro-discharge is over with the event counts dropping to zero.

3.3 | Considerations

The dynamics of the micro-discharges that were observed and presented above can suggest a combination of the effects, for example, of virtual anode and plasma sheath. The dynamics of the electron trajectories can be inferred from the Bremsstrahlung x-ray emission profiles as previously mentioned. From the GEM-collected data we can thus deduce that, at the beginning of the micro-discharges, electrons that normally are going towards the anode are deviated on their path towards the chamber walls. This, as previously mentioned, can be the effect of a local modification of the voltage around the plane electrode (see Figure 14). It is worth pointing out that, as already stated, the experimental session was performed in single

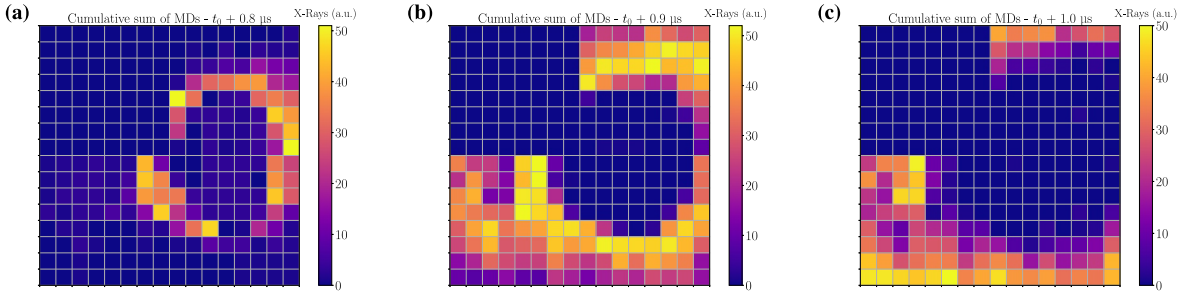

FIGURE 14 Evolution of the spatial distribution of the detected radiation during the bifurcated peak of the micro-discharge. (a) Frame taken at 0.8 µs. (b) Frame taken at 0.9 µs. (c) Frame taken at 1 µs.

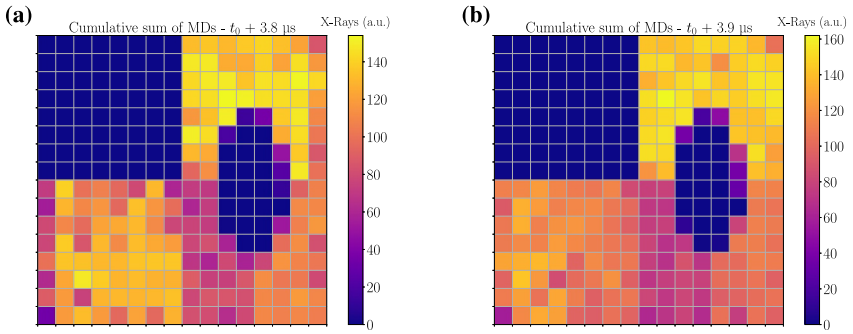

FIGURE 15 Evolution of the spatial distribution of the detected radiation during the high spike of the micro-discharge. (a) Frame taken at 3.8 µs. (b) Frame taken at 3.9 µs.

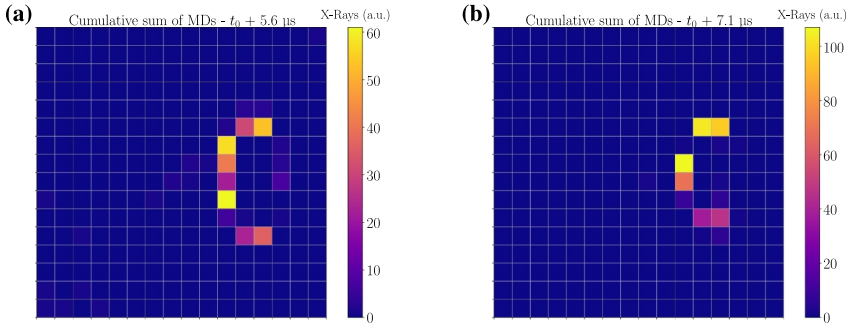

FIGURE 16 Evolution of the spatial distribution of the detected radiation during the descent of the micro-discharge. (a) Frame taken at 5.6 µs. (b) Frame taken at 7.1 µs.

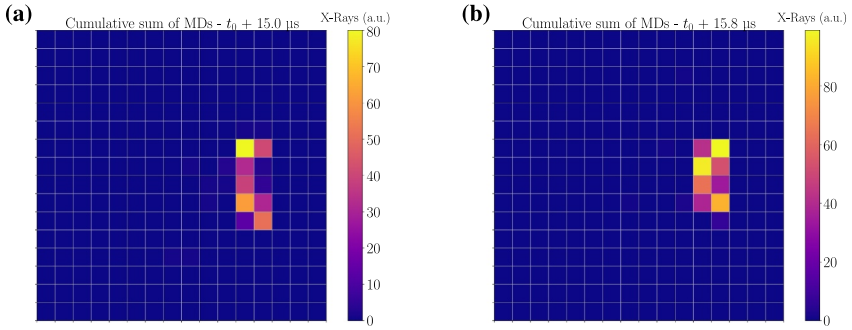

FIGURE 17 Evolution of the spatial distribution of the detected radiation during the final bumps of the micro-discharge. (a) Frame taken at 15 µs. (b) Frame taken at 15.8 µs.

polarity, so that the anode was kept at ground, the same potential level of the surrounding structures in the chambers (walls and electrode supports). This could imply that the variation of local electric field around the plane electrode needed to achieve the deviation effect is not very high. Secondly, we observed from the data that, during the actual spike of emission of the micro-discharge, no x-ray emission is arriving at the GEM detector from the planar anode (as seen in Figure 15). This could indicate the presence, in this time frame, of a plasma layer around the plane electrode itself, which prevents electrons from impinging directly on the plane and stops the Bremsstrahlung radiation going out of the chamber.

4 | CONCLUSIONS AND FUTURE PERSPECTIVES

In this work the analyses performed on the x-ray data collected with the GEM detector installed at HVPTF in 2022 were presented. The needle-plane electrode configuration was observed in order to have large statistics on the micro-discharge occurrence. The study was related to successive high voltage ramps corresponding to conditioning procedures for the electrodes.

The analysis of the temporal evolution of the incoming radiation was useful to identify the microscale dynamics of the emission, becoming visible below the µs sampling time, and common features were made recognisable across all the micro-discharges considered. Additionally, the capabilities of the GEM detector were exploited for a combined space-time analysis, in which the evolution of the spatial distribution of the emission was observed and the contributions of the different channels of the detector commented.

In the context of future analyses concerning HVPTF, a simulation code is under development, based on the calculation of the voltage profiles in the vacuum chamber (with different electrode configurations) and the transport of electrons in said profiles. This could help in an attempt of reproduction of the observed dynamics, in order to understand the conditions that lead to the occurrence of the various phenomena observed and develop a theory to justify them. Additionally, new experimental sessions have been set up at the facility, in order to study different electrode configurations as well (sphere-plane, for example), and a new GEM detector is under development to take the place of the previous one. The new concept has an anode with smaller pads in the middle of the active area (3×3 mm^2), in order to avoid detector saturation and to be able to analyse the micro-discharge spikes in finer detail.

ACKNOWLEDGEMENTS

This work has been carried out within the framework of the EUROfusion consortium, funded by the European Union via the Euratom Research and Training Programme (Grant Agreement No 101052200—EUROfusion). Open access

publishing facilitated by Universita degli Studi di Milano-Bicocca, as part of the Wiley - CRUI-CARE agreement.

CONFLICT OF INTEREST STATEMENT

The authors declare no conflicts of interest. Views and opinions expressed are however those of the authors only and do not necessarily reflect those of the European Union or the European Commission. Neither the European Union nor the European Commission can be held responsible for them. This work was carried out within the framework of the ITER RFX Neutral Beam Testing Facility (NBTF) Agreement and received funding from the ITER Organisation. The views and opinions expressed herein do not necessarily reflect those of the ITER Organisation. This work has been carried out in collaboration and financial support of INFN-Group 5 (Technology Research), in the framework of the PLASMA4BEAM2 experiment.

DATA AVAILABILITY STATEMENT

The data that support the findings of this study are available from the corresponding author upon reasonable request.

ORCID

Federico Caruggi https://orcid.org/0000-0002-5480-1327

REFERENCES

1. Hemsworth, R.S., et al.: Overview of the design of the ITER heating neutral beam injectors. New J. Phys. 19(2), 025005 (2017)
2. Toigo, V., et al.: The PRIMA Test Facility: SPIDER and MITICA test-beds for ITER neutral beam injectors. New J. Phys. 19(8), 085004 (2017)
3. De Lorenzi, A., et al.: HVPTF—the high voltage laboratory for the ITER neutral beam test facility. Fusion Eng. Des. 86(6), 742–745 (2011)
4. Spagnolo, S., et al.: Characterization of x-ray events for a vacuum high voltage holding experiment. In: 2020 29th International Symposium on Discharges and Electrical Insulation in Vacuum (ISDEIV), pp. 58–61. IEEE, (2021)
5. Kushoro, M.H., et al.: Characterization of vacuum HV microdischarges at HVPTF through x-ray bremsstrahlung spectroscopy. J. Instrum. 17(1), C01054 (2022)
6. Sauli, F.: The gas electron multiplier (GEM): operating principles and applications. Nucl. Instrum. Methods Phys. Res. Sect. A Accel. Spectrom. Detect. Assoc. Equip. 805, 2–24 (2016)
7. Caruggi, F., et al.: Performance of a triple GEM detector equipped with Al-GEM foils for x-rays detection. Nucl. Instrum. Methods Phys. Res. Sect. A Accel. Spectrom. Detect. Assoc. Equip. 1047, 167855 (2023)
8. Pezzotta, A., et al.: GEMINI, a CMOS 180 nm mixed-signal 16-channel ASIC for Triple-GEM detectors readout. In: 2015 IEEE SENSORS - Proceedings (2015)
9. Muraro, A., et al.: Development and characterization of a new soft x-ray diagnostic concept for tokamaks. J. Instrum. 14(8), C08012 (2019)
10. Cancelli, S., et al.: Electronic readout characterisation of a new soft x-ray diagnostic for burning plasma. J. Instrum. 17(8), C08028 (2022)
11. Cancelli, S., et al.: Characterisation of N2-GEM: a beam monitor based on Ar-N2 gas mixture. J. Instrum. 18(5), C05005 (2023)
12. Caruggi, F., et al.: Development of a Triple-GEM detector with strip readout and GEMINI chip for x rays and neutron imaging. J. Instrum. 19(2), C02015 (2024)
13. Croci, G., et al.: nGEM fast neutron detectors for beam diagnostics. Nucl. Instrum. Methods Phys. Res. Sect. A Accel. Spectrom. Detect. Assoc. Equip. 720, 144–148 (2013)
14. Muraro, A., et al.: MBGEM: a stack of borated GEM detector for high efficiency thermal neutron detection. Eur. Phys. J. Plus 136(7), 1–14 (2021)
15. Cancelli, S., et al.: Development of a ceramic double thick GEM detector for transmission measurements at the VESUVIO instrument at ISIS. J. Instrum. 16(6), P06003 (2021)
16. Pilan, N., et al.: Study of high DC voltage breakdown between stainless steel electrodes separated by long vacuum gaps. Nucl. Fusion 60(7), 076010 (2020)
17. Caruggi, F., et al.: Development of a data analysis software for the XR-GEM installed at HVPTF and preliminary results. In: 2023 30th International Symposium on Discharges and Electrical Insulation in Vacuum (ISDEIV), pp. 29–32. IEEE, (2023)
18. Spada, E., et al.: Theoretical basis and experimental validation of the breakdown induced by rupture of dielectric layer model. IEEE Trans. Plasma Sci. 47(5), 2759–2764 (2019)
19. Diamond, W.T.: A model of gas desorption and radiation during initial high voltage conditioning in vacuum. J. Appl. Phys. 126(19), 193303 (2019)

How to cite this article: Caruggi, F., et al.: Analysis of micro-discharges fine dynamics via x-ray detection on the high voltage Padova test facility experiment. High Voltage. 10(4), 1043–1052 (2025). https://doi.org/10.1049/hve2.70042